The role of supraglacial debris in Himalaya-Karakoram debris-covered glacier systems

Morgan Jane Jones

(née Gibson)

A thesis submitted in fulfillment of the requirements for the degree of Doctor of Philosophy

18th September 2017

Department of Geography and Earth Sciences
Aberystwyth University

Supervisors: Professor Neil Glasser, Dr Tristram Irvine-Fynn, Dr Ann Rowan (University of Sheffield), Dr Duncan Quincey (University of Leeds)

Abstract

Spatiotemporal variability in supraglacial debris properties have the potential to affect estimations of mass balance for debris-covered glaciers. This thesis is concerned with identifying the extent to which debris properties vary in space and time, and the role of these variabilities in estimations of specific mass balance. The research presented uses a combination of methods, including statistical analysis of field data, mapping and classification of thermal and optical remotely sensed data, and numerical modelling. Near-surface debris temperature was measured in the field to investigate short term spatial and temporal variability in debris properties and its influence on debris temperature over a monsoon season. The strongest correlation between timeseries of near-surface debris temperature and meteorological controls was with air temperature, with lesser correlations between rate of change in air temperature and incoming shortwave radiation. Subtle spatial variability was also identified, controlled by site aspect and slope, grain lithology and size, and potentially moisture content and thermal conductance of the bulk debris layer. The occurrence of spatiotemporal variability in supraglacial debris distribution was identified on Baltoro Glacier over a sub-decadal timescale, considered to be primarily due to differences in input of debris to the glacier system through mass movement events. The importance of variability in debris properties was investigated using a surface energy balance and heat transfer model, where the influence of debris thickness, albedo and aerodynamic roughness length was tested. The modelling results, although not directly comparable to mass balance estimates for Khumbu Glacier, showed a 223% increase in total specific mass balance for Khumbu Glacier's debris-covered area over a monsoon season when a spatially variable debris layer was included. Including spatially variable albedo and aerodynamic roughness length along with debris thickness reduced estimates of specific mass balance, although were still higher than the base line model simulation. Consequently, this thesis confirms the occurrence of spatially and temporally variable supraglacial debris properties, over seasonal and sub-decadal periods, and that such variability is influential for estimates of glacier mass balance.

Acknowledgements

I would firstly like to thank the British Society for Geomorphology, the Royal Society (Research Grant RG120393) and the Department of Geography and Earth Sciences, Aberystwyth University for their contributions to fieldwork costs. I also wish to thank our Nepali guides, Karma, Tindu and Rajesh for their invaluable help during fieldwork. A large number of reviewers have also read my work, providing very useful critique for each of my papers, which. I think, has led to my research to be of higher quality.

The last four years have been full of exciting adventures, amazing opportunities and interesting people, and I am so pleased I accepted my PhD place. There have been a great number of people that I have shared the journey with; who have listened to me talk about my research, and PhD life in general. In particular I would like to thank Stephen Brough, Rachel Smedley, Jayne Kamintzis, Tom Holt, Helen Stockley-Jones, Stephen Jennings and Tristram Irvine-Fynn for listening to me ramble on about debris, glaciers and life in general. It has been a pleasure getting to know them all.

Huge thanks go to my supervisors; Neil Glasser, Tristram Irvine-Fynn, Ann Rowan and Duncan Quincey. They have provided continued support and encouragement throughout my PhD. Their positive approach to my work has been unwavering, and I feel like I am leaving my PhD with a group of friends rather than supervisors.

Last, and definitely not least, are my friends and family. My mum encouraged me to start this journey, and has provided financial backing throughout. Without this support I would not have started my PhD, let alone be handing in my thesis. I also thank my friends around the world, for bearing with me over the last 4 years! My final, and biggest, thank you goes to my husband, Josh Jones, for being there every single time I needed him with advice, a positive attitude, a listening ear and a hug.

Table of contents

List of figures

timeseries and meteorological timeseries for the studied period.

5.4. Box plots of near-surface debris temperature timeseries data.

5.5. Principal component models for the near-surface debris temperature timeseries at Site 14, and the occurrence of these principal components over the study period.

5.6. Correlation coefficient values for the relationship between on-glacier air temperature and near-surface debris temperature for each of the daytime and night-time cycles over the studied monsoon period.

6.1. The regional context of Baltoro Glacier and its tributary glaciers.

6.2. Examples of mass movement deposits and supraglacial water bodies on Baltoro Glacier derived from satellite imagery and associated geomorphological maps.

6.3. Geomorphological map of features identified on a tributary glacier of Baltoro Glacier.

6.4. Geomorphological map of Baltoro Glacier depicting the different supraglacaial debris units and associated features for 2012, with insets of differing debris distribution between 2001 and 2012.

7.1. Location of Baltoro Glacier in a regional and local context.

7.2. Spectral reflectance profiles of different lithologies of supraglacial debris identified on Baltoro Glacier.

7.3. Debris thickness maps of Baltoro Glacier for August 2001, 2004 and 2012.

7.4. Surface velocity maps of Baltoro Glacier for August 2001, 2004 and 2012.

7.5. Geomorphology maps of Baltoro Glacier for August 2001, 2004 and 2012.

7.6. Comparisons of features on Baltoro Glacier from geomorphology, surface velocity, debris thickness and debris thickness change maps.

7.7. Annual debris thickness change maps of Baltoro Glacier from August 2001–2004 and 2004–2012.

7.8. Sediment flux maps of Baltoro Glacier from August 2001–2004 and 2004–2012.

7.9. Schematic diagram of a debris-covered glacier system.

7.10. Geomorphological map and associated oblique satellite image of the moraine ridge between Trango Glacier and Baltoro Glacier.

8.1. A schematic diagram summarising the energy fluxes at the surface and through a supraglacial debris layer.

8.2. Location map of Khumbu Glacier in a regional and local setting, and a map of measurement locations on the debris-covered surface.

8.3. Site photos of locations where aerodynamic roughness length data were collected.

8.4. Timeseries of meteorological data used to force CMB-DEB.

8.5. Maps of debris thickness, albedo and aerodynamic roughness length used as variable inputs in the distributed model simulations.

8.6. Plots of negative mass change with increasing debris thickness, albedo and aerodynamic roughness length for point model simulations in which one variable was varied.

8.7. A surface plot of specific mass change for point-based model simulations in which all variables were varied simultaneously.

8.8. Box plot of specific mass change for each of the distributed model simulations.

8.9. Specific mass balance across Khumbu Glacier's debris-covered area calculated for simulations where all debris properties were spatially constant debris thickness was spatially variable and all variables were spatially variable, and the longitudinal profile of specifc mass balance for each of the model simulations above.

8.10. The subsurface thermal regime through the supraglacial debris layer for the cells with the minimum, mean and maximum specifc mass balance from distributed simulation 10.

8.11. An example Østrem curve formed from the specific mass balance calculated for each cell of the distributed simulation 10.

A1 Temperature differences recorded by free and contained iButton thermochron sensors and TinyTag sensors for air, water and ice in laboratory conditions.

List of tables

6.2. The total area and number of supraglacial water bodies on Baltoro Glacier in 2001, 2004 and 2012.

7.1. Satellite I.D., acquisition date and time for the ASTER datasets used for data analysis in mapping surface features on Baltoro Glacier.

7.2. Comparison of field point data of debris thickness and corresponding pixel values in the associated debris thickness maps.

8.1. Surface reflectance values for each of the supraglacial debris types found on Khumbu Glacier's debris covered surface.

8.2. Aerodynamic roughness length values collected on Khumbu Glacier's debris covered surface.

8.3. Ranges of debris thickness, albedo and aerodynamic roughness length used for model simulations, constrained from field data collected on Khumbu Glacier and previously published values.

8.4. Previously published values of debris layer thickness, albedo and aerodynamic roughness lengths.

8.5. The variable model inputs and specific balance results for the distributed model simulations.

8.6. The variable inputs and specific balance results for the cells with the maximum, mean and minimum specifc mass balance in Distributed Simulation 10.

A2. The rules used to classify clusters on Khumbu Glacier, used to map surface reflectance and aerodynamic roughness length across the debris-covered glacier surface.

A3. Error matrix for the surface reflectance classification undertaken on Khumbu Glacier's debris-covered surface.

A4. Error matrix for the surface roughness classification undertaken on Khumbu Glacier's debris-covered surface.

List of abbreviations

T_s	Near-surface debris temperature
SEB_{net}	Net energy balance at a glacier surface
SW_{net}	Net shortwave radiation (incoming and outgoing)
SW_{in}	Incoming shortwave radiation
SW_{out}	Outgoing shortwave radiation
LW_{net}	Net longwave radiation (incoming and outgoing)
LW_{in}	Incoming longwave radiation
LW_{out}	Outgoing longwave radiation
QH	Sensible heat transfer
QE	Latent heat transfer
QG	Ground heat flux
QR	Energy supplied by precipitation
QT	Energy used for temperature change in ice
SfM	Structure-from-Motion
z_0	Aerodynamic roughness length
GLOF	Glacial lake outburst flood
GPR	Ground penetrating radar
NIR	Near Infrared
ASTER	Advanced Spacebourne Thermal Emission and Reflection Radiometer
SRTM	Shuttle Radar Topography Mission
DEM	Digital Elevation Model
SETSM	Surface Extraction with TIN-based Search-space Minimization
UAV	Unmanned Aerial Vehicle
w.e.	Water Equivalent
iSOSIA	Integrated Second-Order Shallow Ice Approximation
ELA	Equilibrium Line Altitude
a.s.l.	Above Sea Level
T_s	Near-surface debris temperature
T_a	Air temperature
DOY	Day Of Year
T_{aP}	Off-glacier air temperature

T_{aG}	On-glacier air temperature
NR_{in}	Incoming net radiation
PCA	Principal Component Analysis
PC	Principal Aomponent
E	Nash-Sutcliffe efficiency coefficient
P	Precipitation
RH	Relative humidity
dT_a	Rate of change in on-glacier air temperature
SSW_{in}	Cumulative incoming shortwave radiation
SLW_{in}	Cumulative incoming longwave radiation
tP	Time since precipitation
TG	Tributary Glacier
ETM	Enhanced Thematic Mapper
GDEM	Global Digital Elevation Model
T_{ST}	Surface temperature
CMB	Climate Mass Balance model
CMB-DEB	Climate Mass Balance model with a supraglacial layer incorporated
dT/DT	Debris thickness
b_w	Specific water balance

Chapter 1: Introduction

Chapter 1: Introduction

1.1. Project rationale

Debris-covered glaciers exhibit a continuous layer of rock debris over the full width of at least some of their ablation zone (Kirkbride et al., 2011). The presence of a rock debris layer on a glacier surface forms a buffer between underlying glacier ice and the atmosphere, causing a debris-covered glacier ablation regime, hydrological network and response to climate change to differ from those of a clean-ice glacier (Østrem, 1959; Nakawo and Young, 1981, 1982; Nakawo and Rana, 1999; Fyffe, 2012; Nicholson and Benn, 2006; 2013). The effect of a debris layer on ablation is dependent on its thickness; below ~0.05 m a debris layer enhances ablation by lowering the albedo of a glacier surface, whilst debris layers with a thickness over ~0.05 m insulate underlying glacier ice and reduce ablation when compared to debris free ice. The relationship between debris thickness and ablation is non-linear, with a debris layer 1 m thick reducing ablation by at least 90% to that of debris free conditions (Figure 1.1; Østrem, 1959; Nakawo and Rana, 1999; Reznichenko et al., 2010).

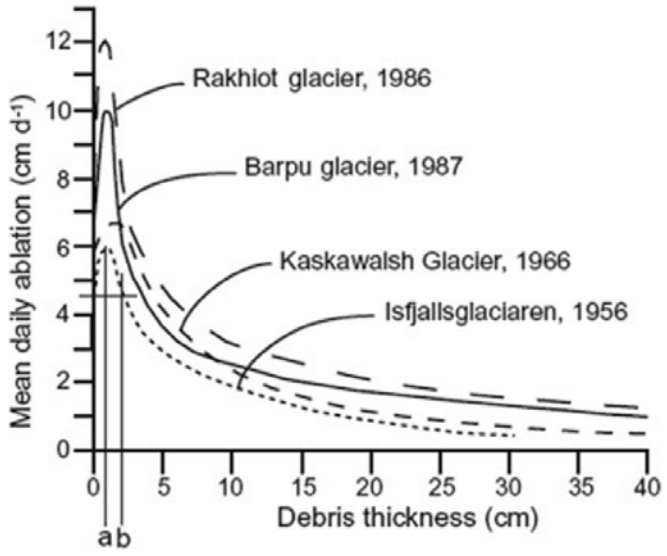

Figure 1.1: The Østrem curve, derived from empirical data, which displays the exponential relationship between debris thickness and ablation as debris thickness increases, and the extent to which this relationship varies between glaciers. (a) is the thickness at which maximum melt occurs (effective thickness), whilst (b) is the thickness at which melt becomes inhibited when compared to debris free conditions (critical thickness) (Nicholson and Benn, 2006).

Spatiotemporal variation in debris input, transport and distribution result in non-uniform debris distribution across a glacier surface (Kirkbride and Deline, 2013). Debris input to a glacier system is controlled by erosion, the rate of which varies temporally with variations in rock uplift and climate (Maisch et al., 1999; Heimsath and McGlynn, 2008). Debris transport is controlled by sub-, en- and supraglacial ice dynamics (Anderson and Anderson, 2016). Accumulation of debris on a glacier surface is controlled by the input of debris into a glacier system and the rate of englacial debris exhumation, which is determined by ablation rate and decreasing longitudinal velocity towards the glacier terminus (Scherler et al., 2011; Rowan et al., 2015). In a glacier system, supraglacial debris layer thickness primarily varies spatially and temporally due to differing rates of debris input by hillslope erosion along the glacier margins and through time (Scherler et al., 2011). Debris layer properties, such as albedo and thermal conductivity, also vary spatially due to differing debris lithologies (Nicholson and Benn, 2013), a result of varying geology of surrounding valley walls. Spatial variability in debris grain size is also dependent on lithology, as well as proximity to the debris source, the mode of debris transport, and the period of time a grain has been in the glacier system (Boulton, 1978; Fushimi et al., 1980).

To date, investigation into spatial variation in supraglacial debris properties has focused on mapping supraglacial debris layer thickness, using a combination of thermal and debris thickness data derived from remotely sensed and *in situ* data (e.g. Mihalcea et al., 2006; Zhang et al., 2011; Foster et al., 2012; Rounce and McKinney 2014; Minora et al., 2015; Soncini et al., 2016). These studies have included minimal, if any, consideration of the evolution of debris distribution through time. Limited exploration of spatial variability in supraglacial debris layer properties and their influence on ablation has also been undertaken. In most of these cases the data sets collected have been limited, and are unlikely to fully represent the extent of spatial variability in debris properties across a glacier surface. For example, Nicholson and Benn (2006; 2013) collected extensive measurements of surface reflectance, a proxy for albedo, on debris-covered ice in Svalbard, the Italian Alps and the Himalaya. However, these data have not been expanded to provide an inventory of albedo values for a wider range of debris-covered glaciers. Awareness that spatial variability

on other debris properties, including moisture content (e.g. Collier et al., 2014), porosity (e.g. Evatt et al., 2015) and surface roughness (e.g. Rounce et al., 2015; Miles et al., 2017; Quincey et al., 2017) also exists, but these data sets are limited and unlikely to show the full extent of spatial variability in these properties across a debris-covered glacier surface. As yet, temporal variability in such debris properties has had little to no research focus.

Consequently, surface energy balance and mass balance calculations for debris-covered glaciers currently omit spatial and temporal variations in debris properties, with the exception of numerical modelling undertaken by Rowan et al. (2015) and Anderson and Anderson (2016). Numerical models of debris-covered glaciers are therefore less developed than equivalent models for clean-ice glaciers, and consequently predictions for the response of debris-covered glaciers to climate change are less well constrained. Identifying the extent and rate at which supraglacial debris distributions vary across a glacier surface would enable numerical models to include more accurate estimations of supraglacial debris layers and their evolution through time, and the effect of such variability on mass balance and glacier dynamics. Ultimately, a more complete understanding of supraglacial debris layers would facilitate improved predictions of the response of debris-covered glaciers to climate change.

Understanding the response of debris-covered glaciers to climate change is particularly pertinent in the Himalaya-Karakoram. The Himalaya-Karakoram has the largest glacierised area outside of the Polar Regions, with over 32,000 glaciers covering an area of 41,000 km^2, which equates to around 6% of the world's glacierised area (Arendt et al., 2012). These glaciers provide meltwater to some of the world's largest rivers including the Indus, Brahmaputra and Ganges (Immerzeel et al., 2010), which provide a vital water resource for a fifth of the world's population (Bolch et al., 2012). Recent climate change has already resulted in area loss and thinning of the majority of glaciers in the Himalaya-Karakoram region, with the exception of the Karakoram (Bolch et al., 2012; Brun et al., 2017). During the mid 21st century decreasing glacier volume is expected to increase river discharge, but as glacier volume reaches a lower threshold in the late 21st to early 22nd centuries, river

discharge is expected to decrease (Immerzeel et al., 2010; Lutz et al., 2014). As the volume of glaciers in the Himalaya-Karakoram reduces in response to climate change, meltwater discharge to the region's rivers will ultimately reduce (Pritchard, 2017), resulting in a greater pressure on water resources for the large, developing populations of countries such as China, India, Bangladesh and Nepal (Akhtar et al., 2008; Kraaijenbrink et al., 2017). Constraining estimates of future changes in glacier mass balance is therefore integral to enable communities in Central and Southern Asia to mitigate against such environmental change.

Debris-covered glaciers are prevalent in the Himalaya-Karakoram, and the poor constraint of mass balance estimations for these glaciers currently hinders predictions of overall future changes in glaciers mass in the Himalaya-Karakoram, alongside large uncertainty in the nature of climatic changes that will occur in the future (Immereel et al., 2010; Bolch et al., 2012). Around 14–18% of the glacierised area in the Himalaya-Karakoram is debris covered, increasing to 36% in the Everest Region, and at least 50% of the ablation areas of many of the largest glaciers in the region are covered in supraglacial debris (Schereler et al., 2011; Kääb et al., 2012; Nuimura et al., 2012; Ragettli et al., 2015; Thakuri et al., 2014). Supraglacial debris is therefore influential to glacier mass balance in the Himalaya-Karakoram. Consequently, to understand the response of glaciers in the Himalaya-Karakoram to future climate change, and the impact of these changes on the human population of the region, it is imperative that the role of supraglacial debris in glacier mass balance is better constrained.

1.2. Thesis aim

The overall aim of this thesis is to investigate the extent of spatial and temporal variations in supraglacial debris properties for debris-covered glaciers in the Himalayan-Karakoram, and the role these variations play in mass balance of such glaciers.

1.3. Research questions arising from previous research

The aim of this thesis is based on a series of specific research questions that have been developed through consideration of the limitations in current understanding of debris-covered glaciers that exists at present and the need to refine predictions of the future response of these glaciers to climate change:

Q1: *How do supraglacial debris layer properties vary in space and time across a debris-covered glacier surface?*

Q2: *Over what timescale does a supraglacial debris layer evolve?*

Q3: *How does incorporating spatially and temporally varying debris characteristics into a surface energy balance model affect estimates of glacier mass change?*

Q4: *Could incorporation of spatiotemporal variability in supraglacial debris layers increase the accuracy of predictions for the response of Himalayan-Karakoram debris-covered glaciers to climate change?*

1.4. Thesis objectives

To achieve the aim of this thesis, and answer the research questions set, the following specific objectives have been identified:

- To explore the extent of spatial and temporal variations in near-surface debris temperature on a debris-covered glacier, as a parameter by which to investigate spatial and temporal variability in energy fluxes at a debris-covered glacier surface. This objective intends to address Question 1, with consideration of Question 3.

- To identify how debris distribution and associated supraglacial features, such as supraglacial ponds and debris thickness, vary over a sub-decadal timescale across a debris-covered glacier surface. This objective intends to address Questions 1 and 2.

- To investigate the extent to which spatial variations in debris thickness, albedo and aerodynamic roughness length affect total glacier ablation over a monsoon season. This objective intends to address Questions 1 and 3.

- To consider the role of spatiotemporal variability in supraglacial debris in the response of glaciers in the Himalaya-Karakoram to current and future climate change. Conclusions drawn from the previous three objectives will be used in the discussion of this objective in Chapter 9, which will consider Question 4.

1.5. Thesis outline

The research is presented in the form of four journal articles, or papers, each of which forms its own chapter and are at various stages of publication, outlined subsequently. Prior to these papers are four introductory chapters:

Chapter 1: Chapter 1 introduces the thesis and provides an overview of the importance of studying debris-covered glaciers in the Himalaya-Karakoram. The chapter outlines currently unanswered questions regarding debris-covered glaciers in the Himalaya-Karakoram and supraglacial debris layers in general, with a particular focus on spatiotemporal variability in supraglacial debris layer properties. The aim and objectives of the thesis are also introduced, followed by a summary of each thesis chapter and the relevance of each paper to the overall thesis aim and objectives.

Chapter 2: Chapter 2 presents an overview of the Himalaya-Karakoram mountain range, including the region's geological and glaciological history, climate, and glaciohydrological network. The aim fo this chapter is to provide rationale for the importance of understanding glaciers in the region. This chapter provides context as to why debris-covered glaciers are prolific in the Himalaya-Karakoram, how debris-covered glaciers in the region are different to other such glaciers around the world, and the importance of understanding the response of these glaciers to climate change.

Chapter 3: Chapter 3 provides a technical overview of current published research on debris-covered glaciers. This chapter specifically focuses on each of the key debris parameters considered important to ablation under a supraglacial debris layer and the potential for spatiotemporal variation in these properties. In Chapter 3 an overview of current published research on observing and monitoring debris-covered

glaciers is presented, as well as the current stage of numerical modelling for debris-covered glaciers.

Chapter 4: Chapter 4 provides a detailed overview of the two study sites; Baltoro Glacier and Khumbu Glacier, including a rationale for why these study sites were chosen and previous research undertaken on each glacier.

The four introductory chapters are followed by four chapters in journal article format. These chapters present the research undertaken for this thesis, and use a suite of techniques to answer the thesis aim and objectives. Research undertaken for Chapter 5 is predominantly based on statistical analysis of field data alongside data derived using a geographical information system. The research presented in Chapter 6 and 7 are based on data collected using remote sensing techniques and analysed in a geographical information system, the results of which have been verified using field data. Research presented in Chapter 7 is based on calculations of specific mass balance calculated using a numerical model, which includes ranges of debris properties derived from field data that were developed alongside remotely sensed data using a geographical information system. A summary of each of the chapters presenting the research undertaken for this thesis is provided subsequently.

Chapter 5: ***Paper I:*** **Gibson MJ,** Irvine-Fynn TDL, Rowan AV, Quincey DJ, Wagnon P, Homer R, Glasser NF. Variations in near-surface debris temperature through the summer monsoon on Khumbu Glacier, Nepal Himalaya.

Current state of publication*: Accepted following minor corrections. Earth Surface Processes and Landforms.*

Paper I aims to address the first objective of this thesis, and is specifically concerned with identifying spatial and temporal variability in near-surface debris temperature, which is controlled by debris layer properties and energy fluxes at and within the debris layer. Near-surface debris temperature controls the gradient at which energy is transferred through a debris layer, which is also a factor of the thickness of the debris layer. Debris surface properties also influence near-surface debris

temperature and energy exchange at the debris surface and within the debris layer. Near-surface debris temperature can therefore provide an insight into the extent to which debris and site properties other than debris layer thickness, such as albedo, debris grain size and site aspect, vary in space and time. The relative importance of these additional parameters, without inclusion of the influence of debris layer thickness, has not previously, to the authors' knowledge, been investigated in detail for a debris-covered glacier. In this study, the influence of debris layer thickness can be largely omitted as a control on debris surface temperature, as data was collected at sites where the debris layer was > 1 m thick; greater than the thickness at which the underlying ice influences debris surface temperature. Consequently, the surface processes, meteorological conditions and debris properties controlling debris surface temperature can be investigated.

Data included in Paper I consists of 16 timeseries of near-surface debris temperature (T_s) collected on Khumbu Glacier between 23rd May 2014 and 30th June 2014 using iButton thermochrons, alongside which site characteristics of each temperature sensor location were recorded. Meteorological data were supplied by Dr Patrick Wagnon, a co-author on the manuscript. Spatial and temporal variation in T_s were investigated using statistical analyses previously used in research of timeseries concerned with climatological investigations (e.g. Hannah, 2000), permafrost environments (e.g. Gubler et al., 2011; Guglielimin et al., 2012) and hydrological data (e.g. Irvine-Fynn et al., 2005). Temporal variation in T_s was investigated during the progression of a summer monsoon season. Seasonal, synoptic and diurnal patterns of T_s were identified, which displayed a decreasing trend in maximum T_s over the study period, and a shift in diurnal pattern as the monsoon progressed, manifested in a reduction in diurnal amplitude. Temporal variation in T_s was found to have a clear relationship with air temperature and incoming shortwave radiation, as well as the rate at which air temperature had changed in the preceding hour. Subtle spatial variations in T_s were also identified, which were controlled by aspect and slope of the site, and grain size and lithology. These spatial variations were therefore linked to albedo, porosity and the variability in the extent of shortwave radiation reaching the debris surface, as well as potentially controlled by moisture content and thermal conductivity of the debris layer.

Paper I confirms the existence of spatial and temporal variations in T_s on a monsoon-influenced glacier, but reinforces the complex interaction between energy fluxes and debris properties that influence T_s. The occurrence of this spatial and temporal variability has implications for temperature-index modelling of debris-covered glaciers and the use of debris surface temperature data to calculate debris layer thickness from satellite imagery, which both assume a direct relationship with debris surface temperature. Ultimately, the variability in T_s identified highlights the need to consider additional controls on the relationship between air temperature or debris layer thickness with debris surface temperature for both these methods.

Chapter 6: ***Paper II:*** **Gibson MJ,** Glasser NF, Quincey DJ, Rowan AV, Irvine-Fynn TDL. 2016. Changes in glacier surface cover on Baltoro Glacier, Karakoram, North Pakistan, 2001–2012.

Current state of publication*: Published on the 10th December 2016 in the Journal of Maps (vol. 13, no. 3, 100–108).*

Paper II aimed to address the second objective of this thesis through geomorphological mapping of Baltoro Glacier, Karakoram, at three time steps in 2001, 2004 and 2012. Specifically, the paper aimed to identify the different lithological units across the glacier surface. Although previous research has investigated distribution of debris thickness, there has been little investigation undertaken into the extent to which supraglacial debris lithology varies across a glacier surface. Identifying spatial variation in lithology is important as lithology controls albedo of a debris surface and thermal conductivity of a debris layer, and can therefore be assumed to be an important control on energy transfer into and through a supraglacial debris layer.

Supraglacial debris units were identified using optical satellite imagery and comparison of spectral reflectance profiles between units, in 2001, 2004 and 2012 on Baltoro Glacier, Karakoram. Lithology of these debris units was undertaken through identification of the valley wall lithology at which each debris unit was initiated. Supraglacial water bodies and mass movement scars were also mapped at each time

step. Whilst change in debris unit area was minimal, total area of supraglacial water bodies increased by 209% over the study period. A number of tributary glaciers showed evidence of dynamic behavior over the study period. Most importantly, supraglacial debris lithology was found to vary spatially and included gneiss, granite, schist and metasediments, all of which are likely to have differing albedo and thermal conductivity values. Consequently, Publication II concluded that incorporation of spatial variability in albedo and thermal conductivity for different lithologies of debris units should be considered when undertaking distributed surface energy balance modelling of debris-covered glaciers.

Chapter 7: ***Paper III:*** **Gibson MJ,** Glasser NF, Quincey DJ, Rowan AV, Irvine-Fynn TDL, Mayer C. Variations in debris distribution on Baltoro Glacier, Karakoram, North Pakistan.

Current state of publication*: Published on 15th October 2017 in Geomorphology (vol. 295, 572–585).*

Paper III aims to address the second objective of this thesis, through production and comparison of distributed debris thickness, surface velocity, debris thickness change and sediment flux maps for Baltoro Glacier, Karakoram, at three time steps between 2001 and 2012. Previous work on the debris thickness of Baltoro Glacier's supraglacial debris layer has been undertaken by Mihalcea et al. (2008a) and Minora et al. (2015), but neither study considered evolution of the debris layer through time. In this study, the debris thickness map initially produced by Mihalcea et al. (2008a) for August 2004 was recreated, and then the same relationship between debris layer thickness and debris surface temperature applied to thermal data acquired in August 2001 and August 2012. The 2012 debris thickness map was compared to field data to determine the uncertainty between satellite-derived debris thickness and true debris thickness point data. Surface velocity was derived from feature tracking of satellite data. Debris thickness change and sediment flux were derived from debris thickness and surface velocity maps. Patterns of debris thickness and debris thickness change were compared to surface velocity patterns across the glacier and geomorphological maps produced for Publication II.

A spatially consistent pattern of increasing debris thickness towards the glacier terminus existed at all time steps, with a transition from a series of medial moraines to a continuous debris cover downglacier. Debris thickness increased by around 0.05–0.09m a^{-1} over the study period, which is greater than calculated errors. Surface velocity was lowest at the glacier terminus, facilitating a build up of debris at the glacier tongue. Supraglacial water bodies were located in areas of thicker debris cover; up-glacier of confluences between tributary glaciers and the main debris tongue and in the lower and mid sections of the glacier. A lack of terminal moraine was observed, considered to be due to the debris fan type terminus, which also facilitated efficient drainage of the supraglacial debris layer, resulting in a lack of supraglacial water bodies near the terminus.

Paper III identified changes in debris thickness on Baltoro Glacier occurred over a sub-decadal timescale. A balance between surface velocity and debris input resulted in temporally constant input of debris into the glacier system. However, differing frequency and magnitude of mass movement events at all glacier margins punctuated the continuous supply of debris, and caused changes in debris distribution through time. It was therefore suggested that future surface energy balance and mass balance models for Baltoro Glacier should incorporate a rate of debris thickness change in input parameters for debris distribution, but that to do so effectively predictions of frequency of mass movement events need to be further constrained. Such evolution of the supraglacial debris layer is also likely on other debris-covered glaciers. Therefore, similar studies for other debris-covered glaciers are suggested to determine the extent to which rate of debris thickness change varies with glacier size, velocity and input of debris to the glacier system. This study concludes that a supraglacial debris layer should not be considered as a static entity, even on relatively short timescales, and that debris distribution is a result of a complex combination of surface velocity, debris input, englacial emergence of debris, and consequently sediment flux, which vary across a glacier surface and through time.

The combination of Paper II and Paper III enable a comprehensive interpretation of debris distribution over a sub-decadal timescale, which has not previously been considered extensively. The minimal research that exists into supraglacial debris

distribution in a glacier system through time is concerned with longer time periods (e.g. Anderson and Anderson, 2016; Rowan et al., 2015). Papers I–III provide a base for Paper IV, confirming debris distribution varies spatially, with regards to supraglacial debris layer thickness, lithology (and therefore albedo), and that surface velocity and magnitude and timing of debris input are temporally variable, which will both affect distribution of supraglacial debris sizes across a glacier surface.

Chapter 8: ***Paper IV:*** **Gibson MJ,** Rowan AV, Collier E, Quincey DJ, Irvine-Fynn TDL, Glasser NF, Wagnon P, Smith M, Porter PR. The role of spatially variable supraglacial debris properties in ablation of a Himalayan debris-covered glacier.

Current state of publication*: In preparation to be submitted to The Cryosphere.*

Paper IV aims to address the third objective of this thesis, through investigation of the extent to which spatial variations in debris layer thickness, albedo and aerodynamic roughness length affect estimations on mass balance for Khumbu Glacier across the 2014 monsoon season. Field data was collected in 2014 to identify the extent to which albedo, aerodynamic roughness length and debris thickness vary across the ablation zone of Khumbu Glacier. These data were used to constrain classifications of the debris surface into different lithologies and roughness categories, whilst the debris thickness map developed by Soncini et al. (2016) for Khumbu Glacier was reproduced. A surface energy balance and heat transfer model was used to undertake a sensitivity analyses for albedo, aerodynamic roughness length and debris thickness. The distributed inputs of albedo, aerodynamic roughness length and debris thickness were then included as inputs into a distributed surface energy balance and heat transfer model, to compare the influence of each spatially variable parameter on mass balance estimations for Khumbu Glacier over a monsoon season. The model simulations results calculated specific mass balance, as accumulation was also simulated using precipitation and air temperature data to determine when precipitation fell as snow.

Three sets of model simulations were undertaken; point simulations in which only one debris property under investigation was varied at any one time, point simulations where all debris properties were varied simultaneously, and distributed simulations where cell-based maps of the three chosen variables were incorporated into the model. The distributed debris thickness map was the reproduced map of that used by Soncini et al. (2016), whilst the maps of albedo and aerodynamic roughness were the result of classification of Pleiades satellite data (acquired 19th May 2016) for the debris surface of Khumbu Glacier, constrained by field data. The cells identified as debris covered in the debris thickness map determined the model domain.

Debris thickness was found to be the first order control on spatial variability in ablation, followed by albedo and then aerodynamic roughness length. In single-variable point model simulations debris thickness reproduced an Østrem curve with an effective thickness of 0.28 m. In multiple-variable point model simulations, albedo and aerodynamic roughness length were most influential when the debris layer was less than 0.2 m thick. Nine distributed model simulations were undertaken, within which each variable was included separately and in all combinations with the two other variables. The inclusion of spatially variable debris thickness, whilst albedo and aerodynamic roughness length (z_0) were spatially constant, resulted in an increase in total specific mass balance for the debris-covered surface of 223%, compared to the base line model simulation in which each of the tested debris variables were spatially constant. The inclusion of spatially variable albedo and aerodynamic roughness length independently resulted in a difference from the base line simulation of 48% and 4%, respectively, whilst when varied together with spatially constant debris thickness resulted in a difference of 47%. The simulation in which all spatially variable inputs were included resulted in an increase of 60% from the baseline model, and a decrease of 51% from the simulation including only spatially variable debris thickness. Although a lack of *in situ* mass balance data inhibited identification of the most accurate of these simulations results, the influence of spatially variable debris properties was confirmed. Inclusion of spatially variable debris properties in previous research has been restricted to spatially variable debris thickness (e.g. Minora et al., 2015; Soncini et al., 2016; Immerzeel et al., 2015; Ragettli et al., 2015).

However, these results suggest that only including spatial variability for a single debris property may lead to increased uncertainty in specific mass balance.

Chapter 9 (discussion) and 10 (conclusion): Chapter 9: Discussion, brings together the four papers preceeding it, and discusses the main findings of the thesis with regards to the thesis aim, research questions and the first three thesis objectives. The fourth objective is subsequently discussed considering all research presented in Chapters 1–8, including critical reflection of the methodology and methods used in this thesis, and the contribution the research presented has made to the academic field. A summary of the thesis and future work to be undertaken is presented in Chapter 10: Conclusion.

The thesis discussion considers each of the questions posed in Section 1.3, ultimately identifying spatiotemporal variation in supraglacial debris properties exists. This conclusion provides a rationale for the numerical modelling undertaken in Paper 4, which confirms that inclusion of spatial variability in debris properties has a notable influence on mass balance estimates for debris-covered glacier surfaces. Consequently, future work should be concerned with constraining spatial variability in debris properties, most notable aerodynamic roughness length, and developing a two-fold modelling approach to enable spatiotemporal variability in debris properties to be incorporating into modelling procedures.

Chapter 2: The Himalaya

2. The Himalaya

2.1. Regional overview

The Himalaya-Karakoram mountain range, which in its entirety also includes the Hindu Kush (not discussed in this thesis), extends from Afghanistan in the west to Myanmar in the east, with a length of around 3,500 km and an area of around 3,441,719 km^2 (Figure 2.1; Sharma and Pratap, 1994; Leech et al., 2010). The Himalaya-Karakoram contains all of the world's mountains higher than 7000 m above sea level (a.s.l.) and the headwaters of the ten largest river systems in Asia, which include the Ganges, Brahmaputra, Indus and Mekong (Figure 2.1; ICIMOD, 2016). Water originating in the Himalaya-Karakoram supplies water to some of the most highly populated countries in the world, including India, China and Bangladesh, providing water for hydroelectrical power, industry and irrigation across Asia; water from the Indus and Ganges is used to irrigate agricultural land covering an area of over 280,000 km^2 (Table 2.1; Immerzeel et al., 2010). The South Asian Summer Monsoon and Mid-latitude Westerlies dominate the climate in the region (Bookhagen and Burbank, 2010; Immerzeel et al., 2010).

Glacier ice covers an area of around 40, 775 km^2 in the Himalaya-Karakoram (Bolch et al., 2012), with the largest glacierised area found in the Karakoram (Figure 2.2; Table 2.2; Bajracharya and Shrestha, 2011; Bolch et al., 2012). Debris-covered ie constitutes around 9% of glacierised area in the Karakoram and between 13 and 15% in the Himalaya (Western, Central and Eastern) (Kääb et al., 2012). Glaciers constitute around 1–3% of the region's river catchment area in the Himalaya-Karakoram (Table 2.1; Immerzeel et al., 2010), the discharge of which provide water to around 1.3 billion people (Akhtar et al., 2009; Bookhagen and Burbank, 2010; Immerzeel, 2010). Summer monsoon-induced precipitation and positive daytime temperatures between June and September cause glaciers in the Central and Eastern Himalayan to ablate and accumulate mass concurrently (Ageta and Higuchi, 1984; Benn and Lehmkuhl, 2000; Bookhagen and Burbank, 2010; Bolch et al., 2012), and are consequently identified as 'summer-accumulation-type' glaciers (Ageta and Higuchi, 1984). The annual ablation regime of glaciers in the Central and Eastern Himalaya play an important role in regulating water supply to the region's human population; glacier

melt provides a supply of water during the 'shoulder season' between summer monsoon-induced and winter precipitation (Xu et al., 2009; Lutz et al., 2014).

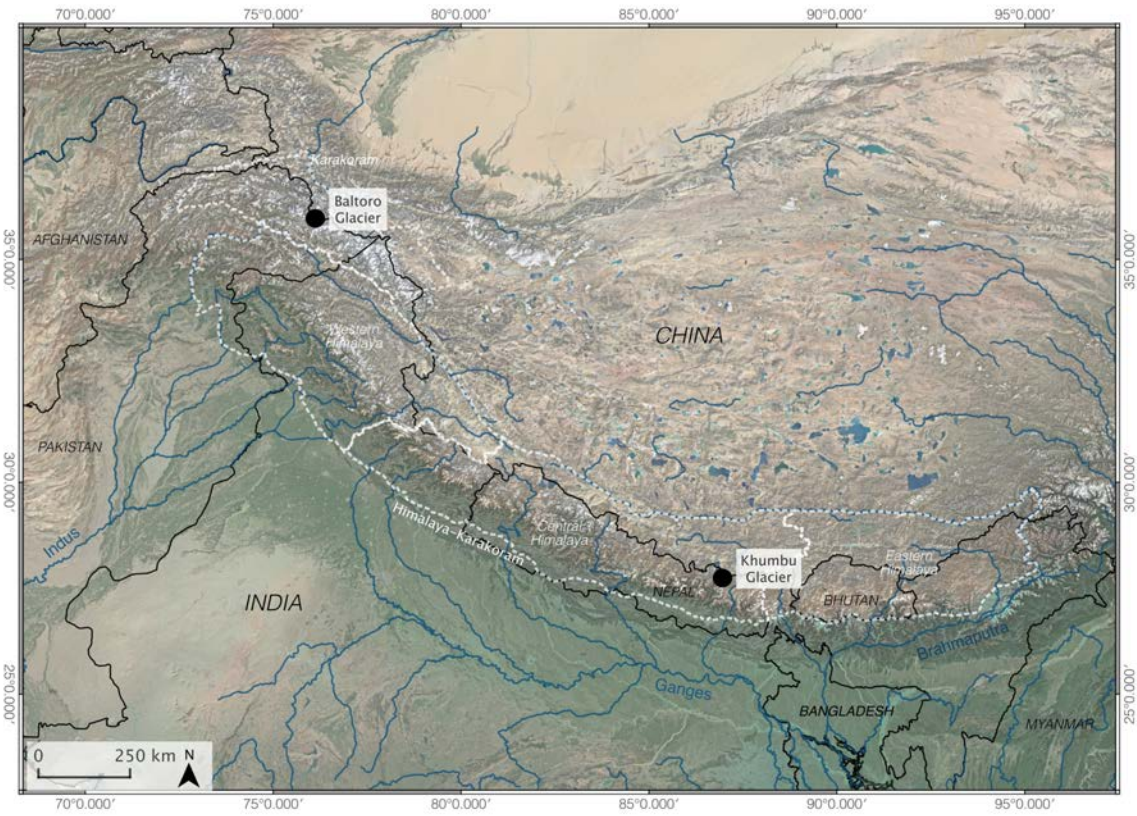

Figure 2.1: The Himalayan-Karakoram, with regions, based on the difference in prevailing climate in each region (Bolch et al., 2012), river networks and topography within the region and the locations of the study sites for this thesis; the Khumbu and Baltoro glaciers.

Table 2.1: Characteristics of four major Southeast Asian river networks. Reproduced from Immerzeel et al. (2010).

Parameter	Indus	Ganges	Brahmaputra	Yangtze
Total area (km²)	1,005,786	990,316	525,797	2,055,529
Total population (10^3)	209,619	477,937	62,421	586,006
Annual basin precipitation (mm)	423	1,035	1,071	1,002
Glacierised area (%)	2.2	1.0	3.1	0.1

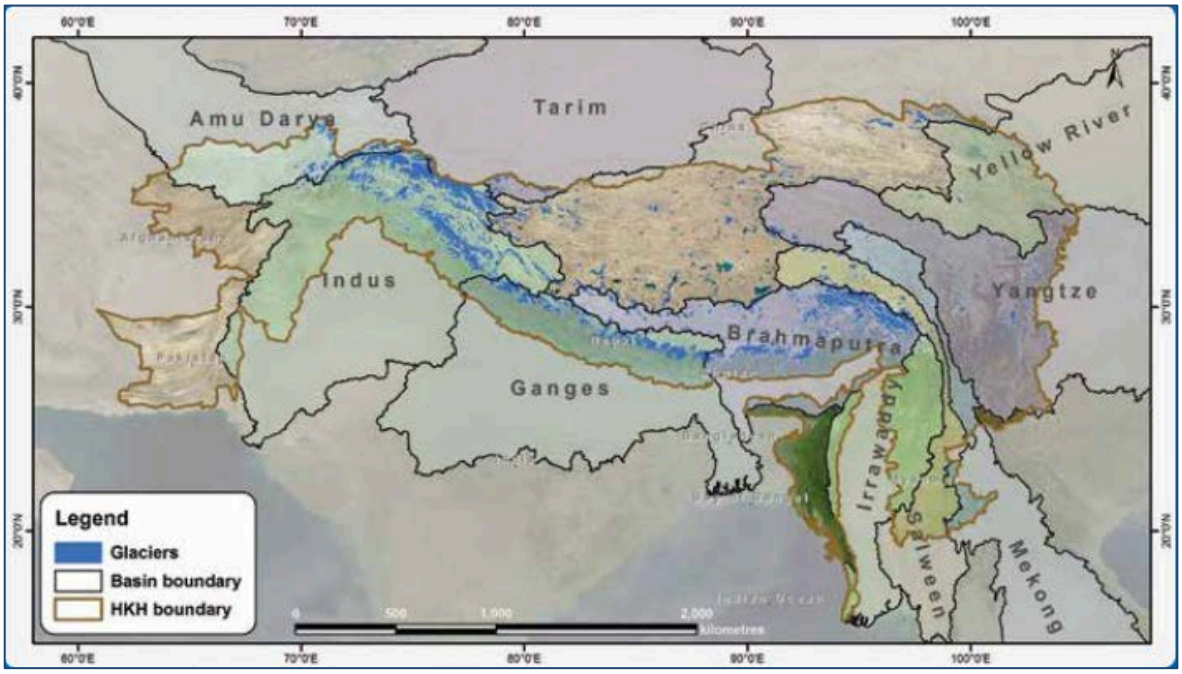

Irrigated area (km²)	144,900	156,300	5,989	168,400

Figure 2.2: Glacierised area in the Himalaya-Karakoram. Reproduced from Bajracharya and Shrestha, 2011.

Table 2.2: Glacierised area in each of the four regions of the Himalaya-Karakoram identified using Landsat ETM+ data acquired in 2006 (Bolch et al., 2012).

Region	Area (km^2)
Karakoram	17,946
Western Himalaya	8,943
Central Himalaya	9,940
Eastern Himalaya	3,946

Countries within the hydrological catchment area of the Himalaya-Karakoram are some of the poorest in the world with dense populations, low economic development and a reliance on agriculture (Shrestha, 2011). Many countries in the Himalaya-Karakoram region have poor infrastructure and are politically unstable, which, alongside struggling economies, means adaptation to and mitigation for climate change is challenging (Stern, 2007). Current and future changes in climate, and subsequent changes in water supply due to glacier melt, are likely to have a significant impact on these developing countries, causing changes in crop growing cycles and long-term reduction in river discharge. Alongside an increasing global population, pressure on water resources in these Asian countries will increase in the coming centuries (Parry et al., 2007; Pritchard, 2017). To predict future pressures on water resources in these Asian countries reliant on rivers originating from the Himalaya-Karakoram, it is imperative that changes in glacier mass balance are estimated accurately.

2.1.1. Geological history

Formation of the Himalaya-Karakoram mountain range was initiated around 20 Ma, following closure of the Indus Ocean and initiation of subduction of the Indian tectonic plate under the Eurasian plate (Powell and Conaghan, 1973). High-grade regional metamorphism and crustal thickening resulted in extensive folding and faulting over the next 20 Ma, and the formation of an accretionary wedge around 75

km thick along the Indus suture zone (Mattauer, 1986). Within the accretionary wedge, sedimentary units derived from the Indus Ocean were uplifted and metamorphosed, resulting in formation of low- to high-grade schist, granite and gneiss lithologies throughout the region, as well as some pockets of original unmetamorphosed sedimentary deposits in some isolated basins across the mountain range (Searle, 1987). Collision of the Indian and Eurasian continental plates is still active today and the range is currently uplifting at a rate of around 0.1 m a^{-1} (Zhong and Ding, 1996).

The formation of the Himalaya-Karakoram mountain range resulted in the development of summer monsoon weather systems and redistributed of the region's hydrological network to form the contemporary river network (Brookfield, 1998; Zhisheng et al., 2001). As a consequence of ongoing continental collision the Himalaya-Karakoram experiences frequent earthquakes. The most notable recent earthquake was the magnitude 7.8 Gorkha Earthquake on the 25th of April 2015, which killed nearly 9,000 people and destroyed infrastructure and buildings throughout Nepal.

Much of the geology in the mountain range has not been mapped in detail due to the remote nature of the region and many exposures being glacierised or on steep, inaccessible hillslopes. However, two regions that have been mapped in detail are the Khumbu region (e.g. Searle et al., 2003) and the Baltoro region (e.g. Searle et al., 2010), both of which are dominated by schist and granite. The bedrock geology of the Khumbu region is characterised by leucogranites, which have facilitated formation of the region's high altitude mountains (Searle et al., 2003). The Baltoro Batholith dominates the Baltoro area, which forms part of the Karakoram metamorphic complex.

2.1.2. Weather and climate of the Himalaya-Karakoram

Climate varies from east to west along the length of the Himalaya-Karakoram. Mid-latitude Westerlies, hereafter known as the Westerlies, influence the Western Himalaya and Karakoram climate (Benn and Owen, 1998; Anders et al., 2006; Bookhagen and Burbank, 2010), whilst the climate of the Central and Eastern

Himalaya is dominated by the South Asian Summer Monsoon (Bookhagen and Burbank, 2010). In addition to large scale weather patterns, the climate along the mountain range is further complicated by microclimatic conditions, which occur due to varying topography between valleys (Bohner, 2006; Dortch et al., 2011). The Westerlies also control the dominant wind direction throughout the Himalaya-Karakoram (Lang and Barros, 2004; Yihui and Chan, 2005), which predominantly travel from west to east. Currently precipitation in the northwest region of the Himalaya-Karakoram is increasing due to increasing temperatures in the Northern Hemisphere, and a resultant increase in moisture content carried in the Westerlies atmospheric system (Lutz et al., 2014).

The South Asian Summer Monsoon, hereafter known as the monsoon, strongly influences the climate in the majority of the Himalayan region (Bookhagen and Burbank, 2010). The monsoon occurs from June to October and provides the Central and Eastern Himalaya with 80% of its annual precipitation (Shrestha et al., 2000). Monsoonal weather patterns are initiated at the end of May by an abrupt reversal in temperature gradient between the Indian Ocean and Tibetan Plateau, due to warming of the Tibetan Plateau by sensible heat fluxes (Li and Yanai, 1996; Yanai and Wu, 2006; Rajagopalan and Molnar, 2013). Consequentially, primary wind direction changes during the monsoon season from westerly to southeasterly, which result in wind flow from the Bay of Bengal to the Tibetan Plateau (Bookhagen et al., 2005; Prive and Plumb, 2007). The Himalaya-Karakoram is an orographic barrier to this wind pattern (Boos et al., 2010), resulting in deposition of water collected by the monsoon weather system in the Bay of Bengal as snow and rain over the mountain range (Bookhagen and Burbank, 2006; 2010; Galewsky, 2009).

The intensity of the monsoon varies annually, with mean variations in summer precipitation of around 10%. Although monsoon-induced precipitation has decreased in the second half of the 20th century, changes in monsoon intensity as a result of current and future climate change are expected to cause an increase in precipitation over the 21st century (Figure 2.3; Turner and Annamalai, 2012). The switch in precipitation trends is attributed to a predicted change in the land–sea temperature gradient in the Bay of Bengal and subsequent increase in atmospheric humidity

(Sutton et al., 2007). In the latter 21st century and 22nd century monsoon circulation is predicted to decrease alongside increasing precipitation, although much uncertainty still exists between Global Climate Models (GCMs) as to the nature of these future monsoonal trends (Douville et al., 2000; Ueda et al., 2006).

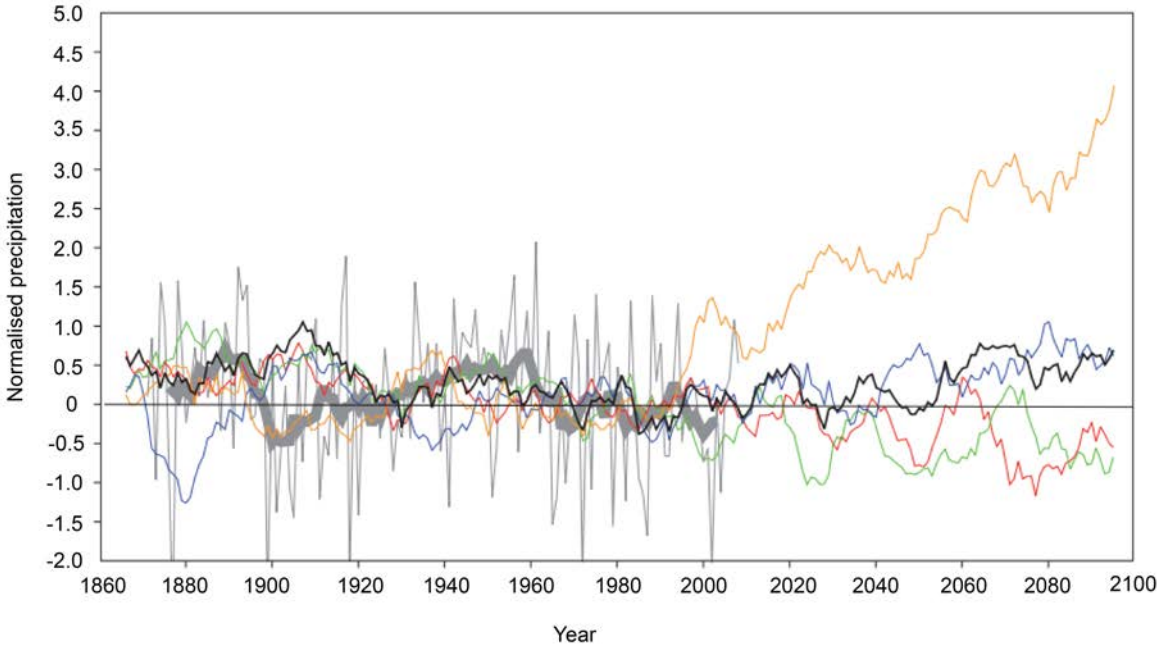

Figure 2.3: Historical patterns of monsoonal rainfall from climate records (grey lines), recreated by four Global Climate Models (yellow, red, green, blue lines), showing a decreasing trend of precipitation between 1860 and 2000. Predictions of future trends of increasing precipitation (2000–2100) are shown, produced by the four Global Climate Models, alongside the mean modelled trend (black line). Disparity between modelled data highlights the difficultly in accurately predicting future monsoon trends. Reproduced from Ueda et al., 2006.

2.1.3. Glacio-hydrological regime of the Himalaya-Karakoram

The Himalaya-Karakoram river network is primarily constrained by fold and fault structures within the mountain range. Beyond their headwaters, these rivers join and flow along the front of the mountain range (Hallet and Molnar, 2001; Jamieson et al., 2004). Annual hydrological regime of rivers in the Himalaya-Karakoram differs

between catchments due to spatially varying climate (Thayyan and Gergan, 2010; Immerzeel et al., 2012). In the west of the region, snowmelt causes peak flow around March, similar to an Alpine catchment, whilst in cold-arid areas such as Ladakh in the Western Himalaya, river runoff peaks in August and is almost entirely controlled by glacier melt (Figure 2.4). In the rest of the Himalaya a combination of monsoon precipitation and concurrent glacier melt means peak flow also occurs in August, but river discharge is several orders of magnitude higher than that of cold-arid regions in the mountain range (Thayyen and Gergan, 2010).

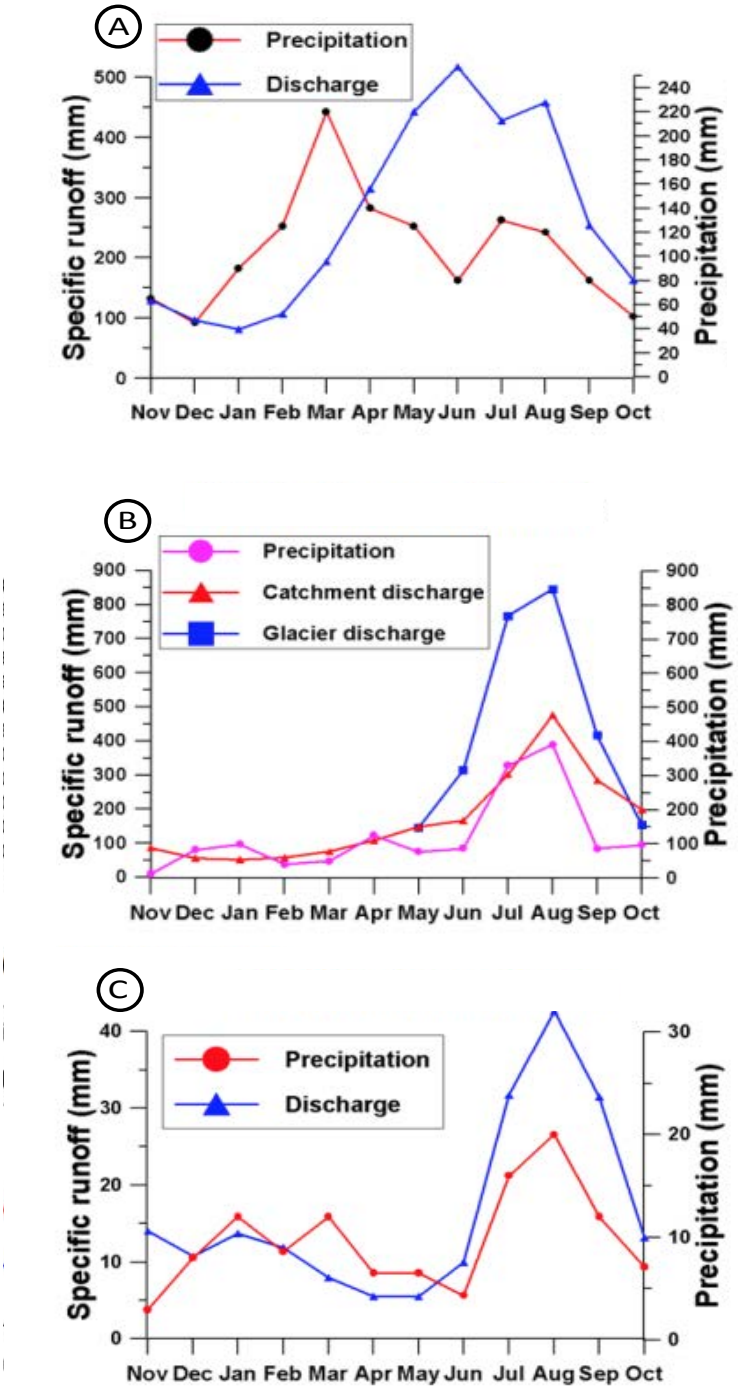

Figure 2.4: The comparative temporal distribution of runoff and precipitation for (a) Alpine, (b) Central-eastern Himalayan and (c) Cold-arid catchments in the Himalayan-Karakoram (Thayyen and Gergan, 2010). Note the difference in y-axis scales between plots.

Predicted changes in temperature and precipitation in the 21st and 22nd centuries are expected to have a substantial effect on the glacio-hydrologlogical network of the Himalaya-Karakoram (Immerzeel et al., 2009). Predicting the response of hydrological regimes to future climate change is challenging, due to high spatial heterogeneity in climate across the region, sparse data due to the remote nature of much of the region, and uncertainty in modelling procedures, including estimations of ablation for debris-covered glaciers (Shrestha, 2000; Beniston, 2003; Immerzeel et al., 2010; Pellicciotti et al., 2012).

With contemporary climate change, river discharge in the Himalaya-Karakoram is initially predicted to increase by around 0.05 m^3 s^{-1} per annum during the 21st century, due to a 10% increase in precipitation and an initial increase in glacier meltwater volume compared to present day (Meehl et al., 2007; Bolch et al., 2012; Immerzeel et al., 2012; Lutz et al., 2014; Pachauri, 2014). However, upstream water supplies, which primarily originates from glacier melt, are predicted to decrease between 2046 and 2065 by -8.4% in the Upper Indus catchment, -17.6% in the Ganges catchment, and -19.6% in the Brahamputra catchment, upon reaching a threshold of glacier volume loss (Immerzeel et al., 2010; Lutz et al., 2014). In the late 21st century and beyond, glacier volume is expected to decrease dramatically. For example, the volume of glacier ice in the Baltoro region is predicted to decrease by 50% between now and 2100 (Immerzeel et al., 2013). Such pronounced glacier shrinkage is predicted throughout the Himalaya-Karakoram, and will result in a reduced contribution of water to river catchments from glacier meltwater and a subsequent decrease in river discharge (Miller et al., 2012). Reduction in glacier melt may be partially compensated for by monsoon intensification and increased precipitation, but glacierised catchments in the Himalaya-Karakoram may evolve to be glacier-free catchments over the next few centuries (Bolch et al., 2012). However, as with climate predictions, confirmation of future trends in hydrological regime of the region is poorly constrained due to disagreement between different numerical models (Pelliciotti et al., 2012; Turner and Annamalai, 2012).

2.1.4. Past glacier extent in the Himalaya-Karakoram

Understanding past and current glacier extent in the Himalaya-Karakoram is integral to effectively predicting future glacier change (Cogley et al., 2011). Past glacier extent, and the climate conditions under which these glacier volumes existed, have been determined using identification of glacially derived landforms and sedimentary sequences throughout the Himalaya-Karakoram (Benn and Owen, 2002; Owen and Dortch, 2014). Recent development in geographical and geochronological techniques, including remote sensing and geochronology, have made it possible to conduct large scale mapping of landforms and sedimentary sequences, and to date glacial sequences in the Himalaya-Karakoram (e.g. Benn and Owen, 2002; Finkel et al., 2003; Richard et al., 2000). Dating glacier successions in the mountain range is challenging due to the lack of organic material for radiocarbon dating and a lack of bleached sediments for luminescence dating (Fuchs and Owen, 2008). However, terrestrial cosmogenic nuclide dating has now been applied to the Himalaya-Karakoram more than any other mountain range in the world, with >1700 ^{10}Be ages from moraines and further ages from bedrock surfaces (Owen and Dortch, 2014), which has led to a more comprehensive understanding of the timing of region-wide glaciation. Glaciers in the Himalaya-Karakoram have consequently been found to have undergone multiple cycles of advance and recession during the Quaternary (Owen, 2009; Owen et al., 2009; Owen and Dortch, 2014).

The most recent period of glacier advance in the Himalaya-Karakoram occurred during the Little Ice Age (LIA; 1300–1850 CE; Owen et al., 2009; Rowan, 2017). Glacial reconstructions suggest alpine-style glaciation throughout the region during the last 2–3 glacial cycles (Shi, 2002), although an alternative suggestion of an extensive ice sheet across the Tibetan Plateau during this period also exists (Kuhle, 1993; 1995). Periods of glacier advance in the Himalaya-Karakoram have been primarily controlled by periods of colder atmospheric temperatures, some of which have led to advances of glacier termini of the order of several kilometres. However, during the Last Glacial Maximum (~18 Ma) glacier advance, due to an increase in monsoon intensity and subsequently increased precipitation, was of the order of 10 km in some cases (Owen et al., 2002).

As is true for the current glacial extent in the Himalaya-Karakoram, glacier extent in past glacial cycles varied spatially in response to climatic gradients and topographic controls (Owen and Benn, 2005; Owen, 2009). In the Central Himalaya at least five major glacial stages have occurred since the Last Glacial Maximum. In the oldest glacial stage, valleys in the region were entirely filled with glacier ice; in the Baltoro valley moraines have been identified from this glacier stage over 80 km downstream of Baltoro Glacier's present-day terminus position (Seong et al., 2007). Glacier cycles in the Central Karakoram have been attributed to variations in intensity of the monsoon, which in more intense periods would have penetrated into the Karakoram and increased precipitation in the region, resulting in positive glacier mass balance (Sirocko et al., 1991; Seong et al., 2007). In the Central Himalaya, specifically the Khumbu Region, at least 8 glacial cycles have been identified during the Quaternary, linked to variations in monsoon intensity. Periods of glacier advance in the Khumbu region also formed broad valley glaciers, similar to those in the Central Karakoram (Owen et al., 2009).

2.1.5. Current glacier extent in the Himalaya-Karakoram

Understanding current glacier extent and rate of glacier change in the Himalaya-Karakoram, and the influence of parameters such as ice thickness, debris-covered area and surge-type behaviour, is integral to the successful prediction of glacier mass loss in response to current and future climate change, as these data will constrain numerical modelling estimations of glacier change. Differing climatic conditions across the Himalaya-Karakoram cause spatial variability in glacier mass balance and their annual ablation regimes. Mass balance data for glaciers in the Himalaya-Karakoram is scarce due to a lack of *in situ* data and difficulty in identifying glacier margins due to the presence of perennial snow cover and supraglacial debris (Paul et al., 2004). However, determining current glacier mass balance in the Himalaya-Karakoram has been aided considerably by the use of remotely sensed data (e.g Scherler et al., 2011), which has allowed inaccessible glaciers to be monitored without the need for fieldwork (Bishop et al., 2000).

Equilibrium Line Altitude (ELA), the elevation at which accumulation is equal to ablation over an annual cycle, varies across the Himalaya-Karakoram by around 1600

m, from around 4600 to 6200 m a.s.l. (Owen and Benn, 2005). Current mean ice thickness of glaciers in the Himalaya-Karakoram, estimated from satellite data, is thought to be around 86 m in the Himalaya and 172 m in the Karakoram (Huss and Farinotti, 2012), whilst ground-based studies have identified ice thicknesses between 15 m and 540 m across the mountain range (e.g. Gergan et al., 1999; Gades et al., 2000; Gantayat et al., 2014). Glaciers in the Karakoram advanced at a mean rate of 8±12 m a^{-1} between 2000 and 2008 (Scherler et al., 2011; Gardelle et al., 2012; Minora et al., 2013). However, the rest of the region's glaciers are experiencing mass loss. In the Western Himalaya glaciers are experiencing mass loss of the order of around –0.85 m a^{-1} between 1999 and 2004 (Berthier et al., 2007), whilst in the Khumbu region around 0.5 m of surface lowering occurred on glaciers between 1962 and 2005 (Bolch et al., 2008). Although studies differ in their estimations total mass change between 2000 and 2016 for glaciers in the Himalaya-Karakoram are between 0.18±0.04 m a^{-1} w.e. and 0.21±0.05 m a^{-1} w.e. and the majority of glaciers in the region are currently considered out of balance with the climate, meaning that even if climate change was fixed at present day conditions glacier mass loss would continue for several more decades (Kääb et al., 2012; Brun et al., 2017). Alongside mass loss of these glaciers, the proportion of debris-covered area has increased by around 5% between 1962 and 2005 (Bolch et al., 2011). As with previous changes in glacier mass balance in the Himalaya-Karakoram, the current trend of mass loss has occurred alongside variability in monsoon intensity. However, numerical modelling of the relationship between glacier mass balance and monsoon variability has demonstrated that glacier mass loss is now greater than can be attributed to monsoon variability (Mölg et al., 2014), and so future glacier extent is expected to be a primarily driven by climate change.

2.1.6. Future glacier extent in the Himalaya-Karakoram

In the Fourth Assessment Report produced by the Intergovernmental Panel on Climate Change (IPCC) in 2007 it was wrongly stated that Himalayan glaciers would disappear by 2035 (Cruz et al., 2007). Attempts to rectify this error highlighted how little was known about the future of glaciers in the Himalaya-Karakoram, which generated a renewed research interest in the region (Cogley et al., 2010). In the following decade much work has been undertaken to further predictions of future

glacier extent (e.g. Scherler et al., 2011; Bolch et al., 2012) and hydrological regimes in the Himalaya-Karakoram (e.g. Immerzeel et al., 2010; Minora et al., 2015; Soncini et al., 2016), both on region-wide scale (e.g. Immerzeel et al., 2010; Scherler et al., 2011; Bolch et al., 2012; Miller et al., 2012) and in more localised areas (e.g. Shea et al., 2015; Rowan et al., 2015; Ragettli et al., 2015).

Projected mass loss of mountain glacier globally is of the order of 10–70% by 2100, under all IPCC Scenarios (Radic and Hock, 2011; Marzeion et al., 2012), with some of the greatest percentage volume predicted to be lost in the Himalaya (Bolch et al., 2012). Glacier change in the Himalaya-Karakoram during the 21st century and beyond will be controlled by changes in atmospheric temperature and precipitation. By 2100 atmospheric temperature is expected to rise by up to 5°C in the Himalaya-Karakoram, around 1.5°C higher than the global average, with up to a 21% increase in precipitation (IPCC, 2014). Much of this change in climate is expected to occur between 2071 and 2100. Due to the summer-accumulation regime of Himalayan glaciers such variations in precipitation and atmospheric temperature will have a twofold impact on glacier mass balance during the summer, with precipitation expected to fall as rain rather than snow, which will enhance glacier ablation rather than contribute to their mass, in addition to a conventional increase in ablation due to higher and more temporally extensive positive air temperatures (Meehl et al., 2007).

Predictions of glacier mass vary considerably between glaciers in the Himalaya-Karakoram, both spatially and from one study to another. In the Langtang catchment, Central Himalaya, a mass loss of 75% is predicted by 2088 by Immerzeel et al. (2012), whilst Ragettli et al. (2015) predicted an area loss of between 35–55% for clean-ice glaciers and 25–33% for debris-covered glaciers by 2100. Shea et al. (2015) predicted glacier mass loss of between 70% and 99% for glaciers in the Khumbu region, whilst Rowan et al. (2015) predict a mass loss of around 10% for Khumbu Glacier over the same period. Disparity between predictions for future glacier mass loss from numerical models is primarily due to variations in modelling techniques and how debris-covered ice is incorporated. Immerzeel et al. (2012) incorporated a basic ablation process beneath a supraglacial debris layer, whilst Ragettli et al. (2015) used a more complex approach, considering spatial variability in debris thickness and

surface energy balance of debris. Shea et al. (2015) assumed temporally constant debris cover, whilst debris in the glacier system modelled by Rowan et al. (2015) evolved over the study period, but did not incorporate the effect of surface energy balance of a debris-covered glacier surface and the subsequent effect this would have on ablation.

Whilst numerical models of debris-covered glaciers that incorporate evolution of the debris layer (e.g. Rowan et al., 2015) provide a more realistic scenario for determining glacier change, they still lack incorporation of detailed spatial variation in debris properties and the influence of supraglacial lakes and ice cliffs on glacier mass balance, which may further explain current discrepancies between predicted and actual mass loss. Additionally, the relative rate of mass loss between debris-covered and clean-ice glaciers is still in contention. A number of studies have calculated comparable rates of elevation change for debris-covered and clean-ice glaciers, termed the 'debris cover anomaly', and attributed to high rates of ablation at ice cliffs and supraglacial ponds (Kääb et al., 2012; Gardelle et al., 2013; Miles et al., 2016). However, more localised and field-based studies (Ragletti et al., 2015; Vincent et al., 2016) found changes in mass balance to differ between debris-covered and clean-ice glaciers. Vincent et al. (2016) found ablation was reduced by around 1.8 m water equivalent a^{-1} due the prescence of debris cover on the Changri Nup Glaicer, Everest region, and attributed this difference to the insulating effect of debris having a greater effect on ablation than the presence of ice cliffs and supraglacial ponds. Differences in scale and the metric used for comparison (e.g. elevation change or surface lowering) may play a role in the discrepancy between these studies. To determine the relative importance of supraglacial debris cover, ice cliffs and supraglacial water bodies in glacier mass loss a complete surface energy balance model approach is needed, which incorporates energy balance models for each of these features present on a debris-covered glacier surface, which should first be validated using past data before predictions of future glacier mass change are estimated. However, as yet no such model exists.

2.2. Chapter summary

The Himalaya-Karakoram has a complex mix of geological, climatological and hydrological regimes, which all vary spatially across the mountain range. The most influential weather system in the region is the South Asian Summer Monsoon, which causes glaciers in the Central and Eastern Himalaya to be of summer accumulation-type. The glacierised area of the Himalaya-Karakoram is extensive and has been throughout the Quaternary, with glacier extent varying over a number of glacial cycles. The current glacio-hydrological regime of the Himalaya-Karakoram provides an important water resource for a fifth of the world's population, with glacier meltwater playing an important role in the annual hydrological regime of the Himalaya-Karakoram through supplying water in periods of low precipitation. However, future climate change is predicted to reduce glacierised area by up to 50% by 2100, and may even cause the Himalaya-Karakoram to become glacier free in the coming centuries. Such predictions of glacier mass loss, and of changes in monsoon intensity and river discharge, are based on a variety of numerical model results. However, there is currently notable disparity between predictions of glacier change in the Himalaya-Karakoram from numerical models and of how the climate will change, both in terms of temperature and precipitation.

Chapter 3: Debris-covered glaciers

3. Debris-covered glaciers

Debris-covered glaciers occur in mountain ranges worldwide, including in the Southern Alps of New Zealand, the European Alps, and the Andes (Benn et al. 2004). Extensive supraglacial debris cover often causes debris-covered glaciers to exist at lower altitudes, and to respond differently to climate change when compared to clean-ice glaciers (Clark et al., 1994; Scherler et al., 2011). The differing response of debris-covered compared to clean-ice glaciers is due to the buffer formed by the debris layer between the ice surface and atmosphere, which either enhances or subdues ablation depending on its thickness (Østrem, 1959). At a critical thickness a debris layer changes from one that enhances ablation to one that subdues it, whilst effective thickness is the point at which ablation under a debris layer is at its maximum (Kayastha et al., 2000; Cuffey and Paterson, 2010). Effective thickness typically lies between 0.01 and 0.1 m, whilst critical thickness is ≥ 0.05 m (Nicholson and Benn, 2006; Cuffey and Paterson, 2010). Both thicknesses vary between glaciers due to spatial variability in debris properties including albedo, lithology and porosity (Figure 3.1; Reznichenko et al., 2010; Nicholson and Benn, 2013; Collier et al., 2014; Evatt et al., 2015). The majority of numerical modelling studies concerned with debris-covered glaciers have not considered spatial variability in debris layer parameters such as albedo, thermal conductivity, moisture content and porosity. However, variability in such properties is likely to result in variations in effective and critical thickness across a glacier surface and between glaciers. Omission of such variability in debris properties is a currently poorly quantified, and as such is a source of uncertainty in calculations of mass balance for debris-covered glaciers. To determine the importance of such spatial variability in debris properties a comprehensive understanding of surface energy balance at and heat transfer through a debris layer is needed, and the influence debris properties have on these fluxes.

Chapter 3 summarises current research on debris-covered glaciers and the knowledge gaps that still exist. First, an overview of debris surface energy balance of and heat transfer through a supraglacial debris layer is presented, which are the fundamental concepts on which this thesis is based. Following this summary is consideration of how and why a debris layer varies spatially and temporally. Finally, current methods of observing, monitoring and modelling debris-covered glaciers are

presented, to provide a base for this thesis' research and background to the methods used.

3.1. Glacier surface energy balance

Glacier surface energy balance dictates the amount of energy available for ablation, and is the sum of all energy fluxes over a given time period (Figure 3.1; Cuffey and Paterson, 2010). Glacier surface energy balance represents the exchange of energy between a glacier surface and the atmosphere, and the key processes for determining ablation of glaciers in response to climate change (Molg and Hardy, 2004; Pellicciotti et al., 2009). The main components of glacier surface energy balance are: net shortwave radiation; net longwave radiation; sensible heat exchange; latent heat exchange and heat supplied by precipitation. Net energy balance at a glacier surface (SEB_{net}) is calculated using Equation 3.1:

$$SEB_{net} = (SW_{in} - SW_{out} + LW_{in} - LW_{out}) + (QH + QE) + QG + QR - QT \quad (3.1)$$

where SW_{in} in incoming shortwave radiation, SW_{out} is outgoing shortwave radiation, LW_{in} is longwave radiation, LW_{out} is outgoing longwave radiation, QH is sensible heat transfer, QE is latent heat transfer, QG is ground heat flux, QR is energy supplied by precipitation, and QT is energy used for phase change in ice. Collectively, SW_{in}, SW_{out}, LW_{in} and LW_{out} are known as the net radiant energy flux, whilst QH and QE are known as the turbulent energy fluxes (Cuffey and Paterson, 2010). If SEB_{net} is positive at the ice surface, incoming energy flux will be greater than outgoing energy flux, and ablation will occur if there is any excess energy in this surface energy balance (Arnold et al., 2006).

A supraglacial debris layer acts as a store of energy and slows down the flux of energy from the debris layer to the ice surface or into the atmosphere. If surface energy balance at the debris surface is positive, heat is transferred into the debris and conducted through the debris layer to the ice surface. A negative surface energy balance occurs when energy stored in the debris is transferred back into the atmosphere (Takeuchi et al., 2000; Reid et al., 2012). The delay in heat flux through the debris layer is primarily controlled by the difference between air, debris and ice

surface temperature, and debris layer properties including layer thickness, porosity, moisture content and thermal capacity of the debris (Nicholson and Benn, 2006; 2013; Collier et al., 2014; Evatt et al., 2015). In addition to modulating the surface energy balance of a glacier, the presence of supraglacial debris changes glacier dynamics (Iverson et al., 2003; Scherler et al., 2011; Shugar et al., 2012). The additional mass of the debris modifies the force balance that controls glacier movement, and alters basal sliding resistance due to large quantities of rock entering the subglacial drainage system (Iverson et al., 2003; Alexander et al., 2011).

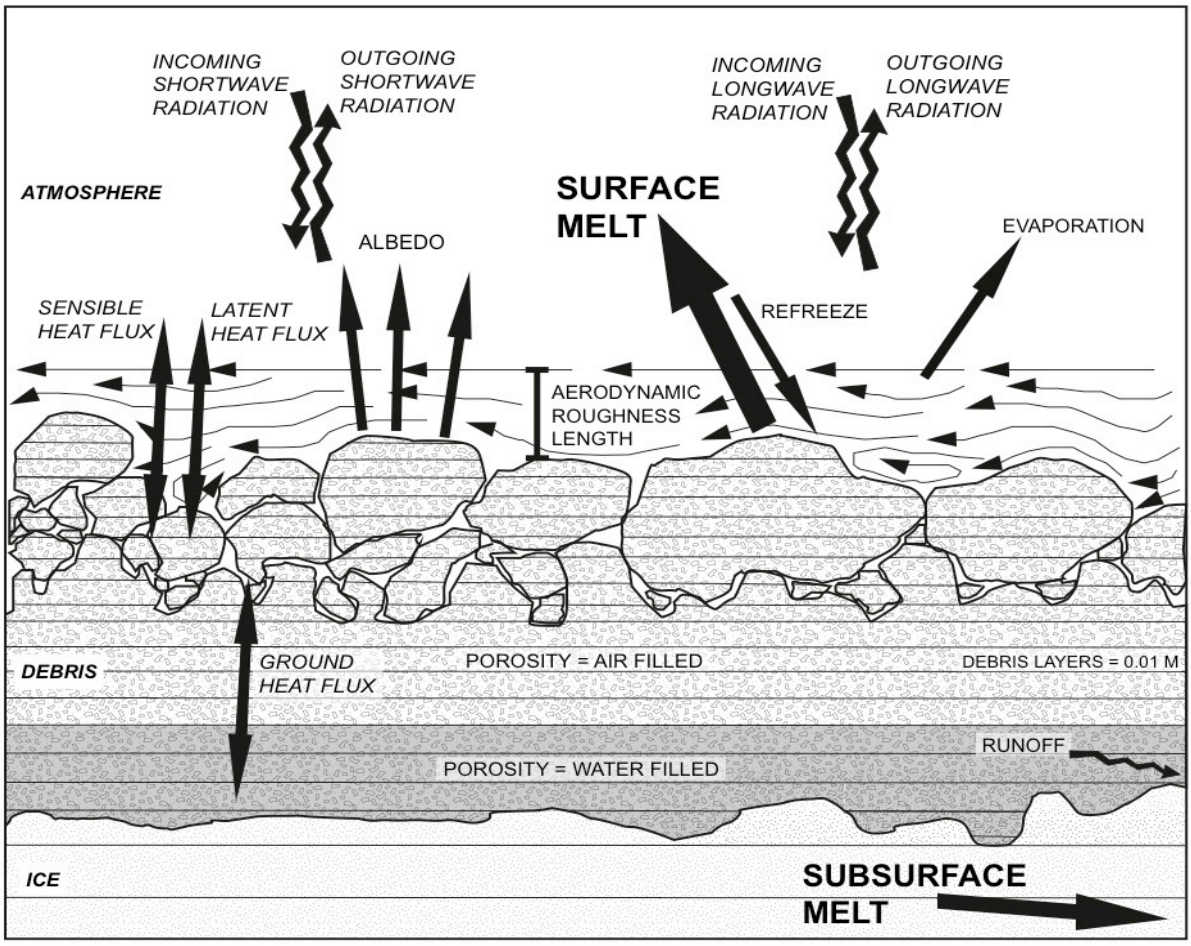

Figure 3.1: A reconstruction of the energy fluxes at a debris-covered glacier surface and through a supraglacial debris layer.

3.1.1. Radiative fluxes

Net radiation (net shortwave and longwave radiation) constitutes between 40% and 90% of energy flux at a glacier surface, which varies with meteorological conditions, solar location, topography, shading of the glacier surface, latitude, and altitude (Hock, 2005). The sun predominantly emits shortwave radiation at visible wavelengths (between 0.4 and 0.7 μm), whilst longwave radiation is emitted by terrestrial and atmospheric sources such as bedrock and clouds at wavelengths between 4 and 120 μm (Niemela et al., 2001). Net shortwave radiation (SW_{net}) is controlled by the ratio of shortwave radiation reflected by a surface compared to that which is absorbed, which is termed albedo (α):

$$\alpha = SW_{out}/SW_{in} \quad (3.2)$$

where SW_{in} and SW_{out} are incoming and outgoing shortwave radiation, respectively. Consequently, SW_{net} is:

$$SW_{net} = SW_{in}\,(1-\alpha) \quad (3.3)$$

SW_{in} in comprised of direct and diffuse components. Direct SW_{in} undergoes no absorption or scattering in its path from the sun to the glacier surface, whilst diffuse SW_{in} reaches the surface after undergoing scattering or absorption and re-emittance within the atmosphere (Benn and Evans, 2010). The amount of SW_{in} that reaches a glacier surface is spatially and temporally variable, predominantly due to glacier topography, specifically aspect and slope, which control the incident angle of SW_{in} reaching a glacier surface (Klok and Oerlemans, 2002; Arnold et al., 2006). Temporal variability in SW_{in} occurs as the position of the sun changes over diurnal and annual cycles, and with varying weather patterns. The proportion of direct to diffuse SW_{in} reaching a glacier surface also varies temporally due to varying sky view factor over annual cycles, and with changing weather patterns, which will affect humidity and cloudiness of the atmosphere and therefore the amount of absorption of SW_{in} (Hock and Holmgren, 2005). The topography surrounding a glacier also affects the proportion of SW_{in} distributed across a glacier surface, controlling temporal patterns of shading and the proportion of sky hemisphere visible at the glacier surface (Arnold et al., 2006).

The low latitude and high altitude of glaciers in the Himalaya-Karakoram influences the incoming shortwave radiation budget they receive, with such a latitudinal location resulting in a high midday solar angle, and therefore a large proportion of the glacier surface able to receive direct solar radiation, whilst filtering and scattering of SW_{in} is minimal due to the high altitude (Benn et al., 2001). In the Himalaya-Karakoram, glaciers are also often located in deeply incised valleys surrounded by high relief topography, causing high spatiotemporal variability in SW_{in} across these glacier surfaces due to surrounding mountains blocking direct SW_{in} (Kayastha et al., 1999).

Albedo of a glacier surface varies with surface type (e.g. snow, ice or debris), ice or snow structure, level of decay of snow and ice, debris lithology, and moisture content (Table 3.1; Paterson, 1994). Lithology influences albedo of debris-covered ice due to different lithologies reflecting different degrees of SW_{out}. On Ngozumpa Glacier, Central Himalaya, where a range of lithologies including granite and schist were identified, albedo was found to vary between < 0.1 and > 0.9, although 62% of the measurements fell between 0.1 and 0.3 (Nicholson and Benn, 2013). For lithologies with high reflectance, such as white granite, albedo may be similar to that of ice or fresh snow. Surface roughness also affects albedo, with rougher surfaces resulting in a greater scattering of SW_{out} (Matthias et al., 2000). Albedo of debris covered ice is also temporally variable as a result of varying debris moisture content, with decreased albedo of a debris surface when it is wet (Nicholson and Benn, 2013; Collier et al., 2014).

Table 3.1: Albedo value ranges for categories of clean- to debris-covered ice, which are used to define the point at which a glacier surface is debris-covered (Paterson, 1994).

Ice cover	Albedo
Dry snow	0.75 – 0.98
Melting snow	0.46 – 0.70
Firn	0.43 – 0.69
Clean ice	0.34 – 0.51
Slightly dirty ice	0.26 – 0.33
Dirty ice	0.15 – 0.25
Debris-covered ice	0.10 – 0.15

The degree of incoming longwave radiation (LW_{in}) depends primarily on near-surface air temperature, whilst outgoing longwave radiation (LW_{out}) is a function of glacier surface temperature. The dependence of longwave radiation flux on temperature is based on the Stephan-Boltzman equation:

$$I = \varepsilon \sigma T^4 \quad (3.4)$$

Where ε is emissivity, σ is the Stephan-Boltzman constant (5.67×10^{-8}) and T is the temperature of the body emitting longwave radiation in Kelvin (Cuffey and Paterson, 2010). LW_{in} can be higher or lower than LW_{out}, depending on the relative difference between glacier surface temperature and atmospheric and adjacent terrain temperature (Ohmura, 2001). LW_{out} also differs between clean-ice and debris-covered glacier surfaces; for clean-ice ice at 0°C LW_{out} is ~309–311 W m^{-2}, whilst at a supraglacial debris surface, which can reach much higher temperatures due to an ability to absorb energy, LW_{out} can reach ~413 W m^{-2} (for a debris surface at 20°C; Benn and Evans, 2010). On debris-covered ice, debris surface temperature is primarily controlled by debris layer thickness, as an increasingly thick debris layer provides greater insulation from cold propagation from ice to a debris surface (Nicholson and Benn, 2006; Foster et al., 2012). Consequently, LW_{out} is higher when debris surface temperature is greater and, therefore, when a debris layer is thicker. On debris-covered ice it is therefore possible for SW_{net} to be balanced by higher LW_{out}, a condition that does not occur on clean-ice glaciers (Takeuchi et al., 2000).

Longwave radiation is particularly important in humid and overcast climates (Muller, 1985; Oerlemans, 2000), such as during the monsoon season in the Himalaya. Water vapour absorbs and re-radiates longwave radiation, increasing longwave radiation flux from the atmosphere to the glacier or debris surface. An overcast sky emits up to 50% more longwave radiation compared to a clear sky (Sicart et al., 2006). However, quantifying cloudiness is difficult (Mölg et al., 2009) and as such is not incorporated into LW_{in} data derived from large-scale meteorological models, such as outputs from the European Centre for Medium-Range Weather Forecast Reanalysis Interim (ERA-Interim) model, which has previously been used for glacier surface energy balance models where local datasets are scarce (e.g. Collier et al., 2013).

Spatial and temporal variability in shortwave and longwave radiation across a glacier are important controls on glacier surface energy balance over an ablation season. Consequently, when modelling surface energy balance of a debris-covered valley glacier such as those found in the Himalaya-Karakoram, it is important to consider the proportion of the glacier area covered in debris and variability in the lithology of the debris layer, to determine albedo of a debris layer. It is also critical that spatial, diurnal and seasonal variability in SW_{in} are considered, caused by high relief topography that often surrounds a valley glacier and variability in solar position, and monsoon weather patterns, which will affect diurnal and seasonal cloudiness and in turn affect incoming radiation flux.

3.1.2. Sensible and latent heat fluxes

Sensible heat is the thermal energy transferred between materials, and on a glacier is the energy transferred between air, ice, snow, debris and water. Latent heat transfer is the energy exchanged through evaporation, condensation and sublimation (Benn and Evans, 2010). Latent heat flux is positive when water vapour condenses on a glacier surface and negative when moisture is lost by evaporation or sublimation (Cuffey and Paterson, 2010). Together, sensible and latent heat transfer components are termed 'turbulent fluxes'.

The degree of sensible and latent energy transfer is dependent on the turbulence of airflow directly above the glacier or debris surface in the surface boundary layer; the atmospheric layer directly about the ice or debris surface. In the case of debris-covered ice, turbulence of airflow is controlled by the roughness of the debris surface, and the difference in temperature and moisture content between the debris surface and the air directly overlying the debris surface. If the air within the surface boundary layer is warmer than the debris surface, turbulent mixing transfers sensible heat to the debris surface. Similarly, if air in the surface boundary layer is dry the turbulent mixing of air above the surface transfers moisture away from the debris surface. To maintain saturation of the overlying air, moisture at the debris surface must either be evaporated from or transferred to the debris surface, both of which consume latent heat (Cuffey and Paterson, 2010). Consequently, turbulent fluxes of debris-covered ice are dependent on debris surface and air temperature and the moisture content of the debris surface and

relative humidity of air (Rounce et al., 2015). Quantifying turbulent fluxes for debris-covered ice, and spatiotemporal variability in these fluxes over a debris-covered glacier surface, is partly restricted by poor constraint of moisture content of a debris layer, which is difficult to measure accurately in space and time.

The roughness of an ice or debris surface is a function of the microtopography of a glacier surface, and affects the turbulent heat flux at the glacier surface (Munro, 1989; Brock et al., 2006). The roughness of a glacier surface is quantified through aerodynamic roughness length (z_0); the height above the glacier or debris surface at which the switch between turbulent and laminar airflow occurs (Munro, 1989). Spectral reflectance, and therefore albedo, of a glacier surface is also affected by surface roughness; a greater surface roughness causes increase topographic shadowing and a greater level of reflectance scatter (Nolin et al., 2002). Turbulent energy exchange is not restricted to a supraglacial debris surface and also occurs in air filled pores within the debris layer. Latent heat flux is an important control on the increase in ablation up to a debris layer's effective thickness; with increasing debris layer thickness the airflow within a debris layer decreases and consequently a reduction in latent energy available for evaporation occurs (Evatt et al., 2015). Therefore, the porosity of a debris layer is an important control on latent heat exchange for debris-covered glaciers.

In glacier surface energy balance modelling, turbulent fluxes are predominantly calculated using the bulk aerodynamic method, which assumes these fluxes are proportional to the exchange of moisture and heat between a glacier surface and overlying air. The bulk aerodynamic method also assumes airflow in the atmospheric layer directly above the surface (in the surface boundary layer) is turbulent and fully adjusted for surface topography (e.g. Munro, 1990; Hock and Noetzli, 1997). Using the bulk aerodynamic approach, wind direction only needs to be measured at one height, as long as z_0 is known (Brock et al., 2006). For glacier surfaces z_0 has predominantly been measured on ice and snow surfaces, although a limited number of measurements for supraglacial debris surfaces do exist (e.g. Brock et al., 2006; Rounce et al., 2015; Miles et al., 2017; Quincey et al., 2017).

A number of methods exist with which to measure z_0 including eddy-covariance (e.g. Cullen et al., 2007), wind profiling (e.g. Hock and Holmgren, 1996; Quincey et al., 2017) and measurement of microtopography (e.g. Brock et al., 2006). The eddy covariance method is based on a direct measurement of z_0, whilst wind profiling measures the vertical profile of wind speed and air temperature, which are then adjusted for surface layer stability using Monin-Obukhov similarity theory to produce z_0 values. Both of these methods are highly sensitive to measurement uncertainties (Brock et al., 2006). Consequently, measurement of microtopography; the measurement of the height of a glacier surface from a horizontal reference plane in a direction perpendicular to wind direction, is now the method most commonly used. z_0 is calculated from these data using the most accepted relationship between surface roughness and z_0 developed by Lettau (1969). Previously microtopography was measured manually along profiles between 3 and 20 m in length (e.g. Munro, 1989; Brock et al., 2006), but more recently microtopography has been measured using digital elevation models derived from structure-from-motion (SfM) photogrammetry. Using this method enables z_0 to be calculated for a large number of longitudinal profiles across the study plot in all directions, enabling a better characterisation of roughness in all directions (e.g. Rounce et al., 2015; Smith et al., 2016; Miles et al., 2017). A z_0 value of 0.016 m has previously been used for supraglacial debris in most surface energy balance models of debris-covered ice (e.g. Reid and Brock, 2010; Foster et al., 2012; Rounce and McKinney, 2014; Collier et al., 2014). However, supraglacial debris grain size can vary across the full range of grain sizes over one glacier surface. Consequently, z_0 of a debris-covered glacier surface is highly heterogeneous (Rounce et al., 2015), but incorporation of such spatial and temporal variation of z_0 in numerical models is yet to be achieved (Hock and Holmgren, 1996; Klok and Oerlemans, 2002).

3.1.3. Precipitation

Precipitation includes snowfall and rainfall, both of which fall on glaciers in the Himalaya-Karakoram depending on the season and altitude at which the glacier is situated (Bookhagen and Burbank, 2010). Snowfall is one of the main components of accumulation in a glacier system (Benn and Evans, 2010), and can act as a buffer for energy exchange between the atmosphere and supraglacial debris (Gubler et al., 2011;

Guglielmin, 2006), and results in less peaked and distributed glacier discharge when compared to precipitation that falls as rain (Immerzeel et al., 2009). As a snow layer overlying a debris-covered ice surface melts, water infiltrates into a debris layer, increasing the debris layer moisture content and filling pore spaces in the debris layer, thus changing its bulk thermal conductivity (Collier et al., 2014). When a snow layer is present on a debris-covered ice surface energy exchange occurs at the snow surface, and albedo and roughness for snow differ from those for debris. Evolution of these parameters with time also occurs, as does heat flux through the snowpack to the debris surface as the snow ages and its density changes (Mölg and Hardy, 2004). The higher albedo of a snow layer reduces the radiative and sensible heat flux entering the snowpack, and therefore the amount of energy reaching the underlying debris and ice (Immerzeel et al., 2009). As the snow pack disappears the resultant meltwater will also cause the debris surface to be wet, lowering the debris surface albedo (Nicholson and Benn, 2006; Immerzeel et al., 2009; Collier et al., 2014).

Rainfall will also lower the albedo and temperature of a debris layer, reducing radiative and latent energy flux at the debris surface. However, rain contributes energy directly to a glacier surface, and has a higher temperature than glacier ice or debris surface temperature in certain diurnal and seasonal periods (Cuffey and Paterson, 2010). The energy flux from rain contributes a minimal amount of energy to a debris surface through latent heat transfer, and only a small proportion of this is transferred through the debris layer and used for ablation, although its influence may vary for debris surface depending on the permeability of the debris layer (Sakai et al., 2004; Reznichenko et al., 2010). Due to the minimal contribution of rain to incoming energy flux, precipitation is often omitted from glacier surface energy balance models. However, in monsoon-influenced regions such as the Himalaya, where rainfall is high during the ablation season, energy flux from precipitation is likely to be more important to glacier surface energy balance (Reid and Brock, 2010).

3.2. Conductive heat transfer through a debris layer

Conductive heat transfer is the dominant energy flux through a debris layer from the debris surface to the ice surface, with non-conductive processes of energy transfer, such as convection from air movement playing lesser roles (Evatt et al. 2015). Energy transferred through a debris layer provides energy to increase ice surface temperature to melting point, which facilitates ablation (Takeuchi et al., 2000; Nicholson and Benn, 2006). A linear temperature gradient through a debris layer throughout the day and across an annual cycle is often assumed in energy balance models (e.g. Nicholson and Benn, 2006; Foster et al., 2012), which assumes a debris layer is in thermal equilibrium (Nakawo and Young, 1981). However, debris surface temperature varies on diurnal and seasonal timescales with variations in meteorological conditions (Figure 3.2; Conway and Rasmussen, 2000; Nicholson and Benn, 2006). Such variations in debris surface temperature cause the temperature gradient through a debris layer to be non-linear for some diurnal and seasonal periods, and also to vary through time (Nicholson and Benn, 2013). Non-linear temperature profiles through a debris layer exist when the bulk debris layer is not at thermal equilibrium, so linear temperature profiles only exist at the warmest and coldest times of day when the debris layer has entirely warmed or cooled sufficiently (Reid and Brock, 2010; Nicholson and Benn, 2013) for all or almost all of the ablation season and through a diurnal cycle (Nicholson and Benn, 2013). Consequently, more recent surface energy balance models are able to reproduce non-linear temperature gradients through a debris layer (e.g. Lejeune et al., 2013; Collier et al., 2014).

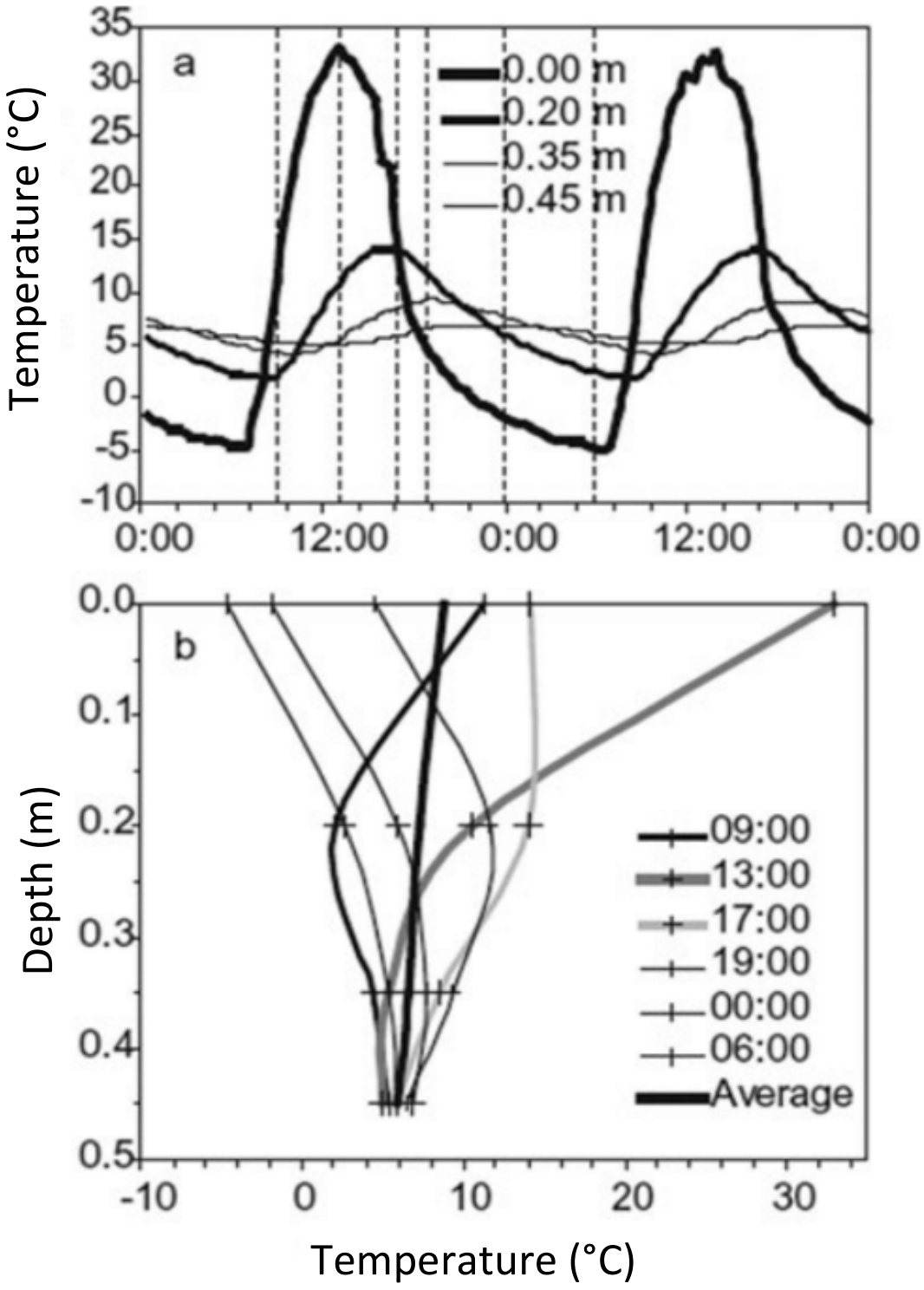

Figure 3.2: (a) Diurnal debris surface temperature patterns over a two-day period for different depths in a debris layer between the debris surface and 0.45m. **(b)** Temperature profiles through the 0.45m thick debris layer at different points over a diurnal cycle between 09:00 and 06:00. Although all measured temperature profiles are non-linear the mean diurnal profile is linear. Both datasets were collected on Ngozumpa Glacier, Central Himalaya (plots reproduced from Nicholson and Benn, 2006).

3.2.1. Thermal conductivity

The rate of heat conduction through a debris layer depends on its thickness and bulk thermal conductivity, the latter of which varies with lithology, porosity, permeability and moisture content (Table 3.2). These debris properties are variable in both space and time due to the geological setting of a glacier, the spatiotemporal variability in dynamics of debris transport, meteorological conditions, and mass movement events on and off the glacier surface (Dricoll, 1980; Hochstein et al., 1995; Reid and Brock, 2010; Reid et al., 2012). Thermal conductivity also increases with depth in a debris layer, as debris becomes more densely packed and air-filled pore spaces, which have a relatively low thermal conductivity, often become filled with water, which has a higher thermal conductivity (Beavers and Joseph, 1967; Brock et al., 2007; Evatt et al., 2015).

In surface energy balance and heat transfer models for supraglacial debris layers constant values for thermal conductivity of ice, snow and debris, and air and water (Table 3.3) are used that calculate heat flux through a debris layer (e.g. Reid and Brock, 2010; Lejeune et al., 2013; Collier et al., 2014; Evatt et al., 2015). One method for calculating thermal conductivity of a debris layer uses heat flux per unit area over the measurement period, assumed equal to the amount of melt that occurs over the same period, and the mean vertical thermal gradient through the debris layer (Brock et al., 2007). An alternative method is to estimate depth averaged thermal diffusivity using an average temperature gradient through the debris layer, from which thermal conductivity is then calculated using standard values of specific heat capacity, density and porosity of each of the different mediums within a debris layer (Conway and Rasmussen, 2000; Nicholson and Benn, 2006). Both methods assume all heat flux to occur only by conduction, and in the case of the second method are limited by the inclusion of constant values of bulk debris layer properties, which will vary with differing porosity, moisture content and lithology, and with depth (Collier et al., 2014).

Table 3.2: The effect of supraglacial debris characteristics on conduction of energy through a debris layer, and therefore on ablation of underlying ice. Additional non-conductive processes of energy transfer are not outlined, but would also vary with differing debris characteristics. Collated from Inoue and Yoshida, 1980; Humlum, 1997; Harris and Pederson, 1998; Juen et al., 2013; Rounce and McKinney, 2014; Evatt et al., 2015.

Debris characteristic	Effect on thermal conductivity of a debris layer
Lithology	Lithologies of lighter colour (e.g. granite) have a higher albedo than darker rock types (e.g. schist). Different lithologies also have differing thermal conductivities, which affects the rate of heat transfer through a debris layer.
Debris layer porosity and permeability	The more porous a debris layer the more air within it. Less heat is transported through a debris layer when the debris is porous as air has a lower thermal conductivity than debris. A greater connectivity of pore spaces within a debris layer will allow air to pass through the it more efficiently, causing sensible heat exchange between the air and debris.
Mean grain size	Debris grain size affects the amount of pore space and therefore air in a debris layer, controlling bulk thermal conductivity of a debris layer. A larger mean grain size will reduce thermal conductivity of a debris layer due to a higher percentage of air in the debris layer when compared to a debris layer with a lower mean grain size. Additionally, wind can transfer heat energy more easily through larger blocky debris than through fine-grained material.
Grain size distribution	A wide distribution of grain sizes will reduce pore space in a debris layer, as small grains will infill cavities between larger grains. The thermal conductivity of the debris layer will, therefore, be greater as the proportion of debris to air is increased.
Moisture content of debris layer	The occurrence of water in debris pore space rather than air increases the thermal conductivity of the layer, as water has a higher thermal conductivity than air.

Table 3.3: Values of thermal conductivity for different mediums found within a debris layer, used in numerical models that calculate heat flux through a debris layer.

Thermal conductivity ($Wm^{-1} K^{-1}$)	Medium	Source
1.0–2.3	Artificial debris layer	Nakawo and Young, 1981
1.4–2.6±0.5	Artificial debris layer	Nakawo and Young, 1982
2.5±0.2	Ice	Mühll and Haerberli, 1990
0.85±0.2	Debris	Conway and Rasmussen, 2000 (Base Camp, Khumbu Glacier)
1.28±0.15	Debris	Conway and Rasmussen, 2000 (Lobuche, Khumbu Glacier)
0.35	Debris	Brock et al., 2007 (Villarrica Glacier - Tephra)
0.96	Debris	Brock et al., 2010 Foster et al., 2012
0.94	Debris	Reid and Brock, 2010 (Miage Glacier)
0.7	Debris	Lejeune et al., 2013
2.51	Ice	Collier et al., 2014
0.024	Air	Collier et al., 2014
0.58	Water	Collier et al., 2014

3.2.2. Porosity and moisture content

Conduction of energy through a debris layer is influenced by porosity and moisture content of a debris layer, as air and water have a lower and higher thermal capacity than rock, respectively (Mattson, 2000; Collier et al., 2014). A debris layer with a higher porosity also has higher turbulent energy flux within it due to a greater amount of air movement between grains (Evatt et al., 2015). Despite the importance of porosity and moisture content in energy transfer through a debris layer, the incorporation of these parameters into surface energy balance and heat transfer models for debris-covered ice

is a relatively new development. Lejeune et al. (2013) initially highlighted the importance of moisture content in a debris layer, citing the lack of ability for their surface energy and mass balance model to incorporate interstitial water between debris grains as a source of uncertainty in the modelling procedure. Lejeune et al. (2013) also identified that phase changes in the water film covering debris grains would cause significant disturbances in the surface energy balance of a debris layer. Following discovery of the sensitivity of surface energy balance models to moisture content, Collier et al. (2014) subsequently included porosity and moisture content in their model, in the form of a simplified reservoir approach, whilst Evatt et al. (2015) incorporated porosity alongside the attenuation of wind speed with depth in the debris layer. Such developments in surface energy balance modelling are vital for understanding processes in debris layers on monsoon-influenced glaciers in the Himalaya, where the highest moisture content in a debris layer is coincident with the ablation season and moisture will therefore have a direct impact on ablation. However, these numerical models are currently all point-based and have reproduced theoretical mass balance of debris-covered ice, meaning they do not consider the extent to which porosity and moisture content will vary spatially across a true glacier surface. Consequently, to determine the importance of such spatial variability collection of *in situ* data on porosity and moisture content are needed, with surface energy balance models subsequently incorporating these parameters constrained by these field data.

3.3. Supraglacial debris distribution

For both clean-ice and debris-covered glaciers, spatial and temporal variation in surface properties causes variations in the degree to which surface energy balance is negative or positive. In the case of debris-covered glaciers the physical properties of supraglacial debris, including lithology, debris layer thickness, moisture content and porosity of the debris layer, have the potential to vary spatially across a glacier surface, and therefore cause the surface energy balance of a debris-covered glacier to vary in space and time. Consequently, accurately quantifying the effect of a supraglacial debris layer on glacier surface energy balance across an entire glacier surface, and therefore the mass balance of a glacier, is reliant on identifying the variation in each of these influential debris parameters across a glacier surface (Driscoll, 1980; Hochstein et al., 1995).

The distribution of supraglacial debris, and the resultant variability in debris properties, is dependent on the processes of input to, transport through and deposition of debris in the glacier system, which are primarily controlled by glacier dynamics and climate (Section 3.3.1; Rowan et al., 2015). Debris layer thickness, lithology and grain size are controlled by the location and amount of debris input into the glacier system, and glacier flow (Anderson and Anderson, 2016). The distribution of debris is also temporally variable as glacier dynamics vary through time in response to changes in glacier mass balance and basal conditions (e.g. proportion of basal lubrication) and climate (Quincey et al., 2009b).

A typical pattern of supraglacial debris distribution is one of increasing debris thickness with distance from the headwall, with the greatest debris thicknesses at the terminus due to emergence of en- and sub-glacial debris through ablation and convergence of debris transport pathways (Hambrey et al., 1999). Many supraglacial debris layers in the Himalaya-Karakoram reach thicknesses of a number of metres near the terminus (Mihalcea et al., 2008; Hambrey et al., 2008; Kirkbride and Deline, 2013). Such a pattern of debris thickness leads to debris-covered glaciers often displaying a decreasing gradient of ablation towards their terminus, which can lead to a low (< 2°) or even reversed ice surface gradient in the ablation zone (Boulton, 1971; Reynolds, 2000; Richardson and Reynolds, 2000; Quincey et al., 2005; Quincey et al., 2009). Such inverted topography causes low to no gravitational driving stresses at the glacier surface in the ablation zone, which ultimately results in ice stagnation and surface lowering, rather than recession of glacier termini as seen on clean-ice glaciers (Reynolds et al., 2000, Bolch et al., 2008, 2011; Scherler et al., 2011; Benn et al., 2012). Consequently, quantifying rates of debris input, transport of debris and debris exhumation are important when determining change in mass balance through time. However, considering the vast suite of processes involved in debris distribution is challenging, and as such studies that have collected data or modelled such processes often focus on specific processes (e.g. Hambrey et al., 1999; Anderson, 2000; Konrad and Humphrey, 2000; Heimsath and McGlynn, 2008; Nagai et al., 2013; Banerjee and Shankar, 2014; Rowan et al., 2015; Anderson and Anderson, 2016). The absence of such a comprehensive approach to debris distribution in numerical models is primarily constrained by an inability to accurately quantify all the processes

involved, such as the rate of headwall erosion and exhumation of debris to the glacier surface, and their interaction with one another, in particular understanding of processes that occur en- and subglacially.

The occurrence of supraglacial water bodies on debris-covered glaciers is intrinsically linked to debris distribution. Supraglacial water bodies are prevalent on debris-covered glaciers due to the low gradient surface of ablation areas that are typical of many debris-covered glaciers, and the undulating debris surface where topographic lows facilitate the ponding of water (Gulley and Benn, 2007; Hambrey et al., 2008). Due to an increased availability of glacier meltwater as the climate warms, which causes increased glacier melting, the frequency and area of supraglacial and proglacial lakes is expected to increase alongside the recession of glaciers that will result in the formation and expansion of large terminal moraines. These developments will increase potential for moraine failures and glacier lake outburst floods (GLOFs) due to large volumes of meltwater in a glacier system and increased frequency of moraine dams (Benn et al., 2012; Westoby et al., 2015; Watson et al., 2016). The extent of changes in supraglacial water bodies induced by climate change and glacier melt is unclear, primarily due to a limited understanding of the contribution these water bodies have to overall glacier ablation rate, and partly due to a lack of understanding of debris-covered glacier hydrology (Miles et al., 2016; Watson et al., 2016). Determining the timing and magnitude of GLOFs is challenging due to a lack of data on stability of terminal moraines. However, it is imperative that the potential hazard GLOFs present is explored fully, as in mountain communities in the Himalaya-Karakoram GLOFs have the potential to wipe out communities, livelihoods and vital hydropower energy supplies (Ives et al., 2010; Rounce et al., 2017). Understanding the response of debris-covered glaciers to climate change and the evolution of supraglacial water bodies within this is therefore integral to the continued existence of Himalaya-Karakoram mountain communities.

3.4. Debris input, transport and deposition

Distribution of supraglacial debris across a glacier surface is primarily controlled by the input, transport and deposition of debris through the glacier system. The amount and lithology of supraglacial debris on a glacier surface is controlled by a number of factors, which include: the topography of the glacier catchment, which facilitates mass

movements events including debris-filled snow avalanches, rock avalanches and rockfalls to a glacier surface (Fort, 2000; Hewitt, 2009); precipitation, which governs the ratio of debris to water and ice mass added to the glacier; glacier size (Scherler et al., 2011); the ease with which bedrock erodes, controlled by lithology and climate (Shroder et al., 2000); and englacial debris emergence rate, controlled by ice flow (Anderson, 2000). Debris is also added to a glacier system through subglacial quarrying and abrasion, although the contribution of debris from sub-glacial sources is considered to be minimal compared to input from rockfalls and rock and snow avalanches (Hambrey et al., 2008; Benn and Evans, 2010; Winkler and Matthews, 2010).

The abundance of supraglacial debris on glaciers in active tectonic mountain ranges is attributed to the oversteepening of topography alongside seasonal freeze-thaw cycles, which cause frequent mass movement events (Hales and Roering, 2005; 2009; Nagai et al., 2013). The concentration of debris-covered glaciers in the Himalaya-Karakoram is attributed to the frequency of mass movement events due to continued, and relatively fast (2–12 mm a^{-1}) rock uplift of the region, which produces large areas of easily weathered shattered bedrock primarily through freeze-thaw (Burbank et al., 1996; Shroder et al., 1999). The key controls on the frequency of mass movement events are the aspect of valley walls and the extent of diurnal fluctuations in air temperature, the latter of which are greatest on southwest-facing slopes and least on north-facing slopes (Regimi and Watanabe, 2009; Nagai et al., 2013). Rate of rockwall retreat, which is the quantifiable parameter of rockfall frequency, is currently poorly constrained; measured and estimated rates of rockwall retreat in present day mountain environments range from 0.05–6.0 mm a^{-1} (e.g. Ballantyne and Harris, 1994; Collins, 1998; Arsemault and Meigs, 2005; Heimsath and McGlynn, 2008). Collins (1998) calculated erosion rates of Batura Glacier, Karakoram, at 3.45–4.21 mm a^{-1}, from suspended sediment load in proglacial stream, whilst Heimsath and McGlynn (2008) calculated retreat rate of the headwall of Milarepa Glacier, a debris-covered glacier in the Central Himalaya, by cosmogenic radionuclide dating and found a horizontal rate of 1.2±0.5 mm a^{-1}. In addition to poor constraint of rockfall frequency, and mass movement frequency in general, an increasing frequency of mass movement events has also been documented in recent years, attributed to climate change and permafrost degradation (Haerberli and Beniston, 1998; Deline, 2013; Evans et al., 2009).

For a typical debris-covered glacier, debris is predominately deposited in the accumulation zone and emerges in the ablation zone (e.g. Boulton and Eyles, 1979; Benn and Owen, 2002; Benn et al., 2012), although additional material can enter a glacier system at any point along the margins through mass movement events and subglacial erosion (Alley et al., 1997; Hambrey et al., 1999). Debris is transported englacially through folding and thrusting of ice and in englacial drainage networks (Alley et al., 1997; Hambrey et al., 1999). Debris is also transported subglacially through glacier bed deformation and in subglacial drainage networks (Alley et al., 1997). Supraglacially, debris is primarily transported passively by glacier flow and is organised into lateral and medial moraines, which increase in width and height with decreasing distance to the glacier terminus, and ultimately coalesce to form a continuous supraglacial debris cover (Hambrey et al., 1999).

Debris deposition occurs in the glacier ablation zone, as debris emerges from en- and subglacial sources and builds up due to reducing longitudinal velocities at glacier termini (e.g. Quincey et al., 2009a; 2009b). In periods of glacier advance or stability, debris is transported to the margins of a glacier to create terminal-lateral moraines, as observed in simulations of Khumbu Glacier (Rowan et al., 2015). These moraines can be used to determine the history of glacier mass balance, which can be used to identify glacial cycles and investigate interaction between past glacier extent and climate (e.g. Owen, 2009; Rowan et al., 2015).

3.5. Observing and modelling debris-covered glaciers

Sections 3.1 to 3.4 emphasise the vast number of parameters to consider when incorporating supraglacial debris in numerical models for debris-covered glaciers, but also highlight the limited understanding of and lack of consideration for spatiotemporal variability in debris properties in current research. Current understanding of supraglacial debris, with regards to its impact on ablation of debris-covered ice, glacier dynamics and glacier change, has largely been achieved through a combination of *in situ* data, laboratory simulations, the utilisation of remotely sensed datasets and development of numerical models. An overview of these methods and their relevance for application to

debris-covered glaciers, with a specific focus on research focused on glaciers in the Himalaya-Karakoram, is presented here.

3.5.1. In situ data collection

Field data is required to understand the characteristics of debris-covered glaciers in detail and to calibrate and evaluate model outputs, and has, until recently, been the method used most frequently when establishing the importance of a supraglacial debris layer on ablation. The relationship between ablation and debris layer thickness was first identified by Østrem (1959) using field data, as was the process of heat transfer through a supraglacial debris layer (Nakawo and Young 1981). Nicholson and Benn (2006), using field data from Ngozumpa Glacier, Central Himalaya, first identified that the temperature gradient through a debris layer was diurnally variable and how heat was transfer through a debris layer. Nicholson and Benn (2013) built on Nicholson and Benn (2006) and used field data and numerical modelling to identify seasonally variable trends in temperature gradient, as well as the extent to which variation in albedo and grain size of debris affects the rate of heat transfer through a supraglacial debris layer.

Following identification of the mechanisms by which heat was transferred through a debris layer, a series of numerical and physical modelling studies were undertaken to explore the controls on the conductivity of a debris layer (e.g. Reznichenko et al., 2010; Lejeune et al., 2013). Alongside field-based studies a series of surface energy balance models of debris-covered glaciers were developed to explore the fundamental controls on ablation underneath a debris layer in greater detail (e.g. Brock et al., 2010; Fyffe et al., 2014; Collier et al., 2014: Evatt et al., 2015). More recently, collection of field data has predominantly used as part of a multi-disciplinary approach alongside analysis of remotely sensed data to constrain surface energy balance and mass balance of debris-covered glaciers (e.g. Steiner and Pellicciotti, 2015; Soncini et al., 2016), heat transfer through the debris layer (e.g. Lejeune et al., 2013) and surface energy balance of ice cliffs and supraglacial ponds (e.g. Sakai et al., 2002; Miles et al., 2016; Brun et al., 2016).

3.5.2. Remote sensing

The use of remotely sensed data has been the most influential tool in the more recent advancement in understanding of debris-covered glaciers and glaciers in the Himalaya-Karakoram, as remote locations can be explored using these data sets. One of the most useful remotely sensed datasets for debris-covered glaciers has been thermal infrared data, which has been used to delineate debris-covered glacier boundaries (e.g. Shukla et al., 2010; Bhambri et al., 2011) and to calculate debris layer thickness (e.g. Mihalcea et al., 2008; Foster et al., 2012; Rounce and McKinney, 2014; Minora et al., 2015).

3.5.2.1. Debris-covered glacier area

To determine debris-covered glacier area it is important that glacier perimeter is known. However, identifying the perimeter of the debris-covered area of a glacier is challenging using optical satellite imagery, as rock debris has similar surface reflectance characteristics to that of bedrock and scree surrounding the glacier (Paul et al., 2004). Consequently, a number of methods have been developed to identify debris-covered glacier area using a variety of datasets. Manual digitisation is deemed the most accurate method of determining debris-covered glacier area but is labour intensive and time consuming, particularly when a number of debris-covered glaciers are being investigated. Automated approaches are therefore more favoured, and a number of such methods have been developed. A Normalised Difference Vegetation Index (NDVI), which is normally used to identify photosynthesising plants using near infrared and red wavelengths, has been used to delineate debris-covered area from vegetated debris around a glacier (Taschner and Ranzi, 2002). However, the use of an NDVI has only been successful for identifying partially debris-covered ice (Bayr et al., 1994) and would not be appropriate for thick, stable debris layers where vegetation may be present.

Thermal infrared data have also been used to delineate glacier boundaries following the idea that debris-covered ice will be colder than the moraines (not ice-cored) and the landscape surrounding a glacier (Ranzi, 2002; 2004; Shukla et al., 2010). Debris layers of the order of tens of centimetres were found to differ in surface temperature by around 4.5°C when compared to surrounding topography (Ranzi et al., 2004). However, the use of thermal data to delineate debris-covered glacier margins is limited to debris layers

with a thickness up to 0.5 m, as for layers with a thickness greater than this surface temperature is no longer controlled by cold propagation from underlying ice (Mihalcea et al., 2008). The use of thermal data is further complicated by differential shading across a debris-covered glacier surface, which affects debris surface temperature to the extent that a shaded debris-covered surface can have the same surface temperature as a clean-ice surface. Consequently, the use of thermal data for the application of determining debris-covered glacier boundaries involves large uncertainties (Bolch et al., 2007).

More recently, multidisciplinary approaches have been favoured for delineating debris-covered glacier boundaries. Paul et al. (2004) used a semi-automated approach using multispectral classification, slope derived from a Digital Elevation Model (DEM), where surrounding bedrock slope is assumed to be greater than debris surface slope, and neighbourhood analysis between pixels, where only pixels can only be classified as debris-covered if they are neighbouring a pixel containing clean-ice or debris-covered ice. Bolch et al. (2007) assessed various methods for identifying debris-covered glacier boundaries and found a mean slope threshold of less than 6° was most useful for identifying a debris-covered glacier surface, but that slope angle threshold was dependent on surface topography and the resolution of the digital elevation model (DEM) used. Curvature of the landscape was also found to aid identification of mountain ridges and moraines effectively, and so Bolch et al. (2007) suggested the most effective method to classify debris-covered glacier area was to use a combination of slope, curvature and thermal data. Shukla et al. (2010) also used a combination of optical, thermal and morphological inputs, and found there were notable differences in surface temperature between debris-covered ice and surrounding topography, even in shaded regions. In all cases, approaches using a DEM for glacier mapping noted the need for accurate, high resolution DEMs, which are difficult to produce for mountainous regions due to the extreme elevation differences and a lack of ground control points (Bolch and Kamp, 2006). Shukla et al. (2010) also noted higher resolution thermal data and more understanding of the thermal properties of debris-covered ice were needed to identify debris-covered boundaries effectively.

3.5.2.2. Debris thickness

Debris thickness has been measured *in situ* using Ground Penetrating Radar (GPR) (e.g. Nobes et al., 1994; McCarthy et al., 2017), but this method only provides thickness for debris over limited areas (10–100s metres), whereas the use of remotely sensed data allows a complete glacier surface coverage of debris thickness. The use of thermal infrared data to calculate debris thickness is based on the relationship between debris surface temperature and debris thickness, in which debris surface temperature increases with increasing debris thickness. This relationship occurs because underlying ice has less influence on debris surface temperature as they debris layer increases in thickness, and subsequently bulk thermal resistance of the debris layer increases (Nakawo and Young, 1982; Taschner and Ranzi, 2002; Ranzi et al., 2004).

Two approaches have been used to derive debris layer thickness from thermal infrared data, the first using the empirical relationship found between surface temperature and debris thickness, based on field data (e.g. Mihalcea et al., 2008a; 2008b; Minora et al., 2015; Soncini et al., 2016) and the second by solving the surface energy balance equation and calculating debris thickness as a residual (e.g. Foster et al., 2012; Rounce and McKinney, 2014; Schauwecker et al., 2015). Both the empirically-based and surface energy balance approaches for calculating debris thickness are limited in their application; the empirically-based approach requires field-derived debris surface temperature measurements and is specific to the glacier on which data is collected, meaning quantification of debris thickness across multiple glaciers with the same equation cannot be achieved. The limited application of the empirically-based approach is due to the variability in the debris surface temperature to debris thickness relationship, which varies with differing debris properties. The surface energy balance approach uses meteorological data from weather stations on or near the glaciers in question, meaning such data has to be available for its application. The surface energy balance approach of Foster et al. (2012) and Rounce and McKinney (2015) also include an arbitrary conversion factor and work most effectively when spatial variability in shortwave radiation across the glacier surface is omitted from calculations, despite the fact that shortwave radiation has been identified as an important control on surface energy balance (Arnold et al., 2006). These energy balance approaches also assume a linear temperature gradient through the debris layer and that the debris is dry, both of which,

as discussed in Section 3.2, rarely occur in a supraglacial debris layer on glaciers in the Himalaya-Karakoram (Nicholson and Benn, 2006; 2013).

3.5.2.3. *Glacier surface velocity*

Timeseries of glacier surface velocity can provide useful information on glacier change, as velocity changes can be an indicator of changes in glacier mass balance and hydrology (Quincey et al., 2009b). Glacier surface velocity can be determined using field data or remotely sensed data, the latter of which allows greater spatial and temporal application (Scherler et al., 2008). Glacier surface velocity can be derived from two time separated synthetic aperture data sets (e.g. Rignot et al., 1996; Kääb, 2005) or cross correlation of features in two time separated optical images (e.g. Quincey et al., 2009a; 2009b). Both methods have been used to calculate surface velocity for a number of glaciers in the Himalaya-Karakoram, including this thesis' study sites; Baltoro Glacier, Karakoram (e.g. Copland et al., 2009; Quincey et al., 2009b), and Khumbu Glacier, Central Himalaya (e.g. Luckman et al., 2007; Bolch et al., 2008; Quincey et al., 2009a). Calculating surface velocity is possible for clean-ice and debris-covered glaciers as surface features such as large boulders are good subjects for feature tracking. Surface velocity analyses have identified near stagnation of heavily debris-covered glacier tongues (e.g. Quincey et al., 2009a), and areas of reduced surface velocity on these glaciers have also been linked to supraglacial lake formation and potential sites for future GLOF events (Bolch et al., 2008).

3.5.2.4. *Surface lowering*

Near Infrared (NIR) remotely sensed data (e.g. Advanced Spacebourne Thermal Emission and Reflection Radiometer (ASTER)) and radar data (e.g. Shuttle Radar Topography Mission (SRTM)) are used to produce DEMs of glacier surfaces. Timeseries of these DEMs have then been used to identify changes in glacier surface elevation in the Himalaya-Karakoram (e.g. Bolch et al., 2011; Nuimura et al., 2012; King et al., 2017). DEMs are derived from stereo pairs; two datasets acquired at almost the same time (within 55 seconds of each other) from two sensors positioned at different angles on the sensor (e.g ASTER 3N and 3B, which are downward- and backward-facing; Abrams and Ramachandran, 2002). In mountainous regions such as the Himalaya-Karakoram accuracy of these DEMs is hindered by a lack of data from steep topography, as these

slopes distort reflection of the micro or visible wavelengths, or can be entirely hidden from sensor view (Kääb et al., 2005). In many cases DEMs derived from remotely sensed data also have relatively low resolution of 15 m (ASTER) or 30 m (SRTM), although some data sets have higher resolutions of less than 10 m (e.g. Surface Extraction with TIN-based Search-space Minimization (SETSM)). DEM resolution is increasing, but to determine a precise pattern of surface lowering on debris-covered glaciers, where a glacier surface is highly heterogeneous, DEM resolutions of the order of centimetres to 1-2 m are needed. GPS-derived DEMs with a vertical accuracy of ~0.17 m have been used to calibrate DEMs derived from remotely sensing data (e.g. Fujita et al., 2008; Nuimura et al., 2012), which increases their accuracy. However, when a timeseries of DEMs are used for calculating surface lowering, cumulative error from each DEM used produces much higher levels of uncertainty in the results, particularly over sub-decadal timescales, where surface lowering is relatively low and may be within calculated uncertainty (Nuimura et al., 2012).

3.5.2.5. Future remote sensing applications

Remotely sensed data used for investigating debris-covered glaciers has, thus far, primarily been acquired using satellites, which have varying resolution most commonly of the order of a number of metres to tens of metres, depending on the sensor type and wavelength. However, with the recent development of relatively low-cost unmanned aerial vehicles (UAVs) there is increased potential for collecting high-resolution data (of the order of a few centimetres). Such data could enable the production of much higher resolution DEMs and debris-covered glacier surfaces to be mapped in detail (e.g. Immerzeel et al., 2014). Such outputs could be used to identify spatially variable debris characteristics and previously satellite- or field-based techniques could be applied to an entire glacier surface at much higher resolution, including identifying patterns of albedo, aerodynamic roughness length, debris thickness and surface lowering (e.g. Mihalcea et al., 2008; Immerzeel et al., 2014; Ragettli et al., 2015; Rounce et al., 2015). High resolution remotely sensed data, such as those derived from UAVs, are still in development, but such techniques are needed to determine spatial variations in properties such as aerodynamic roughness length and surface temperature of supraglacial debris, and the percentage area of supraglacial water bodies on debris-covered glaciers (Watson et al., 2016). The use of

UAVs is currently limited by battery life, a problem that is exacerbated at high altitude. Satellite-derived data will also always have the advantage of covering multiple glaciers in one data set, and such data is increasingly becoming free to access. The recent increase in global availability of radar data (e.g. Sentinel sensors) also has the potential to increase understanding of surface roughness over glacier surfaces, as such data has been used for similar applications for other land cover types such as soil and volcanic terrains (e.g. Oh, 2004; Rahman et al., 2008; Bretar et al., 2013). However, the analysis of radar data in mountainous regions such as the Himalaya-Karakoram is limited due to topographic distortion, although such distortion can be corrected to a point with DEMs.

3.5.3. Numerical modelling for debris-covered glaciers

Supraglacial debris layers are, by nature, heterogeneous, both vertically and across a glacier surface (Reid and Brock, 2010). The ordered, logical nature of numerical modelling therefore means it is challenging to reproduce a naturally occurring heterogeneous debris layer exactly. However, increasingly complex models constrained by greater amounts of and more detailed *in situ* data mean estimations of ablation for debris-covered ice are becoming progressively more accurate. Physically-based numerical models used to calculate ablation, mass balance or hydrological output of glaciers require accurate meteorological data to reproduce precise processes and outcomes (Ragettli and Pellicciotti, 2012). To achieve this, point meteorological data collected adjacent to or on the glacier surface are needed as weather and climate can vary over short distances and between valleys, particularly in mountainous regions such as the Himalaya-Karakoram due to localised weather systems (Immerzeel et al., 2010). Consequently, studies specific to debris-covered glaciers have therefore been centred on a select number of glaciers, in part related to availability of long term meteorological data. These glaciers include Miage Glacier in the Italian Alps, Khumbu Glacier in the Central Himalaya, and Lirung Glacier in the Central Himalaya (e.g. Reid and Brock, 2010; Foster et al., 2012; Immerzeel et al., 2014; Rowan et al., 2015), where automated weather stations have been installed over longer timescales (months to years). Alternatively, some studies for specific glaciers have resampled low resolution modelled outputs (e.g. Mölg et al., 2008; Mölg and Kaser, 2011; Collier et al., 2014), although this approach is primarily used for regional modelling (e.g. Immerzeel et al., 2008; Maussion et al., 2014; Mölg et al.,

2014). For catchment areas interpolated data from a network of meteorological stations have also been used, such as precipitation data from APHRODITE for Asia (e.g. Tahir et al., 2011; Immerzeel et al., 2014) or from the Tropical Rainfall Measurement Mission (TRMM; Bookhagen and Burbank, 2010).

For distributed glacier-specific or localised (e.g. Everest Region) numerical modelling, point meteorological data have to be extrapolated across a glacier surface. Across a single glacier gridded meteorological data is produced using lapse rates for air temperature and air pressure (e.g. Rowan et al., 2015; Shea et al., 2015), or for incoming shortwave radiation by adjustment for topography and sky view factor (e.g. Reid and Brock, 2012; Rounce and McKinney, 2014). Lapse rates also vary between clean-ice and debris-covered glaciers, due to the warming of the near-surface atmosphere through energy lost by the debris layer (Steiner and Pellicciotti, 2015). A typical lapse rate for air temperature over a debris-covered glacier in the Himalaya-Karakoram is between 0.046°C m^{-1} and 0.0064°C m^{-1}, depending on the season and whether the monsoon is present (Immerzeel et al., 2014; Shea et al., 2015). Lapse rates have also been found to vary over diurnal timescales for debris-covered glaciers (Steiner and Pellicciotti, 2015), although, as yet, such variability has not been incorporated into numerical models calculating glacier mass balance.

3.5.3.1. Modelling glacier mass balance

Previous modelling of mass balance for a debris-covered glacier have used three main approaches: (1) temperature-index; (2) Positive degree-day factor and; (3) surface energy balance and heat transfer modelling. A temperature-index approach, in the most basic form, is where mass balance is calculated solely based on air temperature (Pellicciotti et al., 2005; Gabbi et al., 2014). Therefore, temperature index models need little input data and are more appropriate where general trends of ablation are the research focus. Degree-day factor models calculate the amount of melt for every day in which air temperature is above 0°C (e.g. Kayastha et al., 2000), and so are forced with air temperature data alone and omit ablation from sublimation. A surface energy balance approach needs a large number of meteorological and debris input parameters to calculate all energy fluxes at the debris surface (e.g. Reid and Brock, 2010; Lejeune et al., 2013; Collier et al., 2013; 2014). For all model types the accuracy of calculated mass

balance is affected when meteorological data is not collected on the glacier surface (Gabbi et al., 2014). Inclusion of heat transfer through a debris layer in surface energy balance models means an additional set of parameters concerned with the thermal conductivity of the debris layer, its porosity and moisture content are required. Consequently, surface energy balance models are appropriate for investigating small scale variations across a glacier surface such as variation in debris properties, as all parameters controlled by debris properties are considered (e.g. albedo, turbulent sensible and latent heat fluxes), and where meteorological data collected on the glacier surface is available, so that surface energy fluxes accurate for the glacier surface are used.

Temperature index models developed for debris-covered glaciers largely disregard variability in supraglacial debris distribution (e.g. Jouvet et al., 2011; Brown et al., 2014; Immerzeel et al., 2013). Enhanced temperature index models have been developed that incorporate variations in shortwave radiation, albedo and debris thickness across a glacier surface (e.g. Pellicciotti et al., 2005; Carenzo et al., 2016). However, these enhanced temperature index models still rely on surface energy balance models to constrain these additional parameters. Carenzo et al. (2016) incorporated debris thickness using Reid and Brock's (2010) surface energy balance point model to calculate ablation for varying debris thicknesses, and then incorporated the lag time taken for heat energy to pass through the debris layer for differing debris thicknesses into the enhanced temperature index model, with lag time increasing with increasing debris thickness.

Enhanced temperature index models are less demanding than surface energy balance models in terms of input data and can be a useful to avoid incorporation of poorly parameterised processes. However, the reliance of some of these models on a surface energy balance model that may in itself be flawed, due to basic parameterisation of debris properties, means model results should be considered cautiously. Consequently, mass balance calculations derived using the combined surface energy balance and temperature index approach are equally constrained by a less than accurate simulation of a supraglacial debris layer that restricts surface energy balance models. Enhanced temperature index models are therefore advantageous due to little input data requirements, and when compared there has been little difference between calculated ablation from surface energy balance and enhanced temperature index models, but

dependence of the enhanced temperature index model type on surface energy balance models means both model types have the same limitations.

Surface energy balance and heat transfer models for debris-covered ice, such as those developed by Lejeune et al. (2013), Collier et al. (2014) and Evatt et al. (2015) have, thus far, been predominantly point-based rather than distributed, with the exception of Reid and Brock (2012) and Fyffe et al. (2014). Point surface energy balance models of debris-covered ice have now been developed to include detailed aspects of the debris layer such as moisture content, porosity and snow cover (e.g. Lejeune et al., 2013; Collier et al., 2014; Evatt et al., 2015), and hydrological models of debris-covered glaciers are now starting to include distributed debris thickness maps of a glacier surface (e.g. Minora et al., 2015; Ragettli et al., 2015; Soncini et al., 2016). However, despite such development in these numerical models, only one numerical model for calculating glacier surface energy balance and heat transfer for debris-covered ice has, to the author's knowledge, been able to simulate the Østrem curve; the model developed by Evatt et al. (2015). Most surface energy balance models produce exponentially decreasing ablation with increasing debris thickness, omitting the true pattern of increased ablation between zero debris thickness and effective thickness of a debris layer (Lejeune et al., 2013). Although the model developed by Evatt et al. (2015) recreated the Østrem curve through inclusion of airflow through the debris layer, the influence of moisture content in the debris layer was omitted, thus disregarding the importance of this parameter on debris-covered glacier mass balance, which was identified by Collier et al. (2014) as an important control on latent heat flux, and is also likely to be an important control on energy flux within a supraglacial debris layer on monsoon-influenced debris-covered glacier'.

In most cases, surface energy balance models for debris-covered ice assume the ice surface is always at melting point, as these studies have focused on melt through an ablation season (e.g. Nicholson and Benn, 2006; Reid and Brock, 2010; Evatt et al., 2015). However, ice temperature can drop below melting point in some locations where colder air temperatures occur, such as the Himalaya-Karakoram, or outside of the ablation season (Lejeune et al., 2013). Lejeune et al. (2013) tested the significance of this assumption, and found that for thin debris layers (< 4 cm) net heat flux through the debris layer is underestimated by a factor of two, causing an artificial addition of energy

to the debris heat flux. Consequently, models that assume an ice temperature at melting point often overestimate debris surface temperature (Collier et al., 2014). Therefore, more recent surface energy balance models allow ice surface temperature to vary with heat conduction through the debris (e.g. Collier et al., 2014).

One of the most critical limitations of point and distributed surface energy balance models is that many of the debris properties are kept constant, such as albedo and aerodynamic roughness length, whilst on a debris-covered glacier surface these vary in space and time. To identify the importance of spatiotemporal variability in debris properties such as moisture content, porosity, aerodynamic roughness length and albedo on ablation it would be appropriate to investigate the importance of such variability using surface energy balance and heat transfer models for debris-covered ice. However, development of such numerical models is currently inhibited by a lack of quantification of the extent to which these debris properties vary in space and time.

3.5.3.2. Estimating glacier change

Investigation of glacier change in the Himalaya-Karakoram spans a range of spatial extents, from the entire mountain range (e.g. Scherler et al., 2011; Bolch et al., 2012) to specific glaciers (e.g. Rowan et al., 2015; Shea et al., 2015; Soncini et al., 2016). Although studies focusing on future glacier change in the Himalaya-Karakoram use numerical models for their predictions, recent changes in glacier mass balance have been measured through comparison of glacier surface elevation. Bolch et al. (2012) estimated a change in mass balance across the Himalaya-Karakoram of -0.21±0.05 m a^{-1} w.e. between 2003 and 2008 using IceSat (2003–2009) and SRTM (2000) data (Figure 3.4). This figure is lower than the estimates of global mean change for glacier mass balance due to positive mass balance of some Karakoram glaciers. Berthier et al. (2007) used SPOT5 (2004) and SRTM (2000) derived DEMs to calculate an elevation change of -0.7 to -0.85 m a^{-1} w.e. for the Western Himalaya, whilst Gardelle et al. (2013) calculated a change in glacier mass balance of -0.22±0.12 m a^{-1} w.e. for the Eastern Himalaya, -0.33±0.14 m a^{-1} w.e. for the Central Himalaya and -0.45 m a^{-1} w.e. for the Western Himalaya using SRTM and SPOT5 data between 1999 and 2011. The most recent study conducted by Brun et al. (2017) used DEMs to calculate region-wide change in glacier mass balance of 0.13±0.04 m a^{-1}

w.e. between 2000 and 2016. However, King et al. (2017) argue that such region-wide averaging of mass loss of Himalaya-Karakoram glaciers disregards catchment or glacier scale variability of changes in mass balance. Whilst uncertainties do exist for these satellite-derived calculations of glacier change, they provide a useful benchmark against which numerical models results for glacier change can be compared.

Hydrological models have been used for predictions of future glacier change in the Himalaya-Karakoram to determine the influence of climate change on glacier and river discharge change. An approach that combines these three variable parameters is advantageous as changes in glacier and river discharge are dependent on climate change, and future hydrological regimes will be affected by the interaction between these systems. However, the accuracy of hydrological models, such as that produced by Immerzeel et al. (2010), is limited by the use of downscaled global climatic model data and the poor constraint on interannual variability in monsoonal weather patterns and future changes to the climate system (Immerzeel et al., 2013). Although regional models for future change provide an overall picture of changes in hydrological cycles and sea level change, the large spatial resolution of these models means a detailed consideration of spatially variable climate, glacier dynamics and the effect of supraglacial debris cover are often lacking (e.g. Rees and Collins, 2006; Immerzeel et al., 2010). For example, Rees and Collins (2006) used a temperature index model to determine changes in glacier mass balance for a 150-year period (from 1990 to 2140) with a warming of 0.06 °C a^{-1} air temperature change. However, the temperature model omitted variations in precipitation and did not account for spatial variability in the air temperature and glacier ablation across the Himalaya-Karakoram or the influence of debris cover. Such spatially variable response of glacier retreat and lowering across the Himalaya-Karakoram is attributed to spatially variable topography and climate, and varying proportions of debris-covered glaciers across the mountain range (Fujita and Nuimura, 2011; Scherler et al., 2011), and so these omissions are likely to be highly influential to estimations of glacier mass balance.

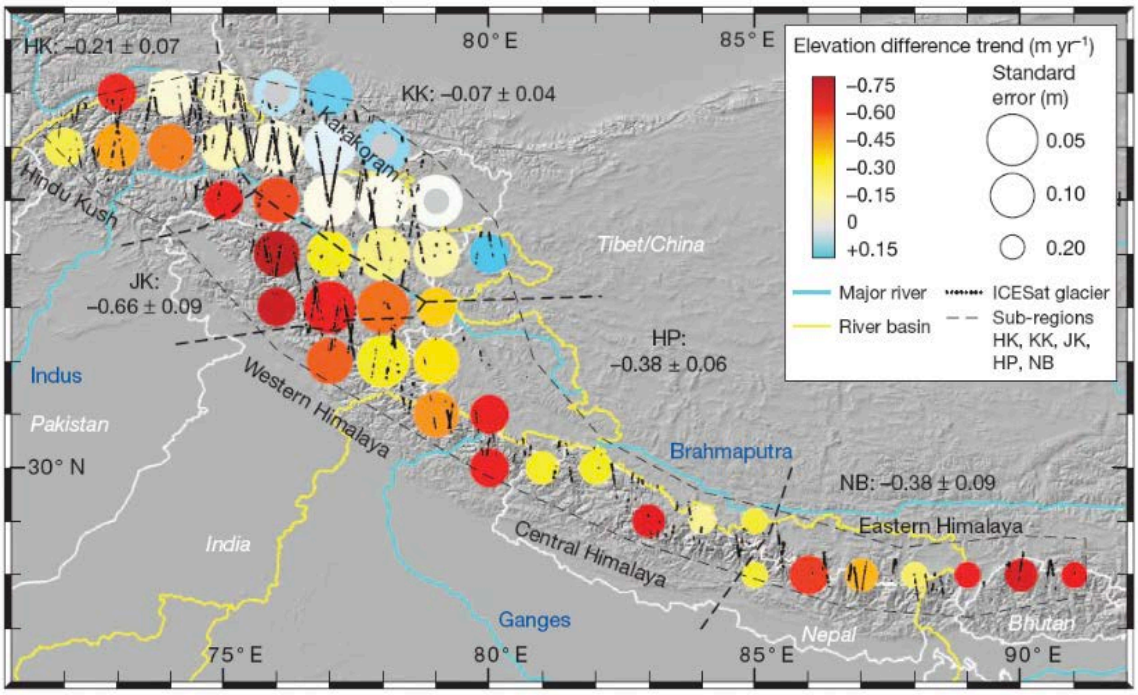

Figure 3.4: Glacier surface elevation change estimated from the Shuttle Radar Topography Mission (2000) and IceSat data (2003–2009) for the Himalaya-Karakoram- -Kush between 2003 and 2008. Reproduced from Bolch et al., 2012.

Regional models often omit debris cover in simulations of glacier mass balance in the Himalaya-Karakoram due to the complexity of its influence on mass balance and high levels of spatial variability across the region. As with estimating glacier mass balance, using a more localised approach to hydrological modelling focused on single glacierised catchments, the influence of debris cover on glaciers can been included, weather data derived from meteorological stations within the catchment can be used to force these models, and more specific variables can be included in the smaller model domains without affecting the computing power needed. Immerzeel et al. (2011) modelled the hydrological response to climate change for the glacierised Langtang catchment in the Central Himalaya using a combined distributed cryospheric and hydrological model. The cryospheric aspect of the model was based on an assumption that the glaciers in the catchment flow solely through basal sliding, and therefore includes estimations of bedrock topography, slope and ice thickness, whilst ablation is estimated using a degree day factor (ablation occurs on days when positive temperatures occur). Runoff from

these glaciers was then taken as a percentage of the ablation calculated; debris cover was considered as a multiplicative factor of 0.7 for most glaciers in the catchment and 0.15 for Lirung Glacier, on which debris cover was particularly thick. Despite a lack of consideration for spatially variable debris layer thickness, Immerzeel et al. (2011) found modelled glacier-derived river discharge was closely correlated with measured discharge (Pearson correlation coefficient of 0.87). Where numerical models have included spatially variable supraglacial debris layers the results, thus far, have agreed well with *in situ* data. Minora et al. (2015) and Soncini et al. (2016) have both considered such spatial variability in debris cover by including debris thickness maps derived from thermal satellite data in their modelling of Karakoram and Everest catchments, and results from both of these studies also showed close correlation with discharge data collected for each catchment.

Alongside hydrological modelling, a limited number of specific glacier modelling studies that have given predictions for past and future changes in glacier mass balance for debris-covered glaciers exist, with two main studies of the Everest Region, Central Himalaya (e.g. Shea et al., 2015; Rowan et al., 2015). The extent to which debris cover was included in these models was variable. A supraglacial debris layer was included in Shea et al.'s (2015) model through the use of subdued degree day factor of 3.34 mm $°C^{-1}$ d^{-1} which, as with Immerzeel et al.'s (2011) hydrological model for the Langtang catchment, assumes the debris layer is constant in space and time, an assumption which is not the case in true debris-covered glacier systems (e.g. Bolch and Kamp, 2006). Using this model, Shea et al. (2015) estimated a change in glacier volume of between -26% and -70% over the next 35 years, depending on climatic conditions. Rowan et al. (2015) did include spatially variable input of debris into the glacier system, the rate of which was derived from headwall erosion rate calculated by Scherler et al. (2011). By simulating the input of debris into the accumulation zone and its emergence rate in the ablation zone the debris cover of Khumbu Glacier evolved over the study period (Little Ice Age to present day, present day to 2200). However, the integrated second-order shallow ice approximation (iSOSIA) model used by Rowan et al. (2015) did not include the influence of debris cover on ablation through surface energy balance, and debris thickness for the glacier surface was estimated using the model outputs. Rowan et al. (2015) is therefore the only study, to the authors' knowledge, which simulated debris as dynamic within a glacier system when

considering glacier change in the Himalaya as a result of climate forcing, but the model is forced solely by temperature change, whereas Shea et al.'s (2015) estimations also included future variations in precipitation. To further understanding of glacier change on specific glaciers it is appropriate to consider precipitation and temperature change in climate scenarios, and to develop a method of incorporating debris into a glacier system following the approach used in Rowan et al.'s (2015) study, as well as including surface energy balance and heat transfer through a debris layer and its effect on glacier ablation.

3.6. Chapter summary

This chapter has provided an overview of supraglacial debris properties and their role in surface energy balance and ablation of a debris-covered glacier, as well as an introduction of how surface energy balance of debris-covered ice and distribution of supraglacial debris are intrinsically linked to the mass balance of a debris-covered glacier. Current research on debris-covered glaciers has also been reviewed, in terms of the methods used for understanding debris-covered glacier ablation, and the current state of numerical models for calculating mass balance of debris-covered glaciers. The limitations of most numerical models for debris-covered glaciers highlight the difficultly in including all aspects of a glacier system, and the vast number of variables need to be constrained to enable spatial and temporal variation in debris distribution to be incorporated into numerical models of debris-covered glaciers. To further understanding of debris-covered glacier mass balance it is important that a debris layer is not disregarded in modelling procedures, and methods for incorporating variability of the debris layer in space and time are developed. To enable inclusion of debris in such a way a greater understanding of the extent of debris distribution is needed.

Chapter 4: Study sites

4. Study sites

The debris-covered glaciers chosen for analysis in this thesis were Khumbu Glacier, Central Himalaya, and Baltoro Glacier, Karakoram (Figures 1.2; 2.1; 4.1a; 4.2a). These glaciers are typical debris-covered glaciers, with rock debris covering the majority of their ablation areas. The Baltoro and Khumbu glaciers have been chosen as the focus for research in this thesis due to their extensive supraglacial debris layers, but also because they vary in their geological and climatological settings, glacierised area, velocity and mass balance regimes, and consequently are at different stages of evolution in terms of their glacier mass balance, debris layer formation and response to climate change. One of the few similarities between these glaciers is the relatively large amount of data that has been collected on or near these glaciers, compared to most other glaciers in the Himalaya-Karakoram. More recently, Baltoro and Khumbu Glaciers have been the focus for a number of numerical modelling studies (e.g. Rowan et al., 2015; Shea et al., 2015; Minora et al., 2015; Soncini et al., 2016). As this thesis aims to develop understanding of supraglacial debris distribution and input of such distribution patterns in numerical modelling, these two glaciers were chosen due to the relatively large range of *in situ* and modelled data available for comparison. In this chapter an overview of each of the study glaciers is presented, followed by a summary of previous work undertaken on each glacier to date. Further detailed study site sections are also included in each of the papers (Chapters 5–8), which are specific to the focus of each of the papers.

4.1. Khumbu Glacier

Khumbu Glacier is located in the Everest region of Nepal, in the Central Himalaya (Figure 4.1; 27°56'N, 86°56'E). The Everest Region experiences monsoonal weather patterns and, consequently, Khumbu Glacier is of summer-accumulation-type (Yao et al., 2012). The prevailing wind directions in the Everest Region are south to north and southwest to northeast, with 90% of the region's precipitation falling between June and September (Ichiyanagi et al., 2007; Salerno et al., 2014), although snowfall at high elevations occurs throughout the year (Benn et al., 2012). Localised circulation is dominated by a southerly wind direction, which is present during daylight hours throughout the year (Salerno et al., 2014). Glaciers in the Everest Region mainly flow north to south due to constraint by geological structures associated with the east to west Main Boundary Fault of the

Himalayan mountain range, which constrains valley formation (Fushimi, 1977). The Everest Region is one of the most heavily glacierised regions in the Himalaya-Karakoram, with one third of the area covered in glacier ice or permanent snow and ice cover, and up to 2% of glacierised area covered by supraglacial water bodies (Salerno et al., 2008; Salerno et al., 2012; Thakuri et al., 2014).

Khumbu Glacier is the highest glacier in the world, and flows from its accumulation area in a glacial cwm surrounded by the peaks of Mount Everest, Lhotse, Hilary Peak and Nuptse, at around 6850 m above sea level (a.s.l.). The glacier initially flows in a northwesterly direction for around 6 km, subsequently flowing through the Khumbu Icefall and changing to a southwesterly direction. Khumbu Glacier covers an area of around 27 km^2 and is around 17 km in length, with ice thickness up to around 400 m thick (RGI Consortium, 2017). The Khumbu Icefall, within which the Equilibrium Line Altitude (ELA) of Khumbu Glacier is located, flows at around 70 m a^{-1}, and is the steepest section of the glacier and heavily crevasses (Benn and Lehmkuhl, 2000; Nakawo et al., 1999; Kadota et al., 2000; Quincey et al., 2009a). The ablation zone, which is located below the icefall, is around 10 km long and has a low gradient with a low to no velocity (< 10 m a^{-1}, within the error of feature tracking; Fushimi, 1977; Luckmann et al., 2007; Quincey et al., 2009a). The ablation area has a mean gradient of < 2°, with a reverse gradient across the final 1 km glacier area adjacent to the terminal moraine (Hambrey et al., 2008). A number of tributary glaciers feed Khumbu Glacier, the most notable being Changri Nup and Changri Shar, both of which are now detached from the tongue of Khumbu Glacier but still feed meltwater to the glacier bed (Vincent et al., 2016). Large lateral-medial moraines with a height of at least 60 m above the debris-covered glacier surface surround Khumbu Glacier (Figure 4.2; Watanabe et al., 1986), and are considered to be the margins of the glacier at the end of the Little Ice Age (Hambrey et al., 2008). Since the Little Ice Age at around 0.5 ka the glacier has undergone less than 1 km terminus recession (Bajracharya et al., 2014). Previous measurements of ablation rates on Khumbu Glacier are of the order of 0.02–0.03 m d^{-1} for debris free ice (Muller, 1968; Inoue and Yoshida, 1980) and around 0.015 m d^{-1} for ice under a 1.2 m thick debris layer (Inoue and Yoshida, 1980). Between 1978 and 1995 10 m of surface lowering is thought to have occurred in the ablation zone of Khumbu Glacier (Kadota et al., 2000; Naito et al., 2000).

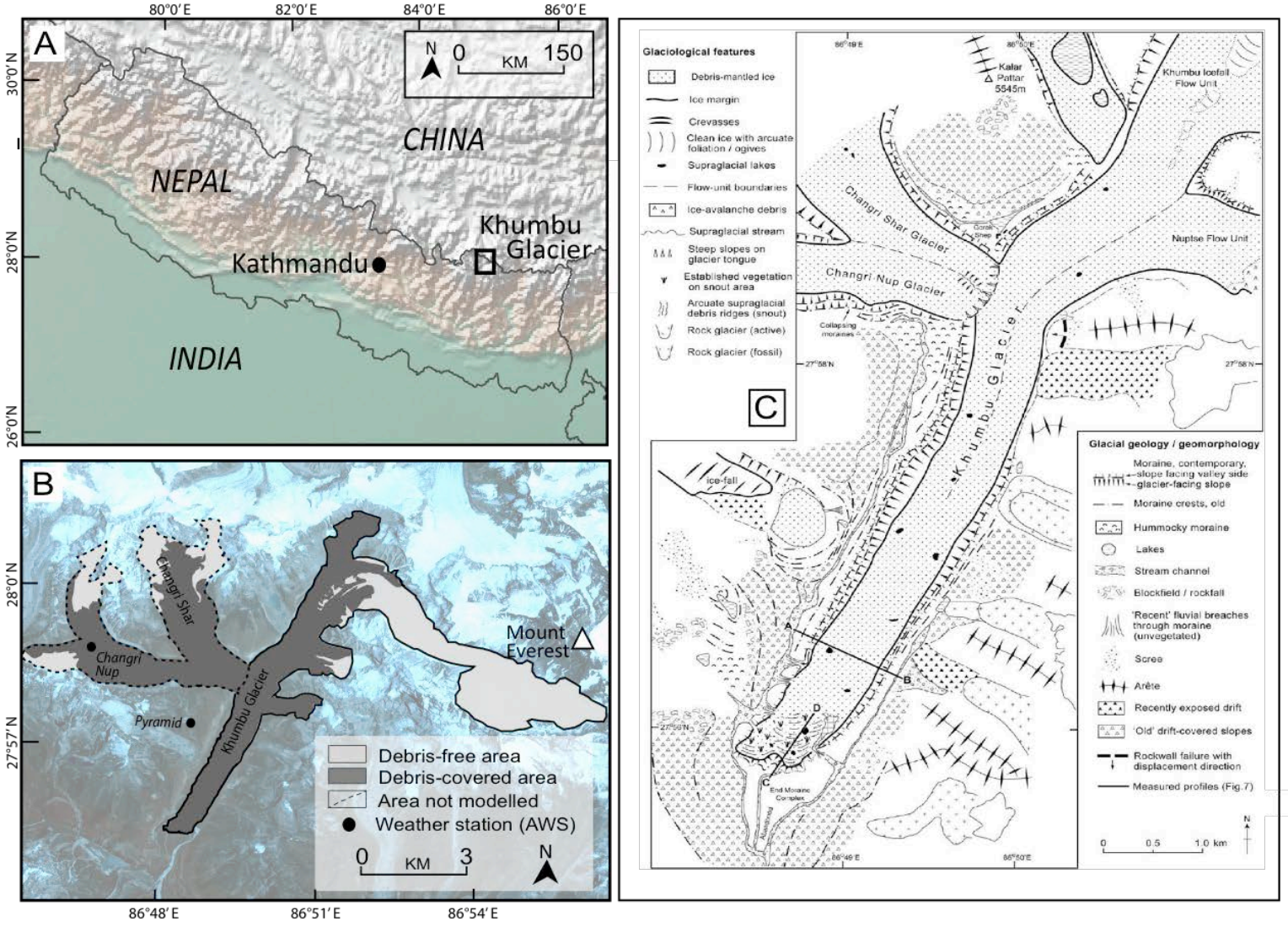

Figure 4.1: Location of Khumbu Glacier in (a) the Himalaya-Karakoram, (b) the Everest Region and (c) A geomorphological map of Khumbu Glacier (Hambrey et al., 2008).

Spatially extensive supraglacial debris cover on Khumbu Glacier commences below Khumbu Icefall and increases in spatial distribution and thickness downglacier (Nakawo et al., 1986), reaching at least 4 m thick at the glacier terminus (Figure 4.2; Soncini et al., 2016). The debris-covered area of Khumbu Glacier has an undulant topography, with large (>20 m) topographic highs and associated depressions across the glacier surface (Hambrey et al., 2008). Many of the topographic depressions on the glacier surface contain supraglacial water bodies and are associated with large (up to around 30 m high) ice cliffs. Khumbu Glacier has developed a chain of connected surpraglacial water bodies since around 2000, which is indicative of future large lake development (Watson et al., 2016). The supraglacial debris layer is very poorly sorted, predominantly made up of sandy boulder-gravel but with grain size varying from silt to large boulders (>10 m) (Figure 5.3: debris types). Lithology of the debris is spatially variable and consists almost entirely of schist and granite, with the debris layer in the southwest area near the terminus now consisting of soil with development of vegetation on the debris surface. A schistose-rich debris layer exists in the centre of the glacier, around which granite-rich debris dominates in marginal zones (Fushimi, 1980; Nakawo et al., 1986). The distribution of different lithologies of supraglacial debris is partially controlled by the geology of the bedrock surrounding the glacier (Figure 4.2), but distribution has been influenced further by glacier flow. Rock debris reaches the glacier surface supraglacially through rockfall, debris avalanches and failure of lateral moraines, the rate of which increases during the summer monsoon (Nakawo et al., 1986).

Two meteorological stations are located in the upper Khumbu valley: The Pyramid Station at 5050 m a.s.l., managed by EvK2CNR and the Nepal Academy of Science and Technology, which has collected data since 1990 and; an Automated Weather Station (AWS) on the debris-covered surface of Changri Nup Glacier that has collected data since November 2012 at an elevation of between 5360 and 5470 m a.s.l. (elevation change due to relocation of station in November 2014) supported by the 570 French Service d'Observation GLACIOCLIM and the French National Research Agency. At both sites, air temperature, relative humidity, air pressure, incoming and outgoing shortwave and longwave radiation, and wind direction and speed are measured. At the Pyramid weather station precipitation is also measured, whilst at the Changri Nup AWS site supraglacial debris temperature and glacier ablation are measured.

A Japanese expedition to Khumbu Glacier undertaken in the 1970s provided the first insight into mass balance, velocity and ablation of the glacier (e.g. Fujii and Higuchi, 1977; Inoue, 1977; Inoue and Higuchi, 1980; Kodama and Mae, 1976), as well as undertaking geomorphological mapping and sediment analysis of supraglacial debris cover, and investigating processes of debris distribution on the glacier (e.g. Iwata et al., 1980; Fushimi et al., 1980; Moribayashi and Higuchi, 1977; Nakawo et al., 1986; Watanabe et al., 1986). These studies identified, among other conclusions, varying lithologies of supraglacial debris on Khumbu Glacier and the potential for such variability to cause spatial variation in albedo, and therefore ablation, across the glacier surface (e.g. Fushimi, 1980; Nakawo et al., 1986). Further research in the 1990s investigated the spatial variability of debris thickness across the glacier and observed the importance of such variability on ablation (e.g. Kadota et al., 2000; Takeuchi et al., 2000), and the evolution of Khumbu Glacier's supraglacial debris layer between 1978 and 1995 (Iwata et al., 2000). Gades et al. (2000) also undertook radio echo sounding of the glacier to determine ice thickness across Khumbu Glacier, which was found to reach 450 m in places.

More recently, remotely sensed data have been used to delineate the glacier's boundaries and monitor changes in area, surface elevation, surface velocity and terminus location (e.g. Bolch et al., 2007; 2008; 2011; Benn et al., 2012; Quincey et al., 2009a; Thakuri et al., 2014; King et al., 2017). Research based on remotely-sensed data has been hindered by frequent cloud cover, low accuracy of data collected in mountainous terrains and a difficulty in delineating glacier area due to debris cover (e.g. Racoviteanu et al., 2008; Thakuri et al., 2014), but as the number of satellite sensors and temporal range of existing sensors has increased the number of useful data sets has consequently increased. Quincey et al. (2009a), using feature tracking of satellite data, first confirmed that the tongue of Khumbu Glacier displays little to no flow, which was first considered to be the case by Fushimi in 1977.

Alongside climatic research undertaken in the area (e.g. Salerno et al., 2014), a culmination of glaciological and climatic data identified volume shrinkage of Khumbu Glacier and surrounding glaciers in the Everest Region has occurred since the latter half of the 20th century. The Everest Region has undergone an increased rate of glacier area shrinkage since the 1960s (Thakuri et al., 2014) and a higher rate of mass loss between

2000 and 2010 (Bolch et al., 2011; Nuimura et al., 2012; King et al., 2017). Changes in glacier area and mass have occurred alongside decreasing precipitation, which is half of the annual amount of precipitation 20 years ago. An increase in minimum air temperatures has also caused a reduction in precipitation falling as snow over glacier ablation areas since the 1980s (Salerno et al., 2014).

Annual retreat rate of glaciers in the Everest Region was calculated as 8.2±0.2 m a^{-1} between 1962 and 2011, although this rate was skewed by the Imja, Langmuche and Kdu_gr38 Glaciers, which each retreated by around 1000 to 2000 m during the study period (Thakuri et al., 2014). Mean annual shrinkage rate of glacier area in the Everest Region over the same period was calculated as 0.51±0.06% a^{-1}, which accelerated from 0.27 % a^{-1} between 1962–1975 to 0.75% a^{-1} since 1992, with Khumbu Glacier losing around 5% of its area since 1962, resulting in a volume loss of 0.19 km^3 over the same period (Bolch et al., 2008). More recent estimations of mass loss suggest a decrease in glacier mass in the Everest region of the order of -0.52±0.22 m w.e. between 2000 and 2015 (King et al., 2017). Debris-covered area in the region is thought to have increased by 17.6±3.0% since 1962, whilst snow line altitude, a proxy for equilibrium line altitude (ELA), has increased in elevation by 182±9 m between 1962 and 2011 (Thakuri et al., 2014).

Numerical modelling has been the focus of the most recent research on Khumbu Glacier, to determine debris thickness across the glacier (e.g. Rounce and McKinney, 2014) and to simulate past and future glacier change (e.g. Rowan et al., 2015; Shea et al., 2015; Soncini et al., 2016). The focus of research on Khumbu Glacier has been based on the relatively high availability of historic and contemporary data for the glacier and surrounding area. Khumbu Glacier is also a globally renowned glacier and understanding its response to climate change will provide useful data to local populations and the tourist industry in the Everest Region, with the aim of identifying changes in the region's hydrology and mitigating for the possible occurrence of glacial lake outburst floods.

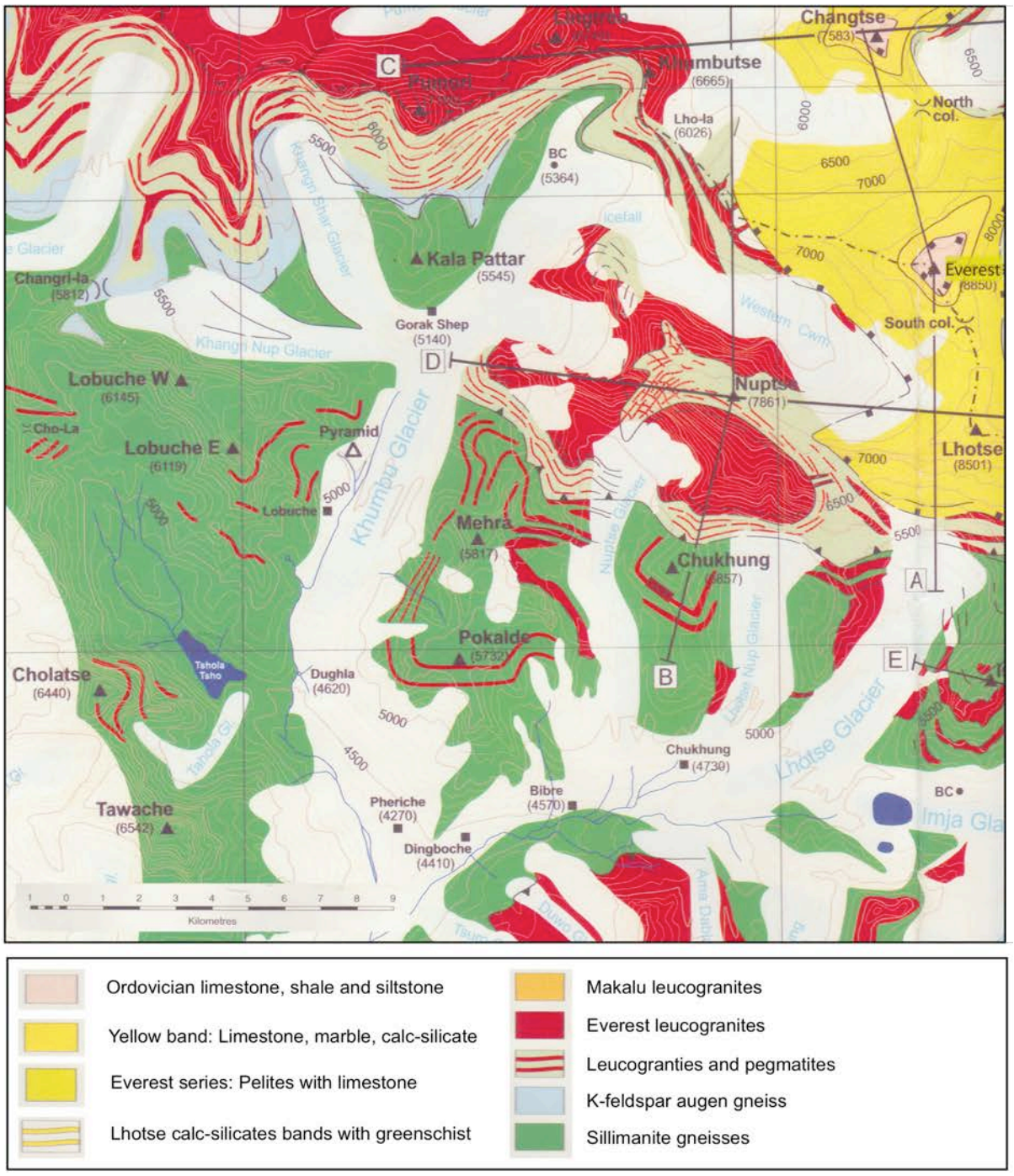

Figure 4.2: Geological map of the Everest Region, showing the main lithologies in the Khumbu Valley are schist (light green), gneiss (dark green) and granite (red), and a prominent yellow band of marble (yellow) at ~8400 m on Everest . Reproduced from Searle, 2007).

4.2. Baltoro Glacier

Baltoro Glacier is located in the Gilgit-Baltistan region of Pakistan in the Karakoram (Figure 4.3; 35°56° N, 76°46° E) and runoff from glaciers in this region flow into the Indus River (Bookhagen and Burbank, 2010). The climate in the Baltoro area is dominated by the Westerlies, with occasional monsoon influence during the summer due to variability in monsoon intensity (Wake, 1989; Young and Hewitt, 1990). Consequently, Baltoro Glacier is of winter-accumulation-type, receiving most of its precipitation in winter and spring, with annual precipitation on the glacier of the order of 0.2–0.15 m a^{-1} at around 2500 m a.s.l. (Decheng, 1978; Archer and Fowler, 2004). Precipitation on glaciers in the Karakoram is spatially variable between valleys and highly dependent on elevation, with a 5- to 10- fold increase in precipitation between glacier termini at around 2500 m and accumulation areas above 4800 m (Young and Hewitt, 1990; Hewitt, 2005). Since the 1960s, meteorological data collected in the Karakoram have shown an increase in winter precipitation and declining mean summer maximum and minimum temperatures, the latter attributed to more frequent summer storms causing increased cloudiness (Hewitt, 2005). A recent regional trend of positive mass balance in the Karakoram has been partially attributed to such changes in climate, and is predicted to occur until at least 2100 (Ridley et al., 2013). It has also been suggested that the large size of glaciers such as Baltoro Glacier causes them to have long response times to climate change, or that due to their size the change in climate during the 20th and 21st centuries has not yet been sufficient to affect glacier mass (Minora et al., 2016).

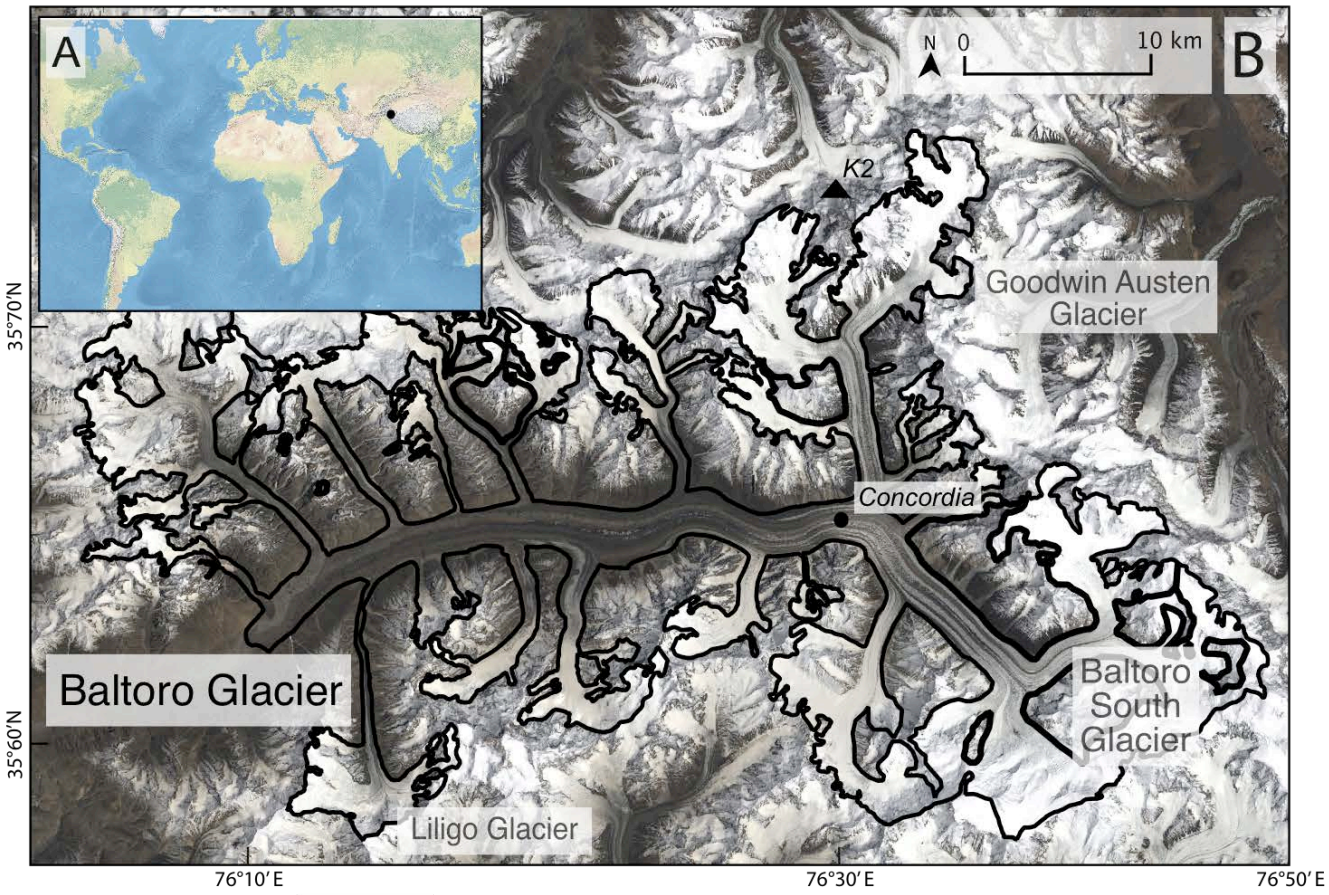

Figure 4.3: The location of Baltoro Glacier in (a) the Himalaya-Karakoram; and (b) the Baltoro region.

Baltoro Glacier is around 62 km long and around 2 km wide, covering an area of around 524 km^2 (Figure 4.3; Mihalcea et al., 2006; RGI Consortium, 2017), and accumulates mass predominantly through ice and snow avalanches (Wissmann, 1959). The glacier extends from an elevation of 8611 m a.s.l. to 3370 m a.s.l., with Goodwin-Austen Glacier and Baltoro South Glacier converging at Concordia (~4613 m a.s.l.) to form the main glacier tongue. Goodwin-Austen Glacier flows in a southerly direction, whilst Baltoro South Glacier flows in a northwesterly direction, with a change in direction as they converge resulting in a westerly flowing main glacier tongue. Around 16 tributary glaciers join the main tongue of Baltoro Glacier with at least two of these being surge-type (Lilligo Glacier; Diolaiuti et al., 2003). The ELA of Baltoro Glacier is between 5300 and 5500 m a.s.l., above which almost all annual precipitation falls as snow (Mayer et al., 2006). Mean velocity of Baltoro Glacier is around 120 m a^{-1}, with the highest velocities occurring just below Concordia of the order of > 200 m a^{-1} (Quincey et al., 2009b). The terminus position of

Baltoro Glacier has been relatively stable throughout the 20th century with maximum fluctuations of the order of 65 m between 1913 and 2004 (Desio, 1961; Mayer et al., 2006). Surface lowering between 1909 and present day have been measured at less than 40 m with many areas along the glacier length showing little to no change in glacier surface elevation (Mayer et al., 2006). Baltoro Glacier's mass has fluctuated during the 20th and 21st centuries, together with variations in ice velocity since 2000, but more recently the glacier is thought to have been gaining mass (Pecci and Smiraglia, 2000; Smiraglia et al., 2007; Copland et al., 2009; Quincey et al. 2009b; Gardelle et al., 2012; Minora et al., 2016).

Spatially extensive supraglacial debris cover on Baltoro Glacier is present below around 5000 m a.s.l. on the glacier surface, initially as medial moraines that then converge below Concordia to form a continuous debris cover > 1 m thick (Mayer et al., 2006; Mihalcea et al., 2008). The debris-covered ablation area of Baltoro Glacier has a low surface slope of around 4° and an undulant topography, with topographic highs and lows varying in elevation of the order of around 25 m, which form due to the presence of supraglacial water bodies and folding of ice in areas where tributary glaciers join the main glacier tongue (Mayer et al., 2006). In the upper section of the main glacier tongue a series of 'ice sails' are present, which are debris-free structures that rise vertically out of the debris cover along the main glacier flow line and may enhance ablation on the glacier in a similar way to an ice cliff (Mayer et al., 2006; Evatt et al., 2016). Supraglacial debris thickness increases towards the glacier terminus and debris is very poorly sorted, ranging from silt to large boulders (Mayer et al., 2006). Lithology of debris cover on Baltoro Glacier varies spatially, with a mixture of granite, gneiss and schist on the glacier surface (Figure 4.4; Desio, 1969; Searle, 1991).

The first documented glaciological research on Baltoro Glacier was carried out by the Italian Karakoram Expedition, undertaken in the 1950s (Desio et al., 1961), and first identified variations in the terminus position of Baltoro Glacier using a reference rock in front of the terminus now referred to as 'Desio Rock'. The geology of the Baltoro valley was originally described in the late 19th and early 20th century (Conway, 1894; Desio, 1930), although a comprehensive geology map of the region was not produced until 2010 (Figure 4.4; Searle et al., 2010). Following a series of early studies, a relatively small

amount of research, glaciological or otherwise, has focused on the Karakoram specifically. Glaciers in the Karakoram have been the focus of few hydrological modelling studies on a catchment scale (e.g. Chevallier et al., 2011; Tahir et al., 2011; Minora et al., 2015), despite the importance of these glaciers to discharge and hydrological regime of the Indus basin (Young and Hewitt, 1990; Hewitt, 2005). Research on Baltoro Glacier in the last decade has started to bridge such a gap in glaciological data from the region, with a series of studies focused on characteristics of the glacier in terms of ablation rates, debris distribution and glacier velocity (e.g. Mayer et al., 2006; Mihalcea et al., 2006; Quincey et al., 2009b). Mayer et al. (2006) found that velocity of Baltoro Glacier varied seasonally, whilst Copland et al. (2009) and Quincey et al. (2009b) identified annual variation in velocity and attributed such changes to basal lubrication of the glacier. Debris distribution for Baltoro Glacier has also been investigated, particularly in terms of debris thickness and its influence on spatially variable ablation of the glacier (e.g. Mihalcea et al., 2008; Collier et al., 2013; Minora et al., 2015), and variation in debris thickness over a decadal timescale has been touched upon in hydrological modelling undertaken by Minora et al. (2015), through updating the 2004 debris thickness map produced by Mihalcea et al. (2008), to produce a 2010 debris thickness map. However, Minora et al. (2015) did not identify or investigate any spatiotemporal changes in debris thickness for Baltoro Glacier between 2004 and 2010.

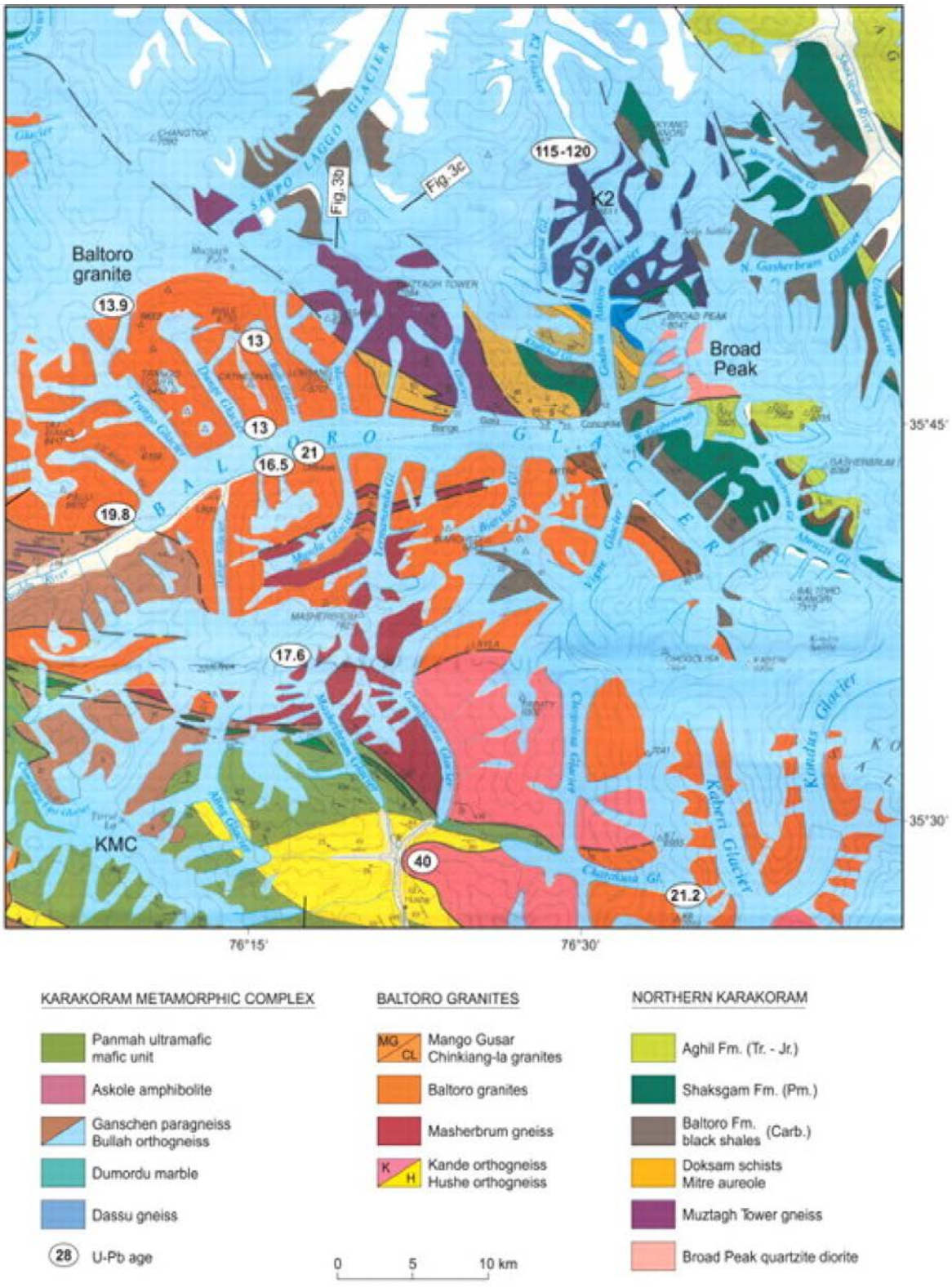

Figure 4.4: Geological map of the Baltoro Region, showing the main lithologies around Baltoro Glacier are gneiss, granite and schist, with some exposure of metasediments in some areas (Searle et al., 2010).

Chapter 5: Paper I

Title: Variations in debris surface temperature through the summer monsoon across Khumbu Glacier, Nepal Himalaya.

Journal: Earth Surface Processes and Landforms

Current status: Accepted

5. Variations in debris surface temperature through the summer monsoon across Khumbu Glacier, Nepal Himalaya.

5.1. Abstract

Debris surface temperature is an important control on ice ablation beneath a debris layer and provides a good indicator of energy fluxes at a supraglacial debris surface. However, spatial and temporal variability in debris surface temperature, and the debris properties that control it, are currently poorly constrained. Here, near-surface debris temperature is reported for 16 sites across the lower elevations of Khumbu Glacier, Nepal Himalaya, for the 2014 monsoon season. The debris layer at all sites was ≥1 m thick, minimising the influence of the underlying ice on measured temperature. Analysis of these data confirm the occurrence of temporal and spatial variability in debris surface temperature over a 67-day period.. Debris surface temperature was found to exhibit marked temporal fluctuations on diurnal, short-term (3–8 days) and seasonal timescales. Over the study period, two distinct diurnal patterns in debris surface temperature were identified that varied in timing, daily amplitude and maximum temperature. Days exhibiting lower diurnal amplitude (mean=23°C) and reduced maximum debris surface temperature (mean=20°C) occurred in the latter half of the study period, and was concurrent with increased seasonal variability in meteorological variables and attributed to increasing cloud cover as the monsoon progressed. Subtle spatial variability in debris surface temperature was also identified, manifested in variability in diurnal amplitude (7 to 40°C) and maximum debris surface temperature (7 to 50°C) between sites. Localised slope, debris grain size and lithology were identified as drivers of spatial variability. The complexity of surface energy fluxes and their influence on debris surface temperature highlight that a simplified assumed relationship between air temperature and debris surface temperature used in temperature index melt models, and a direct relationship between debris surface temperature and debris thickness used for calculating supraglacial debris thickness, omits much of the variability identified here, and should be undertaken with caution.

5.2. Introduction

Debris-covered glaciers exhibit a continuous mantle of rock debris over the full width of at least some of their ablation zones (Kirkbride et al., 2011). These glaciers are common in mountainous regions across the world, including in the European Alps (e.g. Mihalcea et al., 2006), Andes (e.g. Glasser et al., 2016), Southern Alps of New Zealand (e.g. Kirkbride, 2000) and the Himalaya (e.g. Scherler et al., 2011). The presence of a supraglacial debris layer influences glacier ablation, acting as a thermal buffer between the atmosphere and glacier ice surface, and modifying the energy available for melt (Jansson and Fredin, 2002; Kirkbride, 2000). The extent to which a supraglacial debris layer controls ablation is primarily dependent on the thickness of the debris layer (Clark et al., 1994; Mattson, 2000; Østrem, 1959). While a thin layer of debris below a critical thickness causes an increase in ablation due to a reduction of the surface albedo (Nakawo and Rana, 1999), ablation decreases exponentially with increasing debris thickness above a critical thickness, as the debris layer inhibits glacier melting by attenuating and reducing thermal energy transfer to the underlying ice surface (Brock et al., 2010; Mihalcea et al., 2008a; Nicholson and Benn, 2006; Reid et al., 2012).

Supraglacial debris surface temperature is a function of the energy balance at the debris surface and modulates heat transfer through the debris layer (Nakawo and Young, 1981). Therefore, debris surface temperature can provide a useful insight into the extent to which debris properties affect energy transfer at the surface of and through a debris layer. To date, little focus has been given to the influence of spatial and temporal variability in debris surface temperature across supraglacial debris layers, which can be affected by incoming energy fluxes and debris properties including albedo, surface roughness, sediment porosity, and moisture content (Reznichenko et al., 2010; Evatt et al., 2015; Rounce et al., 2015).

Previous studies concerned with the measurement of debris surface temperature on glaciers have had limited spatial or temporal extent. For example, Nakawo and Young (1982) measured debris surface temperature at six plots over a 48-hour period. Nicholson and Benn (2006) measured debris surface temperature at a maximum of 11 plots on one glacier, but only for a maximum period of 11 days, whilst Nicholson and Benn (2012) collected data at six plots over 10 days. Steiner and Pellicciotti (2015)

presented one of the most extensive debris surface temperature datasets from 13 locations over three ablation seasons on Lirung Glacier, Nepal, but the study focused on describing the relationship between air temperature (T_a) and debris surface temperature rather than exploring spatial variability in debris surface temperature. Moreover, Steiner and Pellicciotti (2015) did not state the thickness of the debris layer underlying each of the sensors measuring debris surface temperature, an important factor in the consideration of spatiotemporal variability in debris surface temperature and the influence of underlying ice (Nicholson and Benn, 2006). Consequently, the nature of and controls on debris surface temperature variability remains poorly constrained in glacial environments.

Conversely, ground surface temperature variability has been relatively well studied in other cold regions environments (e.g. Gubler et al., 2011; Guglielmin, 2006; Romanovsky and Osterkamp, 2000) where significant spatial variation arises from localised changes in surface properties and environmental conditions. These studies have concluded that such variability influences the accuracy of surface energy balance modelling in these environments. We therefore suggest that such variability may also be applicable to numerical modelling of debris-covered ice ablation and its response to future climate scenarios.

The importance of studies focused on debris surface temperature on debris-covered glaciers is manifested in the recent application of temperature-index models to debris-covered glaciers, which determine debris surface temperature from T_a (e.g. Carenzo et al., 2016). Furthermore, debris surface temperature has previously been used to determine debris layer thickness through two approaches: the use of an empirical relationship between debris surface temperature and debris layer thickness, based on field data (e.g. Michalcea et al., 2008a; 2008b; Minora et al., 2015); and a surface energy balance approach also using debris surface temperature (e.g. Foster et al., 2012; Rounce and McKinney, 2014). Currently, neither approach has been considered entirely robust, as the empirical approach is only applicable for debris layers thinner than 0.5 m (Mihalcea et al., 2008a) and the energy balance approach is a highly simplified numerical representation of the supraglacial debris layer. To understand the validity of these methods, and discern how to develop them further, confirmation of both the spatiotemporal regime of debris

surface temperature and its controls is needed. Achieving this aim will facilitate refinement of these two methods and, ultimately, increase the accuracy of numerical models used to forecast glacier mass balance and runoff.

Considering these shortcomings, here we aimed to characterise the spatial and temporal variability in debris surface temperature on a debris-covered glacier, using data collected from temperature sensors located in the debris near-surface and distributed over the lower ablation area of Khumbu Glacier, Nepal, in areas of thick (≥1 m) debris cover. On debris layers ≥1 m thick debris surface temperature is independent of debris layer thickness and, consequently, the influence of meteorological variables and debris characteristics can be investigated independent of debris layer thickness. The primary objectives of the study were to (i) examine the extent and nature of temporal and spatial variation of debris surface temperature during an ablation season, and (ii) determine controlling factors underlying variations in debris surface temperature.

5.3. Study site

5.3.1. Khumbu Glacier, Central Himalaya

Khumbu Glacier (27°56'N, 86°56'E) is ~17 km long and has an area of ~27 km^2 including the detached tributary glaciers, Changri Nup and Changri Shar (Figure 5.1: Arendt et al., 2012; Bolch et al., 2008; Vincent et al., 2016). The glacier flows from the southwest flanks of Mount Everest at 8230 m above sea level (a.s.l.) descending to 4816 m a.s.l. The equilibrium line altitude (ELA) is situated at around 5700 m a.s.l. within the Khumbu Icefall (Benn and Lehmkuhl, 2000; Inoue, 1977). Khumbu Glacier is typical of many large Himalayan debris-covered glaciers, with a low-gradient (< 2°), slow-flowing (< 10 m a^{-1}) ablation area (Hambrey et al., 2008; Quincey et al., 2009). The glacier flows at ~70 m a^{-1} near the base of the icefall, whilst the lowermost 3–4 km is thought to be stagnant (Quincey et al., 2009). Surface lowering across the glacier's ablation area between 2000 and 2015 was ~0.81 ± 0.16 m a^{-1} (King et al., 2017).

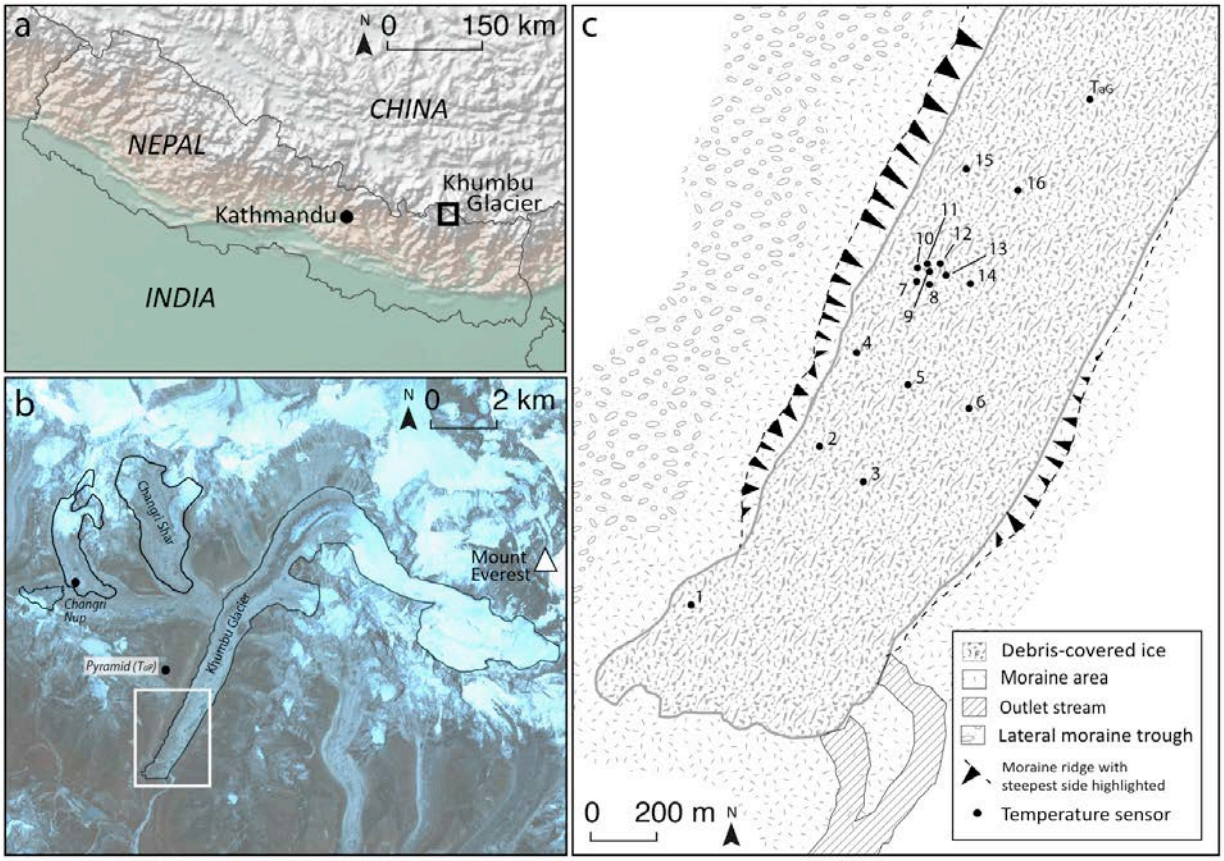

Figure 5.1. Study site location: (a) in a regional context; (b) in relation to Mt Everest, displaying the extent of Khumbu Glacier and location of the meteorological stations (Changri Nup and Pyramid) used in this study, including the extent of Changri Nup and Changri Shar (reproduced from Vincent et al., 2016); (c) the study area and locations of temperature sensors, with corresponding temperature sensor ID, and on-glacier air temperature location (T_{aG}), where increasing sensor ID corresponds to a location further away from the glacier terminus.

The ablation area of Khumbu Glacier is almost entirely debris covered below 5400 m a.s.l., with the debris layer > 2 m thick in places (Gades et al., 2000). The debris-covered ablation area displays a wide range of grain sizes comprising of granitic and schistose lithologies derived from the surrounding hillslopes (Iwata et al., 1980; Nuimura et al., 2011). The debris-covered area is topographically complex and dynamic, being characterized by an undulant surface, punctuated by numerous supraglacial ponds and associated ice cliffs, which changes over seasonal and interannual timescales (Watson et

al. 2016; Nuimura et al., 2011). The more stable, lowermost region of the ablation area shows the early stages of soil formation and is partially vegetated (Kadota et al., 2000).

5.3.2. Central Himalayan climate

The South Asian Summer Monsoon (herein, 'the monsoon') dominates the climate of the Khumbu Glacier catchment, and the Central Himalaya: annually, the highest air temperatures occur between May and October (Ageta, 1976; Nayava, 1974) and ~80 % of precipitation falls between June and September (Bookhagen and Burbank, 2010). During the onset and progression of the monsoon, high pressure over the Tibetan Plateau results in an increased temperature and pressure gradient southward towards the Indian subcontinent (Yasunari, 1976). This pressure gradient produces seasonally variable wind patterns in the Central Himalaya region and, through the monsoon, localised synoptic weather systems are dominated by mountain and valley winds, which vary on sub-diurnal timescales (Bollasina et al., 2002). As the monsoon season progresses, increases in regional precipitation frequency, air temperature, relative humidity and incoming longwave radiation occur, and are coupled with a decrease in shortwave radiation attributed to increasing cloud cover (Salerno et al., 2015; Shea et al., 2015).

5.4. Data acquisition

5.4.1. Near-surface debris temperature

5.4.1.1. Temperature sensors

Near-surface debris temperature (T_s) was measured as a robust proxy for true debris surface temperature using Thermochron iButton™ temperature sensors (model number DS1921G: http://datasheets.maximintegrated.com/en/ds/DS1921G.pdf), which record instantaneous temperature from –30 to +70°C with a manufacturer-stated accuracy of ±1.0°C. iButton thermochrons were chosen due to their low cost, reliability (Hubbart et al., 2005) and previous successful application in a number of environmental settings including permafrost landscapes (e.g. Gubler et al., 2011). Gemini Tiny Tag™ Plus2 data loggers (model number TGP-4520) with encapsulated thermistor probes were used for sensor calibration prior to fieldwork and have a manufacturer–stated accuracy of ±0.4°C. The iButtons were placed in waterproof polycarbonate plastic containers to protect from water damage, following the method of Gubler et al. (2011). The effect of polycarbonate

plastic waterproof casing on temperatures recorded was tested in laboratory conditions prior to fieldwork: temperatures recorded by contained and uncontained iButtons in the same environments varied by less than 2°C, and more typically by ≤0.5°C, which is below the manufacturer's uncertainty estimate (see Appendix; Figure A1).

5.4.1.2. Field experiment design

Near-surface debris temperature (T_s) was measured at hourly intervals at 16 sites between the 21st May and 29th July 2014 (Day of Year (DOY) 141 and 210). The first 48 hours of each T_s timeseries were discarded to allow the sensors to equilibrate with local conditions. For all sites, iButtons were placed in the immediate near-surface of the debris layer, typically between 0.01 and 0.05 m, using a single layer of grains of representative size for each site from the immediate surrounding area as a shield from direct solar radiation, as is common practice in ground surface temperature studies (e.g. Apaloo et al., 2012; Gisnås et al., 2014). Using a handheld GPS, the iButton sensors were distributed across the lowermost 2 km^2 of Khumbu Glacier's ablation area following a gridded pattern (Figure 5.1c). The elevation of sensor sites varied across the study area by ~50 m, and each site had a unique combination of site characteristics, varying in slope, aspect, elevation, shading from direct solar radiation by surrounding topography, curvature, roughness, grain size and sorting, and grain lithology (Table 5.1; see also Section 5.3.2).

To allow examination of the influence of additional debris layer properties and incoming energy fluxes on T_s other than debris layer thickness, all iButton temperature sensors were installed in locations where the debris layer had a thickness of ≥1 m and the effect of cold propagation from underlying ice on T_s was insignificant (Nicholson and Benn, 2006; Foster et al., 2012). Debris thickness was established by excavating the debris layer adjacent to the iButton location to a depth of 1 m; if no ice was present, debris thickness was reported as >1 m. At each site, a textural description of the debris was made, and digital photographs were taken before and after the emplacement of the temperature sensors (Figure 5.2). A subset of the iButton temperature sensors (Sites 7 to 13) were placed within a 90 × 90 m area to investigate the variability of T_s for sites in close proximity to one another, covering an area typical of the resolution of remotely sensed thermal data (e.g. ASTER).

Sensor ID	Elevation (m a.s.l.)	Debris description	Mean clast size (m)	Lithology (% Granite)	Slope (°)	Aspect (°)	Curvature	Roughness ($\times 10^{-2}$; m)	Mean T_s uncertainty (°C)
1	4949	Large cobbles with medium sand matrix	0.058	100	10	202	-0.65	0.05	0.87
2	4952	Large cobbles with medium sand matrix	0.099	100	9	100	1.38	0.09	1.49
3	4945	Small to large cobbles with medium to coarse sand matrix	0.028	50	5	132	-0.82	0.19	0.42
4	4948	Small to large cobbles with coarse sand matrix	0.020	40	2	321	-1.46	0.09	0.3
5	4947	Large cobbles with medium to coarse sand matrix	0.029	50	5	285	-1.22	0.14	0.44
6	4952	Medium grained sand with < 5 % medium granite pebbles	0.002	100	3	173	-1.21	0.04	0.03
7	4949	Medium pebbles to large cobbles with medium sand matrix	0.020	50	5	224	-0.80	0.20	0.30
8	4903	Very coarse pebbles with medium sand matrix	0.010	95	12	290	0.17	0.04	0.15
9	4938	Small cobbles to large boulders with medium to coarse sand matrix	2.930	100	6	86	0.05	0.10	4.39
10	4938	Coarse pebbles to large boulders with consolidated medium sand matrix	0.027	50	6	266	0.88	0.04	0.41
11	4946	Small to large cobbles with consolidated medium to coarse sand matrix	0.055	70	5	103	0.57	0.11	0.83
12	4942	Small to large cobbles with medium to coarse sand matrix	0.016	60	6	125	0.49	0.03	0.24
13	4935	Small cobbles to large boulders with coarse sandy matrix	2.890	90	6	170	0.33	0.06	4.34
14	4937	Small cobbles to small boulders with coarse matrix	0.027	60	5	131	-1.15	0.30	0.41
15	4950	Very coarse pebbles to large cobbles with consolidated medium matrix	0.042	50	7	206	0.03	0.20	0.32
16	4949	Small cobbles to large boulders with medium to coarse sand matrix	0.030	50	8	274	0.11	0.15	0.30

Table 5.1: Topographic and debris characteristics for iButton temperature sensor sites. Mean T_s uncertainty calculated for the near-surface placement of temperature sensors under representative grains at each location. Rows highlighted in grey are timeseries identified as less representative.

Figure 5.2: Site photos before installation of temperature sensors: (a) Site 11: Consolidated medium sand with medium pebbles; (b) Site 3: Small cobbles to large boulders with a medium to coarse sand matrix; and (c) Site 15: Small granite and schist cobbles to small boulders with course sand to medium pebble matrix.

On retrieval of the iButton temperature sensors at the end of the monsoon, comparison with the initial site photographs was used to evaluate any surface change at each site. For all sites reported here, the debris showed little or no disruption after sensor installation, and none of the temperature sensors were exposed at the time of collection. A further 42 iButton sensors were installed on the glacier surface but, due to topographic change during the 2014 monsoon, they could neither be located or retrieved.

Despite following standard methods for measuring ground surface temperature (e.g. Apaloo et al., 2012; Gisnås et al., 2014), placing debris on the contained iButtons to shield them from direct incoming shortwave radiation created an additional source of uncertainty in the 16 retrieved T_s data series, as T_s does not necessarily reflect absolute debris surface temperature (Conway and Rasmussen, 2000). Without detailed knowledge of the specific thermal properties of the debris at each site, more accurate assessment of the uncertainty between near-surface and true surface temperature timeseries is challenging. Here, we assumed our T_s data were sound proxies for absolute T_s. However, to identify any series which were likely to be less representative of true surface temperature, uncertainty at each site was estimated using the diurnally-averaged temperature gradient calculated through a debris layer by Nicholson and Benn (2006), from data collected on near-by Ngozumpa Glacier, and mean grain size for each site. Using the estimated sensor depth for each site based on mean grain size, and a temperature gradient of -10.5 °C m^{-1}, the temperature difference between the depth at

which sensors were located and the debris surface was calculated (Table 5.1). Sites at which the calculated near-surface to surface temperature difference was greater than 0.5°C (the assessed uncertainty in our iButton sensor data) were considered to be less reliable in reflecting absolute surface temperature: T_s timeseries from Sites 1, 2, 9, 11 and 13 were termed 'less representative' for identification. These five timeseries were either noted or omitted from subsequent analyses to avoid potential influence of misrepresentative data.

5.4.1.3. Ancillary data

5.4.1.3.1. Grain size and lithology

Grain size at each site was estimated from 18.0 Mpix digital site photographs acquired using a Canon 550D camera and processed in ImageJ, v. 1.49 (Rasband, 2008), following the method outlined by Igathinathane et al. (2009). At all sites, images covered approximately 1 m^2 and a known scale in each photograph was used to define the metre:pixel ratio. Grains were then selected using a simple random sampling method: for each site photo, every grain identified was assigned a number, and a random number generator was used to subsample 25 grains for measurement within ImageJ. Assuming from the 2D imagery that the long and intermediate grain axes were visible, the intermediate axis length was retrieved and a mean, representative grain size for each site calculated. Where the intermediate axis of a grain was larger than the photo (e.g. Sites 9 and 13) the maximum length measurable from the scaled image was used. Representative grain sizes for each site are detailed in Table 5.1.

Grain lithology was determined in the field using grain shape, colour and mineral inclusions in the grains. Two major lithologies were identified: granite and schist. The dominant lithology at each site (Table 5.1) was then determined by manual classification of lithology of all grains in each of the site photographs based on colour and mineral inclusions in ImageJ and then calculating the percentage of granite for each site (e.g. Solano et al., 2016).

5.4.1.3.2. Local meteorological data

Off-glacier air temperature (T_{aP}) was recorded at hourly intervals 2 m above the ground surface, using an artificially ventilated LSI-Lastem DMA 570 sensor (accuracy ±0.2°C), at the Pyramid Observatory (Figure 5.1b; 27°57'32" N, 86°48'47" E; 5050 m a.s.l.), ~1 km to the northwest of the study area. On-glacier air temperature (T_{aG}) was recorded at 30-minute intervals in a location with schistose debris lithology (Figure 5.1c), using a Gemini Tiny Tag™ Plus2 data logger (model number TGP–4520) with a thermistor probe, with a stated accuracy of ±0.4°C. The on-glacier thermistor probe was placed in a naturally-aspirated radiation shield mounted on a tripod 1 m above the glacier debris surface at an elevation of 4950 m. T_{aG} was subsequently resampled to give hourly values corresponding to the T_s data series resolution.

Incoming shortwave (SW_{in}) and longwave (LW_{in}) radiation (Kipp&Zonen CNR4 sensor, 1.0 m above debris surface, ±3%) and relative humidity (RH: Vaisala HMP45C sensor, 2.15 m above debris surface, ±2%) data were recorded at an automatic weather station on a debris-covered area of the adjacent Changri Nup Glacier (Figure 5.1b; 27°58'55"N, 86°45'52"E; 5363 m a.s.l.). All meteorological data were collected at 30-minute intervals, and were resampled to 1-hour resolution using an hourly mean algorithm. Precipitation (P) was measured by an automatic weather station (Geonor T-200 all-weather rain gauge) 5 km down-valley from the terminus of Khumbu Glacier at Pheriche (27°53'24" N, 86°49’12" E; 4260 m a.s.l.) where summer precipitation predominantly occurs as rainfall; these data were corrected for undercatch of solid precipitation using air temperature and wind speed (Lejeune et al., 2007) and have an estimated accuracy of ±15%.

5.4.1.3.3. Local topography

Topographic analysis of a digital elevation model (DEM) of Khumbu Glacier and *in situ* observations provided topographic data with which we could further analyse potential controls of T_s. The DEM used was derived from a series of Surface Extraction from Triangulated Irregular Network Searchspace Minimization (SETSM) DEMs sourced from the Polar Geospatial Centre (University of Minnesota) at 8 m grid spacing (Noh and Howat, 2015). The DEMs were assessed for the presence of co-registration errors or biases following the three-step approach of Nuth and Kääb (2011), and surface-matched

to the 30 m Shuttle Radar Topography Mission (SRTM) DEM. The mean differences between stable (i.e. non-glacierised) horizontal and vertical terrain was -0.416 m, whilst the standard deviation was 10.12 m. Following correction, the SETSM DEMs for the area were mosaicked to create a single, region-wide dataset to include the mountain topography surrounding Khumbu Glacier. Due to the complex and dynamic nature of the glacier surface, topographic parameters at each iButton site were estimated *a-posteriori* from the high-resolution DEM and are presented here as a generalised local proxies rather than absolute, site-specific values (Table 5.1). Slope (in degrees) and terrain curvature were extracted using ESRI's ArcMap v.10.1 Spatial Analyst toolbox. Curvature and ranged between -1 and +1. Terrain roughness was derived using the 'vector ruggedness measurement toolbox', which calculates the sum change in elevation between the grid cell in which each sensor was located and the eight neighbouring grid cells (Sappington et al., 2007). The terrain roughness values are not a direct measurement of surface roughness or aerodynamic roughness length, but provide an insight into the extent topography varied in elevation at and around each of the study sites, and therefore enables comparison between sites as to the extent of this variation in topography, with greater values suggesting a more undulant surface. *In situ* observations of the local aspect of each iButton site, measured relative to north, were collected in the field using a magnetic compass with an uncertainty of ±2°.

5.5. Results

5.5.1. Debris surface temperature

Daily mean debris surface temperature (T_s) for all 16 sites typically exceeded air temperatures (T_{aP} and T_{aG}) throughout the monsoon period (Figure 5.3a). Mean T_s for the period of observations at the 16 sites ranged from 7.0 to 11.6°C. T_s remained close to 0°C between DOY 146 and 152, which was coincident with heavy snowfall in Khumbu valley and the ensuing persistence of a ~0.4 m snow layer on the glacier surface. Following DOY 152, the snow cover melted and the rate and timing of the return to a T_s of >5°C at each site was highly varied. Subsequently, from DOY 156 onwards, all T_s series exhibited a broadly similar quasi-parallel pattern of change until the end of the observation period. Debris temperature appeared to follow a generally rising trend from DOY 156–166, and then a seasonal decrease of approximately -0.1°C/day until DOY 210. However, these

seasonal rising and falling trends were superimposed with a 5 to 8 day cycle in T_s, potentially reflecting synoptic variations, and intermittent, short (1–3 day) periods with lowered T_s. At all 16 sites, T_s exhibited marked diurnal variation (Figure 5.3b): the highest daily amplitudes of 22–35°C occurred prior to DOY 170, and progressively declining amplitudes (reducing to a mean of 15°C) characterised the period following DOY 170. The diurnal amplitude in T_s also displayed variability in the 5–8 day synoptic periods, although the magnitude of variability differed between these cycles. Over the season, the contrasts in T_s between the sites were greatest at the start of our observations and between DOY 153 and 170, and declined thereafter, with the least difference between sites seen during the short periods of reduced T_s.

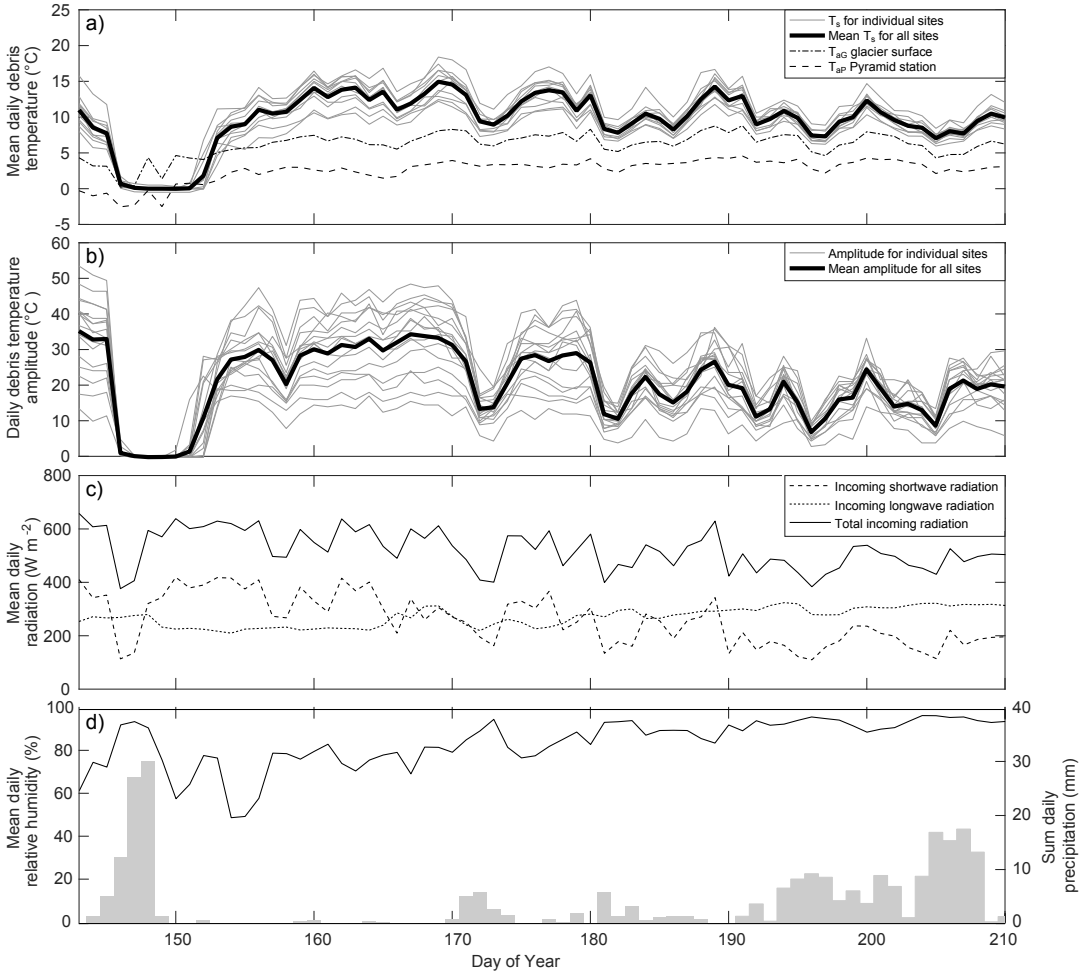

Figure 5.3: (a) Mean diurnal T_s for all temperature sensor sites, alongside on- and off-glacier air temperature series, (b) Daily amplitude in T_s at all sites, (c) Mean daily incoming shortwave, longwave and total radiation (SW_{in}, LW_{in} and NR_{in}, respectively), (d) Total daily precipitation (grey bars) and mean daily relative humidity (black line) across the study period.

5.5.2. Meteorology

Mean daily T_{aG} and T_{aP} followed a similar, but subdued, pattern to the T_s data series (Figure 5.3a). Air temperature increases of the order of 3°C occurred over the entire study period in both T_{aP} and T_{aG}. The seasonal pattern in T_{aG} and T_{aP} was overlain by a subtle synoptic periodicity, with a 5–8 day recurrence. The diurnal amplitudes seen in the T_a series were less than those observed for T_s: daily variation ranged from 2 to 10°C for

T_{aP}, and from 5 to 20°C for T_{aG}. In both T_a records, diurnal amplitude was greatest during the period of snow cover, and showed a general reduction over the course of the observation period albeit punctuated by short (1-3 day) variability. Off-glacier T_{aP} was consistently lower than on-glacier T_{aG} by 5°C between DOY 145 and 190, and by 3°C thereafter.

Mean daily SW_{in} displayed an overall seasonal decrease from 405 W m^2 to 217 W m^2 over the observation period (Figure 5.3c). Between DOY 148 and 149, SW_{in} was lowest at 123 W m^2, which corresponded to snowfall and a coincident decrease in T_s to 0°C. In contrast, mean daily LW_{in} increased from 253 W m^2 to 320 W m^2 from DOY 143 to 210. Total net incoming radiation (NR_{in}) was primarily influenced by the pattern of SW_{in}. All three series of radiative energy displayed synoptic (3–8 days) and short-term (1–3 day) variability. Relative humidity displayed a seasonally increasing trend from around 60% on DOY 143 to around 95% by the end of the observation period; this seasonal change was superimposed with shorter-term variability including a brief increase in relative humidity (to >80%) between DOY 146 and 150, aligned with the snowfall and snow cover event (Figure 5.3c). During the snowfall event, total daily precipitation peaked on DOY 150 at 34 mm, but subsequently remained low until DOY 170 and then, as the monsoon progressed further, the magnitude and frequency of precipitation events increased (Figure 5.3d). Increases in total daily precipitation were typically concurrent with decreased SW_{in} and increased LW_{in} and relative humidity.

5.5.3. Timeseries analysis

A Kolmogorov-Smirnov normality test, used to test whether data sets are normally distributed, showed that at 95% confidence level none of the temperature series (T_s or T_a) were normally distributed. Consequently, non-parametric analyses were required to interrogate these data further.

5.5.3.1. Comparison of timeseries

The overall average of mean T_s for all timeseries was 9.2 ±1.3°C, or 9.6 ±1.2°C if the series considered as less representative were excluded. Analytical tests indicated that the mean T_s series was highly correlated with both T_{aP} (Spearman's r = 0.85, p <0.05) and T_{aG} (r =

0.78, p <0.05) but significantly different from both the two T_a series, with one-tailed tests confirming mean T_s was predominantly higher at the 95% confidence level.

The broad similarity in the individual T_s series (Figure 5.3a,b; Figure 5.4) was highlighted by strong and significant ranked correlation coefficients for the majority of site pairs (Table 5.2). The generally high correlation (r ≥0.88) between timeseries indicated that all sites exhibited a broadly similar general pattern in both periodicity and seasonal trend. However, further comparison using a Kruskal-Wallis test (which tests whether samples originate from the same distribution) showed the T_s series data populations were significantly different (χ^2 = 308.9, or χ^2 = 201.1 excluding outlier series, both p << 0.05). To explore the underlying nature and causes for these differences, we (i) examine the temporal variability in the T_s series, (ii) conduct a more detailed assessment of the spatial differences between timeseries, and (iii) explore any associations between T_s and the local meteorological and site-specific datasets. Each of the three sets of analyses are detailed and developed sequentially in the sections that follow.

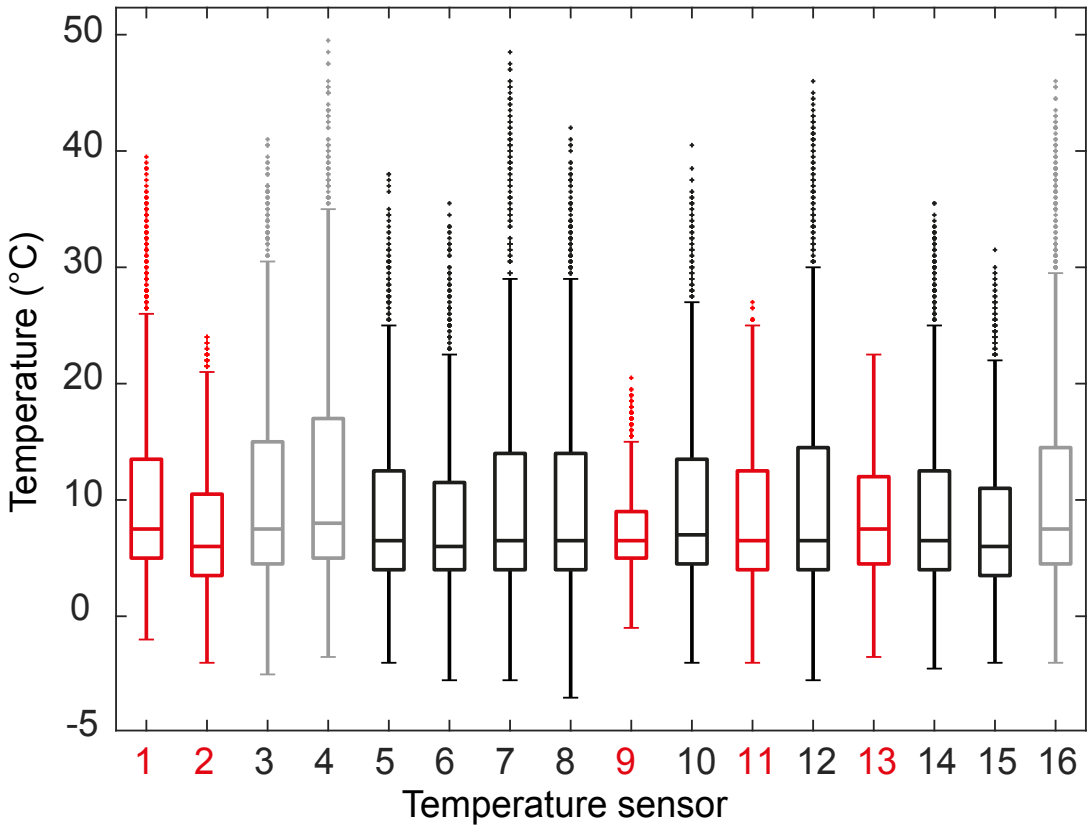

Figure 5.4: Box plots of mean, interquartile range, maximum and minimum near-surface debris temperature and outliers for each of the timeseries. Red box plots are the timeseries identified as less representative, greyed plots are timeseries identified as significantly different from the statistically representative Site 14.

Spearman's correlation coefficient (*r*)

Efficiency criterion (*E*)

Sensor ID	1	2	3	4	5	6	7	8	9	10	11	12	13	14	15	16	Mean T_s
1		0.96	0.96	0.98	0.97	0.97	0.97	0.92	0.94	0.96	0.95	0.97	0.96	0.97	0.94	0.98	0.98
2	0.30		0.96	0.95	0.97	0.94	0.95	0.88	0.97	0.95	0.97	0.96	0.96	0.98	0.98	0.97	0.97
3	0.93	0.69		0.97	0.94	0.97	0.98	0.95	0.92	0.98	0.99	0.98	0.92	0.99	0.96	0.97	0.99
4	0.91	0.52	0.92		0.95	0.97	0.97	0.95	0.91	0.97	0.96	0.98	0.94	0.97	0.93	0.97	0.99
5	0.93	0.80	0.84	0.63		0.95	0.96	0.88	0.95	0.94	0.93	0.96	0.94	0.96	0.96	0.98	0.96
6	0.80	0.81	0.75	0.39	0.87		0.99	0.95	0.9	0.98	0.96	0.99	0.9	0.97	0.94	0.97	0.99
7	0.91	0.63	0.94	0.91	0.86	0.82		0.95	0.91	0.98	0.96	0.99	0.92	0.98	0.95	0.98	0.99
8	0.82	0.57	0.84	0.75	0.77	0.80	0.79		0.84	0.96	0.93	0.95	0.86	0.93	0.89	0.91	0.96
9	-0.12	0.65	-0.17	-0.36	-0.42	-0.04	-0.28	-0.19		0.92	0.93	0.92	0.95	0.94	0.94	0.93	0.93
10	0.92	0.72	0.94	0.81	0.90	0.89	0.87	0.87	0.53		0.97	0.99	0.92	0.98	0.95	0.97	0.99
11	0.66	0.90	0.68	0.16	0.77	0.84	0.35	0.45	0.70	0.75		0.97	0.93	0.98	0.97	0.96	0.98
12	0.90	0.66	0.94	0.91	0.86	0.80	0.96	0.81	0.44	0.93	0.77		0.93	0.99	0.96	0.98	1.00
13	0.37	0.86	0.20	-0.48	0.58	0.60	-0.33	-0.11	0.75	0.35	0.81	-0.20		0.94	0.92	0.94	0.94
14	0.87	0.84	0.90	0.66	0.91	0.88	0.80	0.66	0.60	0.90	0.91	0.85	0.80		0.98	0.98	0.99
15	0.65	0.92	0.65	0.13	0.83	0.84	0.40	0.32	0.71	0.70	0.92	0.47	0.80	0.89		0.97	0.96
16	0.90	0.65	0.94	0.89	0.86	0.78	0.92	0.70	0.41	0.88	0.75	0.94	0.64	0.91	0.78		0.99
SE	10.75	10.52	10.99	7.75	10.99	10.83	9.55	8.85	3.21	11.96	10.42	11.04	5.64	12.38	10.01	11.95	
Mean *E*	0.72	0.7	0.73	0.52	0.73	0.72	0.64	0.59	0.21	0.8	0.69	0.74	0.38	0.83	0.67	0.8	

Table 5.2: A matrix of Spearman rank correlation coefficient (r) and Nash-Sutcliffe efficiency coefficient (E) for each pair of raw (hourly) T_s timeseries. All correlations displayed $p < 0.05$. The greyed rows (Sites 1, 2, 9, 11 and 13) are those identified as being less representative of true debris surface temperature due to site grain size. Correlation between each raw T_s series and the average T_s excluding outlying sensors is shown, and the sum and average E for each sensor and all other sensors is show.

5.5.3.2. Temporal variability in debris surface temperature

The similarity in the daily T_s means and their seasonal pattern, with the exception of the period of snowfall (DOY 146-152), was underlain by a marked reduction in the daily amplitude in T_s at all sites over the study period (Figure 5.3b). To test this observation further, regression analysis was employed, with omission of data from the snowfall period. Sites 1, 4, 7, 10, 12 and 16 showed a significant ($p < 0.05$) decrease in daily mean T_s over the observation period, while all other sites showed no such temporal trend (Table 5.3). However, all sites showed a statistically significant increase in daily minimum T_s during the monsoon, averaging ~0.08 °C/day; and with the exception of Site 13, all sites also showed a significant decrease in daily maximum temperature, typically of around -0.19 °C/day. The concomitant increase in minimum and decrease in maximum T_s between timeseries was reinforced by a significant decreasing trend in daily amplitude of approximately -0.26°C/day over the monsoon period at all 16 sites (Table 5.3). These changes were in contrast to air temperature trends, where mean daily minimum and average T_a increased by approximately 0.1°C/day and 0.04°C/day, respectively. Additionally, there was no significant trend in mean daily maximum T_a, although decreases in daily amplitudes in T_a were significant and of the order of -0.05 to -0.1°C.

Table 5.3: Results of regression analyses to identify seasonal trends in minimum, mean, maximum T_s and the associated daily amplitude. Seasonal trend slope (b, in °C/day) is given with the associated *p*-value, and statistically significant slopes are indicated in *italic*. The greyed rows are those identified as less representative..

	Daily minimum T_s		**Daily mean T_s**		**Daily maximum T_s**		**Daily amplitude T_s**	
Sensor ID	b	*p*	b	*p*	b	*p*	b	*p*
1	*0.06*	<< 0.05	*-0.03*	< 0.03	*-0.22*	<< 0.05	*-0.28*	<< 0.05
2	*0.07*	<< 0.05	-0.01	0.53	*-0.11*	<< 0.05	*-0.18*	<< 0.05
3	*0.08*	<< 0.05	-0.03	0.06	*-0.22*	<< 0.05	*-0.30*	<< 0.05
4	*0.08*	<< 0.05	*-0.05*	< 0.05	*-0.28*	<< 0.05	*-0.36*	<< 0.05
5	*0.07*	<< 0.05	-0.02	0.07	*-0.20*	<< 0.05	*-0.27*	<< 0.05
6	*0.08*	<< 0.05	-0.01	0.60	*-0.19*	<< 0.05	*-0.27*	<< 0.05
7	*0.10*	<< 0.05	*-0.06*	<< 0.05	*-0.37*	<< 0.05	*-0.47*	<< 0.05
8	*0.10*	<< 0.05	-0.01	0.55	*-0.17*	<< 0.05	*-0.27*	<< 0.05
9	*0.03*	<< 0.05	0.00	0.62	*-0.09*	<< 0.05	*-0.12*	<< 0.05
10	*0.06*	<< 0.05	*-0.04*	< 0.05	*-0.18*	<< 0.05	*-0.24*	<< 0.05
11	*0.08*	<< 0.05	0.00	0.80	*-0.10*	< 0.05	*-0.18*	<< 0.05
12	*0.10*	<< 0.05	*-0.04*	< 0.05	*-0.26*	<< 0.05	*-0.36*	<< 0.05
13	*0.05*	<< 0.05	-0.01	0.61	-0.03	0.11	*-0.09*	<< 0.05
14	*0.08*	<< 0.05	-0.03	0.06	*-0.18*	<< 0.05	*-0.27*	<< 0.05
15	*0.08*	<< 0.05	0.00	0.92	*-0.11*	< 0.05	*-0.19*	<< 0.05
16	*0.08*	<< 0.05	*-0.05*	< 0.05	*-0.28*	<< 0.05	*-0.36*	<< 0.05
Average	**0.08**	-	**-0.02**	-	**-0.19**	-	**-0.26**	-

To further examine these seasonal trends in T_s amplitude, and to ascertain if there was systematic change in the diurnal pattern of T_s fluctuation, we adopted the approach commonly used to analyse synoptic climatology (e.g. Brazel et al., 1992; Davis and Kalkstein, 1990), hydrological timeseries (e.g. Hannah et al., 2000; Swift et al., 2005, Irvine-Fynn et al., 2005) and ground surface temperature analyses (e.g. Lundquist and Cayan, 2007). These previous published analyses used Principal Components Analysis (PCA) to classify patterns of change or modes of variation in diurnally fluctuating timeseries. Here, rather than analyse all 16 T_s series, and given the high correlation between all sites excluding those that were less representative (Table 5.2), a 'representative' timeseries from the data set was used. The most representative T_s timeseries was identified using a Nash-Sutcliffe efficiency coefficient (*E*), typically used to determine the fit of modelled to observed data (e.g. Krause et al., 2005; Legates and

McCabe, 1999). E was calculated for each T_s data series pair and then summed and averaged for each individual site (Table 5.2). The timeseries with the highest similarity to all other T_s series was from Site 14 (E = 12.4, mean E = 0.83), and was therefore considered representative.

Debris temperature data from Site 14 were divided into individual diurnal periods of 24 measurements commencing at midnight (00:00). Diurnal periods in which T_s was consistently 0°C (DOY 146 to 152) due to lying snow cover were omitted from the analysis. The resultant 61 diurnal data series were reduced and simplified into a number of 'modes' of variation, or principal components (PCs), using PCA without rotation. The first two PCs provided the primary modes of diurnal variation in T_s (Figure 5.5a): PC1 accounted for 81.3% of the variance and PC2 for 8.8%. The remaining PCs were discounted as 'noise' because they represented less than 10% of the total variance in the data set (e.g. Hannah, 2000; Irvine-Fynn et al., 2005). Although absolute loadings were relatively weak (< 0.5) for both PCs, a total of 30 days were described best by PC1, 19 days associated with PC2. A total of 11 days were very weakly related to either PC1 or PC2 (absolute loadings of < 0.09), and were considered to have an undefined diurnal T_s cycle (Figure 5.5b,c). Of note were the 11 days described by negative loadings on PC2, which contrasted to the consistently positive loadings for PC1, and were suggestive of lagged relationships between the mode of variation and true diurnal T_s pattern. Days associated with PC1 predominantly occurred during the former half of the observation period (76% before DOY 176), whilst 78% of days associated with PC2 and 90% of days with an undefined cycle both occurred following DOY 176 (Figure 5.5c).

The contrast between the days assigned to the two main principal components and the undefined diurnal cycles were illustrated through a comparison of descriptive statistics (Table 5.4). The mean diurnal T_s was greatest for those days defined by PC1 at 10.9°C, whilst the mean maximum temperature and diurnal range was highest compared to days with an undefined T_s variation and those associated with PC2. Days that were best described by PC2 exhibited relatively low mean daily amplitude, and mean and maximum diurnal temperatures. The 11 days that were less well defined by PCs had lowest mean, maximum and range in T_s. Days described by PC1 were characterised by a lower mean minimum T_s (0.9°C) while all other days experienced similar minimum values of T_s. The

mean time at which T_s peaked for each group of days associated with the PCs varied by less than one hour (Table 5.4), but a lagged diurnal cycle in T_s for days described by PC2 was found in the later timing of maximum debris temperature at 13:24.

Table 5.4: Descriptive statistics for groups of days corresponding to each of the key principal components (PCs) and undefined diurnal cycles, identified through PCA. Standard deviations are given in brackets.

Descriptor	PC 1	PC 2	Undefined
Number of days represented by PC	30	19	11
Mean daily T_s (°C)	10.9 (1.9)	9.5 (1.8)	7.9 (1.5)
Mean maximum T_s (°C)	29.8 (3.6)	23.3 (6.0)	16.8 (4.4)
Mean minimum T_s (°C)	0.9 (2.5)	3.3 (1.4)	3.4 (1.4)
Mean T_s amplitude (°C)	28.9 (4.1)	20.1 (6.7)	13.5 (4.1)
Mean time of peak T_s (hrs)	13:06 (±1:12)	13:24 (±1:06)	13:12 (±1:42)

In summary, analysis for temporal variation in timeseries highlighted subtle variation in diurnal patterns. There was a clear progressive shift during the monsoon towards T_s exhibiting a lower daily mean, maximum and range, but with a seasonal increase in the minimum T_s. The combination of *E* and PCA analyses detailed this further, showing that at all sites a gradual daily rise and fall in minimum and maximum T_s for the former part of the monsoon occurred, while there was a systematic shift to more variable and delayed diurnal cycles in the latter half of the observation period. These shifts in magnitude of T_s were aligned with the observed seasonal changes in meteorological conditions, specifically with increased precipitation, relative humidity and LW_{in} from around DOY 180.

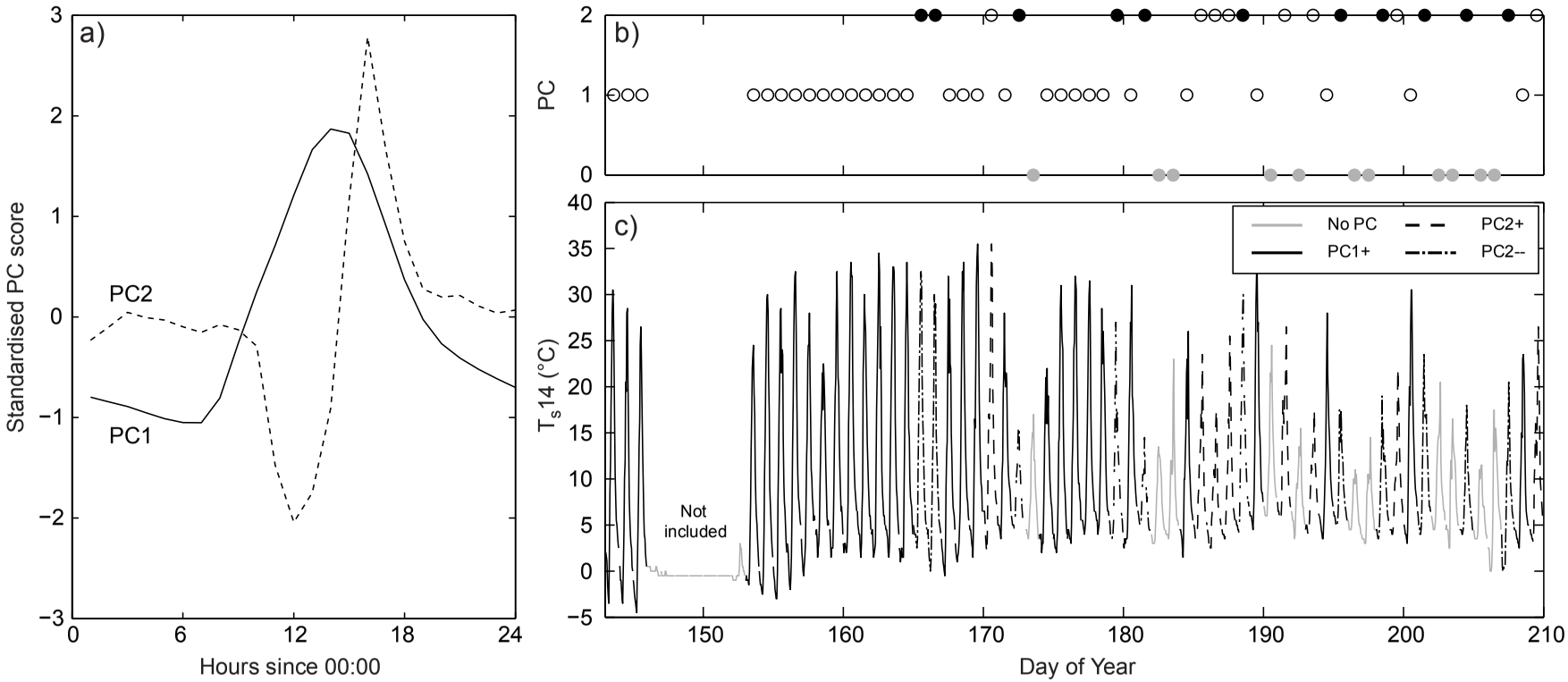

Figure 5.5: a) The two modes of variability in T_s for Site 14, described by PC1 and PC2, b) plot to identify days described by PCs 1 or 2, filled circles identify days with a negative or lagged relationship to PC2 and greyed circles mark days not described by either dominant PC, c) T_s timeseries for Site 14 highlighting each day's mode of variation.

5.5.3.3. Spatial variability in debris surface temperature

With evidence of spatial variability between sensor sites most clearly evidenced by the differences in diurnal amplitude of T_s, further exploration of the spatial contrasts was undertaken. Following the identification of significant difference by a Kruskal-Wallace test, a signed rank pairwise Wilcoxon test provided further detail on spatial variations by comparing pairs of timeseries data populations. The representative series from Site 14 was the most similar to all other series, being statistically dissimilar to only Sites 1, 3, 4 and 16 (Figure 5.3). Removal of the series considered as less representative made relatively minimal difference to the analysis, suggesting that even the outlying series (Sites 2, 9, 11, 13) were broadly similar to the remaining T_s data sets despite the uncertainty arising from the debris grain size affecting whether T_s was representative of true surface temperature. A further set of Wilcoxon tests were undertaken on the positively skewed distribution of series of maximum, minimum and mean diurnal amplitude of T_s. The results of the site comparison data showed 86% and 89% of site pairs had significantly different diurnal amplitudes and maximum T_s from one another ($p < 0.05$), respectively, whilst 39% of the site pairs displayed significantly different minimum T_s ($p < 0.05$).

Mean minimum daily T_s for all timeseries varied between sites of the order of 3°C, between -1°C and -4°C, whilst mean maximum daily temperature varied of the order of 6°C, between 10°C and 17°C. Whilst non-parametric correlation coefficients (r) suggested minimal variability between sites, with 86% of correlations displaying a coefficient ≥0.90 (Table 5.2), such correlations only reveal similarity in data series pattern, rather than magnitude (Borradaile, 2013). Consequently, notwithstanding the sensitivity of the efficiency criterion (Krause et al., 2005), E was used to compare the strength of each relationship with regards to similarity in both value and pattern for the T_s series (Table 5.2). The E values displayed high variability and ranged from -0.42 (Sites 5 and 9) to 0.96 (Sites 7 and 12). The outlier timeseries displayed predominantly lower E values, particularly in their relationships with each other. Spatial variability between the sites appeared relatively small: 84% of E values were ≥0.75, suggesting a good similarity in pattern and magnitude between pairs of T_s data series. For times series sites located in close proximity to one another (Sites 8–14, omitting less representative timeseries) all the site pairs displayed r ≥0.87 and 80% of these site pairs displayed an E value ≥0.81.

However, the contrast in *E* between the timeseries suggests subtle spatial variability in T_s did exist between study sites.

Although *r* and E provide an insight into the relationship between timeseries, the persistent diurnal cycle within each timeseries causes raw timeseries to be highly correlated, as evidenced in the *r* and *E* values for timeseries pairs (Table 5.2; Horvatic et al., 2011). Therefore, when attempting to identify longer term and seasonal associations between timeseries such diurnal cycles are considered to be noise (Horvatic et al., 2011). To overcome this issue and to compare longer-term trends in timeseries, all T_s timeseries were detrended to exclude the diurnal cyclicity from the timeseries, following the method of Kristoufek (2014). These detrended timeseries were subsequently correlated (Table 5.5). Correlations between detrended timeseries were all ≥0.87, showing that when the diurnal cycles were removed, these data were still highly correlated and all T_s records exhibited similar short-term and seasonal variations, despite varying sensor locations.

Cross-correlation between the detrended timeseries was used to identify any lag between T_s timeseries (Table 5.5). Lag times were present between detrended timeseries from Sites 1 and 2, and with both Sites 8 and 15 for a number of sites. All sites lagged the timeseries at Site 8 by 1 or 2 hours, whilst Site 15 displayed a 1-hour lag with seven sites. Site 8 and 15 were located under 0.010 m and 0.042 m of debris, respectively, neither of which represent the extremes of the depths at which sensors were placed, and neither sites had been identified as less representative or statistically dissimilar. With regards to the site characteristics, Site 8 was placed in the most northerly facing aspect and lowest elevation of all iButton sensor locations, whist Site 15 had one of the highest elevations and roughness metrics (Table 5.2). Despite a broad statistical similarity in the T_s data series, there were a number of contrasts in the magnitude, distribution and timing of T_s values between timeseries. The analysis of the T_s data sets suggested subtle spatial variability in T_s was primarily manifested in variability in diurnal T_s amplitude, which was principally controlled by variability in maximum T_s between sites.

Lag time (hours)	Correlation coefficient (*r*)															
	Ts1	**Ts2**	**Ts3**	**Ts4**	**Ts5**	**Ts6**	**Ts7**	**Ts8**	**Ts9**	**Ts10**	**Ts11**	**Ts12**	**Ts13**	**Ts14**	**Ts15**	**Ts16**
Ts1		0.95	0.98	0.99	0.99	0.98	0.98	0.94	0.95	0.98	0.96	0.98	0.93	-0.97	0.95	0.97
Ts2	-1		0.96	0.94	0.96	0.93	0.93	0.84	0.98	0.94	0.98	0.96	0.97	0.98	0.99	0.97
Ts3	0	0		0.99	0.98	0.99	0.98	0.94	0.94	0.99	0.98	0.99	0.92	0.98	0.97	0.98
Ts4	0	1	0		0.98	0.99	0.98	0.95	0.94	0.99	0.96	0.98	0.92	0.97	0.94	0.97
Ts5	0	0	0	0		0.98	0.98	0.92	0.97	0.98	0.97	0.98	0.94	0.98	0.97	0.98
Ts6	0	1	0	0	0		0.99	0.96	0.92	0.99	0.95	0.98	0.89	0.96	0.94	0.97
Ts7	0	1	0	0	0	0		0.95	0.92	0.99	0.96	0.99	0.87	0.97	0.95	0.98
Ts8	1	2	1	1	1	1	1		0.85	0.96	0.90	0.94	0.82	0.89	0.86	0.90
Ts9	0	0	0	-1	0	0	0	-1		0.93	0.96	0.94	0.97	0.96	0.96	0.95
Ts10	0	1	0	0	0	0	0	-1	0		0.97	0.99	0.91	0.97	0.95	0.97
Ts11	0	0	0	0	0	0	0	-1	0	0		0.98	0.95	0.99	0.98	0.97
Ts12	0	0	0	0	0	0	0	-1	0	0	0		0.92	0.99	0.97	0.99
Ts13	0	0	0	0	0	0	0	-1	0	0	0	0		0.94	0.94	0.93
Ts14	0	0	0	0	0	0	0	-1	0	0	0	0	0		0.99	0.99
Ts15	-1	0	-1	-1	-1	-1	-1	-2	0	-1	0	0	0	0		0.98
Ts16	0	0	0	0	0	0	0	-1	0	0	0	0	0	0	0	

Table 5.5: Correlation coefficient and lag time for pairs of detrended T_s timeseries for which the persistent 24-hour diurnal cycles have been removed. The grey rows are those identified as being less representative of debris surface temperature due to site grain size.

5.5.3.4. Controls on temporal and spatial variability in near-surface debris temperature

To investigate whether meteorological conditions and site characteristics were associated with controlling T_s, and particularly maximum T_s, assessment of the influence of meteorological drivers and site-specific traits was undertaken using multivariate techniques.

Controls on temporal variability in T_s over the monsoon were investigated for all hourly timeseries, omitting the period of sustained 0°C in T_s in which the debris surface was snow covered. Analysis was undertaken using Stepwise Multilinear Regression (SMR), with meteorological timeseries as predictor variables to determine the control and combined control of meteorological variables on T_s. Assessment of the meteorological data demonstrated none of the timeseries were normally distributed, as was also true for all T_s and T_a data series. Consequently, to transform the T_s and meteorological variables to more approximately normal distributions, a simple natural logarithmic conversion was applied. The multivariate models described $*T_s$ (where * reflects a log-transform) as a function of *SWin, *LWin, $*T_{aG}$, *RH (relative humidity) and *P (precipitation). The output from the primary SMR is detailed in Table 5.6 highlighting the relative strength of the relationships between T_s and each of the meteorological variables between sites. $*T_{aG}$ was ranked as the most influential predictor of $*T_s$ for all sites, with a coefficients of determination between R^2 = 0.44 and R^2 = 0.67. The addition of $*SW_{in}$, $*LW_{in}$, *RH and *P resulted in only minimal incremental increases in the strength of the correlation between predictor variables and $*T_s$, in all cases resulting in an increase in R^2 of ≤ 0.1. In all cases, *RH was only the third of four most significant predictor variable, while *P was not significant in terms of contributing to improving prediction of $*T_s$. Typically, the sites with the weakest SMR model were those classed as less representative, although there were exceptions (e.g. Sites 16).

	SMR 1: raw transformed meteorological variables				SMR 2: minus $*T_{aG}$		SMR 3: combined radiation minus $*T_{aG}$			SMR 4: $*T_{aG}$ and alternates	
Site	**$*T_{aG}$**	**$*SW_{in}$**	**$*LW_{in}$**	***RH**	***SWin**	***SWin +*LWin, *RH, *P**	***NR**	***NR+dT$_a$**	**+All *RH, SSWin, SLWin, *P, tP**	**$*T_{aG}$+dTa**	**All *RH, *P, tP**
1	1 (0.59, 0.373)	2 (0.60, 0.368)	3 (0.60, 0.367)	4 (0.62, 0.358)	1 (0.33,0.476)	1+ (0.45, 0.432)	1 (0.37, 0.462)	1+2 (0.45, 0.432)	+3+ (0.49, 0.415)	1+2 (0.69, 0.326)	+3+ (0.69, 0.325)
2	1 (0.47, 0.313)	2 (0.50, 0.304)	3 (0.52, 0.298)	4 (0.55,0.287	1 (0.21, 0.383)	1+ (0.39, 0.335)	1 (0.26, 0.370)	1+2 (0.38, 0.339)	3+ (0.42, 0.328)	1+2 (0.62, 0.266)	+3+ (0.62, 0.265)
3	1 (0.55, 0.342)	2 (0.57, 0.335)	3 (0.57, 0.333)	4 (0.59, 0.325	1 (0.27, 0.433)	1+ (0.40, 0.394)	1 (0.32, 0.422)	1+2 (0.37, 0.405)	+3+ (0.42, 0.387)	1+2 (0.62, 0.314)	+3+ (0.63, 0.311)
4	1 (0.61, 0.362)	2 (0.62, 0.360)	4 (0.64, 0.349)	3 (0.62, 0.357)	1 (0.35, 0.466)	1+ (0.46, 0.425)	1 (0.39, 0.453)	1+2 (0.43, 0.438)	+3+ (0.48, 0.418)	1+2 (0.66, 0.336)	+3+ (0.67, 0.334)
5	1 (0.53, 0.344)	4 (0.57, 0.329)	2 (0.55, 0.338)	3 (0.56, 0.334)	1 (0.28, 0.426)	1+ (0.41, 0.385)	1 (0.32, 0.412)	1+2 (0.42, 0.381)	+3+ (0.45, 0.371)	1+2 (0.65, 0.298)	+3+ (0.65, 0.297)
6	1 (0.56, 0.289	4 (0.60, 0.277)	2 (0.58, 0.283)	3 (0.59, 0.280)	1 (0.31, 0.364)	1+ (0.43, 0.329)	1 (0.36, 0.350)	1+2 (0.40, 0.338)	+3+ (0.45, 0.322)	1+2 (0.62, 0.270)	+3+ (0.62, 0.268)
7	1 (0.58, 0.361	4 (0.60, 0.350)	2 (0.59, 0.357)	3 (0.60, 0.352)	1 (0.33, 0.453)	1+ (0.44, 0.413)	1 (0.38, 0.438)	1+2 (0.43, 0.417)	+3+ (0.47, 0.405)	1+2 (0.65, 0.329)	+3+ -
8	1 (0.67, 0.279	4 (0.68, 0.275)	2 (0.68, 0.277)	3 (0.68, 0.276)	1 (0.40, 0.376)	1+ (0.49, 0.348)	1 (0.44, 0.362)	1+2 (0.47, 0.355)	+3+ (0.51, 0.342)	1+2 (0.68, 0.276)	+3+ (0.68, 0.273)
e	1 (0.44, 0.295	2 (0.50, 0.281)	3 (0.50, 0.278)	4 (0.52, 0.274)	1 (0.17, 0.360)	1+ (0.31, 0.328)	1 (0.21, 0.351)	1+2 (0.31, 0.329)	+3+ (0.36, 0.316)	1+2 (0.57, 0.260)	+3+ (0.60, 0.251)
10	1 (0.61, 0.326	2 (0.62, 0.321)	4 (0.64, 0.315)	3 (0.63, 0.319)	1 (0.33, 0.426)	1+ (0.43, 0.392)	1 (0.37, 0.415)	1+2 (0.40, 0.402)	+3+ (0.46, 0.384)	1+2 (0.66, 0.302)	+3+ (0.68, 0.297)
11	1 (0.52, 0.332	2 (0.55, 0.319)	3 (0.56, 0.316)	4 (0.58, 0.308)	1 (0.23, 0.420)	1+ (0.38, 0.376)	1 (0.27, 0.407)	1+2 (0.34, 0.388)	+3+ (0.41, 0.365)	1+2 (0.61, 0.298)	+3+ (0.62, 0.293)
12	1 (0.59, 0.366	2 (0.60, 0.360)	3 (0.60, 0.357)	4 (0.62, 0.651)	1 (0.31, 0.470)	1+ (0.44, 0.426)	1 (0.36, 0.454)	1+2 (0.43, 0.431)	+3+ (0.46, 0.416)	1+2 (0.67, 0.328)	+3+ (0.67, 0.327)
13	1 (0.49, 0.299	2 (0.51, 0.293)	3 (0.52, 0.290)	4 (0.55, 0.283)	1 (0.24, 0.365)	1+ (0.39, 0.328)	1 (0.29, 0.355)	1+2 (0.38, 0.330)	+3+ (0.41, 0.322)	1+2 (0.61, 0.262)	+3+ -
14	1 (0.54, 0.349	2 (0.56, 0.341)	3 (0.56, 0.338)	4 (0.59, 0.328)	1 (0.27, 0.439)	1+ (0.41, 0.393)	1 (0.31, 0.427)	1+2 (0.39, 0.401)	+3+ (0.45, 0.381)	1+2 (0.64, 0.307)	+3+ (0.65, 0.304)
15	1 (0.54, 0.349	2 (0.56, 0.341)	3 (0.56, 0.339)	4 (0.59, 0.327)	1 (0.18, 0.447)	1+ (0.35, 0.397)	1 (0.22, 0.434)	1+2 (0.35, 0.397)	+3+ (0.42, 0.376)	1+2 (0.60, 0.310)	+3+ (0.62, 0.305)
16	1 (0.45, 0.366	2 (0.50, 0.350)	3 (0.51, 0.344)	4 (0.53, 0.336)	1 (0.27, 0.466)	1+ (0.40, 0.421)	1 (0.31, 0.453)	1+2 (0.41, 0.419)	3+ (0.45, 0.405)	1+2 (0.64, 0.327)	+3+ (0.64, 0.327)

Table 5.6: Results of SMR models describing natural logarithm transformed T_s timeseries ($*T_s$) from meteorological variables and additional predictors derived from the meteorological timeseries (see text for full details). Predictive variable importance (e.g. 1, 2 etc.) or sequence (e.g. variables 1+2, or all indicated by +3+) is shown, with coefficients of determination and root mean squared error for each model given in parentheses (R^2, RMSE). The grey rows are those identified as being less representative of debris surface temperature due to site grain size.

One of the potential weaknesses in the first pass SMR models is the co-linearity between variables, particularly for SW_{in} and T_a, for which $r = 0.84$ ($p << 0.05$). There is typically positive relationship between incident solar radiation and T_a, due to the direct influence SW_{in} has on T_s (Hock, 2003), and the strong covariant relationship present between T_s and T_a (Foster et al., 2012; Shaw et al., 2016). Consequently, the SMR analyses were re-run with $*T_{aG}$ removed from the model (Table 5.6: SMR 2). Results highlighted that, in the absence of T_{aG}, all models exhibited $*SW_{in}$ as the dominant predictor for T_s, but with coefficients of determination much reduced ($0.17 \leq R^2 \leq 0.40$). Inclusion of the other meteorological variables, while increasing the models' performance (with R^2 increasing to ≤ 0.49) maintained less than 50% efficacy in predicting T_s (Table 5.6). Conflating the radiation terms (SW_{in} and LW_{in}) into 'net incident radiation' (NR_{in}) and continuing the omission of T_{aG} in a third set of SMR analyses (SMR 3) yielded similar results to SMR 2, with $*NR_{in}$ being the dominant predictor variable; moreover, opting for inclusion of 'rate of change in T_{aG}' (dT_a) for the preceding hour, and cumulative radiation variables ($*SW_{in}$ and $*LW_{in}$) and 'time since precipitation' (tP) as a potential drivers for T_s in SMR 3 showed similarly incremental improvements but only to $R^2 = 0.51$. In all cases in SMR 3, dT_a was the second most significant predictor variable. A final SMR model (SMR 4) excluded all radiation terms and utilised $*T_{aG}$, dT_a, *RH, *P and tP. In SMR 4 dT_a was the most significant predictor variable, while all other predictors, despite being significant in cases, increased R^2 by ≤ 0.02. The multivariate analyses clearly indicated that all T_s timeseries were most readily predicted by T_a, and this numerical model could be improved by considering the rate of change in T_a. Despite the close association between incident radiation and T_a, the multivariate models using SW_{in}, LW_{in} and NR_{in} were less effective in describing T_s change over the monsoon.

To gain a deeper understanding of the extent to which T_s and T_{aG} were related, and whether the two parameters have a varying temporal relationship, the relationship between T_s and T_{aG} was also investigated for daytime (06:00–18:00) and night-time (18:00–06:00) periods separately. A number of previous studies have investigated the seasonal and diurnally variable relationship of T_{aG} (e.g. Brock et al., 2010; Steiner and Pellicciotti, 2015), and in some cases its relationship to T_s (e.g. Fujita and Sakai, 2000). As elsewhere, days when T_s was consistently 0°C (DOY 145–153) were excluded from the correlation analysis. The relationship between T_s and T_{aG} varied across the study period

for both day and night (Figure 5.6). The relationship between T_s and T_{aG} was predominantly stronger at night (mean r = 0.86) than in the day (mean r = 0.75). Daytime T_s-T_{aG} correlations varied between r = -0.01 (DOY 190) and r = 0.97, whilst night-time correlations varied between r = 0.48 (DOY 188) and r = 0.99 (DOY 199). The seasonal and diurnal variation in the relationship between T_s and T_{aG} therefore suggests that T_{aG} was the dominant driver of T_s but that the strength of this relationship varied across a diurnal period and seasonally, due to diurnal and seasonal variation in additional incident or outgoing energy fluxes that also influence T_s.

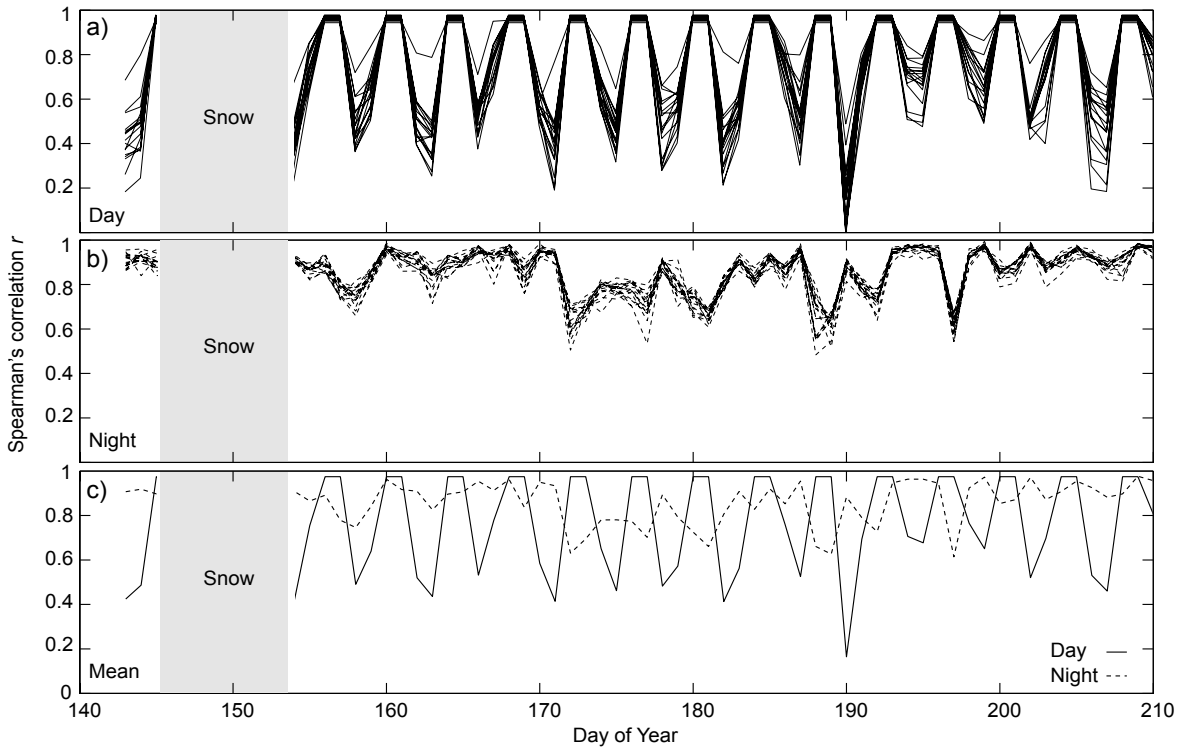

Figure 5.6: The correlation coefficient values (r) for the relationship between on-glacier air temperature (T_{aG}) and near-surface debris temperature (T_s), for (a) each daytime cycle (06:00–18:00) and (b) night-time cycle (18:00–06:00) over the study period, c) presents the across-sites average r-values for day and night.

To determine whether possible links between site characteristics and relationships between timeseries existed, as suggested by contrasting diurnal amplitudes and the lags between T_s timeseries, stepwise generalised linear models (SGLMs) were explored to investigate possible controls on variability in T_s. SGLMs were undertaken rather than SMR due to the small sample size, and the resultant need to relax the assumptions of normal distribution of each data series. The SGLMs examined debris temperature metrics that included means for daily mean T_s, maximum T_s, minimum T_s and the mean daily amplitude of T_s for each site as the dependent variables. However, following the identification of marked changes in the mode of diurnal variation in T_s (Section 5.5.1) and increasingly variable meteorology following DOY 170, a subset of the T_s metrics limited to the first part of the observation period (prior to DOY 170, excluding the snow-cover event) were examined. Site characteristics were used as predictor variables, including elevation, slope, aspect, mean grain size, lithology, terrain curvature and terrain roughness. A simple linear model was used, and potential interactions between site characteristics were not included. The less representative sites (1, 2, 9, 11, 13) were omitted from the SGLMs, and 5% significance levels were used to eliminate weaker predictors. A SGLM identifies the combination of predictor variables that explain the most variation in the dependent variables, and so provide one R^2 and RMSE value for the best combination of predictor variables and the values in the predictor variable columns are the coefficients for the calculated linear gradient. Consequently, results of a SGLM identify the statistically significant predictor variables for each temperature metric, but do not provide a hierarchy of these predictors.

Results of the SGLMs are given in Table 5.7. In all cases, the predictor models for T_s metrics limited to period prior to DOY 170 performed more poorly than those for the entire monsoon period, with low R^2 and route mean squared error values. None of the models were improved through inclusion of site curvature or roughness, and aspect was only considered important for prediction of minimum T_s, in which elevation was also critical. Elevation was also the dominant predictor for maximum T_s and daily amplitude, where grain size, lithology and slope also played significant roles in the SGLMs, with coefficients of determination of ~0.9. Consequently, these results suggested that by considering the entire monsoon the relative importance of site characteristics can be better understood. Specifically, debris size and lithology are considered to impact on

absorption and transfer of solar radiation through their influence on albedo, porosity and moisture content, while slope is a critical factor influencing solar radiation receipt. The southerly facing aspect of the majority of the sites reported here may undermine identification of the merit in describing T_s metrics using aspect, but the influence on minimum T_s highlighted potential importance of the environmental variable. While the sample set was relatively small, the SGLMs illustrated the potential for physical site characteristics to modulate T_s, and its behaviour, controlling the mode of diurnal variation in T_s, and the lag times and spatial variation identified in Section 5.5.2.

Table 5.7: Stepwise generalised linear models (SGLMs) for describing debris temperature metrics based on environmental variables for the iButton sensor sites. Models detail the coefficients for each significant ($p < 0.05$) predictor variable, and summarise the model performance using the coefficient of determination and root mean square error (R^2, RMSE).

Ts metric	K (Constant)	Elevation (Z)	Grain size	Lithology	Slope	Aspect	R^2	RMSE
Min. T_{s170}	0.050						n/a	0.731
Min. T_s	-106.460	0.022				0.004	0.58	0.292
Mean T_{s170}	23.754		-218.120	-0.152	0.323		0.89	0.531
Mean T_s	19.590		-165.260	-0.111	0.259		0.82	0.514
Max. T_{s170}	-674.740	0.151	-845.740	-0.487	1.942		0.92	1.456
Max. T_s	55.461		-566.370	-0.354	1.087		0.93	0.969
Amplitude T_{s170}	-689.860	0.154	-890.540	-0.495	2.118		0.89	1.737
Amplitude T_s	50.819		-555.460	-0.342	1.185		0.93	0.992

5.6. Discussion

The timeseries analyses detailed above identified a number of key aspects in the variability in T_s on the debris-covered ablation area of Khumbu Glacier. A seasonal trend of decreasing maximum and mean T_s was identified at the majority of sites, while an increase in minimum T_s was in contrast to seasonal changes in T_a. A systematic shift from a dominant smooth diurnal cycle in T_s early in the monsoon to a lagged and less transitional cycle as the monsoon progressed occurred, alongside which meteorological conditions became more varied. In terms of spatial contrasts, there was evidence of subtle differences between sites, illustrated by disparities in how closely the T_s series paralleled each other, and short term (≤ 2hr) lags in T_s between sites. Exploring these differences through consideration of meteorological drivers and potential site characteristic controls enabled identification of a dominant association between T_a and T_s, and the influence that the rate of change in T_a has on the debris heat budget, and the important role grain size, lithology and slope appeared to have on T_s metrics at each site. Here, we discuss the processes that may underlie the observed variability in T_s on a debris-covered glacier.

5.6.1. Temporal variability in near-surface debris temperature

The debris temperature (T_s) timeseries were most notably perturbed between DOY 145 and 153, during which a period of sustained 0°C occurred following a major snowfall event. No further periods of $T_s \sim 0$°C were observed during the study period, suggesting later snowfall events were either not of sufficient magnitude to subdue variation in T_s, or that precipitation fell as rain during the rest of the study period. Such a switch in precipitation type from snowfall in the onset of the monsoon to rainfall in the main monsoon period has previously been documented and attributed to higher T_a during the main period of the monsoon, as was observed in both T_{aP} and T_{aG} timeseries (Figure 5.3b).

Following the period of 0°C, short-term variability of the order of 3–8 days and a seasonal trend in decreasing maximum T_s were observed in all T_s timeseries. The timing of short-term variability in T_s and SW_{in}, LW_{in}, RH and precipitation was simultaneous, whilst the seasonal decrease in maximum T_s occurred alongside a trend of decreasing SW_{in},

increasing T_a, LW_{in} and RH, and increased frequency of precipitation (Figure 5.3). The coincidence of the seasonal trends in meteorological variables provide a strong indication of increased cloudiness over the study period (Mölg et al., 2009; Sicart et al., 2006; Van Den Broeke et al., 2006). This illustrates two main aspects of the surface energy balance of the debris layer: firstly, decreased energy input at the debris surface due to increasing cloud cover; and secondly, the amount of thermal energy the debris layer can store, through increased moisture content in the debris (Juen et al., 2013).

Increasing cloud cover results in a decreasing amount of SW_{in} reaching the debris surface, causing maximum T_s to decrease, which occurs in all timeseries presented here, and a delay in the time at which maximum T_s is achieved as the incoming energy flux to the debris surface is reduced and the debris therefore takes longer to heat up. Consequently, such an increase in cloudiness over the study period would have resulted in the decrease in the diurnal amplitude of T_s, and a delay in timing of peak diurnal T_s, both of which are observed in changing modes of variation in T_s identified in the PCA (Figure 5.4). An additional control on decreasing SW_{in} would be that following midsummer (DOY 172) regional SW_{in} and solar angle would decrease, reducing the intensity and duration of SW_{in} a debris surface would receive. No clear distinction between the effect of cloud cover and a decrease in the regional radiation budget can be specifically identified, although the decrease in SW_{in} was initiated before DOY 172, which would suggest this trend was primarily dependent on increasing cloud cover.

A seasonal increase in cloud cover, relative humidity and the frequency of precipitation would also increase moisture content in the debris layer. Moisture content of the debris layer has the potential to affect T_s considerably, but is challenging to quantify and thus not reported here. The presence of moisture in a debris layer affects its thermal capacity, and therefore the energy needed to increase its bulk temperature. An increased amount of energy would therefore be needed to heat water-filled pores to the same temperature as air-filled pores within the debris layer (Collier et al., 2014; Evatt et al., 2015). Consequently, as incoming energy to the debris surface decreased during the season, and the amount of energy needed to maintain the temperature of a bulk debris layer increased due to presence of moisture- rather than air-filled pores in the debris layer, mean T_s would decrease. Additionally, an increasingly abundant presence of moisture in a

debris layer would have decreased T_s due to increased latent heat exchange and subsequent loss of heat through evaporation in the debris surface layer (Cuffey and Paterson, 2010; Takeuchi et al., 2000). These trends in T_s are observed in the timeseries presented here, and alongside the precipitation timeseries, debris moisture content is considered to have been a factor in controlling T_s. However, direct collection of data for moisture content is needed to confirm the link between T_s and debris moisture content.

The 5–8 day cyclic perturbations of T_s were also synchronous with periods of markedly lower SW_{in}, higher LW_{in} and relative humidity, and higher precipitation. These perturbations suggest the intensity of cloud cover was also temporally variable, resulting in periods of T_s with decreased diurnal amplitude and lower maximum T_s. The perturbations of T_s were increasingly frequent in the latter half of the study period, evidenced by the majority of days loaded to PC2 being present in the latter half of the study period. These perturbations suggest that alongside seasonal increase in cloud cover due to progression of the monsoon, more localised weather patterns still contribute to variability in meteorological parameters that also affect T_s.

5.6.2. Spatial variability in near-surface debris temperature

The asynchronous transitions from a period of 0°C T_s to positive T_s between sites (Figure 3a) suggest the onset and completion of snow melt was spatially variable. This spatial variability is likely due to contrasts in snow accumulation, incoming energy fluxes as a result of varying slope and aspect of sites, and in the thermal capacity of the debris layer, due to varying moisture content between sites and the effect of this moisture on latent heat exchange (Guglielmin et al., 2012). Despite the period of asynchrony in T_s between sites, for the majority of the study period all T_s timeseries displayed high similarity, evidenced in the *r* and *E* values for the raw data and the *r* values for the detrended timeseries. *E* values suggested subtle variability did exist between sites, which was primarily manifested in the range and magnitude of temperature recorded at each site rather than the pattern of T_s.

Variability in temperature sensor depth may have caused some variability in *E* between site pairs. Although sensor depth variability was accounted for using the temperature gradient through a debris layer calculated by Nicholson and Benn (2006), this was an

averaged gradient over a diurnal period. Applying such a gradient to determine uncertainty estimates the effect of sensor depth on recorded T_s, whereas the temperature gradient through a debris layer varies across a diurnal cycle, which would affect the magnitude and pattern of T_s recorded between sites (Nicholson and Benn, 2006). However, after the sites identified as less representative were omitted, sensor depth varied by < 0.03 m, which would have produced a maximum uncertainty of 3°C between sites even for the steepest gradients previously identified (at 13:00 by Nicholson and Benn (2006)). Variability of T_s between sites reached up to 10°C throughout the study period, which exceeds discrepancies exclusively due to sensor depth and so instead suggests other drivers of spatial variability in T_s between sites.

The subtle spatial variability in T_s was identified in the differing daily maximum T_s data sets, which varied by up to 22°C between sites. Variability in maximum T_s could be indicative of variable site aspect, affecting the shading and sheltering of the site from incoming solar radiation and wind (Hock, 2003; Gao et al., 2007). Such sheltering would affect both the incoming energy to the debris surface through shortwave radiation, turbulent energy exchange, and also the rates of snow melt and evaporation from the debris layer (Verbunt et al., 2003). The rate of evaporation from the debris layer would become increasingly important as the moisture content in the debris layer increased due to increased relative humidity and frequency of precipitation over the study period.

5.6.3. Controls on variability in near-surface debris temperature

Coincident trends in T_s and meteorological variables suggest a high level of interconnection between meteorological variables and T_s. However, determining a hierarchy of controls by these meteorological variables on T_s is more complex. T_{aG} appeared to explain the majority of the relationship identified between meteorological variables and T_s through SMR for all sites (e.g. Petersen et al., 2013), while other variables were less effective as predictors. Models describing T_s were improved through using a rate of change in T_a, indicating the direction of change during the preceding hour had influence on T_s. The relationship between additional meteorological parameters identified in subsequent SMR model results suggests it is vital that temperature-index models that employ T_s as a driver for numerical predictions of glacier ablation should

also include these identified additional meteorological parameters, specifically SW_{In} (e.g. Carenzo et al., 2016) and potentially RH, which also play an important role in energy transfer and may indicate the moisture content of the debris to an extent. Omission of T_{aG} in SMR models identified SW_{in}, LW_{in} and RH as contributory drivers of T_s, and reiterates the complexity of the energy balance at a debris-covered surface where all of meteorological parameters play some role in controlling T_s. However, within the SMR models, the strongest relationship between T_{aG} and T_s was $R^2 = 0.67$, and inclusion of additional variables only improved models performance to $R^2 < 0.70$ (Table 5.6). This suggests additional factors controlled temporal variability in T_s, but determining an ultimate hierarchy of potential controls on temporal variations in T_s is challenging with the data set collected here.

Due to the covariate relationship between T_{aG} and T_s a high correlation between the two does not conclusively identify T_{aG} as the primary driver of T_s, but does suggest temperature index models based on the relationship between T_{aG} and T_s are appropriate for debris-covered glaciers. Unravelling the relationship between T_{aG} and T_s is complex, as the two variables are interdependent on one another (Shaw et al., 2016), particularly when T_a is collected below the standard height of 2 m above the glacier surface in the boundary surface layer (e.g. Reid et al., 2012; Wagnon et al., 1999). Critically, here, T_{aP} and T_{aG} were highly correlated ($r = 0.72$, $p < 0.05$), but accounting for the elevation difference using lapse rates of -0.0046°C/m appropriate for the monsoon season on Khumbu Glacier (Shea et al., 2015) and a standard -0.0065°C/m, exhibited mean residuals of -1.9 and -1.3°C, respectively, T_{aG} was consistently significantly higher than T_{aP}. This on-/off- glacier contrast is due to heat loss from the thick supraglacial debris layer to the near-surface atmosphere through turbulent heat exchange (Takeuchi et al., 2000). Our results mirror those of Steiner and Pelliccioti (2015) where air temperature collected off-glacier from equivalent elevations was consistently lower than on-glacier air temperature, highlighting the need to use off-glacier temperature records with caution when driving numerical models of glacier ablation.

The control of specific meteorological controls of T_s was also spatially variable (Table 5.6). Although a difference in elevation between the T_s sensors and the T_a sensor existed, variability in the relationship between T_{aG} and T_s is predominately attributed to spatial

variability between the sites at which T_s was recorded. The maximum elevation variation between T_s and T_{aG} sensors was 47 m, which, using the range of potential lapse rates described above, would result in variations in T_{aG} of up to 0.3°C across the study site, (below the T_{aG} sensor uncertainty), and differences between T_{aG} and T_s were greater than 0.3°C for all sites. The reason for such spatial variability in T_s is assumed to be due to varying topography and characteristics between sites, causing the duration and intensity of SW_{in} to vary and because of differences in the thermal capacity and conductivity between sites.

The results of the SGLM analysis support previous work on clean-ice and debris-covered glaciers, and permafrost environments, where topographic controls including aspect, slope (e.g. Gao et al., 2017; Gubler et al., 2011; Guglielmin et al., 2012; Hock and Holmgren, 1996; Strasser et al., 2004), albedo and surface roughness (considered a factor due to the importance of grain size) (e.g. Brock et al., 2000; Mölg and Hardy, 2004) were found to influence spatial variability in the incoming energy flux to the ground surface, and would therefore be anticipated to control T_s. The most dominant variables describing metrics of the T_s series from each site on Khumbu Glacier were slope, grain size and lithology. These clearly control incident radiation receipt through solar geometry and albedo, moisture content and evaporation, and affect local thermal conductance. Despite this potential control responding to SW_{in}, SMR results showed SW_{in} to have a less pronounced control on T_s than would be expected (e.g. Willis et al., 2002), and support Rounce et al.'s (2015) assertion that SW_{in} is less important in controlling incoming energy flux on a debris-covered glacier surface than on a debris-free glacier surface. Aspect was only found to influence minimum T_s, but the majority of sites reported here were southerly facing and provide a systematic bias, hindering identification of this topographic variable. The potential environmental controls on T_s were best identified through consideration of the entire monsoon period, which likely emphasised spatial differences arising from the influence of moisture from precipitation, increasing LW_{in} and more variable meteorological conditions in the latter half of the observation period.

The temporal variability in the relationship between T_{aG} and T_s, both diurnally and seasonally, builds on the conclusions of Steiner and Pellicciotti (2015), who identified a variation in relationship between the two parameters between night and day and with

differing climatic conditions. The occurrence of a seasonal influence in this variable relationship is attributed to variability in meteorological parameters, with decreased correlation coefficients occurring concurrently with perturbations in SW_{in}, and peaks in LW_{in} and relative humidity (e.g. around DOY 173). Such variability is attributed to differences in the capacity of air and debris to hold thermal energy, and the addition of moisture in either or both environments, causing the relationship to vary between T_{aG} and T_s seasonally as well as diurnally. Understanding the importance of the high relative humidity values and precipitation is also important for understanding the effect of turbulent heat flux on glacier ablation for these monsoon-influenced debris-covered glaciers (Suzuki et al., 2007). The correlation coefficients for the T_s–T_{aG} relationship presented here also reinforce the findings of Steiner and Pellicciotti (2015), displaying stronger relationships at night due to T_s increasing at a greater rate and magnitude than T_{aG}. Consequently, temperature-index models that rely on the relationship between T_{aG} and T_s need to incorporate such diurnal and seasonal variability in this relationship, particularly for monsoon-influenced debris-covered glaciers, and ultimately surface energy balance models are considered more appropriate for these complex glacier systems.

5.6.4. Implications of variability in near-surface debris temperature

A development of surface energy balance models to incorporate spatiotemporal variations in debris properties would be appropriate for modelling ablation, but also for constraining surface energy balance models used for estimating debris thickness (e.g. Foster et al., 2012; Rounce and McKinney, 2014). This study's findings advocate the use of a surface energy balance approach for calculating debris layer thickness rather than the use of a direct empirical relationship between T_s and debris layer thickness used by Mihalcea et al. (2008a; 2008b) and Minora et al. (2015). The latter of these approaches over-simplifies the relationship between T_s and debris thickness, and omits the additional factors identified here that influence T_s over space and time, independent of debris layer thickness. However, the simplified energy balance approach for calculating debris thickness used by Foster et al. (2012) and Rounce and McKinney (2014), needs to undergo substantial developments to provide accurate estimations of debris layer thickness, in line with full surface energy balance models such as those produced by Collier et al. (2014) and Evatt et al. (2015). It is only once a comprehensive consideration

of all controls on T_s are incorporated into estimations of debris thickness calculated from T_s that debris thickness maps will exhibit a much-reduced uncertainty. In the meantime, estimations of debris thickness using both methods should identify the possible uncertainty involved in disregarding spatial variability in debris properties and compare their debris thickness estimates with direct field measurements of debris thickness.

5.7. Conclusion

This study presents the most comprehensive near-surface debris temperature (T_s) dataset for a monsoon-influenced debris-covered glacier to date. The timeseries presented here extend beyond describing the influence of debris layer thickness on near-surface debris temperature, and confirm both temporal and spatial variability in debris surface temperature on Khumbu Glacier, Nepal. Records of T_s from 16 sites across Khumbu Glacier's debris-covered ablation area displayed marked daily cycle in T_s, overlying seasonal, short-term and spatial variation in maximum debris surface temperature and diurnal amplitude. A clear transition in the mode of diurnal variation was associated with increasing cloud cover and precipitation; the latter considered to control debris moisture content. Subtle differences in the magnitude and range of variation in T_s were apparent between sites, and were indicative of contrasts in response of T_s to meteorological or environmental variables. A close association between on-glacier air temperature and T_s was evident, while radiative energy was less effective in terms of describing T_s and highlighted the potential influence of precipitation, and potentially moisture content within the debris layer. Analyses of these timeseries also demonstrated the role that site characteristics including slope, lithology and grain size hold in controlling spatial variability in T_s. Consequently, this study specifically identified the variables controlling temporal and spatial variability in T_s for a debris-covered glacier surface; previously the majority of controlling variables on T_s for a debris-covered glacier surface were assumed to be the same as for a clean-ice glacier.

The results presented here reinforces the complexity of the surface energy balance at a supraglacial debris surface, identifying a number of energy fluxes at the debris surface regulate debris surface temperature. Hence, these results suggest that, although temperature-index models can be useful for estimations of supraglacial debris thickness or ablation, such models need to incorporate other aspects of energy exchange and

account for spatial and temporal variation in debris properties to reduce uncertainties. Studies that simulate ablation or derive debris thickness maps must consider including more spatially abundant measurements of T_s and debris thickness in model validation, and consider the influence of variability in site characteristics on calculated results. Finally, the datasets presented here were limited to debris layers > 1 m thick, and so future research should look to assess the role of debris characteristics and local topography in defining the energy exchange and T_s across thinner debris layers as well.

Chapter 6: Paper II

Title: Changes in glacier surface cover on Baltoro Glacier, Karakoram, north Pakistan, 2001–2012.

Journal: Journal of Maps

Current status: Published 10th December 2016

Gibson MJ, Glasser NF, Quincey DJ, Rowan AV, Irvine-Fynn TDL. 2016. Changes in glacier surface cover on Baltoro Glacier, Karakoram, North Pakistan, 2001–2012. *Journal of Maps* 13 (3) 100–108.

6. Changes in glacier surface cover on Baltoro Glacier, Karakoram, north Pakistan, 2001–2012

6.1. Abstract

The presence of supraglacial debris on glaciers in the Himalaya-Karakoram affects the ablation rate of these glaciers and their response to climate change. To understand how supraglacial debris distribution and associated surface features vary spatially and temporally, geomorphological mapping was undertaken on Baltoro Glacier, Karakoram, for three time-separated images between 2001–2012. Debris is supplied to the glacier system through frequent but small landslides at the glacier margin that form lateral and medial moraines and less frequent but higher volume rockfall events which are more lobate and often discontinuous in form. Debris on the glacier surface is identified as a series of distinct lithological units that merge downglacier of the convergence area between the Godwin-Austen and Baltoro South tributary glaciers. Debris distribution varies as a result of complex interaction between tributary glaciers and the main glacier tongue, complicated further by possible surge events on some tributary glaciers. Glacier flow dynamics mainly control the evolution of a supraglacial debris layer. Identifying such spatial variability in debris rock type and temporal variability in debris distribution has implications for glacier ablation rate, affecting glacier surface energy balance. Accordingly, spatial and temporal variation in supraglacial debris should be considered when determining mass balance for these glaciers through time.

6.2. Introduction

Debris-covered glaciers, where the majority of the ablation area is covered in rock debris, are ubiquitous in mountainous regions globally (Benn & Lehmkuhl, 2000), including the Southern Alps of New Zealand, European Alps, the Andes and in High Asia. The Himalaya - Karakoram contain the largest area of glacial ice outside of the Polar Regions, with one-fifth of the world's population depending on the run-off from these glaciers as a water resource (Bolch et al., 2012). Approximately 23% of glacier area in the Himalaya is covered by debris, and 33% in the Everest region (Scherler et al., 2011; Thakuri et al., 2014). The input of debris to glaciers in the Karakoram is driven by high rates of rock uplift in the mountain range and correspondingly high rates of erosion, ranging between 0.06 and 2.5 mm a^{-1} (Seong et al., 2007). Debris distribution is controlled by the delivery

of rock debris and debris transport by ice flow, which slows as the glacier loses mass, resulting in a constantly changing distribution of supraglacial debris (Bolch et al., 2008; Rowan et al., 2015; Thakuri et al., 2014). Understanding the nature of these changes in debris distribution is currently limited, due to the lack of data describing how supraglacial debris layers evolve through time. However, our knowledge of these glaciers needs to progress to determine their response to current climate change, and the impact these changes will have on the people who rely on them.

Supraglacial debris distribution is an important consideration when calculating glacier mass balance, as such debris layers attenuate the ablation of the underlying ice depending on the debris thickness (Evatt et al., 2015; Østrem, 1959). A thin debris layer (up to around 0.05 m thick), when compared to clean ice, enhances melt by increasing the albedo of the glacier surface, causing it to absorb more solar radiation and melt more quickly than debris-free ice. Above the critical thickness, which differs between glaciers, the ablation rate of underlying ice decreases exponentially with increasing debris thickness (Kayastha et al., 2000; Nicholson and Benn, 2006; Østrem, 1959). In addition to meteorological parameters, the resultant ablation rate of ice under a debris layer is affected by debris characteristics, including lithology and porosity of the debris layer. The thermal capacity and conductivity of the debris is partially dependent on lithology and so will affect how much thermal energy is held in and transferred through the debris layer (Conway and Rasmussen, 2000; Nicholson and Benn, 2013). Incorporating the evolution of debris distribution, thickness and lithology into calculations of the mass balance of debris-covered glaciers will result in better constraint of the role of debris in modifying the response of these glaciers to climate change.

Geomorphological mapping of debris distribution using satellite imagery is a useful tool to identify temporal changes in debris distribution across an entire glacier surface, reducing the need for expensive and often challenging fieldwork. By identifying the sources of debris, and the interaction of different debris units and glacier flow, controls on spatiotemporal variations in debris distribution can be determined. A greater understanding of the interaction between hillslope and glacial processes can also be developed with regard to the input of supraglacial debris into the glacial system. Baltoro Glacier is highly appropriate for supraglacial debris mapping due to its location in a

region of high erosion rates and concurrently extensive debris cover, and the large number of tributary glaciers which form the glacier system and lead to a complex flow regime and spatially varied debris distribution.

6.3. Study site

Baltoro Glacier is located in the Karakoram mountain range in northern Pakistan. The glacier and its tributaries cover an area of ~524 km^2, with a centre-line length of ~62 km (Figure 6.1). The second highest mountain in the world, K2, is located ~12 km north of the main glacier tongue. The main tongue of Baltoro Glacier flows from Concordia (4600 m above sea level (a.s.l.)) in an east to west direction, to its terminus at ~3410 m a.s.l., and has 12 tributary glaciers along its lengths (Tributary Glaciers (TGs) 3–14, Main Map). Above Concordia Godwin- Austen Glacier (TG 1) and Baltoro South Glacier (TG 2) converge to form the main tongue of Baltoro Glacier. Baltoro Glacier has an extensive debris cover, with ~38% of its area covered by supraglacial debris (Mayer, et al., 2006). Debris thickness has a general pattern of increasing thickness downglacier, reaching around 3 m in thickness at the glacier terminus (Mihalcea et al., 2008).

Figure 6.1: The regional extent of the Baltoro Glacier system and relevant locations, including Concordia and name tributary glaciers.

6.4. Previous work

Baltoro Glacier is relatively well studied despite its location in a remote and politically unstable region. Much of the existing research literature is almost exclusively based on remote sensing datasets (e.g. Collier et al., 2014; Quincey et al., 2009b), although some studies have been complemented by fieldwork (e.g. Mayer et al., 2006; Mihalcea et al., 2008; Searle et al., 2010). Supraglacial debris thickness for the entire glacier was calculated by Mihalcea et al. (2008) and Minora et al. (2015) for 2004 and 2011, respectively, but these maps omit consideration of lithology and the potential impact of spatial differences in thermal energy stored in the debris due to different lithologies across the glacier surface. Lack of segregation between debris lithology may cause errors in these debris thickness output maps, as thermal capacity of rock debris influences debris surface temperature, the parameter used to calculate debris thickness in these two studies (Steiner and Pellicciotti, 2015). Collier et al. (2013) incorporated a debris layer with a simulated thickness into a distributed energy balance model for the glacier, but did not consider spatial variations in debris lithology either. Omitting lithological variation is a potential error in the resultant ablation rates calculated by the study, as differing albedo, thermal capacity and rates of heat transfer for different debris lithologies were not incorporated into calculations. Other studies focused on different aspects of the Baltoro Glacier system; Quincey et al. (2009b) investigated the changing velocity of the glacier between 1993 and 2008 and linked their observations to climatic variability, while both Diolaiuti et al. (2003) and Belò et al. (2008) identified the historical surging nature of the confluent Liligo Glacier (TG 7) (Figure 6.1) and reconstructed its recent dynamic history.

6.5. Methods

Geomorphological features of Baltoro Glacier were mapped using three time-separated and orthorectified Advanced Spaceborne Thermal Emission and Reflection Radiometer (ASTER) images. The three images were acquired in August 2001 (29th August), 2004 (14th August) and 2012 (20th August), at a resolution of 15 m, and were selected because of low levels of cloud cover (46%, 1% and 13%, respectively). Images from the same month in each year also allowed direct comparison of seasonally controlled aspects of the glacier geomorphology (e.g. supraglacial water bodies and mass movement scars). ASTER

images were georeferenced and orthorectified in ENVI (v.5.0) prior to using them for mapping surface cover on Baltoro Glacier. Georeferencing was undertaken using the ASTER georeferencing tool in ENVI (v.5.0) and a Landsat 7 ETM+ image (acquired on 9th August 2002), which is georeferenced and orthorectified prior to downloading. Tie points between each ASTER and the Landsat 7 Enhanced Thematic Mapper (ETM+) images were created as part of the georeferencing process. Georeferenced ASTER images were then compared to the Landsat 7 ETM+ image and to each other to confirm that there was no pixel shift present between images. Orthorectification was then undertaken on each ASTER image using the ENVI (v.50) ASTER orthorectification tool, which corrects the effects of sensor tilt and terrain, and creates a planimetric image.

An additional Landsat 7 ETM+ image, acquired in August 2001 at 30 m resolution, was used to map upper regions of the glacier that were covered in cloud in the ASTER 2001 imagery. Additionally, Quickbird data, accessed through Google Earth (2016) were used to investigate specific features at a horizontal resolution of 2.4 m. Features were mapped from ASTER imagery using a false-colour composite (Bands 3N, 2, 1) at 15 m resolution and were manually digitised in ESRI ArcGIS 10.1. Geomorphological features were initially mapped at a glacier wide scale, then the boundaries of features identified at a finer scale to increase mapping accuracy. Debris units were identified manually using colour differences between pixels on the glacier surface, aided by comparison of the red, green and blue spectral signal of these pixels with different colours (Lillesand et al., 2014). The units were then traced up-glacier to their source area and lithology was identified by matching the source area with geological units identified by Searle et al. (2010) in the geology map of the Karakoram. Mass movement deposits were identified by the presence of two features: a scar, identified as a lighter, elongate feature on the valley side, and an associated debris fan deposit on or near the glacier surface (Figure 6.2a,b). Pixels containing supraglacial water were identified using a normal difference water index (NDWI) (Gao, 1996) in ENVI, (v. 5.0) calculated from ASTER Bands 3 and 4 using Equation 6.1:

$$NDWI=(NIR(Band\ 3)-SWIR(Band\ 4))/(NIR(Band\ 3)+SWIR(Band\ 4)) \quad (6.1)$$

Manual identification and digitisation of supraglacial features resulted in some misclassification of pixels, particularly where changes in debris distribution or supraglacial pond size were of the order of a few pixels. The extent of this error was reduced by repeated digitisation of each feature three times and the three outputs were then compared against the imagery to determine the most appropriate outline. Digitised margins of debris-covered glaciers in previous studies have been calculated to have errors between 2.5% and 4.5% (e.g. Bolch et al., 2010; Paul et al., 2011). Consequently, changes of the order of less than 4.5% of the feature area were disregarded in this study.

The map associated with, and which follows, this paper is the 2012 geomorphological map of Baltoro Glacier, with insets from 2001, 2004 and 2012 showing changes in surface cover through time. The map is in a Universal Transverse Mercator (UTM) WGS 1984 projected coordinate system with off-ice 250 m contours, derived from the ASTER Global digital Elevation Model (GDEM) (2000, 30 m resolution) using the contour tool in ArcGIS (v.10.1). The glacier outline used is adapted from the Randolph Glacier Inventory (Arendt et al., 2012; Bajracharya et al., 2014).

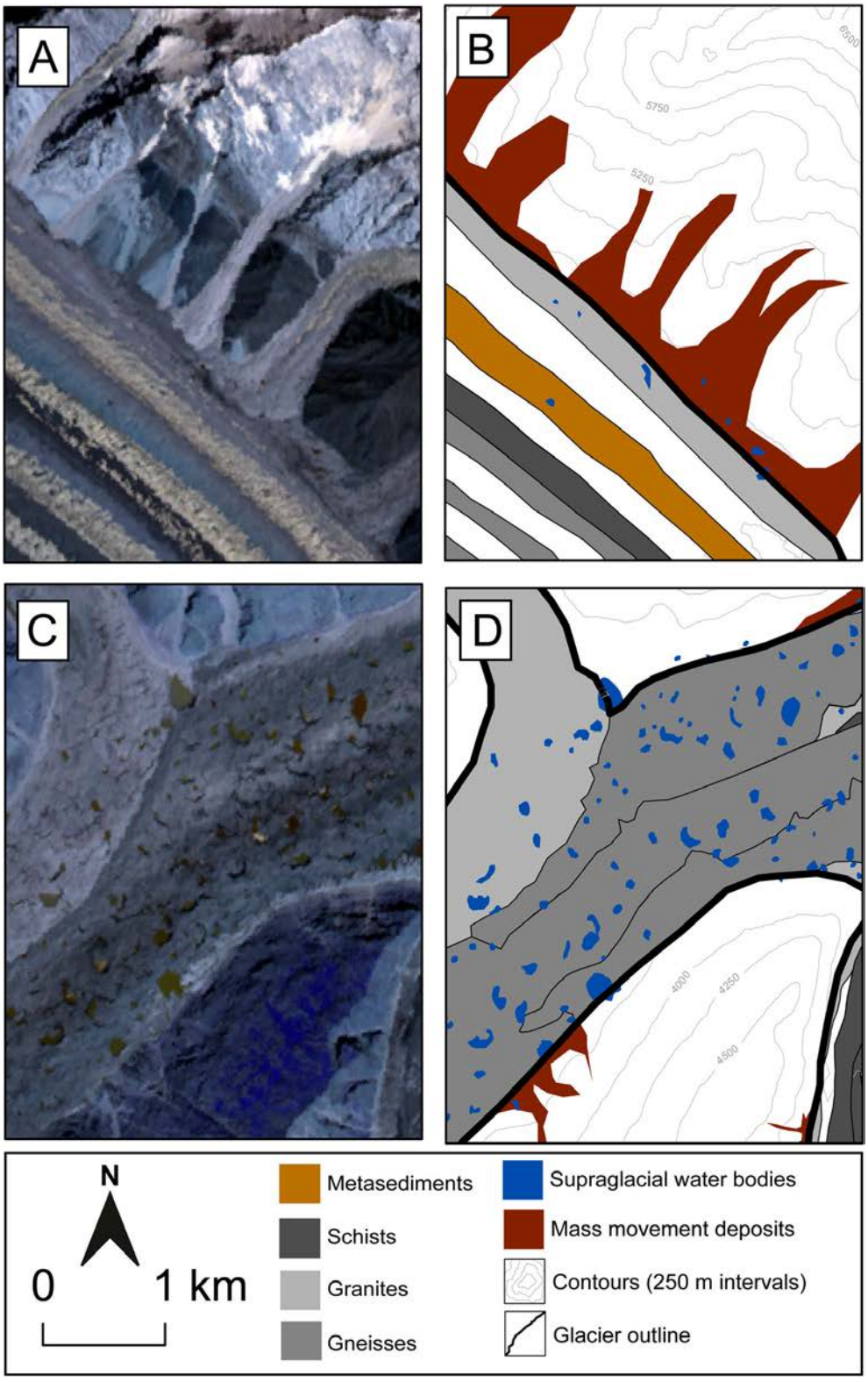

Figure 6.2: Examples of mass movement deposits (a, b) and supraglacial water bodies (c, d) in the original ASTER 2012 images and mapped examples, respectively.

6.6. Features related to debris distribution

6.6.1. Debris units

The schist, gneiss and granitic debris units are part of the Baltoro Batholith and associated metamorphosed rock units, while the metasediment debris unit originates from a small exposure of metamorphosed limestone near the headwall of TG2. The debris-covered glacier area has varied between 2001 and 2012 by ~5%, but gneiss debris dominates the debris distribution on Baltoro Glacier throughout this period, covering ~53% of the area (Table 6.1). The metasedimentary debris has the most variable area between 2001 and 2012 and does not reach the glacier terminus. It is likely that the increase in the area of the metasediment debris unit is due to it being a younger deposit than other debris units, and so it has not reached the terminus yet, or that it has reached the terminus but has been mixed or covered by other debris units before the terminus. All debris units form moraine structures, both lateral and medial, which are fed by debris input from the glacially incised valley walls and associated valley spurs at the confluences of glacier flow units through small but frequent landslide events, as seen in mountain valley environments (Rowan et al., 2015). These units are initially separated by debris-free ice, but converge below Concordia. The debris units have distinct margins in the upper and mid-sections of the main glacier tongue, but converge to a massive debris unit in the lower 10 km of the glacier. The moraines increase in width with increasing distance from their source until they converge, due to increased debris input from englacial meltout and slumping of the moraines over time (Hambrey and Glasser, 2003). Little change in the main debris unit boundaries occurs in the mid- and lower sections of the main glacier tongue between 2001 and 2012, suggesting that once units converge their width is constrained by the other debris units.

Table 6.1: The total area of each debris unit type, based on lithology, for 2001, 2004 and 2012, and the percentage of each debris type as a proportion of the total debris cover for Baltoro Glacier and its tributary glaciers.

Year	2001	2001	2004	2004	2012	2012
Debris type	**Area (km^2)**	**% of total debris**	**Area (km^2)**	**% of total debris**	**Area (km^2)**	**% of total debris**
Gneiss	81.48	52.9	79.83	51.2	79.48	52.9
Metasediment	8.60	5.6	11.41	7.3	8.28	5.5
Schist	17.76	11.5	18.54	11.9	17.71	11.8
Granite	46.29	30.0	46.20	29.6	44.71	29.8
Total debris (m^2)	154.13		155.97		150.17	

6.6.2. Supraglacial water bodies

The number of supraglacial water bodies, also referred to as 'ponds', increased from 234 to 570 over the study period, occupying 0.66 km^2 of the debris surface in 2001, and 2.04 km^2 in 2012, an increase in pond area of 209% (Table 6.2). Pond formation is associated with spatially varying ablation that results in the formation of hummocky topography where water accumulates in the depressions on the debris surface (Reynolds, 2000). Identifying areas of supraglacial water bodies is important for determining the state of a debris-covered glacier. Over decadal timescales, increasing supraglacial ponds can suggest build up of debris cover and a lowering of the glacier surface gradient, resulting in a reduction of the driving stress and hence glacier stagnation (Quincey et al., 2009a; Wessels et al., 2002). In the case of this study, it is likely that increased pond number and area are responses to temporal variation in climatic conditions, specifically an increase in precipitation since 2000, which was also attributed to increasing surface velocity in 2005 (Quincey et al., 2009b). Such water bodies increase the local glacier ablation rate through increased absorption of incoming shortwave radiation (Sakai et al., 2002). Ice cliffs are often concomitant with supraglacial ponds, and are a focus for a large proportion of a

debris-covered glacier's net ablation (Juen et al., 2014; Reid and Brock, 2014; Sakai et al., 1998). Identifying the number of supraglacial ponds is therefore integral to understanding the controls on the ablation rate of a debris-covered glacier and the relative importance of these controls over time as the debris cover evolves. Although conditions may not be entirely comparable, a similar increase in pond number and area on Khumbu Glacier was thought to be a result of a period of recession following a period of heightened activity during the middle part of last decade (Quincey et al., 2009b), and similar conditions could also be true for Baltoro Glacier, but would need further investigation of variations in past surface velocity and mass balance.

Table 6.2: The total area and number of supraglacial water bodies identified using an NDVI index for each time step between 2001 and 2012.

	2001	**2004**	**2012**
Number of water bodies	234	404	570
Area (km^2)	0.66	1.79	2.04

6.6.3. Areas of mass movement

Mass movement scars and deposits are visible along most of the tributary and main glacier margins, with an increasing number appearing between 2001 and 2012, particularly between 2001 and 2004. An increasing number of mass movement events may be related to a higher frequency of seismic activity or increased precipitation between 2001 and 2004 (Barnard et al., 2001; Bookhagen et al., 2005). The most evident mass movement deposits in the Baltoro Glacier system are found on TGs 4 and 5 (Inset B, main map, p. 155). Two mass movement deposits on TG5 and a series of smaller but more frequent protrusions on TG4 are interpreted as being sourced from intermittent mass movement events. The mounds of debris have then been transported with glacier flow to the north, at a rate of ~20 m a^{-1} (calculated from the distance the deposits have travelled between images, divided by the number of years between images). These periodic events, occurring on sub-decadal to decadal timescales, deliver an additional source of

supraglacial debris to the glacier system, which are subsequently dissipated and result in thickening of the debris layer.

6.6.4. Tributary glacier convergence

In addition to Godwin-Austen and Baltoro South Glaciers, 12 tributary glaciers flow into the main tongue of Baltoro Glacier (Tributary Glacier inset, main map, p. 155). These tributary glaciers, flowing perpendicular to the main tongue, have spatially and temporally varying covers of supraglacial debris, which affects the distribution of debris onto the main glacier tongue. TG 4 in Inset B (main map, p. 155) is predominantly debris free, with the exception of two longitudinal schistose debris bands. A series of supraglacial ponds have developed on the main glacier tongue to the east of the two debris bands on TG 4 between 2001 and 2012. Pond development also occurs on TG 3 and on the glacier surface below Concordia, where TGs 1 and 2 converge. Pond development in the convergence area below Concordia is likely due to the same process as found on clean ice glaciers where water ponding occurs in surface depressions (Banwell et al., 2012). For TGs 3 and 4, the formation of the water bodies is likely due to a constriction of the main glacier tongue causing an undulant surface topography. These constrictions in glacier flow also manifested in debris thickening in the same areas, observed on the debris thickness map of Baltoro Glacier produced by Minora et al. (2015). TG 8, flowing southeast into the terminus of Baltoro Glacier, is unique in the Baltoro Glacier system, as no obvious extensive debris cover is identifiable on its surface in satellite imagery. The lack of debris cover is attributed to its steep surface slope and high velocities likely to be associated with this, resulting in little time for debris to accumulate on the surface, as well as its relatively short length in comparison to all other tributary glaciers in the system, reducing the valley side area from which debris can be supplied (Young and Hewitt, 1993).

6.6.5. Dynamic tributary glaciers

The schistose debris unit on Liligo Glacier (TG 7, Inset C, main map) shows an apparent advance and subsequent retreat of the schistose debris unit extent between 2001 and 2004 and 2004 and 2012, respectively. However, retreat of the debris unit is unlikely, as movement of rock debris upslope would have had to occur. Therefore, the changes in

debris unit boundary between 2001 and 2012 are attributed to dissipation and reorganisation of the debris, as the surface morphology changes following the active surge phase of Liligo Glacier between 1973 and 2001 (Belò et al., 2008; Diolaiuti et al., 2003). The distribution of the debris unit succeeds the ultimate advance of the glacier, likely to result from slumping of the debris into the depression in the proglacial area as the tributary glacier commences its quiescent phase and decouples from the main Baltoro Glacier tongue. The associated supraglacial pond identified by Belò et al. (2008) in 2001 persists until 2004, but had drained by 2012, likely due to downwasting of ice and redistribution of the debris in the area between Liligo Glacier and Baltoro Glacier. Changes in surface morphology associated with pond drainage may have also contributed to the shift in debris unit boundary.

Geomorphological features present on TG 12 (Inset A, main map, p. 159) also suggest that a dynamic period, such as a surge event, has occurred recently and that the glacier is now in a quiescent phase. This tributary glacier has not been documented to surge previously. The sinuous nature of the debris unit margins at the confluence of TGs 12 and 13, and the development of a fold-type structure on the eastern schistose debris unit ~1 km from the convergence of these glaciers (Figure 6.3), are both evidence for a possible surge event, where TG 13 would have accelerated and its terminus advanced, folding the debris units downglacier from this confluence, analogous to folding of the debris bands on Susitna Glacier, Alaska (Meier and Post, 1969). Additional evidence for the occurrence of a possible surge event include heavy crevassing of the TG 13, up-glacier from the main fold in the schistose debris unit, while the area below the folded schist units are heavily ponded with a hummocky surface, suggesting downwasting of the ice below the surge front as the glacier recedes following a surge event (Evans and Rea, 1999).

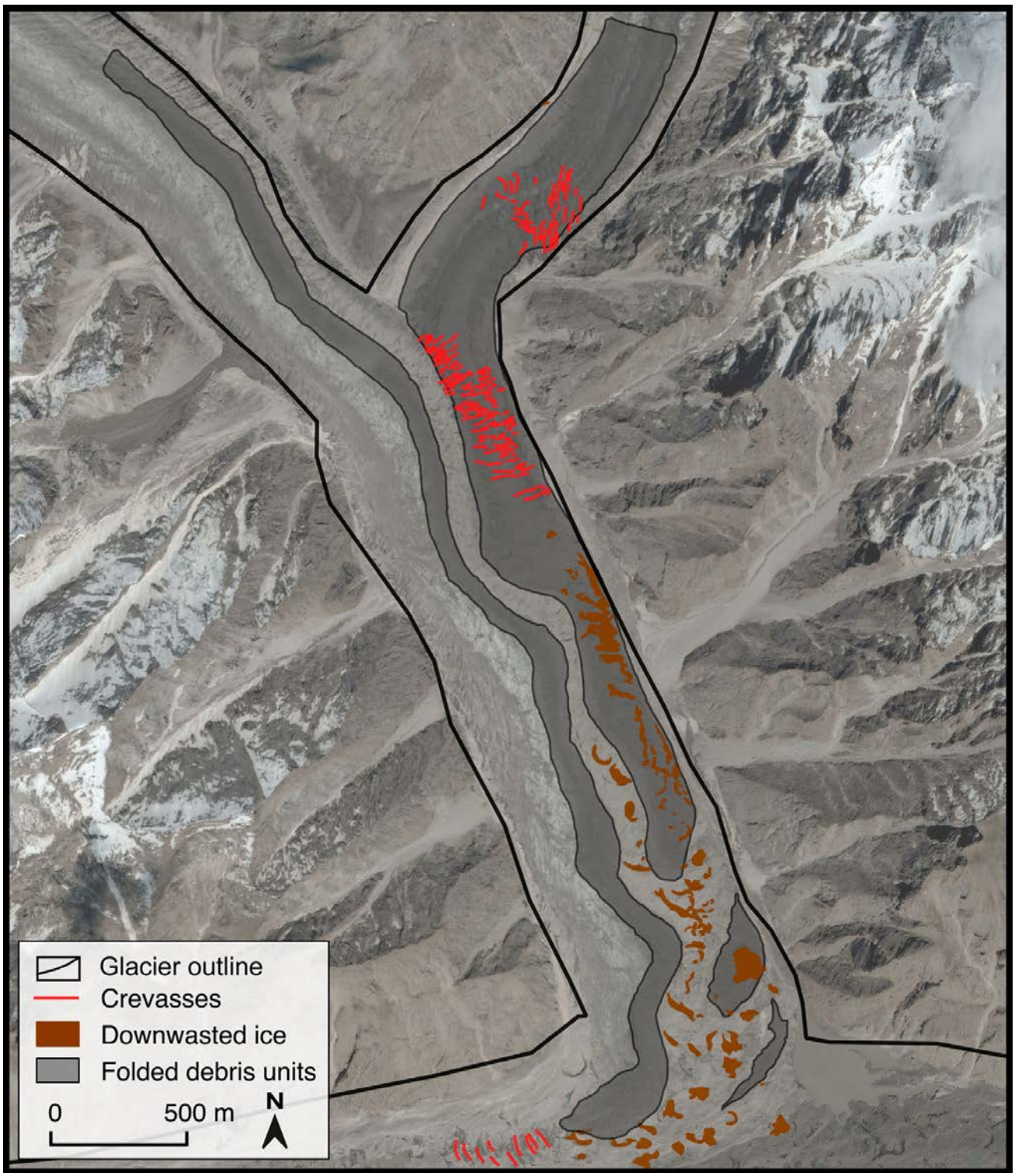

Figure 6.3: The geomorphological features on Baltoro Glacier's tributary glacier showing evidence of a possible surge event (Google Earth, 2016). Glacier outline reproduced from Randolph Glacier Inventory (v. 5.0; Arendt et al., 2012) .

6.7. Conclusions

Supraglacial debris units were segregated into four lithologies, with each debris type, particularly metasediments, being composed of different minerals that would cause them to have different thermal capacities and albedo. Supraglacial cover varies both spatially and temporally on Baltoro Glacier. Temporal variations in supraglacial pond number and area are attributed to climatic conditions in this study, but should be monitored in the future on Baltoro Glacier to determine whether this trend continues and if it is linked to other aspects of glacier dynamics. Debris distribution is controlled by the input of material from frequent rockfalls in the upper reaches of the glaciers up-glacier of Concordia, subsequently entrained into medial and lateral moraines. Larger and less frequent mass movement events in the ablation area add additional debris to the system and occur on sub-decadal to decadal timescales. Once debris has entered the glacial system, variability in its distribution is controlled by the interaction of flow units between tributary glaciers and the main Baltoro Glacier, complicated by the advance and recession of tributary glacier termini due to surge events. The changes in debris unit areas between 2001 and 2012 are attributed to error in identification of debris-covered pixels in the analysis of remotely sensed data, as the difference in glacier area is near to the assumed error value and so may due to error in manual digitisation. However, it is likely that variations in debris distribution do occur through time due to variations in glacier dynamics and input of debris to the glacier system.

Consequently, analyses of variations in debris distribution over longer timescales are needed as spatial variation in debris unit lithology and layer thickness will affect the energy balance of the supraglacial debris layer, which would cause spatio-temporal variation in glacier ablation. It is therefore appropriate to undertake further investigations into rates of change in supraglacial debris distribution and debris thickness through time, as well as to determine the influence of debris lithology on heat transfer and subsequent ablation of underlying ice. Such spatial and temporal variations could then be incorporated into glacier surface energy balance modelling to refine subsequent calculations of ablation rates for debris-covered glaciers, to aid in determining the role of a supraglacial debris layer in the response of these glaciers to climate change.

Figure 6.4 (overleaf): Geomorphological map displaying the supraglacial debris units and associated surface features of Baltoro Glacier, Karakoram in 2012, with insets of changes in geomorphological features between 2001 and 2012.

Chapter 7: Paper III

Title: Temporal variations in supraglacial debris distribution on Baltoro Glacier, Karakoram.

Journal: Geomorphology

Current status: Published on 9th August 2017

Gibson MJ, Glasser NF, Quincey DJ, Rowan AV, Irvine-Fynn TDL, Mayer C. 2017. Variations in debris distribution on Baltoro Glacier, Karakoram, North Pakistan. *Geomorphology* 295, 572–585.

7. Temporal variations in supraglacial debris distribution on Baltoro Glacier, Karakoram, between 2001 and 2012

7.1. Abstract

Distribution of supraglacial debris in a glacier system varies spatially and temporally due to differing rates of debris input, transport and deposition. Supraglacial debris distribution governs the thickness of a supraglacial debris layer, an important control on the amount of ablation that occurs under such a debris layer. Characterising supraglacial debris layer thickness on a glacier is therefore key to calculating ablation across a glacier surface. The spatial pattern of debris thickness on Baltoro Glacier has previously been calculated for one discrete point in time (2004) using satellite thermal data and an empirically based relationship between supraglacial debris layer thickness and debris surface temperature identified in the field. Here, the same empirically based relationship was applied to two further datasets (2001, 2012) to calculate debris layer thickness across Baltoro Glacier for three discrete points over an 11-year period (2001, 2004, 2012). Surface velocity and sediment flux were also calculated, as well as debris thickness change between periods. Using these outputs, alongside geomorphological maps of Baltoro Glacier produced for 2001, 2004 and 2012, spatiotemporal changes in debris distribution over a sub-decadal timescale were investigated. Supraglaclacial sediment flux remained constant throughout the 11-year period. The greatest changes in debris thickness occurred along medial moraines, the locations of mass movement deposition and areas of interaction between tributary glaciers and the main glacier tongue. The study confirms the occurrence of spatiotemporal changes in supraglacial debris layer thickness on sub-decadal timescales, independent of variation in surface velocity. Instead, variation in rates of debris distribution are primarily attributed to frequency and magnitude of mass movement events over decadal timescales, with climate, regional uplift and erosion rates expected to control debris inputs over centurial to millennial timescales. Inclusion of such spatiotemporal variations in debris thickness in distributed surface energy balance models would increase the accuracy of calculated ablation, leading to a more accurate simulation of glacier mass balance through time, and greater precision in quantification of the response of debris-covered glaciers to climatic change.

7.2. Introduction

Debris-covered glaciers are commonly found in tectonically-active mountain ranges including the Andes, the Southern Alps of New Zealand and the Himalaya-Karakoram (Kirkbride and Warren, 1999; Scherler et al., 2011). High rates of rock uplift and erosion and steep hillslopes in these regions cause large volumes of rock debris to be incorporated into glacier systems, and ultimately form supraglacial debris layers of varying thicknesses and extents (Anderson and Anderson, 2016; Shroder et al., 2000). The presence of a supraglacial debris layer affects ablation of the underlying ice (Evatt et al., 2015; Østrem, 1959), because the debris acts as a thermal buffer between ice and atmosphere, ultimately resulting in a non-linear response of debris-covered glaciers to climate change (Benn et al., 2012; Scherler et al., 2011). Glaciers in the Himalaya-Karakoram supply water to some of the largest rivers in the world, including the Indus, Brahmaputra and Ganges (Bolch et al., 2012). Consequently, the response of glaciers in the Himalaya-Karakoram to recent and current climate change will affect the lives of the 1.4 billion people in central Asia who rely on these rivers as their primary water resource (Immerzeel et al., 2010).

Given that the proportion of debris-covered glacier ice area in the Himalaya-Karakoram region is increasing (Deline, 2005; Mihalcea et al., 2006), gaining a full understanding of the influence of debris layers on melt-rates is becoming increasingly pertinent. Typically, supraglacial debris is initially entrained into lateral and medial moraines in the upper reaches of the glacier. As moraines coalesce with increasing distance from their source the debris layer becomes more spatially extensive (Anderson, 2000; Kirkbride and Deline, 2013). The thickness of the supraglacial debris layer increases down-glacier and reaches its maximum near the glacier terminus (Anderson, 2000). In areas where supraglacial debris cover extends across the entire glacier surface, spatially variable debris distribution results in differential melting and forms an undulating glacier surface topography (Hambrey et al., 2008; Kirkbride and Deline, 2013). Supraglacial debris thickness varies in space and time as a result of differing spatial extents and temporal rates of debris input, transport and exhumation (Rowan et al., 2015). Ablation rates of debris-covered glaciers are therefore also spatially and temporally variable (Benn et al., 2012; Reid et al., 2012; Fyffe et al., 2014; Rounce and McKinney, 2014). Studies that consider the response of debris-covered glaciers to climate change currently do not

account for this variability (e.g. Bolch et al., 2012; Scherler et al., 2011; Shea et al., 2015), which increases the uncertainty in estimations of glacier ablation rates, and thus the subsequent predictions of the response of debris-covered glaciers to climate change.

The impact of supraglacial debris layers on melt rates is well established (e.g. Østrem, 1959); thin debris layers (typically <0.05 m thick, depending on local conditions) enhance ablation by increasing albedo of the glacier surface, while thicker debris layer attenuate melt by insulation of the underlying ice (Mihalcea et al., 2008b; Nicholson and Benn, 2006; Østrem, 1959). Ablation is maximized at an effective debris thickness (commonly 0.01–0.02 m), while the critical thickness of debris (typically ranging from 0.02 to 0.1 m), where ablation under debris-covered ice is equal to that of debris-free ice, is defined by debris properties such as lithology, porosity, grain size distribution, moisture content and surface roughness of the debris layer (Brock et al., 2010; Kayastha et al., 2000). The amount of ablation under a debris layer is also affected by external factors such as the transfer rate of precipitation through a debris layer, glacier surface topography, and the occurrence of suprafluvial networks and associated sediment transport processes, all of which are spatially and temporally variable (Seong et al., 2009).

Measuring the thickness distribution of a supraglacial debris layer is challenging in the field due to high spatial variability in debris layer thickness over short distances, difficulties in excavating such debris layers (Mayer et al., 2006), and an inability to capture such variability with point data. Early work put forward the idea of using thermal characteristics of supraglacial debris to define its extent from satellite data (Ranzi et al., 2004). Subsequent projects developed the use of such thermal satellite data to estimate debris thickness for entire glacier surfaces; a glacier-specific relationship between surface temperature and debris thickness is identified using field point data, which is subsequently applied to satellite-derived thermal data of the entire glacier area (e.g. Foster et al., 2012; Rounce and McKinney, 2014; Mihalcea et al., 2008a; Mihalcea et al., 2008b; Soncini et al., 2016). These maps have advanced understanding of spatial variability in debris thickness, but usually only represent a discrete point in time. Minora et al. (2015) enabled the observation of temporal changes in debris thickness by producing a second debris thickness map of Baltoro Glacier for 2011, in addition to the one produced by Mihalcea et al. (2008b) for 2004. However, Minora et al. (2015) did not

explore the extent of debris thickness change between the two periods. Consequently, little is known about the rate at which changes in supraglacial debris layer thickness occur, an essential parameter for understanding the transport of debris by ice flow and the localised redistribution of the debris over a glacier surface, which can be used to validate precise numerical modelling of the dynamics of debris-covered glaciers through time (e.g. Anderson and Anderson, 2016; Rowan et al., 2015).

In this study, we investigated supraglacial debris on Baltoro Glacier in Pakistan to: (1) identify the spatiotemporal variation in supraglacial debris distribution on Baltoro Glacier between 2001 and 2012; (2) consider some of the processes that control these variations in debris distribution using surface velocity and geomorphological mapping; and (3) calculate annual rates of debris thickness change and supraglacial sediment flux (hereafter referred to as sediment flux) on Baltoro Glacier using debris thickness and surface velocity maps and (4) to consider the validity of such debris thickness maps through comparison with geomorphological analysis. We subsequently comment on how such calculations can be used in numerical models for glaciers.

7.3. Study area

Baltoro Glacier is located in the eastern Karakoram mountain range in northern Pakistan (35°35' N, 76°04' E; Figure 7.1). The glacier is 62 km long and flows from near the peak of K2 (8611 m above sea level (a.s.l.)) to an altitude of 3410 m a.s.l. (Mayer et al., 2006; Mihalcea et al., 2008b) (Figure 7.1a). A number of tributary glaciers feed Baltoro Glacier (Figure 7.1b), including Baltoro South and Godwin-Austen Glaciers, which converge to form the main Baltoro Glacier tongue at Concordia (4600 m a.s.l.). The surface velocity of Baltoro Glacier varies along its length, with a maximum surface velocity of ~200 m a^{-1} below Concordia, decreasing to less than 15 m a^{-1} close to the glacier terminus (Copland et al., 2009; Quincey et al., 2009). Surface velocity was observed to increase in 2005 (Quincey et al., 2009b), attributed to an abundance of meltwater being routed to the bed and thus reducing basal friction.

The ablation area of Baltoro Glacier is almost entirely debris covered. Up-glacier of Concordia, supraglacial debris is predominantly entrained into medial and lateral moraines that punctuate the clean ice surface, with a lesser contribution of mass movement deposits along the glacier margins (Mihalcea et al., 2006). The debris layer is thinnest (0.01–0.15 m) in the upper ablation area of the glacier and exceeds 1 m at the glacier terminus (Mihalcea et al., 2008b). Supraglacial debris units have differing lithologies across the debris-covered glacier surface, which include granite, schist, gneiss and metasediments (Gibson et al., 2016).

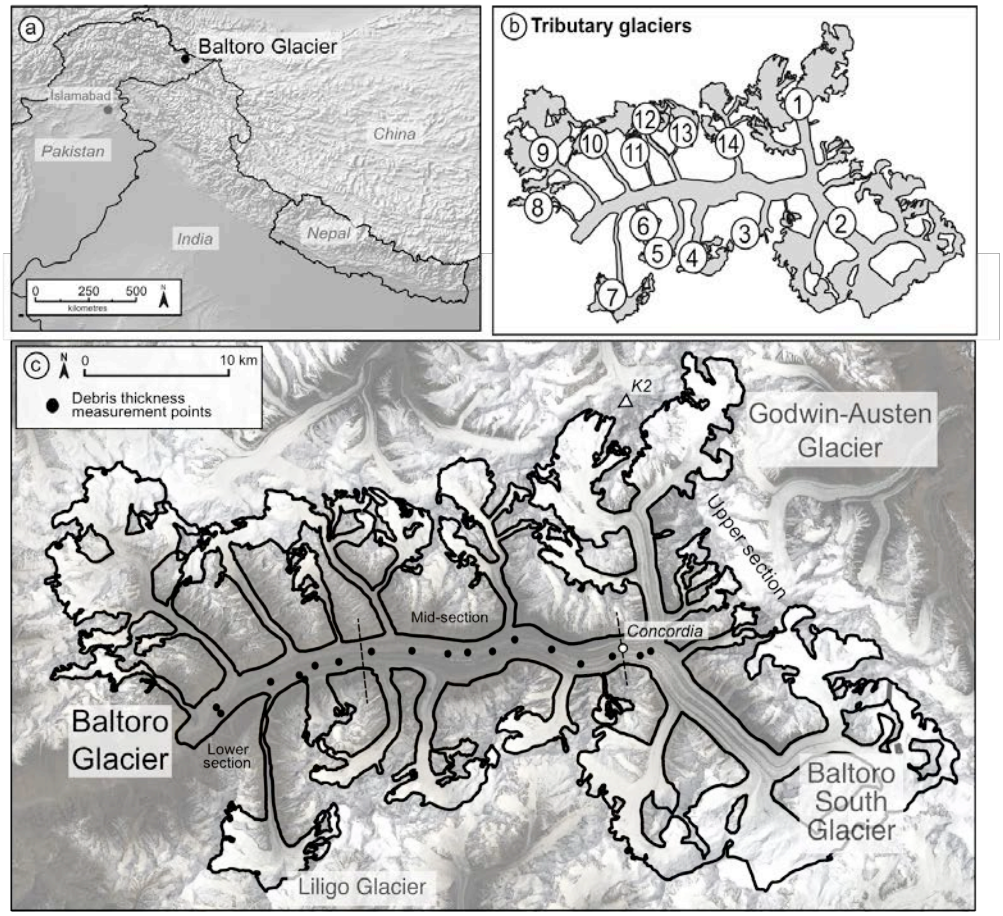

Figure 7.1. (a) Baltoro Glacier in a regional context; (b) the tributary glaciers of Baltoro Glacier (numbered) and (c) Baltoro Glacier and its tributary glaciers.

7.4. Methods

7.4.1. Debris thickness

Advanced Spaceborne Thermal Emission and Reflection Radiometer (ASTER) thermal data were used to derive debris thickness on Baltoro Glacier for three discrete periods in time; 2001, 2004 and 2012 (Table 7.1). The 2004 dataset used was the same as that used by Mihalcea et al. (2008b) for production of their 2004 debris thickness map of Baltoro Glacier. The 2001 and 2012 data sets were chosen due to their low cloud cover, resulting in minimal glacier area being obscured. ASTER imagery was downloaded from NASA's Earth Observing System Data and Information System (http://reverb.echo.nasa.gov) as a Level 2 surface kinetic temperature product (AST_08). Level 2 surface kinetic temperature data are comprised of mean surface temperature calculated from thermal bands 11–15. Prior to delivery, surface kinetic temperature data are atmospherically corrected and converted from top-of-atmosphere temperature to surface temperature. ASTER thermal data have a spatial resolution of 90 m and temperature resolution of 0.5°C (Abrams and Ramachandran, 2002). All outputs were co-registered to within a pixel through manual placement of 50 tie points between each image pair prior to calculation of debris thickness, to avoid any spatial mismatch between the input layers. The images were also orthorectified using the rigorous orthorectification tool in ENVI (v. 5.0) and the ASTER digital elevation model (2011) at 30 m resolution, which corrects for the effect of sensor tilt and terrain, and produced an RMSE of 5.82 m. Debris thickness was derived using the methods detailed in Mihalcea et al. (2008b). Equation 7.1 was applied to the same satellite image used by Mihalcea et al. (2008b) to yield debris thickness for 2004:

$$DT = exp\,(0.0192\,T_{ST}) - 58.7174 \qquad (7.1)$$

Where DT is debris thickness, calculated in mm, and T_{ST} is surface temperature in Kelvin. DT is subsequently converted to metres. The same method was then applied to the 2001 and 2012 ASTER data for Baltoro Glacier to yield a timeseries of debris thickness maps.

Table 7.1. Satellite ID, acquisition date and time and mean debris thickness for ASTER datasets used for calculating debris thickness (grey boxes) and surface velocity.

Satellite data I.D.	Acquisition date and time	Mean debris thickness (m)
AST_08_00308292001060003 _20140108123858_15605	29/08/2001 06:00	0.14
AST_08_00310032002055404 _20151109052624_814	03/09/2002 05:54	
AST_08_00308142004054614 _20151109052424_30691	14/08/2004 05:46	0.21
AST_08_00310122008054700 _20151109052644_888	12/09/2008 05:47	
AST_08_00305052011055248 _20151109052354_30515	05/09/2011 05:52	
AST_08_00308202012054630 _20151109052624_816	20/08/2012 05:46	0.45

Debris thickness change was calculated between the 2001–2004 and 2004–2012 debris thickness maps. In both cases the earlier debris thickness map was subtracted from the later map to yield debris thickness change for each time period, and then divided by the number of years between the two maps to calculate mean annual debris thickness change.

Uncertainty in the calculated debris thickness was estimated for the 2012 debris thickness map using field debris thickness measurements collected in 2013 (Figure 7.1c). Mean annual debris thickness change calculated from the 2004–2012 debris change map (0.03 m a^{-1}) was added to the 2012 debris thickness to provide projected debris thickness for 2013. To calculate uncertainty the 17 field-derived debris thickness point

measurements were compared to debris thicknesses from the corresponding pixels in the projected 2013 debris thickness map (Table 7.2). Mean variation in debris thickness between 2013 field data and projected 2013 debris thickness was 0.090 m, 0.064 m above the uncertainty calculated for the 2004 debris thickness map by Mihalcea et al. (2008b) of 0.026 m. Consequently, in this study uncertainties for the debris thickness maps were estimated as 0.026 m for 2004 and 0.090 m for 2012. Uncertainty for the 2001 debris thickness map could not be calculated due to a lack of field data collected prior to 2004. Additional parameters such as moisture content in and thermal inertia of the debris layer may have also affected estimations of supraglacial debris layer thickness calculated using Mihalcea et al.'s (2008b) method, but the low uncertainty values calculated here suggest they have minimal effect on the outputs presented.

Due to a lack of field data in debris layers with a thickness greater than 0.5 m uncertainty values calculated here are only applicable for debris layers with a thickness ≤0.5 m. Above 0.5 m debris surface temperature is considered independent of debris layer thickness (Nicholson and Benn, 2006). Consequently, analysis of these debris thickness maps is focused on areas of the glacier where debris thickness is ≤0.5 m, and are presented alongside geomorphological evidence for justification.

An additional source of uncertainty in the debris thickness maps arises from applying an empirical relationship between T_{ST} and DT calculated at a single point in time to a series of data collected in different years and at different seasonal periods. This uncertainty is due to differences in the energy balance at the supraglacial debris surface between data collection as a result of varying meteorological conditions, such as solar radiation budget and air temperature, which cause temporal variance in T_{ST}, and differences in supraglacial debris properties, such as moisture content of the debris layer, which affects the transfer of thermal energy through the debris layer (previously discussed in Chapter 5). The thermal satellite data used here were all collected in different years, but the 2001 and 2012 ASTER datasets were both acquired within 15 days of the original 2004 dataset. Whilst there was therefore a minimal difference in time of year at which the data were acquired, uncertainty still exists due to anticipated differences in meteorological conditions a the time of data acquisition, and variations in seasonal conditions from year to year. To address this uncertainty the results of the debris thickness maps are

compared to visual satellite imagery and geomorphological maps, in order to provide evidence for any changes in supraglacial debris layer thicknesses between years.

Table 7.2. Comparison of field point debris thickness data to corresponding pixel value (plus one year's annual rate of debris thickness change), used to calculate error between the 2012 satellite-derived debris thickness map and field data.

Point I.D.	2013 *in situ* debris thickness (m)	2013 satellite-derived debris thickness (m)	Difference (m)
1	0.02	0.01	0.01
2	0.00	0.07	0.07
3	0.09	0.23	0.14
4	0.13	0.15	0.02
5	0.01	0.04	0.03
6	0.06	0.03	0.03
7	0.04	0.02	0.02
8	0.05	0.14	0.09
9	0.075	0.02	0.05
10	0.04	0.23	0.19
11	0.12	0.39	0.27
12	0.07	0.18	0.11
13	0.17	0.06	0.11
14	0.04	0.14	0.10
15	0.26	0.28	0.02
16	0.1	0.01	0.09
17	0.43	1.16	0.73
		Mean difference:	0.09
		Standard deviation:	0.50

7.4.2. Glacier dynamics and surface morphology

7.4.2.1. Surface velocity analysis

Glacier surface velocity analysis was undertaken in ENVI (v.5.0) using the feature tracking plugin tool Cosi-Corr (Leprince et al., 2007). Cosi-Corr is a Fourier-based image correlation tool that offers sub-pixel accuracy for the measurement of horizontal offsets (Scherler et al., 2011). ASTER Band 3N data (Visible Near Infrared, Wavelength: 0.760–0.860 nm, resolution: 15 m) were used for feature tracking. Image pairs used were acquired in 2001 and 2002, 2003 and 2004, and 2011 and 2012 (Table 7.1), and were co-registered to sub-pixel level prior to calculation of surface displacement. All results were converted to annual displacements for comparison. A variable window size between 128 and 64 pixels and a step size of one pixel was used for all velocity outputs, and absolute surface velocity derived from north-south and east-west velocity fields. North-south and east-west velocity fields were used for identification of direction of maximum surface velocity in the calculation of sediment flux. Velocity outputs were masked using a velocity threshold of 200 m a^{-1} to exclude erroneous results in ENVI (v. 5.0), and clipped to the extent of a manually-improved Baltoro Glacier outline based on the Randolph Glacier Inventory outline (v. 5.0; Arendt et al., 2012), used in Gibson et al. (2016) in ArcMap (v.10.1). Pixels with erroneous surface velocity values (less than zero or above 200 m a^{-1}, or pixels with substantially different velocity values to the surrounding pixels) were masked from the final surface velocity maps.

7.4.2.2. Geomorphological mapping

Geomorphological features on the surface of Baltoro Glacier, including debris units, mass movement deposits, supraglacial water bodies and crevasses, were mapped using the optical bands (15 m resolution) of the same three time-separated and orthorectified ASTER data sets used for deriving debris thickness (August 2001, 2004 and 2012). ASTER images were orthorectified using the ASTER digital elevation model at 30 m resolution. Additionally, a Landsat 7 Enhanced Thematic Mapper (ETM+) image, acquired in August 2001 at 30 m resolution, was used to map regions of the glacier covered in cloud in the ASTER August 2001 imagery. All satellite datasets used were co-registered prior to mapping. Features were mapped using a false-colour composite (Bands 3N, 2, 1) and were manually digitised in ESRI ArcGIS (v. 10.1). Debris units were classified using their

differing spectral reflectance profiles (Figure 7.2; Lillesand et al., 2014). The debris units were then traced up-glacier to their source area and lithology identified using the regional geological map produced by Searle et al. (2010). Spectra from 200 pixels were then compared to spectra from the USGS spectral library in ENVI to confirm correct classification. 91% of sampled pixels were correctly classified based on these independent data. Mass movement deposits were identified by the presence of two features: a scar, identified as an elongate feature on the valley side which differed in colour to the surrounding valley wall, suggesting erosion and loss of vegetation had occurred, and an associated lobate debris fan deposit on or near the glacier surface. A Normal Difference Water Index (NDWI) was used to identify pixels containing supraglacial water, calculated from ASTER bands 3 (Near Infrared; NIR) and 4 (Shortwave Infrared: SWIR) after Gao (1996):

$$NDWI = (NIR\ (Band\ 3) - SWIR\ (Band\ 4))/\ (NIR\ (Band\ 3) + SWIR\ (Band\ 4)) \quad (7.2)$$

The classification of water was verified through manual comparison of 100 randomly selected features classified as water in the 2011 ASTER imagery with high resolution (2.5 m) Quickbird imagery from 2011 for the same locations. All 100 features were identified as water in both images, and so were assumed to be correctly classified. The area of debris units and supraglacial water bodies were derived using the geometry calculator in ArcGIS (v.10.1).

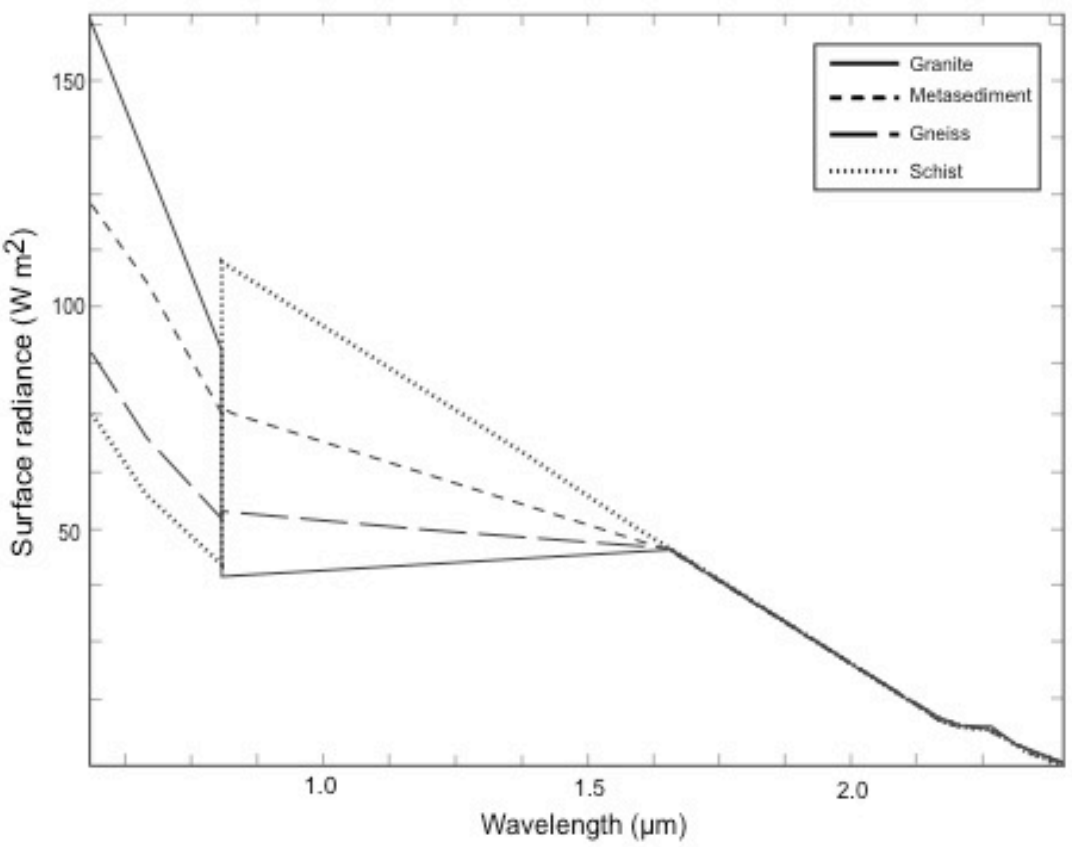

Figure 7.2: Spectral reflectance profiles for the different lithology types identified on Baltoro Glacier.

7.4.3. Sediment flux

Supraglacial sediment flux across the glacier surface was calculated using derived debris thickness and surface velocity data, following the method developed by Heimsath and McGlynn (2008) to determine headwall retreat rate on Milarepa's Glacier in Nepal. Heimsath and McGlynn (2008) measured debris thickness and surface velocity along one transect near the glacier headwall, then calculated cross-sectional area of the debris using the debris thickness transect, and multiplied the cross-sectional area by surface velocity, calculating one-dimensional sediment flux. Here, we calculated supraglacial sediment flux for each pixel by multiplying debris thickness by the pixel width at right angles to the direction of maximum surface velocity to give supraglacial debris layer cross-sectional area, and then multiplied cross-sectional area by surface velocity for the same pixel. As surface velocity and supraglacial debris thickness were used to calculate sediment flux these results only represent debris transported supraglacially. The resulting sediment

flux maps were normalized to annual datasets to obtain comparable sediment flux values, and were masked using the same masks applied to the surface velocity and debris thickness maps to exclude pixels with erroneous results and cloud cover.

7.5. Results

7.5.1. Debris thickness

A similar pattern of debris thickness distribution was present in 2001, 2004 and 2012 (Figure 7.3). In the upper section of the glacier above and around Concordia, debris was distributed in alternating bands of thicker debris (around 0.2–0.3 m thick) and thin, sparsely-distributed or non-existent debris layers (≤0.02 m), in a longitudinal pattern parallel to ice flow. Thicker bands of debris originated from the glacier margin, primarily at confluences between tributary glaciers and the main glacier tongue, which were interpreted to be medial moraines. In the glacier mid-section, debris coverage became increasingly spatially extensive with decreasing distance from the glacier tongue, and a general thickening of debris towards the glacier terminus occurred. No build up of debris, such as that expected where a terminal moraine is present, was observed at the glacier terminus from satellite data, confirming the absence of such a feature previously observed in the field by Desio (1954). Debris covered the entire glacier surface in the lower section of the glacier and was predominantly >0.5 m thick, although due to the uncertainty in debris thicknesses >0.5 m variation in this thickness is not considered.

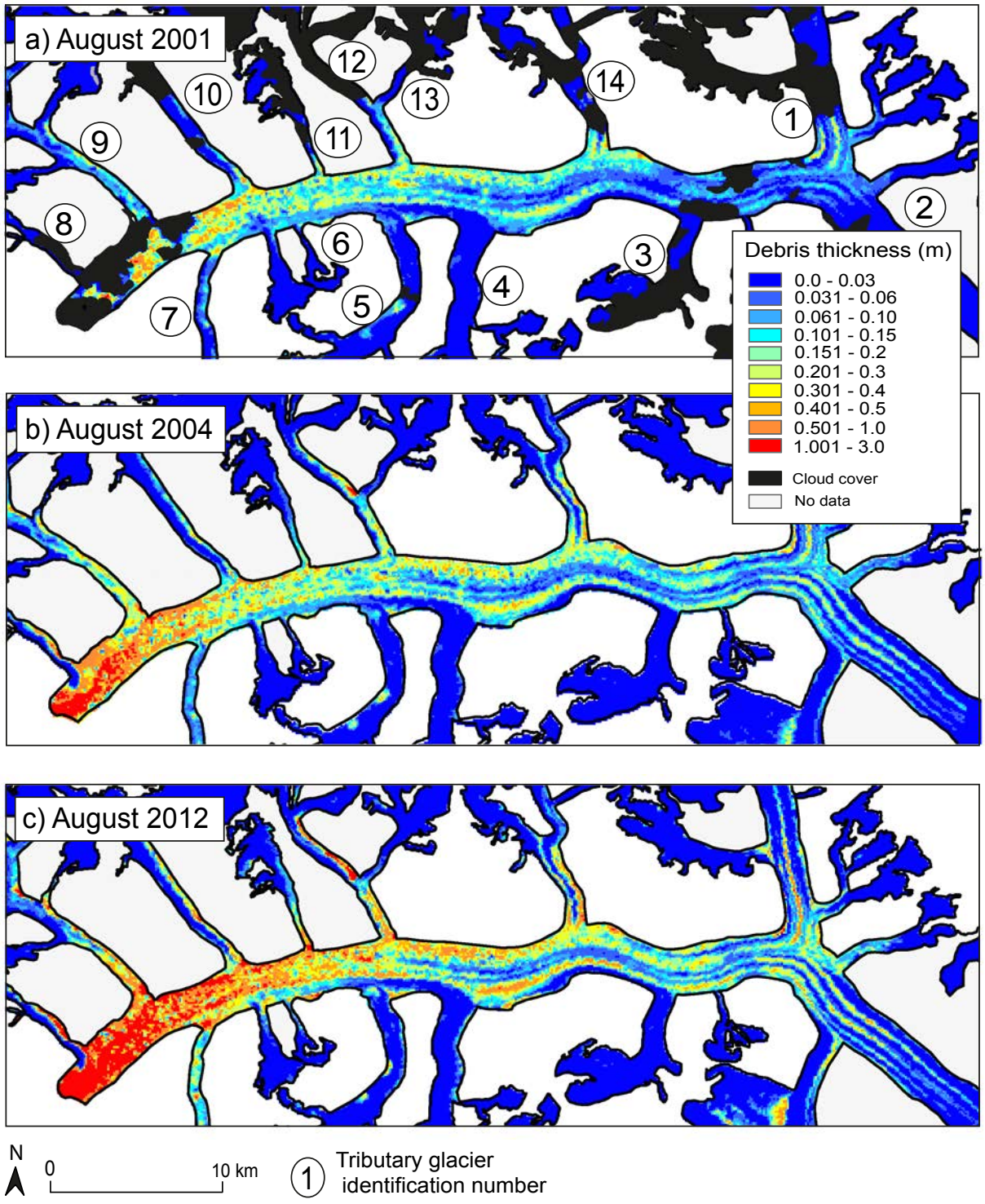

Figure 7.3: Debris thickness maps of Baltoro Glacier for: (a) August 2001; (b) August 2004; (c) August 2012. Areas with a debris thickness >0.5 m are presented but not discussed further due to the large uncertainties involved with using debris surface temperature to derive debris thicknesses greater than 0.5 m thick.

The broad, glacier-wide pattern of debris distribution displayed minimal change between 2001 and 2012, suggesting that a pattern of debris input and transport was already established across the glacier and persisted over the study period. However, the thickness of the debris layers across the glacier varied over the 11-year study period. Cloud cover in 2001 restricted comparison between 2001 and 2004 in the glacier's lower section, but thickening of the medial moraines in the glacier upper-section of the order of around 0.1 m was seen during this 3-year time period. A general trend of increasing debris thickness in the glacier mid-section was seen between 2001 and 2012, with a mean debris layer thickness in the glacier mid-section of ~0.28 m in 2001, ~0.34 m in 2004 and ~0.41 m in 2012. Debris thickness was most variable in the glacier lower section between 2004 and 2012, with a mean debris layer thickness of ~0.71 m in 2004 and ~1.5 m in 2012, and an apparent thickening of debris at the terminus, although further field data would be needed to confirm these mean debris thicknesses due to the independence of debris surface temperature with debris layer thickness above 0.5 m. Increasing debris thickness in the lower and mid sections suggests a progressive backing up of debris through time causing the area of thickest debris to increase up-glacier from the terminus.

In 2004 a sharp boundary between debris layer thicknesses was observed running longitudinally from the glacier terminus to the location at which Trango Glacier (Tributary Glacier 9) joins the main glacier tongue (Figures 7.1b; 7.3). South of the boundary debris thickness was above 0.5 m thick, whilst north of the boundary debris layer thickness was less than 0.5 m thick. The debris thickness boundary correlates with the boundary between a granite debris unit originating on Trango Glacier and gneiss debris units of the main glacier tongue, presumed to also be the boundary between the main glacier flow units and Trango Glacier flow unit.

7.5.2. Glacier surface velocity

A general trend of highest velocity at Concordia, where Baltoro South and Godwin-Austen Glacier converge, and subsequently decreasing surface velocity down-glacier of Concordia towards the terminus was observed at all time periods, with very low (less than 20 m a^{-1}) to no glacier flow near the terminus (Figure 7.4). Variations in surface velocity occurred between 2001 and 2012, with an average decrease in surface velocity of around 50 m a^{-1} along the longitudinal profile of the glacier (Figure 7.4a) between 2001 and 2004, followed by an increase of the same order of magnitude between 2004 and 2012 (Figure 7.4d). Higher surface velocities were observed at Concordia where the Godwin-Austen and Baltoro South Glaciers join, and subtle velocity increases at some but not all tributary glacier confluences were also noted (e.g. Yermanendu and Mandu glaciers; Tributary glaciers 4 and 5, respectively). In 2012 glacier surface velocity was lowest (~0–20 m a^{-1}) in the northwest region of the terminus, a triangular shaped area which extended from the glacier terminus and pinched out at around 5 km up-glacier of the terminus and downstream of Trango Glacier. However, in 2004 no such pattern was evident and a patchy distribution of velocity between 0 and 50 m a^{-1} across the glacier width for around 10 km up-glacier of the terminus occurred.

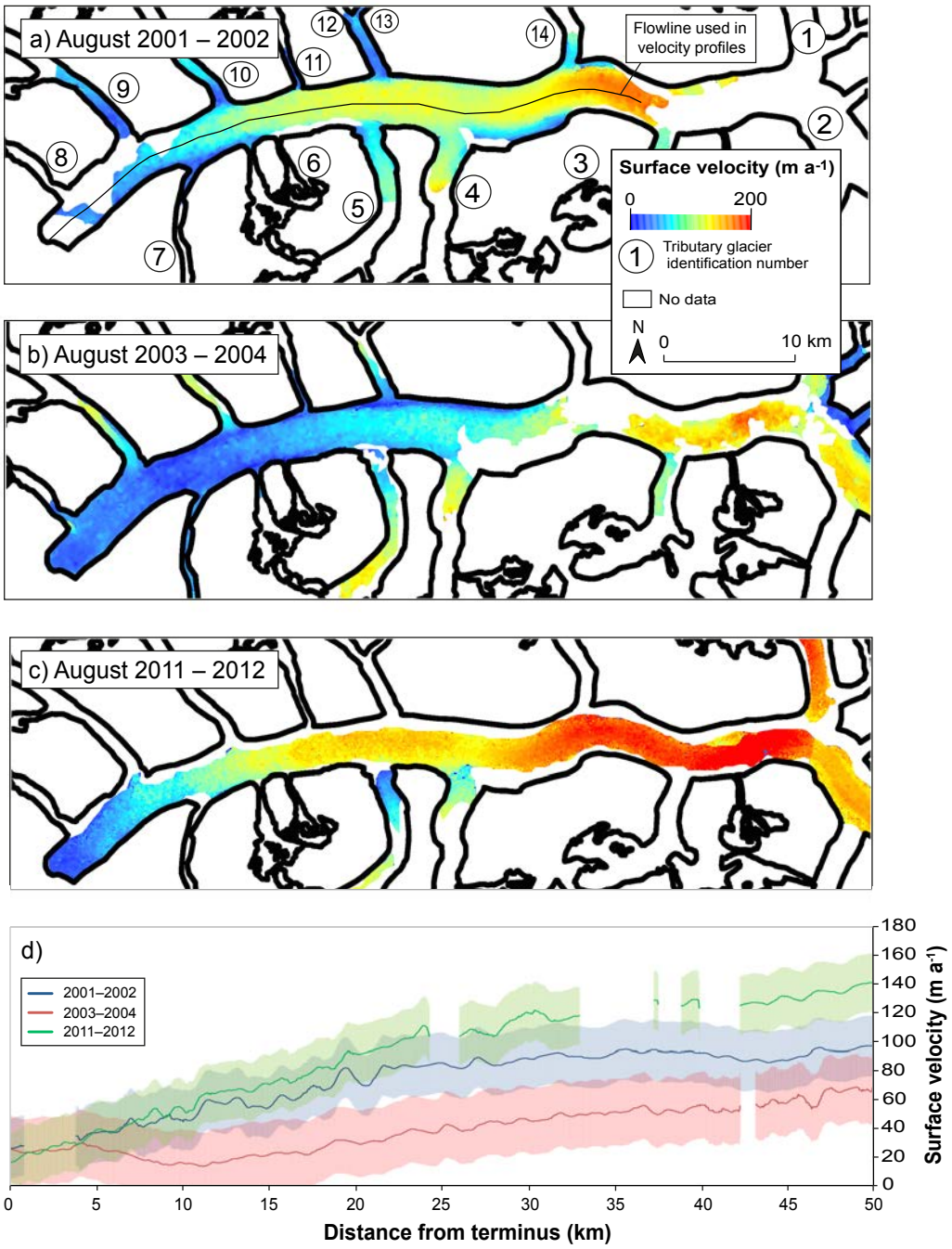

Figure 7.4: Surface velocity maps in m a^{-1} for Baltoro Glacier for: (a) 2001, (b) 2004 and (c) 2012, and (d) surface velocity profiles along the centre line of the main glacier tongue with uncertainty values of each velocity line displayed with shaded regions.

7.5.3. Geomorphological features

Supraglacial debris lithology was identified through comparison of ASTER pixel spectra with spectra of lithologies from the USGS spectral library and with reference to the geology map produced by Searle et al. (2010). The supraglacial debris on Baltoro Glacier was dominated by gneiss (~51–53% of the debris-covered glacier area), whilst ~47–49% was composed of granite (~27%), schist (~12%) and a small proportion of metasediment (~6%) (Figure 7.5, Table 7.3). Across the main glacier tongue, negligible change in debris unit boundaries occurred between 2001 and 2012 and change in percentage cover of debris units was attributed to errors produced by manual digitisations (Gibson et al., 2016; Table 7.3). However, small scale variations in debris distribution did occur on tributary glaciers between 2001 and 2012, which have been attributed to these glaciers being in various periods of instability, possibly related to surge phases, and input of debris material from surrounding valley walls through rock- and snow avalanches (Gibson et al., 2016). For example, patches of thicker debris on Mandu Glacier (Tributary Glacier 5) can be tracked down-glacier between 2001 and 2012 in geomorphological maps (Figure 7.6d) and debris thickness maps (Figure 7.6e), with debris initially deposited on the glacier by a mass movement event and then transported as a bulk volume.

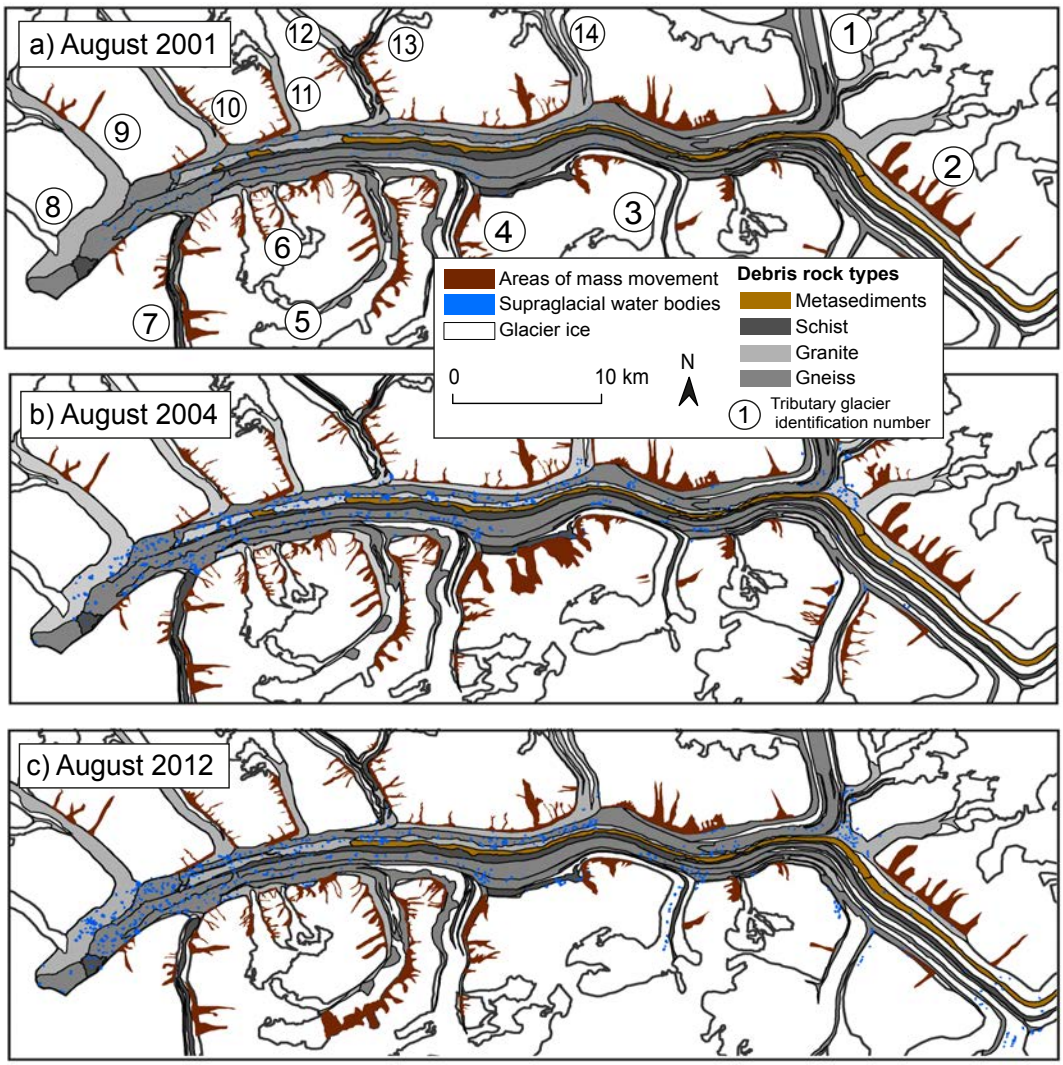

Figure 7.5: The surface geomorphology of Baltoro Glacier in (a) August 2001, (b) August 2004 and (c) August 2012.

Table 7.3. Total area of each debris unit type, based on lithology, for 2001, 2004 and 2012, and the percentage of each debris type as a proportion of the total debris cover for Baltoro Glacier and its tributary glaciers (Gibson et al., 2016). Variability in total debris area is attributed uncertainty produced by manual digitisation.

Year	**2001**	**2001**	**2004**	**2004**	**2012**	**2012**
Debris type	**Area (km^2)**	**% of total debris**	**Area (km^2)**	**% of total debris**	**Area (km^2)**	**% of total debris**
Gneiss	81.48	52.9	79.83	51.2	79.48	52.9
Metasediment	8.60	5.6	11.41	7.3	8.28	5.5
Schist	17.76	11.5	18.54	11.9	17.71	11.8
Granite	46.29	30.0	46.20	29.6	44.71	29.8
Total debris (km^2)	154.1		155.9		150.2	

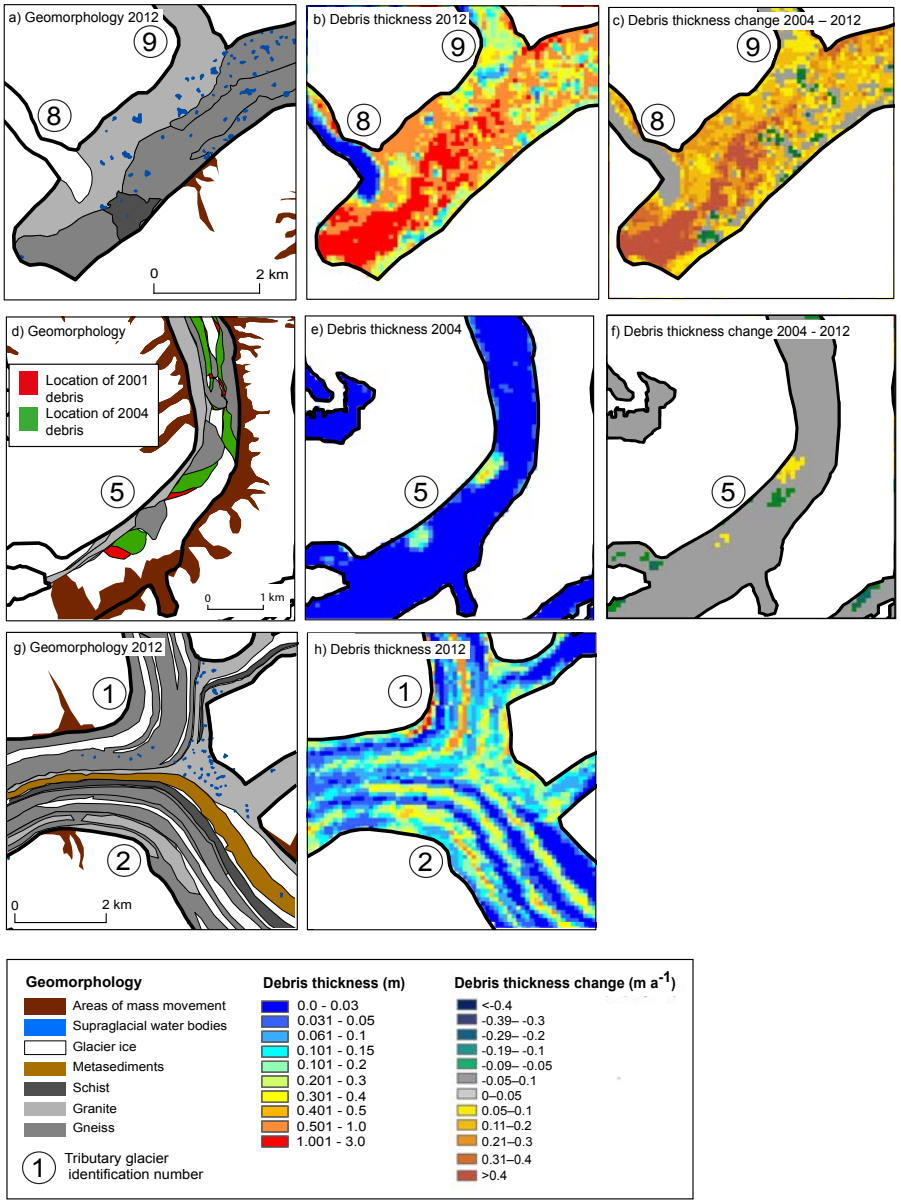

Figure 7.6: Comparison of: (a) geomorphology, (b) debris thickness and, (c) debris thickness change at the terminus of Baltoro Glacier, showing a distinct boundary between debris thickness values and debris units of different lithologies; (d) geomorphology, with previous positions on areas of supraglacial debris from 2001 (red) and 2004 (green) displayed, (e) debris thickness and (f) debris thickness change on Mandu Glacier (Tributary Glacier 5) showing the down-glacier movement of debris pockets through time; (g) geomorphology and (h) debris thickness of the confluence area between Godwin-Austen Glacier and Baltoro South Glacier in 2012, showing an area of thick debris up-glacier of where the tributary glaciers join and change direction to form the main glacier tongue.

Supraglacial water bodies occurred most frequently in the lower to lower-mid-sections of the glacier between 2001 and 2012, and in areas of relatively thick debris, such as east of the confluence between Goodwin-Austen and Baltoro South Glaciers (Figure 7.6g and 7.6h). However, at all time points an absence of supraglacial water bodies was present in the gneiss debris unit at the terminus of the main glacier tongue and around the terminus of Tributary Glacier 8 (unnamed). The number of supraglacial water bodies increased by 336 over the study period, from 234 in 2001 to 570 in 2012 (Table 7.4). Total area of supraglacial water bodies increased by almost 400% during the same period. Temporally, the greatest change in water body number and area occurred between 2001 and 2004, whilst spatially the greatest increase in water body number occurred in the lower mid-section and east of Concordia at up-glacier margin of the confluence between Godwin-Austen and Baltoro South Glacier.

Table 7.4. Supraglacial water area and number on Baltoro Glacier in 2001, 2004 and 2012 (Gibson et al., 2016).

	2001	**2004**	**2012**
Number of water bodies	234	404	570
Area (km^2)	0.66	1.79	2.04

7.5.4. Annual debris thickness change

Mean annual debris thickness change (Figure 7.7) showed areas of debris thickness increase predominantly occurred in the lower section of the glacier and along medial moraines, and were of the order of 0.05 to 0.3 m a^{-1}, greater than uncertainty values for debris thickness maps. In areas of decreasing debris thickness a reduction in thickness of the order of 0.05–0.09 m a^{-1} was observed, with most change occurring between 2001 and 2004, although these areas of decrease were lower than the uncertainty values associated with the debris thickness maps. Such areas of decreasing debris thickness occurred on the northern margin of the main glacier tongue and parallel to debris layer thickening of medial moraines. Debris thickening occurred at a similar rate and pattern in the lower section of the glacier between the two periods, with the greatest increase along

the boundary between the main glacier tongue and Trango Glacier (Section 4.1). During both periods, increase in debris thickness was primarily along the moraine crests in the mid-section of the glacier, with more extensive increases between 2001 and 2004, extending to the glacier upper-section. Debris thickness change on tributary glaciers was of the order of ±0.05 m a^{-1}, with specific areas of debris change apparent, including deposits on Mandu Glacier, considered to have been derived from mass movement events which moved down-glacier through time, revealed through a loss of thickness in their previous position and an increasing debris thickness in the current position (Figure 7.6f).

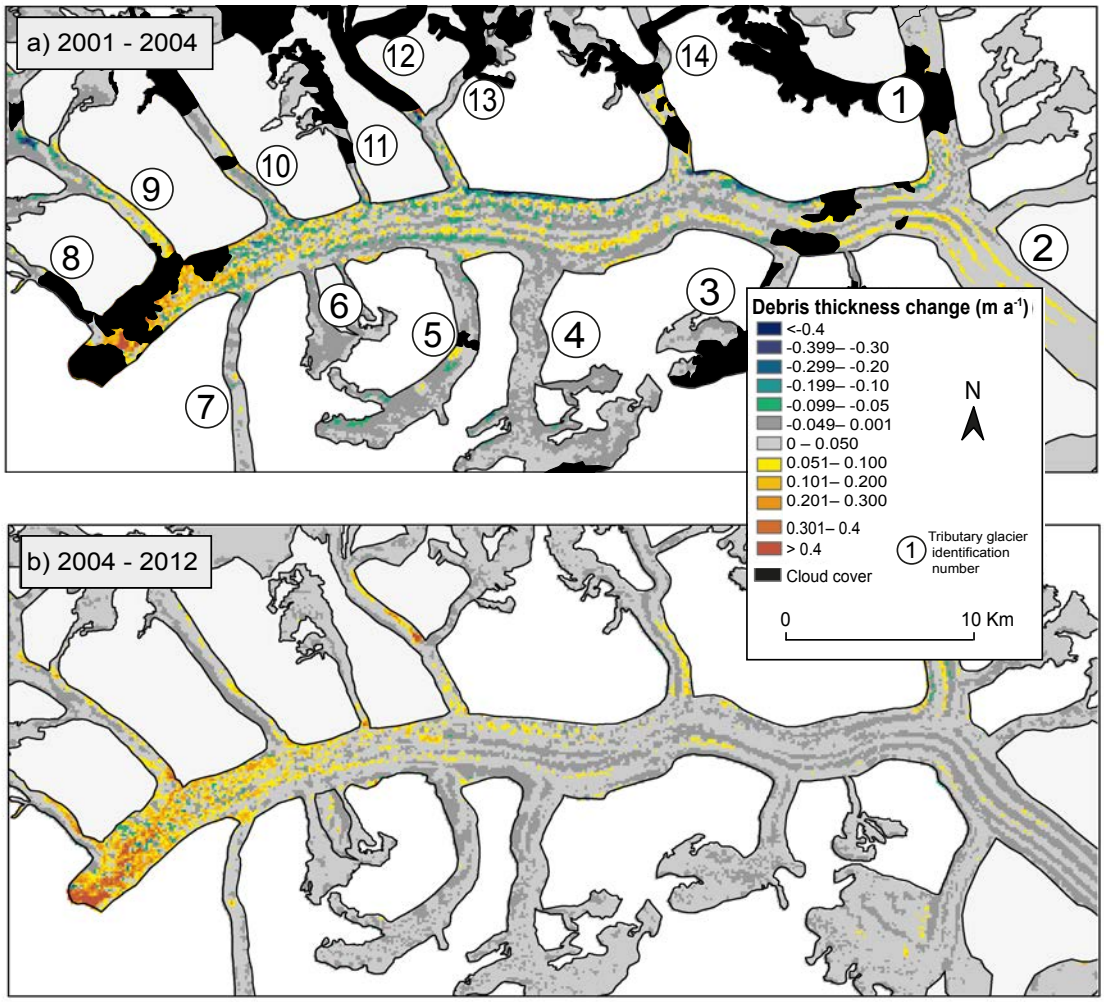

Figure 7.7: Annual debris thickness change, calculated by subtracting the earlier debris thickness map from the later, and then divided by the number of years between the two maps, for (a) 2001 – 2004 and (b) 2004 – 2012. Areas where debris thickness is >0.5 m (see Figure 7.3) are presented but not discussed further due to the large uncertainties involved with using debris surface temperature to derive debris thicknesses greater than 0.5 m thick.

7.5.5. Annual sediment flux

Supraglacial sediment flux (Figure 7.8) showed a similar spatial distribution for all points in time, with the highest sediment flux (between 11000 and 12000 m^3 a^{-1}) in the lower section of the glacier and along the northern glacier margin in the glacier mid-section. Areas of higher sediment flux (>9000 m^3 a^{-1}) were also found at the confluence of tributary glaciers and the main glacier tongue, such as east of Concordia (2003-2004), Yermanendu Glacier (Tributary Glacier 4; 2001-2002) and Tributary Glacier 6 (unnamed; 2001-2002, 2003-2004). For a large proportion of the mid- and upper sections of the glacier, sediment flux was generally less than 1000 m^3 a^{-1}, with some areas of relatively higher sediment flux along moraine features (4000–6000 m^3 a^{-1}).

A general pattern of increasing sediment flux was seen between 2001–2002 and 2011–2012 along medial moraines in the lower section of the glacier, with an increase in sediment flux of the order of between 5000–6000 m^3 a^{-1} between 2001 and 2002 to 6000–8000 m^3 a^{-1} between 2001 and 2012. In the upper-mid and upper-sections of the glacier these medial moraines had a constant sediment flux of around 6000 m^3 a^{-1}. Although the sediment flux maps do not extend to the initiation point of many of the medial moraines where debris is introduced into the upper glacier system, consistency in sediment flux along moraine features suggest input from valley wall erosion and entrainment was stable over the sub-decadal period. In the 2001–2002 and 2003–2004 sediment flux maps pockets of sediment flux less than 1000 m^3 a^{-1} in the lower section of the glacier corresponded to the location of supraglacial water bodies.

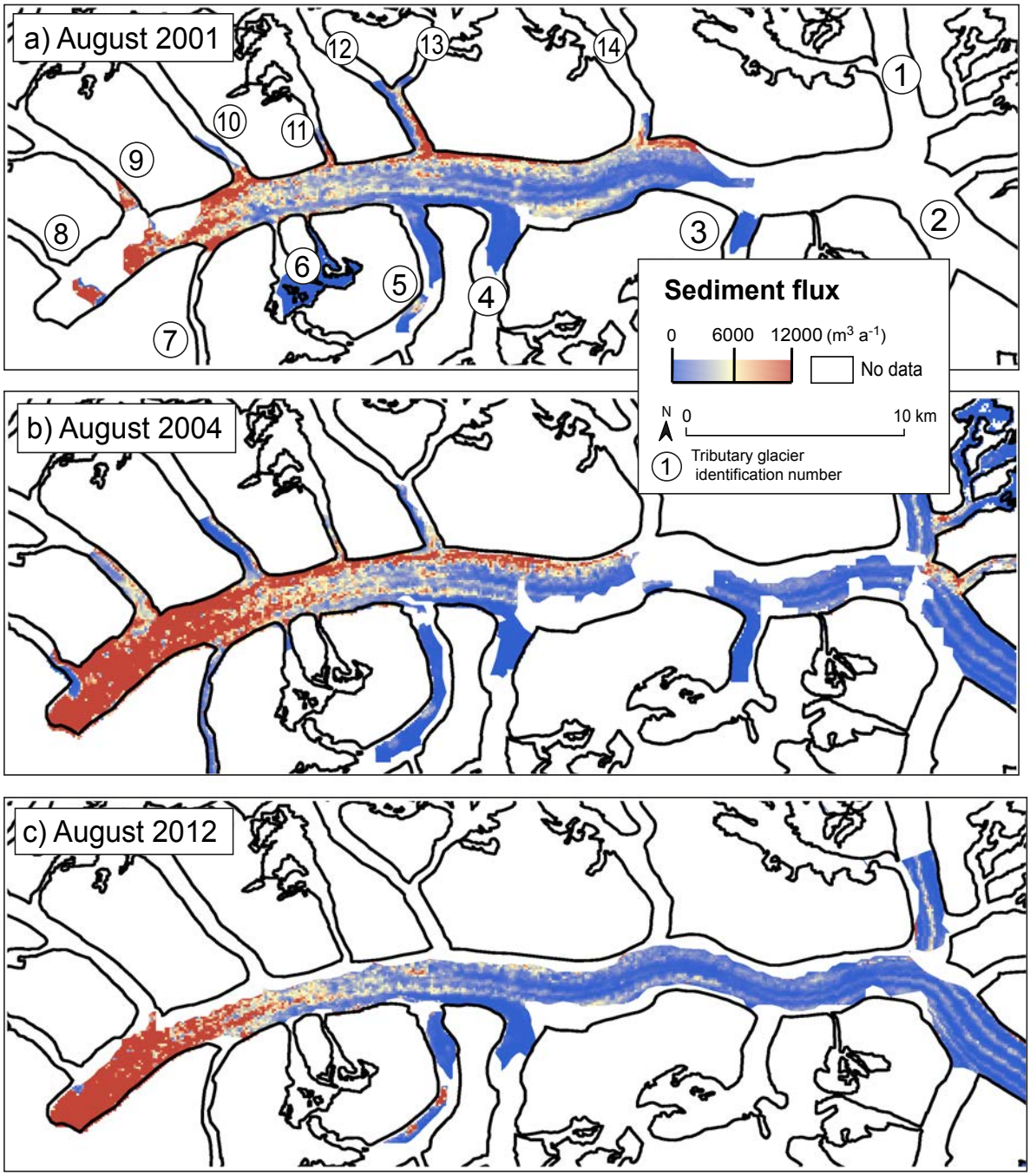

Figure 7.8: Sediment flux; debris cross-sectional area for each pixel multiplied by surface velocity, for (a) 2001–2002, (b) 2003–2004 and (c) 2011–2012. Areas where debris thickness is >0.5 m (see Figure 7.3) are presented but not discussed further due to the large uncertainties involved with using debris surface temperature to derive debris thicknesses greater than 0.5 m thick.

7.6. Discussion

7.6.1. *Spatiotemporal change in supraglacial debris distribution*

A debris distribution common to the majority of debris-covered glaciers is evident on the surface of Baltoro Glacier throughout the study period, with the thickest debris occurring near the terminus and along moraine crests, and an increasingly thick debris layer towards the terminus (e.g. Figure 7.9; Fushimi et al., 1980; Kirkbride and Warren, 1999; Mihalcea et al., 2006b; Zhang et al., 2011). A progressive increase in the area covered by debris through time would be expected due to debris being constantly transported to the glacier terminus; such a pattern is observed on Baltoro Glacier between 2001 and 2012, and combined with continued glacier flow would result in a build-up of debris in the lower sections (Kirkbride and Warren, 1999), particularly where there is no efficient sediment evacuation down-valley. A mean increase in debris thickness of between 0.05 and 0.10 m across the glacier surface occurred during the study period. In areas where the debris layer thickness was less than 0.5 m, the thickness at which ablation of underlying ice is most variable with debris thickness, the rate of debris thickness change identified here could lead to areas of the debris layer evolving from a thickness that enhances melt to one that insulates it over relatively short timescales (e.g. several years). The rapidity of such changes could render debris thickness maps previously published to be inapplicable for any year other than the one in which debris surface temperature data were collected (e.g. Mihalcea et al., 2008), although such maps would still be important for observing historical debris distribution.

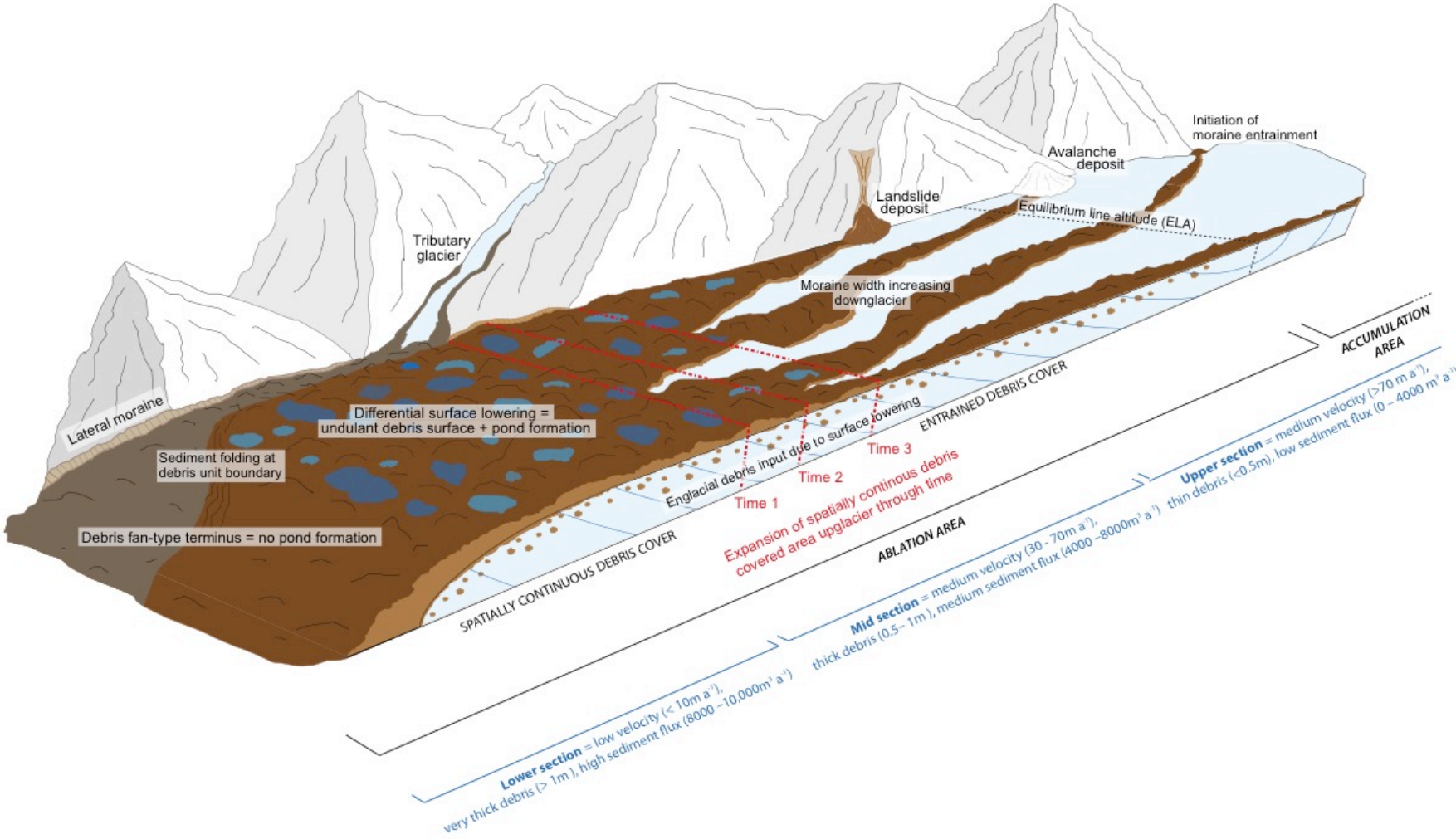

Figure 7.9: Schematic diagram of a debris-covered glacier system with input, transport and depositional processes alongside glacier dynamics for each section of the glacier, and the change in debris-covered area through time (T_1–T_3).

Debris thickness change in the lower- and mid-sections of Baltoro Glacier is attributed to a combination of differential surface ablation resulting in debris shift between topographic highs and lows, collapse of medial moraines, and redistribution of debris following input from mass movement events, all processes that commonly occur on debris-covered glaciers (e.g. Anderson and Anderson, 2016; Hambrey et al., 1999; Hambrey et al., 2008; Heimsath and McGlynn, 2008). The presence of a sharp change in debris thickness between the main glacier tongue and Trango Glacier is attributed to variations in relative surface velocity between the two flow units and the subsequent entrainment along flow unit boundaries. In high resolution Quickbird imagery (accessed from Google Earth (2017) on 16/01/17) a ridge at the boundary between the main glacier tongue and Trango Glacier flow units is observed, which has been mapped alongside other glaciological features such as sediment folds and ogives (Figure 7.10). The ridge extends from the bedrock at the up-glacier confluence between the two debris units (Figure 7.10a), suggesting the ridge is a medial moraine between the two flow units. Parallel to the supraglacial debris ridge are a series of deformation structures in the debris cover (Figure 7.10a), attributed to progressive supply and subsequent compression of debris through time as continuation of flow of the main glacier flow unit towards the terminus is constricted and blocked by the incoming flow unit of Trango Glacier. Variation in debris distribution near the terminus is further complicated by Trango Glacier displaying signs of a period of dynamic instability prior to the study period, with increasingly sinuous moraines on its surface through time (Figure 7.10a) and propagation of an area of high velocity along the tributary glacier's length between 2001 and 2004 (Figure 7.5). These geomorphological features alongside the temporal pattern observed on the glacier over the study period are consistent with a glacier that may have undergone a surge event, or at least a change in relative velocity to the ice flow unit it interacts with (Meir and Post, 1969). An arc of granitic debris that mirrors the terminus shape of Tributary Glacier 8 appears to suggest that this glacier is also dynamically linked to the terminus (Figure 7.10a). These geomorphological patterns suggest the main debris units were transported and deposited prior to input of debris from Tributary Glacier 8 and Trango Glacier, and indicate that initiation of debris supply along the main glacier and tributary glaciers were not contemporaneous.

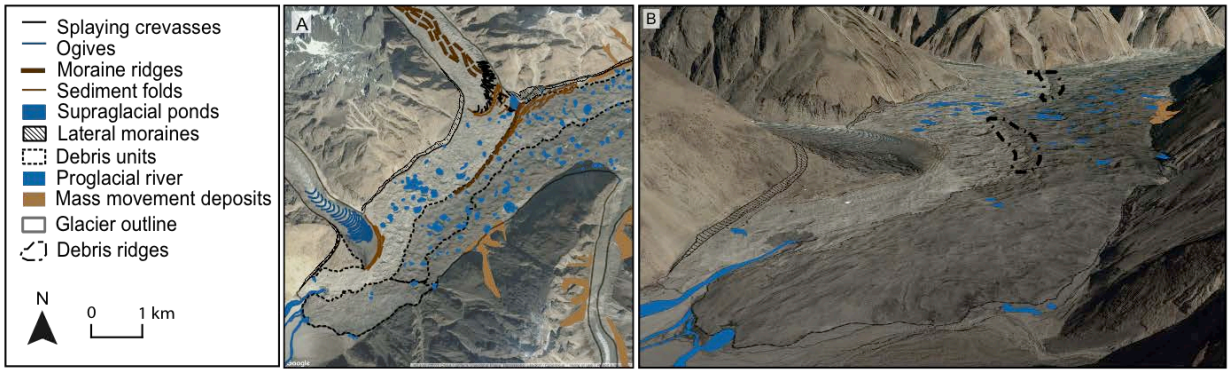

Figure 7.10: A (a) geomorphological map and (b) annotated oblique Quickbird image displaying the moraine ridge structure and associated sediment folds at the boundary between Trango Glacier (Tributary glacier 9) and the main glacier tongue, and the difference in debris lithology between the two glaciers. Accessed from Google Earth (2017) on 16/01/17.

7.6.2. Processes controlling debris distribution

Sustained debris thickening between 2001, 2004 and 2012 was observed, although notable spatial variability exists. Sediment flux also appeared to be temporally constant across much of the glacier despite variations in surface velocity, although some small-scale variations in sediment flux did occur. Changes in sediment flux in the lower section of the glacier were considered to be a product of increasing debris thickness near the terminus and sustained surface velocity as more debris was delivered to the slow-flowing terminus area through time. Variation in sediment flux between 2001–2002 and 2003–2004 in the glacier mid-section, south of Dunge and Biale Glaciers (Tributary Glaciers 10 and 11), is attributed to a combination of increasing debris thickness and increasing area of thicker debris up-glacier of the terminus and to an increase in surface velocity, as sediment flux varied considerably in this region between the two periods despite a lack of time separation. However, the overall glacier-wide stability in the rate of debris thickening and the pattern of sediment flux suggests that supraglacial debris transport was not the sole control of spatiotemporal changes in debris layer thickening. In periods of higher velocity (e.g. 2011–2012) it is likely that less debris built up on the glacier surface prior to transportation, causing a thinner layer of debris to be transported down-glacier than in previous years, albeit at a faster rate, and vice versa for periods of low velocity. Variability in surface velocity and its influence on debris transport is particularly

pertinent for Baltoro Glacier, where velocity has been found to vary from year to year, observed here and by Quincey et al. (2009b). Longer term studies (of the order of a number of decades) considering the interaction between surface velocity and debris distribution are needed to determine the relationship of these two parameters over decadal to centurial timescales. Consequently, the rate of debris input over sub-decadal timescales is thought to control temporal variations in debris layer thickening across the glacier. Over sub-decadal timescales, debris input will vary as a result of the frequency of mass movement events, which would significantly increase local supraglacial debris volume and affect velocity if the volume was great enough (e.g. Tovar et al., 2008). Over longer timescales (>100 years) debris input would be controlled by regional erosion rates, which are in turn controlled by climatic conditions, most notably precipitation, and tectonics, including rates of uplift and deformation in active tectonic regions such as the Karakoram (Molnar et al., 2007; Scherler, 2014). Regional erosion rates therefore control the long-term (centurial to millennial) rates of debris input to a glacier system, but over shorter (sub-decadal) periods the frequency and location of mass movement events are important controls on spatiotemporal variations in supraglacial debris distribution.

The total area and number of supraglacial water bodies increased between 2001 and 2012, and temporal changes in these parameters were notably larger than the uncertainty involved in incorrect classification of pixels containing water. The greatest percentage change in supraglacial water body number (73%) and area (171%) occurred between 2001 and 2004. Increase in supraglacial water body area and number has previously been attributed to changes in precipitation since 2000 (Quincey et al., 2009; Gibson et al., 2016). However, increasing supraglacial water body frequency on debris-covered glaciers is often considered analogous with stagnation and surface lowering of debris-covered glaciers (e.g. Sakai et al., 2000). Such differential surface lowering forms undulating debris-covered glacier surface topography, which then promotes the formation of supraglacial water bodies (Hambrey et al., 2008). Since 2004, Baltoro Glacier has showed no sign of stagnation but has undergone surface lowering of the order of 40 m between 2000 and 2008 (Gardelle et al., 2012). Such surface lowering is apparent up-glacier of the confluence between Trango Glacier and the main glacier tongue, where the debris surface displays a high density of topographic highs and depressions (Figure 7.10). Surface lowering of some glaciers in the Karakoram has been attributed to negative

mass balance of glaciers in response to recent climate change (Gardelle et al., 2012), although in the case of Baltoro Glacier it could equally be a consequence of its tributary glaciers being in various phases of dynamic instability. Glacier dynamic instability would cause temporal variation in ice flux to the main glacier tongue. Following the end of these phases of dynamic instability, ice mass delivery to the main glacier tongue would reduce, causing temporary reduction in surface velocity, as observed between 2001 and 2004 on Trango Glacier, and thus surface lowering. To understand the relative controls of climate change and dynamic instability of tributary glaciers on surface velocity and lowering of Baltoro Glacier longer-term records of surface lowering, glacier mass balance and localised meteorological data are needed.

Debris thickness maps presented here show no evidence for a thicker accumulation of debris at the glacier terminal margin, the presence of which has previously been interpreted as a terminal moraine on maps of debris thickness for topographically confined glaciers such as Khumbu Glacier in Nepal (Rounce and McKinney, 2014; Rowan et al., 2015; Soncini et al., 2016). Baltoro Glacier is thought to lack such a terminal moraine due to the glacier being of debris-fan-type, the occurrence of which is linked to glaciers located in wide, gently sloping valleys (Kirkbride, 2000). Debris-fan termini have a steeply sloped topography relative to the near horizontal glacier surface up-glacier of the terminus. The presence of a sloped debris surface suggests the same is true for the underlying ice surface (e.g. Figure 7.9), both of which would facilitate more efficient supra- and englacial drainage systems and inhibit the formation of undulating topography in the supraglacial debris layer near the terminus, as debris will be less stable and is more likely to be transported more evenly when located on a slope. The lack of depressions near the glacier terminus would therefore inhibit ponding of supraglacial water in the area.

7.6.3. Incorporating debris distribution change into numerical modelling

The debris thickness results presented here provide an interesting insight into debris thickness distribution across Baltoro Glaicer. However, the method of deriving debris thickness from debris surface temperature is only applicable to debris thickness below 0.5 m, due the relationship between DT and T_{ST} becoming disconnected in debris layers above 0.5 m as T_{ST} is less influenced by the underlying ice and controlled by debris

surface conditions (Nicholson and Benn, 2006; Rounce and McKinney, 2014). Furthermore, whilst the debris thickness data presented here (Figure 7.3), and subsequent debris thickness change (7.6) and sediment flux results (Figure 7.8), provide potential indicators to help establish the period over which a glacier has become debris covered and the rate at which supraglacial debris layers evolve, the issue of applying a time-specific empirical relationship between T_{ST} and DT variability to a series of time separated data due to temporal variations in meteorological conditions (e.g air temperature and radiation fluxes), means further validation of debris thickness at these different points in time, particularly for debris lyaers over 0.5 m thick, is needed to ultimately confirm the observed temporal changes in supraglacial debris layer thickness. Such additional data could be collected through field campaigns and by calculating empirical relationships between T_{ST} and DT for each However, the results presented here suggest that debris distribution for supraglacial debris layers less than 0.5 m thick is dynamic over annual to decadal timescales (Figure 7.3; Figure 7.9), which is in direct disagreement with current numerical models of debris-covered glacier change in which supraglacial debris layer thickness is largely considered to be static in time (e.g. Collier et al., 2014; Reid and Brock, 2010; Shea et al., 2015). Consequently, if the results presented here could be validated with further data collection, incorporation of annuals rate of debris thickness change, such as those presented here, could be used to constrain model outputs in glacier change models, such as those of Rowan et al. (2015), in which, currently, a supraglacial debris layer is formed through glacial processes and hillslope erosion rates are used to control input of debris to a glacier system.

The results presented here also suggest that using temporally constant annual erosion rates for control of debris input to glacier systems, such as those used by Rowan et al. (2015) and Anderson and Anderson (2016), are appropriate on sub-decadal timescales, but should be set on a case by case basis as these erosion rates would be affected by localised variability in headwall retreat and precipitation (Bookhagen et al., 2005; Pan et al., 2010). For longer-term studies the effect of a changing climate should be considered in regional erosion rates used for such numerical models (Peizhen et al., 2001; Scherler, 2014). Additionally, the rate of debris layer thickness change is likely to vary between glaciers due to varying input of debris, glacier size, landscape, climate and bedrock lithology, and needs to be evaluated for individual cases.

In addition to validating the methods used here to accurately determine the rate of formation and evolution of a supraglacial debris layer, a greater understanding of the volume of debris contributed from englacial debris input and the role varying ice velocity with depth plays in englacial debris transport is needed. At present, calculation of englacial debris meltout has not been attempted in great detail (e.g. Rowan et al., 2015; Anderson and Anderson, 2016). Recent work on debris-covered glaciers has highlighted rockfall in accumulation areas can be incorporated rapidly to englacial locations (Dunning et al., 2015), but very little is known regarding the volume of debris contained within the glacier ice of debris-covered glaciers (Anderson 2000). Enhanced ablation and surface lowering, as seen on Baltoro Glacier from the start of the 21st century (Gardelle et al., 2012) is likely to result in an increased rate of debris meltout (Bolch et al., 2008; Kirkbride and Deline, 2013). By quantifying the volume of debris contributed to a glacier surface through englacial meltout a more comprehensive understanding of processes by which debris distribution is controlled, both in space and time, could be gained. Such data have previously been collected through the use of ground penetrating radar (e.g. McCarthy et al., 2017), but a greater spatial coverage of such data across glacier surfaces is needed to understand spatial variability in englacial debris distribution.

7.7. Conclusion

The distribution of supraglacial debris on Baltoro Glacier predominantly follows the expected pattern for a debris-covered glacier, with increasingly thick debris towards the terminus. However, debris distribution is complicated by the interaction between tributary glaciers, some of which show signs of dynamic instability, and the main glacier tongue. An overall increase in debris thickness was observed between 2001 and 2012, indicating that supraglacial debris distribution varies over sub-decadal timescales. Short-term variations in debris thickness are primarily attributed to input from mass movement events. The area of Baltoro Glacier covered by a spatially continuous debris layer increased over the study period, suggesting that the debris layer is still evolving. The number and area of supraglacial water bodies on Baltoro Glacier also increased through the study period, with changes attributed to differential surface lowering. However, ponding is not observed at the terminus because the glacier displays a debris-fan type terminus that inhibits formation of undulating debris topography and facilitates

efficient drainage. Additionally, surface lowering of the glacier surface up-glacier of the terminus may be important for debris layer thickening due to exhumation of debris transported englacially.

Quantifying the influence of mass movement deposits and englacial meltout on supraglacial debris distribution is important to better understand the evolution of debris-covered glaciers through time, particularly to determine the mass balance of glaciers accurately in response to recent and future climate change. However, quantifying such inputs is challenging; mass movement events are temporally and spatially variable and dependant on climate, topography, tectonic processes and lithology, and identifying debris contributed from englacial sources requires quantification of the volume of debris held englacially, which can only really be gained through fieldwork. Despite such limitations, this study shows that incorporating some aspects of spatiotemporal change in supraglacial debris distribution into numerical modelling is achievable, and is likely to be significant in accurately determining debris-covered glacier systems.

Chapter 8: Paper IV

Title: The role of debris thickness, albedo and surface roughness in controlling variability in ablation of a Himalayan debris-covered glacier

Journal: The Cryosphere

Current status: In preparation for submission.

8. The role of debris thickness, albedo and surface roughness in controlling variability in ablation of a Himalayan debris-covered glacier

8.1. Abstract

Supraglacial debris is highly influential to the mass balance of glaciers in mountain ranges worldwide, the effect of which primarily depends on thickness of the supraglacial debris layer. Supraglacial debris thickness is both spatially and temporally variable due to differing rates of debris input, transport and distribution. However, numerical models of debris-covered glaciers have largely assumed a spatially uniform debris thickness, as well as uniformity in other debris characteristics that vary in space and time. Omitting variations in debris characteristics from glacier mass balance calculations inhibits our ability to accurately simulate the response of debris-covered glaciers to climate change. Here, we test the role of variability in debris thickness, surface albedo and aerodynamic roughness length using data derived from remotely sensed data sets and measurements made on Khumbu Glacier in the Nepal Himalaya, using a climate mass balance model specifically developed for supraglacial debris. Change in debris thickness caused the greatest variations in mass balance of +223%, whilst inclusion of spatially variable albedo and aerodynamic roughness length in addition to spatially variable debris thickness reduced total mass change by 60%, but had less influence on mass balance estimates individually (+48% for albedo and +4% for aerodynamic roughness length, respectively). Consequently, incorporating spatially variable debris properties alters estimates of mass balance, but to verify the consequence of incorporating such variability in model simulation these simulations should be validated with *in situ* data for a specific ablation season.

8.2. Introduction

The majority of glaciers in the Himalaya are currently losing mass (Bolch et al., 2012), which is predicted to affect future regional water supplies (Immerzeel et al. 2010; Kraaijenbrink et al., 2017). Recent changes in Himalayan glacier mass have been attributed to anthropogenically induced climate change (Allen et al., 2014). As well as increasing atmospheric temperatures, climate change is altering the timing, duration and intensity of the summer monsoon (Turner and Annamalai, 2012) which affects seasonal air temperature and precipitation type in high mountain environments, and is

consequently impacting on glacier mass balance in the central and eastern Himalaya (Bookhagen and Burbank, 2010; Bolch et al., 2012). Accurately determining how glacier mass balance is changing in response to climate change is complicated by the occurrence of extensive supraglacial debris layers on glaciers across the region (Scherler et al., 2011; Bolch et al. 2011; King et al., 2017). Around 14–18% of glacierised area in the Himalaya is debris covered (Kääb et al., 2012), although this percentage varies regionally, with the highest proportion in the Everest region at around 36% (Nuimura et al., 2012; Thakuri et al., 2014). Many of the large glaciers have ablation areas almost entirely covered in supraglacial debris, up to at least 4 m thick in places (e.g. Rounce and McKinney, 2014; Soncini et al., 2016).

8.2.1. Controls on ablation beneath a supraglacial debris layer

The presence of a supraglacial debris layer modifies ablation by acting as a thermal buffer between the atmosphere and the underlying ice (Nicholson and Benn, 2013). The magnitude of the effect of a supraglacial layer on ablation depends on the thickness of the debris layer, which is the case until debris thickness reaches about 1.0 m thick, after which the effect of any further increase in thickness is considered negligible (Østrem, 1959). Thin debris (typically less than 0.05 m thick) enhances ablation by decreasing glacier surface albedo, whereas thick debris (greater than about 0.05 m thick) reduces ablation by insulating the underlying ice (Evatt et al., 2015; Nicholson and Benn, 2006; Reid et al., 2012; Østrem, 1959). Debris thickness varies in space and time due to variations in debris input, transport and deposition in and on the glacier, which are dictated by regional and local erosion rates, climate, hillslope and glacier coupling, and ice flow (Anderson and Anderson, 2016). As a result of this variability in debris layer thickness, differential ablation occurs across a debris-covered glacier surface. Differential surface lowering commonly creates a hummocky surface topography on these debris-covered glaciers (Hambrey et al., 2008; Benn et al. 2012).

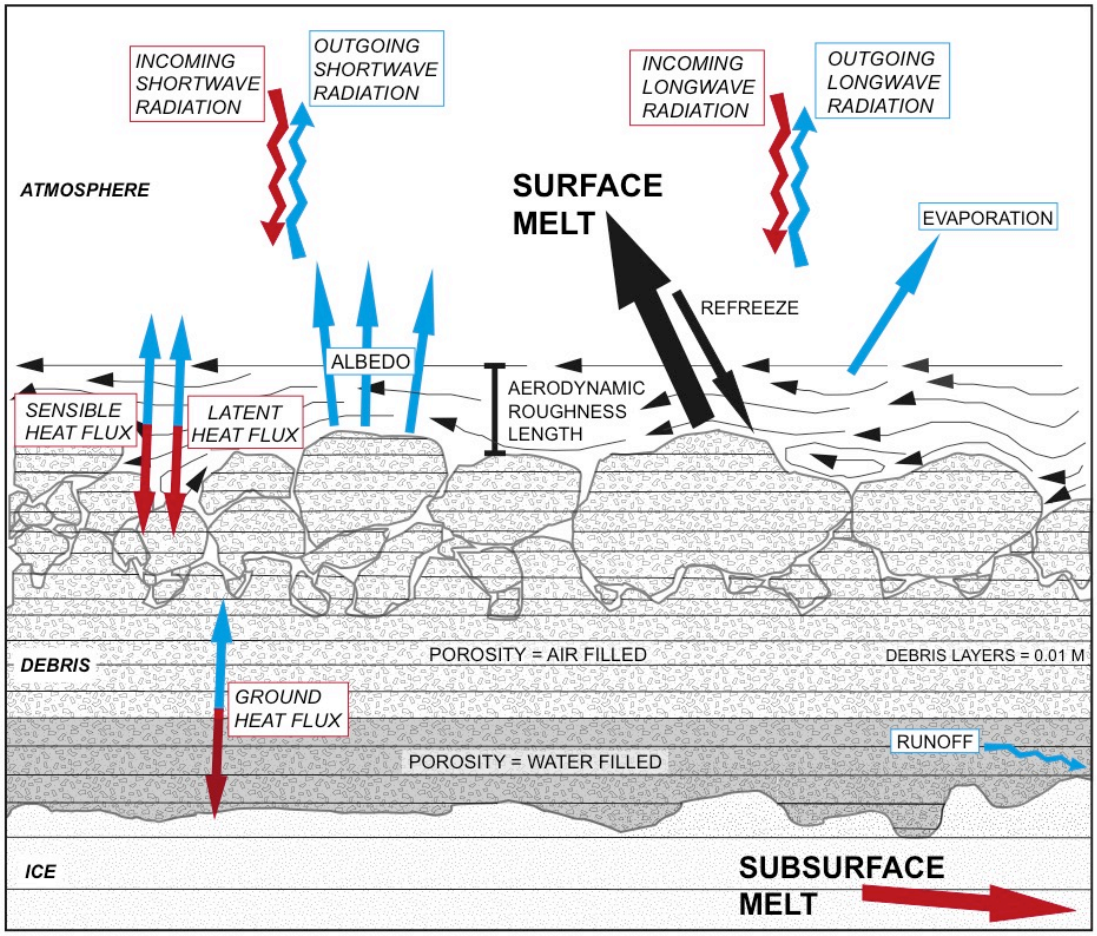

Figure 8.1: A schematic diagram summarising the energy fluxes at the surface and through a supraglacial debris layer, including the main incoming fluxes in red and outgoing fluxes in blue.

Although debris layer thickness is a first order control on glacier ice ablation (Kayastha et al., 2000), other debris properties including albedo, grain size, lithology, surface roughness, porosity and moisture content also influence the degree of ablation that occurs beneath a supraglacial debris layer (Collier et al., 2014; Evatt et al., 2015; Nicholson and Benn, 2013; Ranzi et al., 2004; Rounce et al., 2015). These supraglacial debris properties can vary over scales of a few metres, potentially resulting in considerable heterogeneity in ablation across a debris-covered glacier surface (Paper I). Albedo of supraglacial debris cover is primarily controlled by debris lithology (Kayastha et al., 2000; Matthias et al., 2000; Warren, 2017). The darker colour of rock debris compared to ice results in increased absorption of incoming shortwave radiation

(Reznickenko et al., 2010). Although previous studies have found large variations in albedo across debris-covered glaciers (e.g. Casey, 2012; Nicholson and Benn, 2006; 2013), little research has been undertaken as to the importance of such variability on ablation.

Investigation into spatiotemporal variability of surface roughness and its influence on glacier ablation is similarly sparse. Surface roughness, quantified through aerodynamic roughness length (z_0), is the height above the surface at which extrapolated horizontal wind speed reaches zero (Brock et al., 2010; Smith et al., 2016). z_0 controls the rate of heat transfer between the glacier surface and atmosphere and influences turbulent sensible and latent heat fluxes to the glacier surface (Brock et al., 2006; Cutler and Munro, 1996; Irvine-Fynn et al., 2014; Miles et al., 2017; Cuffey and Paterson, 2010; Quincey et al., 2017). z_0 increases with increasing surface roughness, a factor of the form, dimensions and density distribution of a debris surface (Brock et al., 2006). Currently, differences in z_0 are restricted to a simplified differentiation between snow, ice and debris (e.g. Fyffe et al., 2014; Reid et al., 2012; Smith et al., 2016). However, grain size on a debris-covered glacier can range from silt to large (>5 m diameter) boulders, potentially resulting in variations of z_0 of several orders of magnitude (Brock et al., 2000). An order of magnitude difference in z_0 can result in a doubling of the value of the turbulent fluxes (Brock et al., 2006; Brock et al., 2000). Therefore, applying one z_0 value to all debris-covered areas is likely to give a poor representation of surface roughness across the debris surface (Rounce et al., 2015), resulting in poor estimation of the turbulent flux at a debris surface, and therefore the amount of energy available for ablation of ice underling a supraglacial debris layer.

8.2.2. *Modelling ablation beneath supraglacial debris*

To date, ablation under a supraglacial debris layer has been modelled using two approaches: through simulation of surface energy balance and heat transfer (e.g. Collier et al., 2013; 2014; Evatt et al., 2015; Fyffe et al., 2014; Lejeune et al., 2013; Reid and Brock, 2010) and using enhanced temperature index models (e.g. Carenzo et al., 2016; Immerzeel et al., 2014; Ragettli et al., 2015). These models are predominantly either point-based, and therefore not concerned with spatial variability in supraglacial debris

layer thickness, or consider spatial variability in debris thickness in a much-simplified way.

Here, the Climate Mass Balance (CMB) model for debris-covered ice (CMB-DEB) is used, developed by Mölg et al. (2008) and Collier et al. (2014) to explore the role of debris thickness, albedo and surface roughness in controlling variability in ablation on debris-covered glaciers. The CMB model has previously been used to simulated mass balance for glaciers in Tibet (Mölg et al., 2012), the Karakoram (Collier et al., 2013), Kenya (Nicholson et al., 2013), Chile (MacDonell et al., 2013) and the Italian Alps (Collier et al., 2014), although inclusion of a supraglacial debris layer was restricted to the studies by Collier et al. (2014; 2013). These studies have demonstrated the robust nature of this model for simulating glacier-wide surface energy balance. For example, comparison between simulated ablation and *in situ* measurements of surface lowering by Mölg et al. (2008) showed minimal variation, whilst MacDonell et al. (2013) calculated the Nash-Sutcliffe efficiency coefficient of 0.99 between measured and simulated mass balance (*b*).

The ability of CMB-DEB to simulate complex glacier-climate relationships on mountain glaciers is due to the model's high level of interaction between climatic parameters (air temperature, incident radiation, wind speed, precipitation, relative humidity) and mass balance, alongside a developed simulation of surface energy balance and heat transfer through a supraglacial debris layer. The model's capability to simulate seasonally variable solid precipitation, and to include the effect of pore moisture content in the supraglacial debris layer, means that this model is highly appropriate for use in investigating seasonal mass balance for Himalayan glaciers during the summer monsoon. An independent model similar to CMB-DEB was developed by Evatt et al. (2015), which incorporated porosity into a surface energy balance model, and to date is the only surface energy balance model to simulate a realistic Østrem curve, reproducing the relationship between debris thickness and ablation observed empirically (e.g. Nicholson and Benn, 2006; Østrem, 1959).

Here, we investigated the impact of variability in debris thickness, albedo and surface roughness on the surface energy balance of a debris-covered glacier, to consider their influence on ablation. A point-based version of CMB-DEB was used to calculate mass

balance sensitivity to the variables in question by testing a wide range of values for each variable, both individually and in combination with each other, the ranges of which were set by field observations from Khumbu Glacier in Nepal and previously published data. Local meteorological data were used to force the model, and also defined the presence and impact of snowpack on the debris surface, which controlled the pore water content of the debris. A distributed version of CMB-DEB was then used to estimate specific mass balance across the ablation area of Khumbu Glacier during a summer monsoon season.

8.3. Study site and data collection

Simulations were undertaken using data collected on Khumbu Glacier, a typical monsoon-influenced Himalayan debris-covered glacier (Hambrey et al., 2008) located in the Everest region of Nepal (27°56'N, 86°56'E) (Figure 8.2). Khumbu Glacier is a summer accumulation-type glacier due to the dominance of the summer monsoon on the region's annual climate regime, which results in positive air temperatures occurring concurrently with the period in which of the majority of the region's annual precipitation falls (Salerno et al., 2015; Benn and Lehmkuhl, 2000). The glacier is around 17 km long with an area of 27 km^2, excluding the now disconnected Changri Nup and Changri Shar Glaciers (Vincent et al., 2016), and flows from the southwest flanks of Mount Everest at 8230 m to 4816 m above sea level (a.s.l.) (Figure 8.2b) (Arendt et al., 2012; Bolch et al., 2008). The equilibrium line altitude (ELA) is situated between 5700 m and 6000 m a.s.l. within the Khumbu Icefall, below which lies the debris-covered ablation area (Benn and Lehmkuhl, 2000; Inoue, 1977; Rowan et al., 2015).

Khumbu Glacier is typical of many large Himalayan debris-covered glaciers, with a low-gradient (<2°), slow-flowing (<10 m a^{-1}) ablation area which has extensive supraglacial debris coverage that exceeds 4 m in thickness in some areas (Gades, 2000; Hambrey et al., 2008; Quincey et al., 2009; Soncini et al., 2016). The ablation area below 5300 m a.s.l. is almost entirely debris-covered, comprising of granitic and schistose lithologies derived from the surrounding hillslopes (Iwata et al., 2000; Nuimura et al., 2012). The stable, lowermost region of the ablation area is in the early stages of soil formation and is partially vegetated (Kadota, 2000). Lithology and grain size of supraglacial debris is highly heterogeneous across the debris-covered ablation area, ranging from fine sand to large (>5 m diameter) boulders (Figure 8.3; Hambrey et al., 2008).

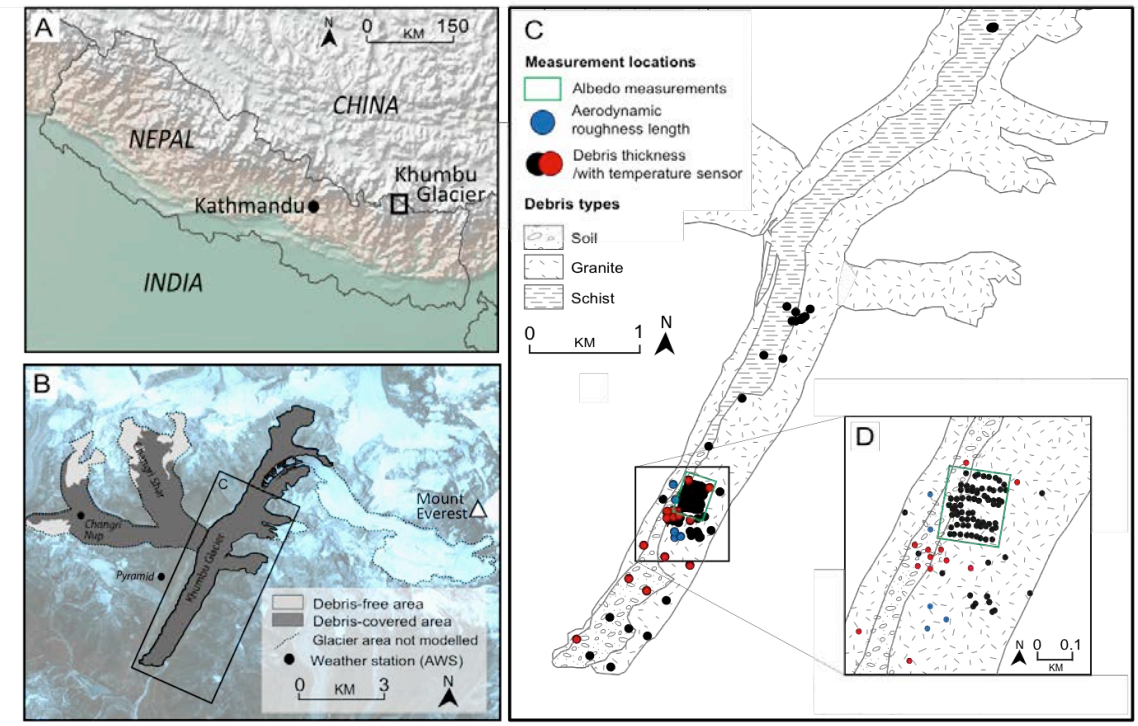

Figure 8.2: Location map of Khumbu Glacier: (a) in a regional Himalayan setting, (b) in relation to Mt. Everest, including the location of the meteorological stations used and (c) the study area of the glacier with lithology of debris across the study area and locations of *in situ* measurements taken in May 2014.

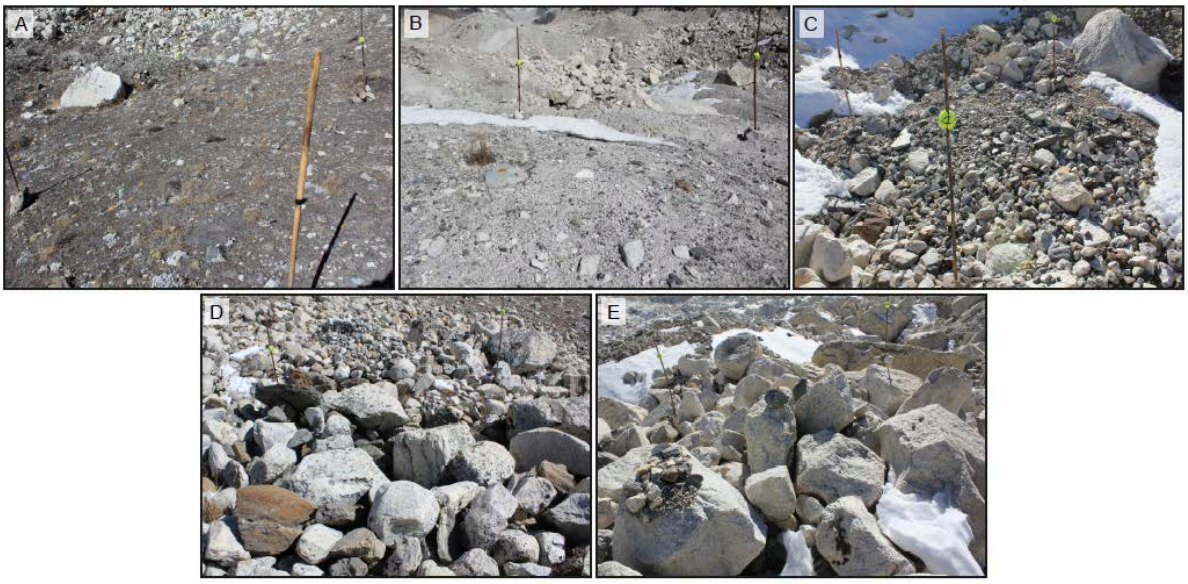

Figure 8.3: Site photos of each of the locations at which photographs were taken for use in calculating aerodynamic roughness length, which show the variety of debris type that exist on the debris-covered surface of Khumbu Glacier. Bamboo pole and tennis balls were used as control points to constrain the size of the plots used to calculate z_0.

8.3.1. Meteorological data

The CMB-DEB model was forced using hourly timeseries of incoming shortwave radiation, incoming longwave radiation, air temperature, surface pressure, relative humidity, wind speed and precipitation collected in 2014 between 01 May 00:00 and 27 October 23:00 (local time is GMT+05:45) (Figure 8.4). Incoming shortwave and longwave solar radiation were measured using a Kipp&Zonen CNR4 sensor 0.6 m above the surface. Relative humidity was measured using a Vaisala HMP45C sensor, 1.65 m above the surface. Wind speed was measured using a Young 05103-5 sensor, 2.4 m above the surface. Incoming radiation, relative humidity and wind speed timeseries were collected on a debris-covered area of Changri Nup Glacier (Figure 8.2b; 27°58'55"N, 86°45'52.92" E; 5363 m a.s.l.) immediately adjacent to Khumbu Glacier. Air temperature and precipitation amount were measured using a Geonor T-200BM sensor that captures all precipitation phases, and were recorded at the Pyramid Observatory, located off-glacier about 1 km to the northwest of the study area (Figure 8.2b; 27°57'32" N, 86°48'47" E; 5030 m a.s.l.). Precipitation was corrected for snow undercatch following World Meteorological Office recommendations (Forland et al., 1996; Sherpa et al. 2017). *In situ* atmospheric surface pressure measurements were unavailable, so downscaled ERA-Interim data were used (retrieved from: http://apps.ecmwf.int/datasets/data/interim-full-daily/levtype=sfc/ on 1st May 2017). All meteorological data were collected at 30-minute intervals, apart from precipitation amount, which was collected at 15-minute intervals, and resampled to hourly data.

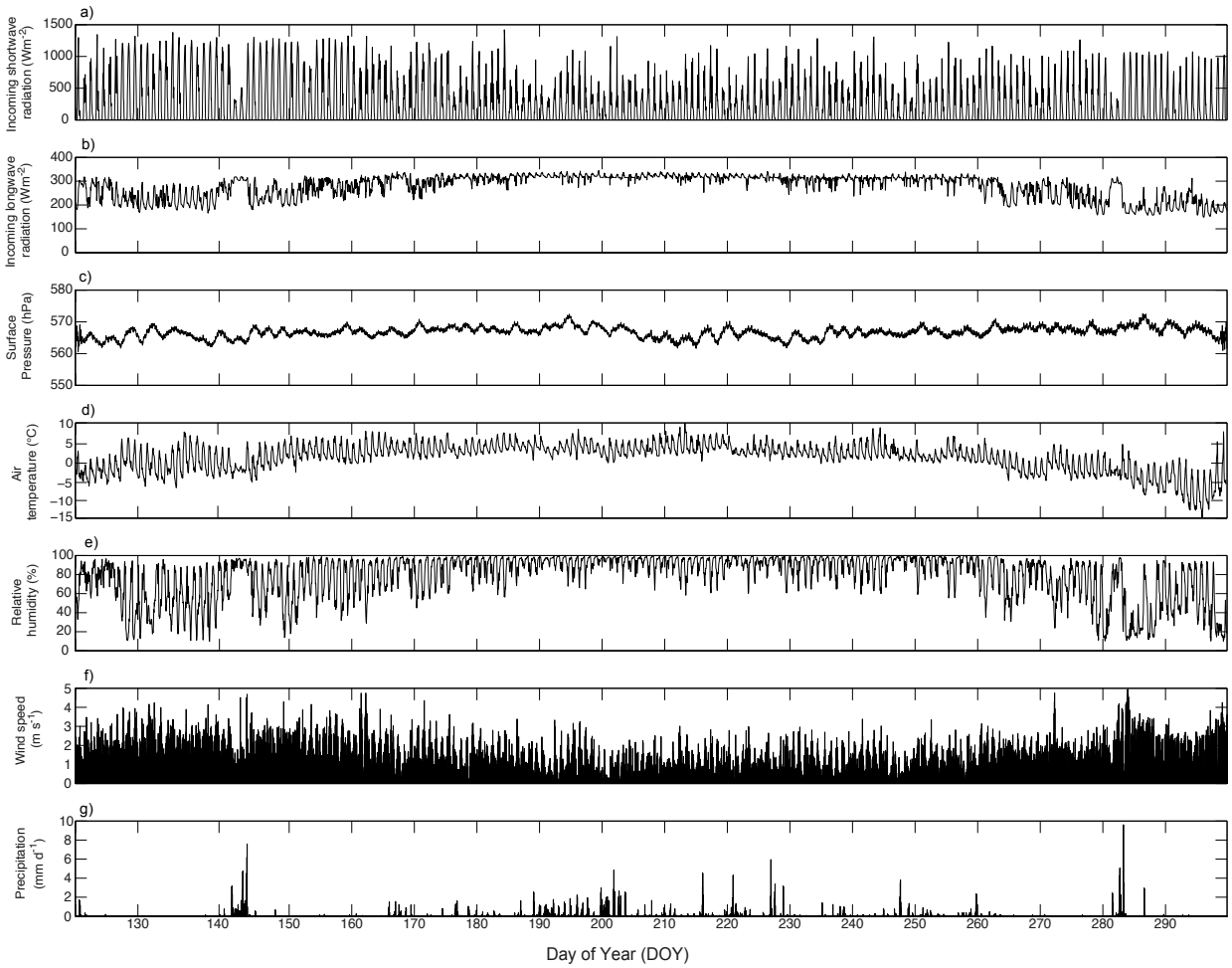

Figure 8.4: A timeseries of meteorological data collected over the 2014 monsoon season: (a) incoming shortwave radiation; (b) incoming longwave radiation; (c) atmospheric surface pressure; air temperature; (d) relative humidity; (e) wind speed; (f) total daily precipitation amount.

8.3.2. Debris thickness

Debris thickness was measured at 143 locations (Figure 8.2c) on a theoretical grid covering the lowermost 2 km^2 of the lower ablation area located using a handheld GPS unit (Garmin GPSMap 64; 3m horizontal accuracy). Each site had a unique combination of characteristics: slope, aspect, elevation, grain size, sorting, roundness, and grain lithology. An additional 81 debris thickness measurements were also made in a 180 × 180 m area at 20 m intervals to investigate variations in debris thickness over short distances. Debris thickness was measured by excavating into the underlying ice, but due to the practical

challenge of this method the debris thickness was reported simply as greater than 1 m where no ice was present at 1 m depth. These measurements were used to constrain the range of possible values for debris thickness in the point-based CMB-DEB model.

A gridded debris thickness map was produced using the empirical relationship between debris thickness (dT; cm) and surface temperature (T_{ST}; °C):

$$dT = 0.03\, exp(0.33\, T_{ST}) \tag{8.1}$$

The thermal band 10 of the Landsat 8 thermal data acquired on the 22nd May 2014 at 10:26 (local time) was used for calculation of debris layer thickness at a 30 m grid spacing. Soncini et al. (2016) calculated a correlation of 0.70 between point measurements of debris thickness and their corresponding pixels, with an uncertainty of 0.09 m. Soncini et al.'s (2016) map was reproduced using the same thermal data as an input to the distributed CMB-DEB model (Figure 8.5a), and the area in which debris was present was used to constrain the model domain (Figure 8.5).

8.3.3. Surface reflectance

Surface reflectance was measured as a proxy for albedo, as is standard practice as surface reflectance only represents the reflectance of the material for one point in time in one direction (Lilliesand et al., 2014), and is referred to as albedo hereafter. Surface reflectance was measured at five sites in the same locations as z_0, and a further 33 sites with varying debris types where debris thickness was also sampled (Figure 8.2c) using a StellarNet™ BLUE-wave VIS compact spectrometer in a spectral range of 350–1150 nm. At each of the five sites corresponding to the z_0 measurements, 50 spectral measurements were taken ~0.2 m above the debris surface, and at the other sites three spectral measurements were taken. Each measurement was the mean of five spectra. All measurements were collected between 11:00 and 13:00, within one hour of solar noon, on 24th May 2014 in clear sky conditions. At each site, a Halon (> 97% reflectance) 'white reference' panel was used to collect a total incoming reflectance value prior to and following collection of debris surface spectra. Surface reflectance was calculated as the ratio of the area under the reflectance curve for wavelengths between 400 to 2800 nm for

each site. A photo of each site was taken covering a 0.5 × 0.5 m area, and the ratio of schist to granite grains for non-soil sites was calculated through classification of dark and light debris (both grains and matrix) using ImageJ (v. 1.50i; Rasband, 2008). Sites were then categorised into three types: soil; dark debris (>50% schist) and light debris (>50% granite) (Table 8.1).

Table 8.1: Median surface reflectance *in situ* values for soil, dark and light debris categories, and standard deviation of values for each category.

Supraglacial debris surface categories	Median surface reflectance (albedo)	Standard deviation
Soil	0.27 (*n*=30)	0.08
Dark (schistose) debris	0.43 (*n*=22)	0.28
Light (granitic) debris	0.61 (*n*=31)	0.21

A map of theoretical surface reflectance (Figure 8.5b) was produced using Pleiades optical data, acquired on 19th May 2016 12:36 at a resolution of 0.5 m, which was the highest resolution data set with the lowest cloud cover, and therefore the greatest glacier area, available. The Pleiades data were orthorectified and pan-sharpened using the panchromatic band, and then clipped to the model domain (Figure 8.2c). Segmentation was undertaken using the image segmentation module in RSGISLib (Shepherd et al., 2013) using a minimum cluster size of 3600 pixels, equivalent to a 30 × 30 m area (the resolution of the debris thickness map). A supervised object- and rule-based classification was then undertaken using the classification module in RSGISLib (Bunting et al., 2014; Supplementary Table A2), to produce a Level 1 classification of surface reflectance for granite, schist, soil, ice and water classes. Pixels containing water were identified using a Normalised Difference Water Index (NDWI; McFeeters, 1996):

$$NDWI = (Green\ (Band\ 3) - NIR\ (Band\ 4))/\ (NIR\ (Band\ 4) + Green\ (Band\ 3)) \quad (8.2)$$

Pixels containing soil were identified in part using a Normalised Difference Vegetation index (NDVI, (Lillesand et al., 2014):

$$NDVI = (Red\ (Band\ 1) - NIR\ (Band\ 4))/(NIR\ (Band\ 4) + Red\ (Band\ 1)) \quad (8.3)$$

Classes were then assigned surface reflectance values based on mean field data values for granite, schist and soil (Table 8.1). A surface reflectance of 0.34 was used for ice (Brock et al., 2010; Collier et al., 2014) and clusters that were classified as ice were subsequently omitted from the model domain. Pixels containing water were also omitted from the model domain. An accuracy assessment was undertaken on the classified map: georeferenced field-derived photos, in which the surface cover type had been identified, were compared to the corresponding pixel of the surface reflectance map to confirm correct or incorrect classification of pixels. The classification yielded an overall accuracy of 74% (Supplementary Table A3), viewed as a 'good classification' by Lillesand et al. (2014).

8.3.4. Surface roughness

Aerodynamic roughness length (z_0) was calculated using the full point-cloud method detailed by Smith et al. (2016), based on the work of Lettau (1969) and adopted in previous glaciological studies (e.g. Rounce et al., 2015, Brock et al., 2010; Quincey et al., 2017). The Lettau approach defines roughness 'elements' and includes a drag coefficient to account for sheltering, such that:

$$z_0 = 0.5h\frac{s}{S} \quad (8.4)$$

where h is the mean vertical extent of microtopographic variations, s is the silhouette area facing upwind and S is the unit ground area occupied by each element. While many previous studies have used topographic profiles to calculate z_0 (e.g. Munro, 1989; Arnold and Rees, 2003; Brock et al., 2006), use of the full point cloud permits a comprehensive analysis of the variability across the plot area (Smith et al., 2016). Debris topography (h) was derived using Structure-from-Motion (SfM) photogrammetry (Westoby et al. 2012), which uses images acquired from multiple viewpoints in order to determine three-

dimensional geometry, a method which has been used successfully on debris-covered glaciers previously (e.g. Rounce et al., 2015; Miles et al., 2017; Quincey et al., 2017). Five plots, taken to represent the five main debris cover types on the surface of the glacier, were classified using the Wentworth (1914) grain size scale as silt and sand, sand and gravel, cobbles and small boulders, medium boulders and large boulders (Figure 8.3). Each 3 × 3 m plot was aligned with the four cardinal compass points. Between 20 to 30 photos were collected for each plot using a Canon EOS 550D 15.1 megapixel camera at approximately 1.5 m above and oblique to the surface, to avoid the doming effect that commonly occurs in vertical image surveys (James and Robson, 2014). Bamboo canes 2 m in height were placed at each corner of the plots at 90° angles to one another. These markers formed a network of ground control points that were measured relative to the first reference point rather than in absolute coordinates and elevation (e.g. Irvine-Fynn et al., 2014). Distances between reference points were measured to sub-centimetre accuracy using a compass, spirit level and measuring tape. Agisoft Photoscan Professional (v.1.2.5 Agisoft LLC, 2016) was used to align photos for each plot and subsequently construct dense point clouds comprising of the order of 10–20 × 10^6 points and extract digital elevation models (DEMs) of each site (Smith et al., 2016; Westoby et al., 2012). Four z_0 values were calculated for each plot, one for each principal wind direction, and the mean was taken to represent the final roughness length used in the modelling (Table 8.2).

Table 8.2: Aerodynamic roughness values calculated for four plots on different supraglacial debris surface: silt and sand; sand and gravel; cobbles and small boulders; medium and large boulders.

Supraglacial debris surface type	Aerodynamic roughness length – z_0 (m)	Range of z_0 values calculated (m)
Silt and sand	0.00136	0.00015
Sand and gravel	0.00218	0.00079
Cobbles and small boulders	0.00878	0.00228
Medium to large boulders	0.01473	0.00593

A second tier of classification was undertaken on the Pleiades data following classification of land surface for surface reflectance to produce a map of surface roughness (Figure 8.5c). Standard deviation of near infrared wavelengths were used to classify silt and sand, sand and gravel, cobbles and small boulders and medium to large boulders within each of the surface reflectance classes, a method based on previous research that found soil surfaces had a greater scatter of near infrared wavelengths with increasing surface roughness (Cierniewski and Verbrugghe, 1997; Wu et al., 2009). Initial thresholds of rules based on standard deviation of Near Infrared of silt and sand, sand and gravel, cobble and small boulders and medium to large boulders were identified through observation of the debris surface. Areas of medium to large boulders were identified as areas where grains were visible in a true colour image, whilst silt and sand were identified as areas where no grains were visible and there was little to no shadowing on the debris surface. The surface roughness of the surface reflectance classes (schist, granite and soil) were classified separately as each grain size had differing thresholds for each of the roughness classes. Near infrared scattering is also affected by the presence of moisture at the debris surface (Wu et al., 2008), but each of the different debris types were of uniform colour in the Pleiades data, and so the surface of the debris layer was considered to be unaffected by the presence of moisture at the time of data acquisition. Once classified into different surface roughness types the z_0 calculated from field data for the corresponding surface roughness cover type was assigned to each class, and the map was resampled to a 30 × 30 m grid (Figure 8.5c). An accuracy assessment was undertaken between the classified surface roughness map and site photographs, which yielded an overall accuracy of 76% (Supplementary Table A4).

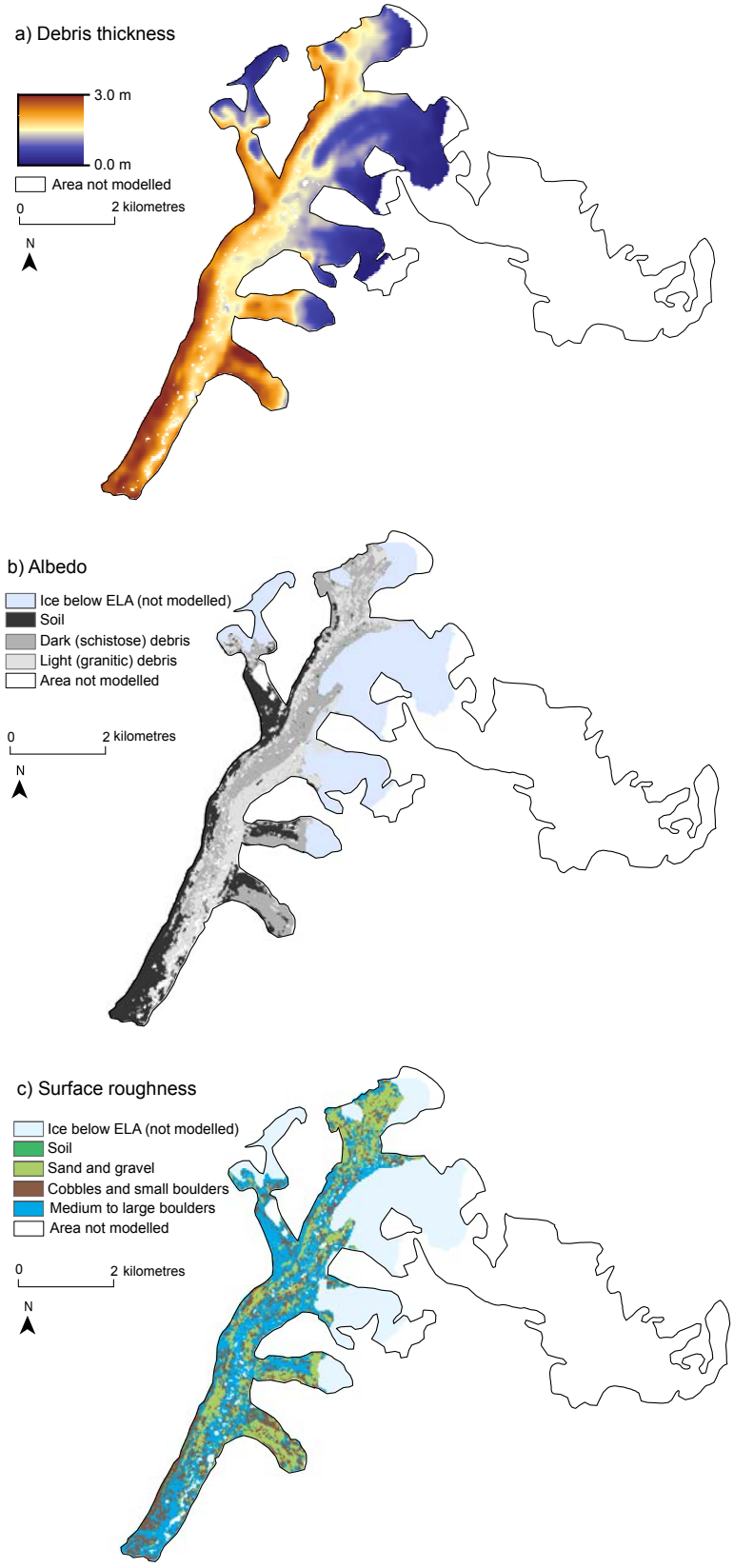

Figure 8.5: Distributed maps of (a) debris thickness, (b) albedo and (c) aerodynamic roughness length, used as the spatially variable inputs in the distributed simulations.

8.4. Mass balance modelling

8.4.1. Model description

The CMB-DEB model (Mölg et al., 2008; Collier et al., 2014) solves the surface energy balance as:

$$S\downarrow\left(1-\alpha\right)+L\downarrow+L\uparrow+QH+QE+QG+QR=Fnet \quad (8.5)$$

Where S is shortwave radiation, α is albedo, L is longwave radiation, QH is turbulent sensible heat flux, QE is turbulent latent heat flux, QG is ground energy flux, QR is the heat flux from precipitation and $Fnet$ is the resulting energy flux. Mass loss occurs through sublimation and melt (Mölg et al., 2008). $Fnet$ represents the energy available for ablation, provided the ice surface temperature has reached melting point (Collier et al., 2014). CMB-DEB solves for $Fnet$ in two stages: (i) in its surface module, for debris-free or debris-covered ice and then (ii) in the subsurface module, within which heat transfer through the vertical column is solved using the Crank-Nicholson method (Smith, 1985).

Debris surface temperature is calculated iteratively at each hourly time step using the Newton-Raphson method, previously implemented by Reid and Brock (2010). Following current understanding of heat transfer within a debris layer (e.g. Lejeune et al., 2013; Nicholson and Benn, 2006; Reid et al., 2012) the model does not assume a linear gradient through the debris layer, instead explicitly simulating heat conduction through the debris layer at each time step. Additionally, the physical properties of the glacier subsurface (debris density, thermal conductivity and specific heat capacity) are varied for each 0.01 m debris layer using a weighted mean of whole rock values, whilst porosity is estimated using an assumed linear function (Collier et al., 2014). Turbulent sensible and latent heat fluxes are computed using the bulk aerodynamic formulae corrected for atmospheric stability according to the bulk Richardson number, as is standard for surface energy balance models (e.g. Braithwaite, 1995; Fyffe et al., 2014; Reid and Brock, 2010).

The CMB-DEB model incorporates solid precipitation to enable the model to calculate specific mass balance rather than ablation alone for the debris-covered area. The model

also incorporates calculation of surface vapour fluxes, surface and subsurface melt, and refreezing of liquid water in the snowpack to achieve specific mass balance (Collier et al., 2014). The presence of solid precipitation is assumed when air temperature is below 0°C and precipitation occurs. Alongside the incorporation of solid precipitation, CMB-DEB also includes evolution of snow surface albedo and roughness with depth and age, snowpack compaction and densification by refreezing, the influence of penetrating solar radiation, and the refreezing and conduction of the near-surface englacial temperature distribution (Collier et al., 2014).

Moisture content within the debris layer is included through a reservoir system, which allows moisture accumulation and phase changes. The depth of the reservoir is determined using the sum of the porosity divided by the debris thickness, and so a single reservoir for the whole debris vertical column is used rather than individual reservoirs for each vertical layer. Moisture is assumed to occupy the lowest debris layers, following instant infiltration of water that has resulted from rainfall or melt of the overlying snowpack. During periods when the ice surface is at melting point, a minimum amount of water for saturation of the lowermost debris layer is assumed (Collier et al., 2014). Drainage of the reservoir is represented by the runoff timescale and is a linear function of terrain slope (Reijmer and Hock, 2008).

8.4.2. Experimental design

The CMB-DEB model was used to investigated the role of debris thickness, albedo and surface roughness on ablation using two versions of CMB-DEB to calculate specific water balance (b_w) for the debris-covered area of Khumbu Glacier: (1) A point model to investigate the extent of variability in ablation over an ablation season using field data, and; (2) A distributed model using gridded inputs produced from remotely sensed satellite data and field observations. The results presented in this study do not represent ablation for a specific year due to difference in the year in which input data were acquired.

All model simulations used a vertical column of between 0 and 15 m thickness with 0.01 m intervals to represent the debris-covered ice and to simulate the supraglacial debris

layer (up to 5.35 m thick) and overlying layer of solid precipitation (up to 2.85 m thick), with a 6 m thick column of ice underlying the debris layer.

All simulations were forced using meteorological data collected over a 173-day period between 1st May 2014 00:00 and 27th October 2014 23:00, which included the summer monsoon season. CMB-DEB included gridded incoming shortwave radiation timeseries to bring the model in line with other glacier models that consider the influence of aspect on ablation (e.g. Immerzeel et al., 2011; Ragettli et al., 2015). Short timescale variations in shortwave radiation were refined through incorporation of temporal variability in solar azimuth angle and solar zenith angle (sourced from NOAA, 2017), and hillshade for each hour of the study period (calculated used ArcGIS toolboxes, 2017). Spatial variability in incoming shortwave radiation was incorporated using the aspect and slope of the simulated debris surface, following the method of Hock and Noetzli (1997).

8.4.3. Point CMB-DEB model

The point model was used to test the effect of a range of values for each variable on ablation, firstly by testing each variable individually, and then in combination with one other. Tested values for debris thickness, albedo and z_0 were defined by the values collected during fieldwork (Table 8.3) and published values (Table 8.4). In simulations when only one variable was changed, the others were set to published values; supraglacial debris albedo was 0.13 (Collier et al., 2014; Brock et al., 2010), debris thickness was 0.38 m (the mean value for Khumbu Glacier; Soncini et al., 2016); and z_0 was 0.016 m (Brock et al., 2010). Variability in incoming solar radiation was included through the use of constant aspect (120°), slope (7°) and elevation (4950 m a.s.l.) values.

Table 8.3. Data ranges and the associated increments tested for supraglacial debris layer thickness, albedo and aerodynamic roughness length for point simulations, collected from fieldwork undertaken on Khumbu Glacier between 9th May 2014 and 26th May 2014. Where the maximum or minimum values derived from field data were lower than previously published values the field-derived values are in brackets.

Debris parameter	Data range	Increments tested in simulations
Debris thickness (m)	0 – (2.0) 3.0	0.02
Albedo	0.06 – 0.82	0.02
Aerodynamic roughness length (m)	0.001 – (0.02) 0.03	0.001 (single variable point model) 0.005

Table 8.4: Published values of supraglacial debris layer thickness, albedo and aerodynamic roughness length for supraglacial debris, or ice and snow where stated.

Mean supraglacial debris thickness (m)		
0.42	Imja-Lhotse Shar Glacier, Nepal Himalaya	Rounce and McKinney (2014)
0.38	Khumbu Galcier, Nepal Himalaya	Soncini et al (2016)
0.23	Miage Glacier, Italian Alps	Reid and Brock (2010) Foster et al. (2012)
Albedo (%)		
0.07	Mean dry debris Larsbreen, Svalbard	Nicholson and Benn (2006)
0.03	Mean wet debris, Ghiaccaio del Belvedere, Italian Alps	Nicholson and Benn (2006)
0.3	Ngozumpa Glacier, Nepal Himalaya	Nicholson and Benn (2012)
0.13	Miage Glacier, Italian Alps	Brock et al. (2010)
0.1	Schistose debris Khumbu Galcier, Nepal Himalaya	Inoue and Yoshida, 1980
0.2	Granitic debris Khumbu Glacier, Nepal Himalaya	Inoue and Yoshida, 1980

0.18–0.6	Diurnal variation Khumbu Galcier, Nepal Himalaya	Kayastha et al. (2000)
0.2	Ngozumpa Glacier, Nepal Himalaya	Nicholson and Benn (2012)
0.34	Miage Glacier, Italian Alps	Reid and Brock (2010)
	Fresh snow Zhadang Glacier, Tibet	Molg et al. (2012)
0.34	Ice, Miage Glacier, Italian Alps	Brock et al. (2010)
0.27	Artificial debris	Lejeune et al. (2013)
Aerodynamic roughness length (m)		
0.016	Miage Glacier, Italian Alps	Brock et al. (2010)
0.0063	Khumbu Glacier, Nepal Himalaya	Takeuchi et al. (2000)
0.0035	Khumbu Glacier, Nepal Himalaya	Inoue and Yoshia (1980)
0.011	Cobble to gravel debris (0.05–0.25 m) Imja-Lhotse Shar Glacier, Nepal Himalaya	Rounce et al. (2015)
0.030	Cobbles (0.15–0.25 m) Imja-Lhotse Shar Glacier, Nepal Himalaya	Rounce et al. (2015)
0.007	Sand to cobbles (up to 0.15 m) Imja-Lhotse Shar Glacier, Nepal Himalaya	Rounce et al. (2015)
0.011	Cobbles to boulders (0.25–0.40 m) Imja-Lhotse Shar Glacier, Nepal Himalaya	Rounce et al. (2015)
0.03	Moraine, McMurdo Dry Valleys	Lancaster, 2004
0.001	Ice Miage Glacier, Italian Alps Villarrica Glacier, Chile	Reid and Brock (2010)
0.003	Rough glacier ice	Smeets et al. (1999)
0.05	Very rough glacier ice	Obleitner (2000)
0.0002	Fresh snow	Poggi (1977)
0.0009	Glacier snow	Greuell and Smeets (2001)
0.018	Supraglacial debris – sandy gravel with cobbles	Quincey et al., 2017
0.02	Cobbles and boulders	Quincey et al., 2017

8.4.4. Distributed CMB-DEB model

The distributed model simulated specific mass balance for the debris-covered area of Khumbu Glacier (Figure 8.2b) at a grid spacing of 30 m. Specific mass balance was calculated independently for each cell. Debris thickness was 0.38 m when not varied, which is the mean value derived from the thickness map for Khumbu Glacier (Soncini et al., 2016). Albedo was set to 0.13 when not varied, which was derived from Miage Glacier (Brock et al., 2010) and has been used in the majority of previous simulations of surface energy balance of debris-covered ice (Collier et al., 2013; Collier et al., 2014; Fyffe et al., 2014; Reid and Brock, 2012). z_0 was set to 0.016 m when not varied using a value calculated for debris-covered ice at Miage Glacier by Brock et al. (2010), and subsequently used in surface energy balance models for debris-covered ice (e.g. Collier et al., 2013; Fyffe et al.,2 014; Reid and Brock, 2012). Mean values for albedo and aerodynamic roughness length were also used, with mean values calculated from the distributed input data. Debris thickness, albedo and z_0 were varied through including the debris thickness map produced for Khumbu Glacier (see Section 2.2; Figure 8.5a), and the two maps derived of albedo and z_0 derived from classification of the 2016 Pleiades data (Figures 8.5b and 8.5c).

To account for spatial variability in meteorological variables, lapse rates were applied to air pressure (–0.0617 HPa m^{-1} from Baltoro Glacier, Karakoram following Mihalcea et al., (2006)) and air temperature (–0.0046 °C m^{-1} for the monsoon period at Khumbu Glacier following Shea et al. (2015)). Incoming solar radiation was incorporated on a cell-by-cell basis by correcting incoming shortwave radiation using aspect, slope, daily solar azimuth angle, daily solar zenith angle and hourly hillshade calculations. Consequently, when included in a simulation, incoming solar radiation was temporally variable for each cell. Cells identified as containing supraglacial water were excluded from the model domain (these cells were given values of NaN (no data)), due to the complex surface energy balance processes that occur on these supraglacial water bodies (Miles et al., 2016), which was beyond the scope of this study.

Ten simulations were run using the distributed model. Simulation 1 was the baseline result, in which no inputs were varied. Simulations 2, 3 and 5 included spatially variable debris thickness, albedo and z_0 individually, whilst the other two variables were spatially

constant. Simulations 7, 8 and 9 kept one variable spatially constant whilst the other two were varied. Simulation 10 varied debris thickness, albedo and z_0 to test the combined influence of these three variables on mass balance of debris-covered ice. Mean values for albedo and aerodynamic roughness length were substituted for variable inputs in Simulations 4 and 6, respectively. These simulations were undertaken to determine whether a mean value for a input variable, which has been constrained by empirical data and calculated from the spatially-variable input variable, would constrain specific mass balance estimates to the same degree as using spatially-variable input variables , as would be expected.

8.5. Results

CMB-DEB calculates both the input of mass to each cell from snowfall and the loss of mass by ice surface ablation. Therefore, the results in each case are given as the specific mass balance (b_w) in water equivalent (w.e.) for either the point or the debris-covered area.

8.5.1. Point model simulations

8.5.1.1. Single variables

In the first experiment with the point model, one variable (debris thickness, albedo or z_0) was tested in each simulation using values derived from field and published data (Tables 8.1 and 8.2). The results followed the expected pattern observed in the field; as debris thickness increased b_w initially increased to a maximum of 2.2 m w.e. at a debris layer thickness of 0.028 m, and then exponentially decreased to approach zero when debris thickness exceeded 1.5 m (Figure 8.6a). Contrary to previous simulations undertaken using CMB-DEB, the Østrem curve was simulated by this point model, which is attributed to the inclusion of variable incoming shortwave radiation. Increasing albedo from 0.06 to 0.82 resulted in a linear decrease in b_w from 0.32 to 0.02 m w.e., with a lessening effect on ablation as albedo increased further to 1 (Figure 8.6b). An increase in z_0 from 0.0001 to 0.03 m resulted in a slight decrease in b_w from 0.31 to 0.29 m w.e. (Figure 8.6c). b_w was most sensitive to debris layer thickness and least sensitive to z_0 across the realistic range of values tested here. These results confirm the importance of debris thickness on ablation from debris-covered ice, but also indicate that variations in albedo and z_0 values are still influential to specific mass balance.

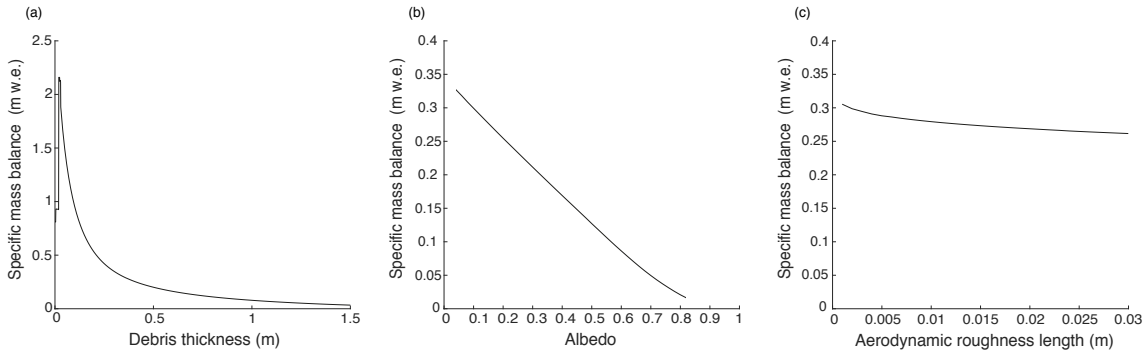

Figure 8.6: Plots of specific mass balance with (a) increasing debris thickness, (b) increasing albedo and (c) increasing aerodynamic roughness length. The ranges of each parameter were constrained using field-derived and previously published data. Values of specific mass balance are negative in all cases.

8.5.1.2. Multiple variables

In the second experiment using the point model, debris thickness, albedo and z_0 were varied alongside one another in a factorial experiment that used the values derived from field data and previously published studies (Table 8.3). This experiment confirmed an exponential decrease in b_w due to increasing debris thickness, and the critical threshold of 0.5 m below which the rate of change in this relationship was less (Figure 8.7), as previously identified by Nicholson and Benn (2006) and Foster et al. (2012). Where debris was less than 0.5 m thick, b_w decreased rapidly between from 6.0 to 1.5 m w.e. (across all variable albedo and z_0 simulations), but when debris was greater than 0.5 m thick, only a minimal decrease in b_w occurred from 1.5 to 0 m w.e.. Albedo had the most influence on b_w when the debris layer was 0–0.2 m thick, with an increase in albedo of 20% (0.2) resulting in a decrease in b_w of about 1 m w.e.. Where debris was greater than 0.2 m thick, an increase in albedo of 20% resulted in less than a 0.1 m w.e. decrease in b_w. z_0 had the weakest influence on b_w when varied alongside the two other parameters. An increase in z_0 of 0.05 m resulted in a decrease in b_w of about 0.1 m w.e. for debris less than 1.8 m thick, whilst negligible variation in b_w occurred with increasing z_0 when the debris layer was greater than 1.8 m thick. This experiment shows the same the hierarchy of controls of b_w as the single variable experiments with debris thickness being the primary control, succeeded by albedo and then z_0. Consequently, when supraglacial

debris layers are below 0.2 m variability in albedo and z_0 should be included in simulations of glacier mass balance. However, for supraglacial debris layers thicker than 0.2 m spatial variability in albedo and z_0 will have little effect on model results.

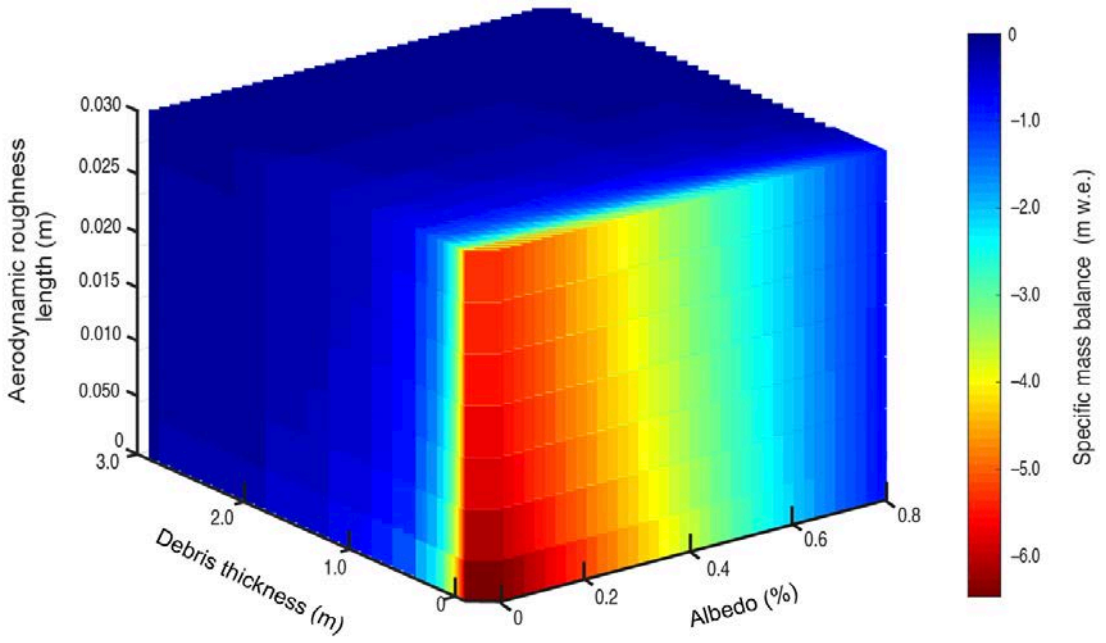

Figure 8.7: A surface plot of specific mass balance calculated from the point-based model simulation in which each combination of the variable parameters (debris thickness, albedo and aerodynamic roughness length) were tested, showing the majority of variability in ablation with differing albedo and z0 occurs in debris layers <0.2 m thick.

8.5.2. Distributed model simulations

Ten experiments were performed with the distributed model, with a range of combinations of variables in each simulation (Table 8.5). All simulations gave negative mean values for b_w (Figure 8.8). The most notable variations in total and mean b_w were observed when the variable debris thickness was included (Table 8.5; Figure 8.8; Figure 8.9b). Simulations 2 (Figure 8.9a) and 10 (Figure 8.9c) showed decreasing b_w with decreasing distance to the glacier terminus (Figure 8.9d) as the debris layer thickens towards the terminus (Figure 8.5). Simulation 1 displayed an almost constant b_w with

distance to the terminus as debris thickness was constant for all cells, although some variability was displayed along the profile due to varying incoming shortwave radiation flux. The inclusion of variable debris thickness resulted in an increase of +223% in total b_w between Simulation 1 (fixed parameters; Figure 8.9a; Table 8.5) and Simulation 2 (variable debris thickness; Figure 8.9b; Table 8.5). The mean and median b_w for Simulation 2 (mean b_w: -0.85 m w.e., median b_w: 0.66 m w.e.; Table 8.5) were greater than Simulation 1 (mean b_w: -0.26 m w.e., median b_w: 0.26 m w.e.) with a much greater range of values and higher maximum b_w (Simulation 1: -0.62 m w.e., Simulation 2: -4.1 m w.e.; Table 8.5). Inclusion of variable albedo (Simulation 3) and z_0 (Simulation 5) individually resulted in a decrease of 48% in b_w for albedo, and of 4% for z_0, compared to the baseline (Simulation 1). The combined influence of albedo and z_0 (Simulation 7; fixed debris thickness) resulted in a decrease in total b_w of 47%, when compared to the baseline simulation (Table 8.5).

Table 8.5: The variable model inputs and statistics for each of the ten distributed simulations in which specific balance (b_w; m w.e.) was calculated over the 2014 ablation season across the debris-covered area of Khumbu Glacier. Standard deviation values are that of all cells in the model domain. 'Y' displays when a variable is spatially-variable in a simulation, 'M' is where the mean value is used, and 'N' is when the variable is spatially constant. In the case of debris thickness, the mean and non-variable values were the same.

Model run no.	dT	Albedo	z_0	Specific mass balance (kg m^2)	Mean b_w (m w.e.)	Median b_w (m w.e.)	Minimum b_w (m w.e.)	Maximum b_w (m w.e.)	St. Dev. b_w (m w.e.)
1	M	N	N	-3436.3	-0.262	-0.259	-0.006	-0.631	0.111
2	Y	N	N	-11107.9	-0.847	-0.656	-0.001	-4.105	0.812
3	M	Y	N	-1801.6	-0.137	-0.124	-0.006	-0.528	0.083
4	M	M	N	-1801.6	-0.137	-0.124	-0.006	-0.528	0.083
5	M	N	Y	-3588.4	-0.273	-0.271	-0.006	-0.716	0.123
6	M	N	M	-3588.4	-0.273	-0.271	-0.006	-0.716	0.123
7	M	Y	Y	-1809.2	-0.138	-0.122	-0.006	-0.566	0.087
8	Y	N	Y	-11314.7	-0.863	-0.664	-0.006	-4.302	0.832
9	Y	Y	N	-5543.8	-0.422	-0.308	-0.001	-2.669	0.427
10	Y	Y	Y	-5490.2	-0.419	-0.302	-0.006	-2.684	0.428

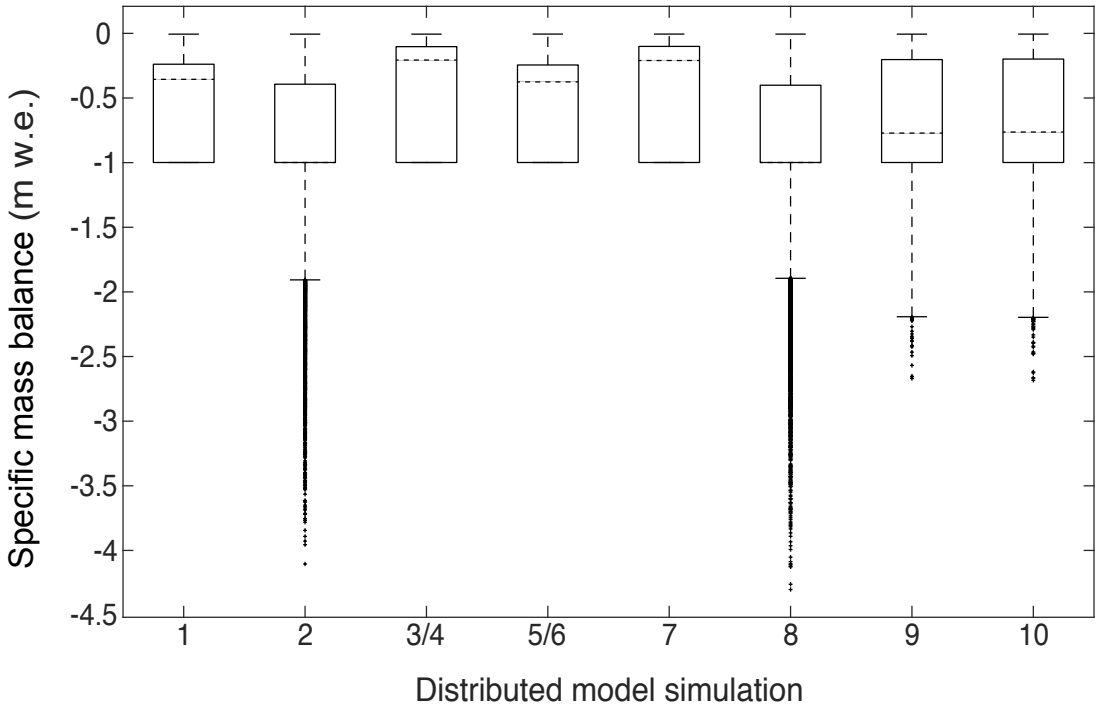

Figure 8.8: Box plots of specific mass balance calculated for each distributed model simulation. Median is depicted by the dashed line, specific mass balance is shown to have the greatest range of values when spatially variable debris thickness is included, and median specific mass balance varies considerably between distributed model simulations. Identical box plots are labeled the box plot is displayed once and corresponding model simulation numbers are displayed below.

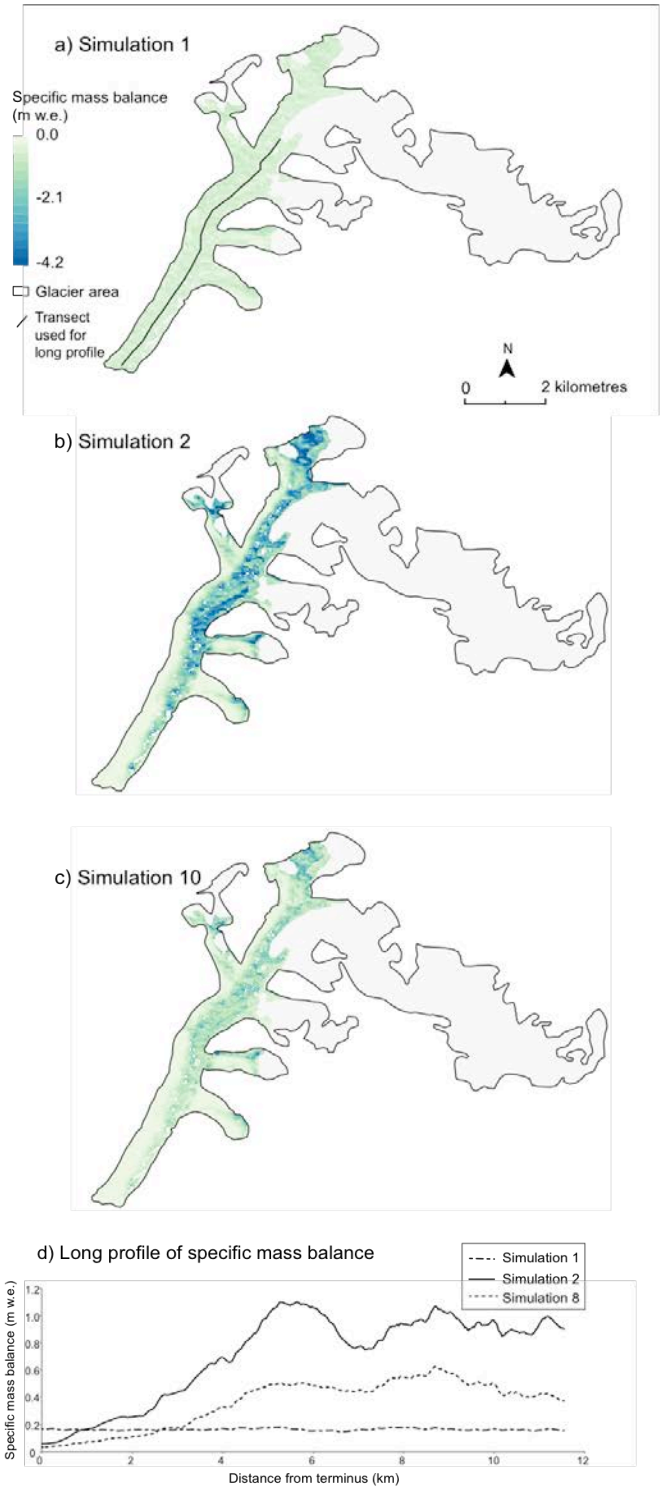

Figure 8.9: Specific mass balance variability (b_w) across Khumbu Glacier's debris-covered area calculated for three model simulations in which (a) debris properties were spatially constant (Simulation 1), (b) spatially variable debris thickness was included (Simulation 2) and (c) all variables debris properties considered were varied (Simulation 10). (d) The longitudinal profile of total b_w for each of the three model runs displayed in (a)–(c). The location of the longitudinal profile displayed in (d) is shown in (a).

Simulation 10 (all variables included) displayed an increase in b_w of 60% when compared to Simulation 1 (baseline), and a decrease in b_w of 51% when compared to Simulation 2 (variable debris thickness). The difference in mean, median and maximum b_w was also notably different for Simulation 1, 2 and 10, with maximum b_w in Simulation 10 (maximum b_w: -2.68 m w.e.) being 2 m w.e. greater than Simulation 1 (maximum b_w: -0.63 m w.e.), and 1.4 m less than Simulation 2 (maximum b_w: -4.11 m w.e.). A similar pattern existed for the mean and range of b_w in each of these results, whilst median b_w for Simulation 10 was 0.16 m greater than Simulation 1 and less than half that for Simulation 2.

To gain an insight into the difference in temperature through the debris layer, the debris temperature profiles through the debris layer at each time step were extracted for cells with the maximum, median and minimum b_w values occurred from Simulation 10 (Figure 8.10). These three cells displayed differing site characteristics including in their slope, aspect and elevation, in addition to variability in debris thickness, albedo and z_0 (Table 8.6). The cells were all located near to the mid line of the glacier, with the maximum b_w cell located in the upper debris-covered area, the minimum b_w cell in the middle of the glacier, and the median b_w cell location near the terminus. All three cells showed diurnal variability in temperature through the debris layer, and the debris layer and underlying 1.2–1.95 m of ice were above 0°C almost exclusively during the months of July and August in all simulations. During July and August the cell that displayed the minimum b_w had a consistently lower temperature and less pronounced diurnal variation that the other two cells, with any diurnal variation that did occur not penetrating the entire debris layer. Consequently, in periods where higher temperature occurred in the upper and mid sections of the debris layer sufficient thermal energy was not transmitted far enough through the debris layer to raise the temperature at the debris-ice interface.

Table 8.6: Variable values and resultant specific mass balance (b_w) for the cells with the minimum, maximum and median b_w in Simulation 10, in which all variable debris inputs were included.

	Albedo	Debris thickness (m)	Z_0 (m)	Slope (°)	Aspect (°)	Elevation (m a.s.l.)	b_w (m w.e.)
Minimum b_w	0.43	0.63	0.00878	35.8	33.7	5198	-0.006
Maximum b_w	0.27	0.05	0.01473	31.8	203.8	5143	-2.684
Median b_w	0.27	0.46	0.01473	17.1	181.5	5101	-0.302

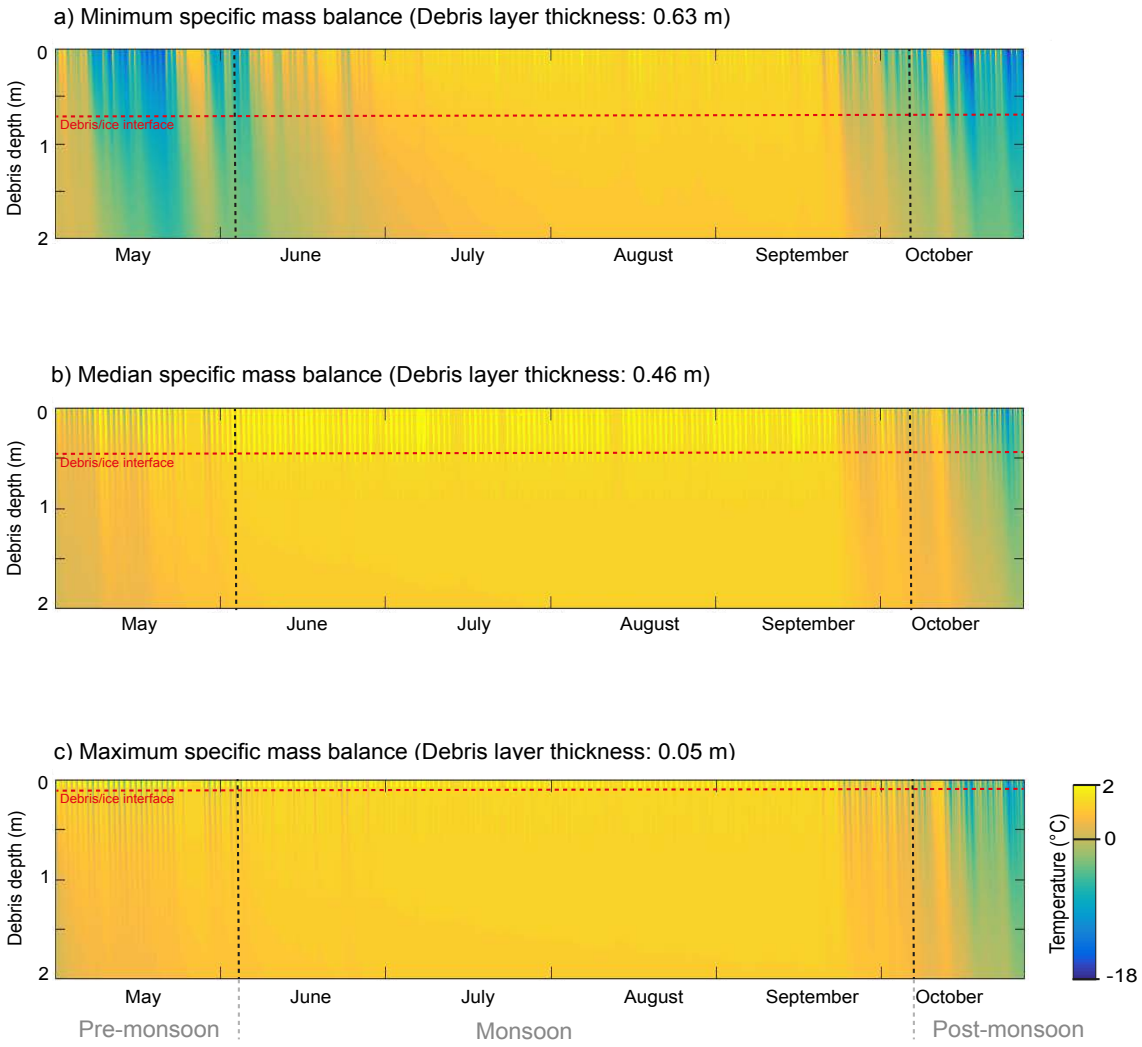

Figure 8.10: The subsurface thermal regime through the supraglacial debris layer and underlying ice over the modelled monsoon-influence ablation season period for (a) the cell with the minimum b_w, (b) the cell with the median b_w and (c) the cell with the maximum b_w in the distributed simulation 10.

The difference in the thermal regime of the three cells was most apparent during the onset of the monsoon (May and June) and as the monsoon subsided (end of September and October). For the cell with maximum b_w the temperature at the debris-ice interface decreased to around -18°C during diurnal cycles in the monsoon onset, whilst in the cell with median b_w this decreases in temperature did not penetrate to the debris-ice interface. As the monsoon subsided, the debris layer stayed below 0°C from mid-October

onwards for the cell with the minimum b_w, whilst the colder temperatures did not consistently penetrate lower layers of the debris layer in the median cell until near the end of October. The cell with the minimum b_w displays a markedly different thermal regime; despite having a relatively thick debris layer (0.63 m), which is attributed to the cell's north-north-westerly aspect (33.7°), whilst the other two cells had a southerly aspect, resulting in cooler mean diurnal temperatures during the Pre-monsoon, end of the monsoon and post-monsoon periods. The difference in aspect would have affect the total daily incoming solar radiation received at the cell and would have resulted in less thermal energy transferred from the air into the debris surface. The combination of a relatively thick debris layer (0.63 m) and an aspect of 33.7° have resulted in a relatively low transfer of thermal energy into the debris layer due to the aspect, and then little of this thermal energy transferred intot he underlying ice due to thickness of the debris layer.

Finally, to explore how b_w calculated in Simulation 10 corresponded to the Østrem curve, mean b_w was plotted against debris thickness for all cells in the model area (Figure 8.11). Between 0.01 and 0.5 m thickness, the mean and standard deviation of b_w was calculated in 0.01 m increments. No cells contained a debris thickness less than 0.01 m. For debris thicknesses between 0.5 and 1.0 m, b_w was calculated in 0.1 m increments, and then for debris thickness between 1.0 and 3.0 m in 0.5 m increments. A peak in b_w occurred where debris was between 0.02 and 0.03 m thick, followed by decreasing b_w with increasing debris thickness, indicating the critical debris thickness for Khumbu Glacier was between 0.02 and 0.03 m, in line with previous investigations on glaciers globally (Østrem, 1959; Mattson et al., 1993; Nicholson and Benn, 2006). All distributed model results also resulted in an Østrem curve with an effective thickness of between 0.02 and 0.03 m.

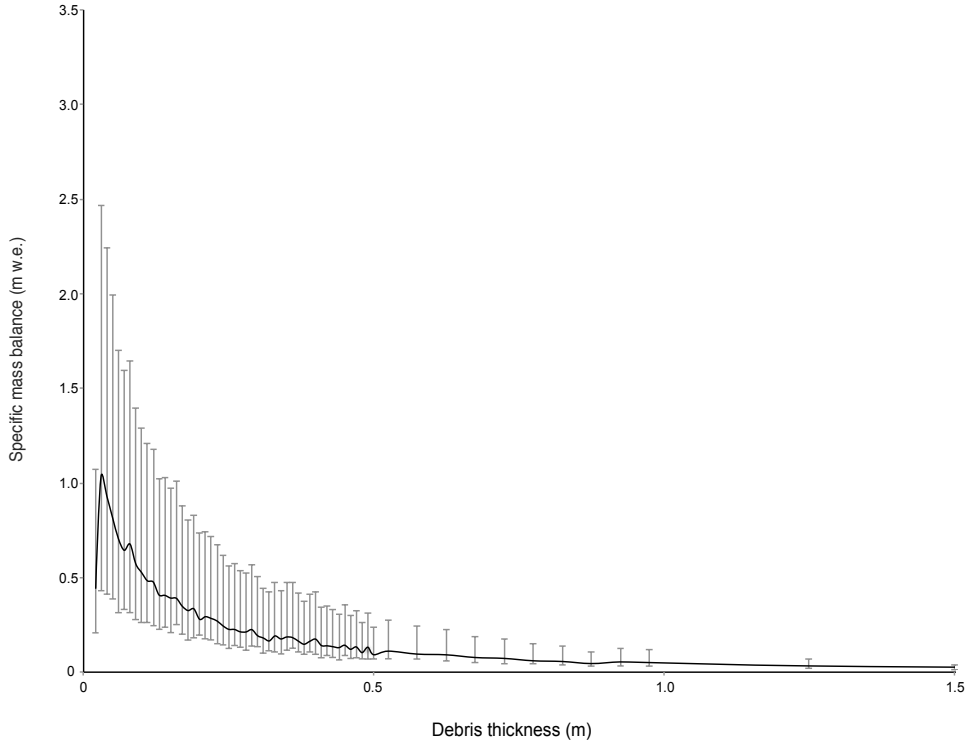

Figure 8.11: An example on one of the Østrem curves formed from each of the distributed model simulations: Mean total (negative) b_w and associated standard deviation plotted against debris thickness for all cells in Simulation 10, displaying the Østrem curve now simulated in CMB-DEB, and an effective thickness of between 0.02 and 0.03 m. Mean b_w was calculated for 0.01 m increments between 0.1 and 0.5 m, 0.1 m between 0.5 and 1.0 m, and 0.5 m increments thereafter.

8.6. Discussion

8.6.1. Mass balance calculations

Although the results of the model simulations do not represent ablation for a specific year on Khumbu Glacier, the results from the distributed simulations indicate spatial variability in supraglacial debris layer surface properties can have an important influence on spatial variability in b_w across a monsoon-influenced debris-covered glacier surface. These results also suggest such spatial variability in debris properties affects the transfer of heat to the debris-ice interface during the transition between pre-monsoon, monsoon and post-monsoon seasons (Figure 8.10). Of the three parameters tested; debris thickness, albedo and aerodynamic roughness length, a hierarchy of parameters was

identified, displayed by their relative influence on b_w in the point and distributed simulations. The distributed model results showed that these parameters had a varying influence on b_w, confirming that incorporation of spatially variable debris thickness has a sizeable effect on calculated mass balance in surface energy balance models, with an increase in b_w of +233% compared to the simulation where debris thickness was constant between cells. Conversely, the inclusion of spatially variable albedo and aerodynamic roughness length decreased the range and total b_w when compared to inclusion of variable debris thickness alone. The notable differences between b_w from each of the distributed model results, which each include different combinations of spatially variable debris properties, suggests that incorporation of debris thickness may not be sufficient to provide accurate estimations of b_w, and that additional spatially variable properties such albedo and aerodynamic roughness length also need to be incorporated. However, to confirm whether there is an optimal combination of spatially variable debris parameters that simulate b_w most accurately, *in situ* data mass balance data is needed for comparison to model results.

Whilst inclusion of spatially variable input variables, such as those use in the majority of the distributed simulations, provides an interesting insight into the pattern of spatially variable b_w across a debris surface with spatially varying debris properties, the use of mean values for tested debris properties (e.g. debris thickness, albedo and aerodynamic roughness length) provided the same total specific mass balance values. Using such mean values instead of spatially variable input variables allows modelling time to be decreased dramatically and results would still incorprate the influence variability in debris properties have on total specifc mass balance. Ssuch streamlining of the modelling process would provide results that were viable when comparing total b_w between mass balance years and if temporal variability in debris properties was considered, as such change would subsequently influence the mean values for debris properties. However, simplification of the modelling procedure in such a way would omit the advantage of visual analysis for b_w, as presented in Figure 8.9, which could provide particularly useful for understanding the role of supraglacial debris properties on b_w in localised regions of a glacier and the interaction between debris properties. Consequently, with regards to whether spatially variable debris properties or mean values for debris properties are

used in a modelling process would be dependent on the outcome required and the nature of the analysis to be undertaken.

8.6.2. Assumptions of mass balance modelling

As with all surface energy balance models of debris-covered ice (e.g. Reid and Brock, 2010; Lejeune et al., 2013; Collier et al., 2014; Evatt et al., 2015), CMB-DEB does include a number of assumptions with regard to the different energy fluxes at the debris surface and through the debris layer, and represents a simplified version of the processes by which glacier mass balance is influenced by a supraglacial debris layer with a variety of data sets collected at different points in time between 2014 and 2016. One of the most notable limitations of previous CMB-DEB models used in Collier et al. (2013; 2014) was that the model did not reproduce the Østrem curve. However, through the incorporation of temporally variable incoming solar radiation into the numerical model, CMB-DEB now simulates this curve, which causes sufficient diurnal variability in incoming energy to the debris layer to recreate the diurnal variations in thermal transfer through the debris layer, and thus the true pattern of ablation with debris layer thickness, observed in the field. Previous proposals for why CMB-DEB did not simulate the Østrem curve were attributed to low nighttime air temperatures producing freezing events, changes in the surface albedo as debris cover becomes more continuous, and wind-driven evaporation inside the debris layer (Collier et al., 2014). The former of these reasons is considered invalid, as similarly low nighttime air temperatures occurred over the study period on Khumbu Glacier simulated here, and caused freezing events in the debris layer, yet an Østrem curve was still produced in all point and distributed model simulations.

When considering albedo variability, the point model simulations in which all variable parameters are varied simultaneously (Figure 8.7) reiterates the importance of albedo in thinner debris layers (less than 0.2 m thick). Consequently, the extent to which debris cover is continuous would affect albedo of a debris surface, and is spatially variable. The influence of patchy supraglacial debris cover will therefore be important for mass balance estimates where spatial variability in debris properties are considered. Porosity, and its influence on turbulent fluxes as detailed in Evatt et al. (2015), will also be a spatially variable parameter, and may therefore affect total b_w calculations from CMB-DEB if the effect of spatially variable as well as depth variable porosity were to be included.

Additionally, spatial variation in porosity will affect moisture content within the debris layer. Consequently, inclusion of spatially variable porosity and therefore wind-driven evaporation and moisture content through a debris layer, and further parameterisation of debris cover on a finer resolution to enable consideration of patchy debris and its potential effect on glacier albedo, should both be explored as new developments for CMB-DEB to further refine the model.

8.6.3. Accuracy of spatially variable debris properties

Assigning z_0 to cells using surface roughness is a much-simplified approach to forming an accurate map of z_0 across the glacier ablation area. Specifically, issues arise with scaling of the roughness parameter from the calculated plot size of 3 × 3 m to a 30 × 30 m cell size in the resultant map, and the application of spatial variability in z_0 without interaction between model cells. As mentioned in Section 8.1, aerodynamic roughness length is scale-dependent, with a doubling in z_0 resulting in increase of turbulent fluxes by around a third (Brock et al., 2010), and varies dependent on the scale measured due to multiple scales of topographic variability (Smith et al., 2016). Aerodynamic roughness length also varies due to the turbulence arising from the topography over which air has passed (Cuffey and Paterson, 2010; Smith et al., 2016). Despite the simplification of the approach used here to produce a glacier-wide map of z_0, such an investigation as this is deemed appropriate to provide an initial understanding of how z_0 varies over a debris-covered glacier, and the influence of such variability on mass balance. Combining the methods of this study with other discrete data, such as those collected by Rounce et al. (2015), Miles et al. (2017) and Quincey et al. (2017), will improve quantification of z_0 on a debris-covered glacier surface and its variability in time and space.

To model spatial variability in z_0 accurately the influence of surrounding topography on z_0 needs to be included in modelling procedures, through developing a method by which interaction between cells in distributed models can be incorporated, and using z_0 values appropriate to the resolution of the remotely sensed data used. An optimum resolution of other spatially variable input parameters also needs to be identified, in which the extent to which spatial variability in debris properties occurs is considered alongside computational power needed for high resolution classification of remotely-sensed data and for running numerical models with increasingly smaller cell sizes. Also, as observed

from the comparison of distributed model results in which spatially variable debris thickness was included with and without additional variables, the inclusion of different combinations of spatially variable debris properties affect estimates of b_w substantially. Consequently, to simulate the surface energy balance of and heat transfer through a debris layer more precisely, inclusion of a full suite of spatially variable debris properties in distributed surface energy balance and heat transfer models should be explored and, most importantly, their influence compared to *in situ* mass balance data.

The variability in b_w with variability of albedo and aerodynamic roughness length for debris layers less than 0.2 m (observed in Figure 8.7) suggests particular focus should be given to the influence of spatially variable debris parameters in these thinner debris layers, such as in the upper reaches of a glacier ablation area or on glaciers where the supraglacial debris layer has not yet evolved to be continuous across the ablation area. A further consideration is the influence of temporal variability in debris distribution and associated properties; Gibson et al. (2016; 2017) identified sub-decadal variation in supraglacial debris distribution across a debris-covered glacier surface, which would affect the distribution of debris properties through time due to varying rates of debris input, transport and deposition. Future work that considers spatial variability in debris properties and their effect on mass balance should therefore also consider the influence of temporal variability in such properties.

8.7. Conclusion

This study employed the full surface energy balance and heat transfer model, CMB-DEB, to the debris-covered area of Khumbu Glacier over a monsoon season, to explore the influence of spatial variability in debris layer thickness, albedo and aerodynamic roughness on mass balance estimations. These model results indicated a notable variation in the extent of specific mass loss over an ablation season depending on the combination of spatially variable debris parameters included in simulations. Whilst incorporating spatially variable debris thickness into a distributed model more than doubled specific mass balance (b_w) calculated, the addition of spatially variable albedo and aerodynamic roughness length reduced calculated specific b_w estimates. To compare the extent to which the inclusion of each of the spatially variable debris parameters tested affects the accuracy of specific b_w estimates further investigation is needed in

which all data are collected from a single ablation season alongside *in situ* measurements of mass loss.

A supraglacial debris layer is neither static in space or time, due to variability in debris input, transport and deposition. Such variability in supraglacial debris distribution will affect, among other properties, the distribution of debris lithologies, debris grain size and debris layer thickness. The results presented here suggest that such spatial variability in debris properties are influential on the rate at which glacier b_w occurs. Consequently, to accurately simulate the response of Himalayan, and other debris-covered glaciers globally, to current and future climate change it is imperative that future numerical models simulating mass balance for debris-covered glaciers include spatially variable supraglacial debris properties. Additionally, future work should consider including the temporal variability in debris properties if undertaking multi-year estimates of mass balance.

Chapter 9: Discussion

9. Discussion

The research presented in this thesis was undertaken with the aim of investigating the extent of spatial and temporal variations in supraglacial debris properties across two debris-covered glaciers in the Himalayan-Karakoram, and the role these variations may play in mass balance of such glaciers. This aim was chosen to address the lack of previous research focused on the spatiotemporal nature of supraglacial debris layers. Until now, an absence of consideration for spatiotemporal variability in a supraglacial debris layer and its properties have led to the inclusion of supraglacial debris in numerical models of debris-covered glaciers to be undertaken in a much-simplified way, largely without any spatially or temporally variable element (e.g. Shea et al., 2015; Carenzo et al., 2016), or to omit the influence of supraglacial debris on mass balance entirely. Such a simplification stems, in part, from a lack of quantification of how supraglacial debris layers and their properties vary in space and time.

To achieve this thesis' aim a series of objectives were set in Chapter 1, based on four specific questions that arose from previous research, and could not be answered through current understanding of supraglacial debris and its role in ablation. The four questions posed in Chapter 1 are used as structure for this discussion, within which the thesis aim and objectives will be referred to. The discussion focuses on using the research undertaken in Chapters 5–8, which is based on two specific glaciers, and considering what can be gained from these studies of specific glaciers for general understanding of debris-covered glaciers in the Himalaya-Karakoram, and globally. A critical reflection of the methodology and methods used in this thesis, and areas of research still to be achieved are also included throughout the discussion.

Q1: *To what extent do supraglacial debris layer properties vary in space and time across a debris-covered glacier surface?*

The extent to which supraglacial debris properties vary across a debris-covered glacier surface was addressed in Chapters 5, 6, 7, and to some extent, 8. In all cases spatial variability in supraglacial debris properties was identified, whilst spatiotemporal variability in debris distribution was identified on Baltoro Glacier from remotely sensed data presented in Chapter 7. On Khumbu Glacier spatial variability in supraglacial debris

properties was identified over distances of the order of less than ten metres, with variability in debris grain size and lithology all occurring between sites in close proximity, and controlling variability in near-surface debris temperature. These controls were independent of debris layer thickness as all temperature sensor sites were located on debris layers greater than 1 m thick. Statistical analysis undertaken on the field data presented in Chapter 5 also demonstrated that slope and aspect of sites were important drivers of spatial variability in near-surface debris temperature, and in Chapter 8 slope and aspect were also identified as important controls on spatiotemporal variability in ablation, enabling the simulation of an Østrem curve in distributed model results. These site characteristics have been incorporated into simulations of ablation for debris-covered glaciers previously (e.g. Immerzeel et al., 2011; Ragettli et al., 2015), but absolute evidence for the nature of the control that slope and aspect have on supraglacial debris surface energy exchange has not been explicitly confirmed for debris-covered ice previously.

Three debris parameters; debris thickness, albedo and aerodynamic roughness length were the focus of investigation into spatiotemporal variability of debris properties across a debris-covered glacier surface. Whilst spatial variability in debris layer thickness is well documented (e.g. Mihalcea et al., 2008a; 2008b; Zhang et al., 2011; Foster et al., 2012; Minora et al., 2015; Soncini et al., 2016), the most straightforward variability in these three debris properties to identify, due to the ability to identify its variability from spectral reflectance differences in remotely sensed data, was lithology. Analysis of Baltoro Glacier's supraglacial debris cover in Chapters 6 and 7 identified the variability in lithology that can occur between debris units across a glacier surface and it's influence on debris distribution, due to the differences in surrounding geology and erosion rate of different rock types (Anderson and Anderson, 2016). Nicholson and Benn (2006; 2012) first measured the variability in albedo with differing debris lithology through finding debris albedo varied from <0.1 to >0.9 over the surface of Ngozumpa Glacier in the Central Himalaya. A similarly wide range of variability in albedo was confirmed by the field data presented in Chapter 8, in which surface reflectance was found to vary from 0.06 to 0.82 over the debris-covered surface of Khumbu Glacier. However, variability in lithology not only affects debris albedo, but also bulk thermal conductivity of the debris layer (e.g. Kayastha et al., 2000; Reid and Brock, 2010; Brock et al., 2010; Juen et al.,

2013). Thermal conductivity was not varied with lithology in the numerical modelling undertaken in this thesis, as the focus of the debris properties chosen to investigate in the modelling was dictated by the site variables investigated in field data collection presented in Chapter 5. However, based on the modelling results presented in Chapter 8, which strongly suggest models simulating mass balance should include variability in debris properties, future distributed modelling procedures undertaken for debris-covered glaciers should investigate the importance of spatial variability in albedo alongside variations in thermal conductivity, as the latter of these two variables is considered to be an important control on heat conduction through a debris layer (Kayastha et al., 2000), and if including variation in lithology both variables should be varied accordingly.

The focus on aerodynamic roughness length in this thesis stemmed from a recent research focus highlighting spatial variability in this debris property, and due to the identification of grain size as a driver of spatial variability in near-surface debris temperature in Chapter 5, which has previously been identified as a control on surface roughness, and therefore aerodynamic roughness length, of a supraglacial debris layer (Nield et al., 2013). Additionally, recent research has suggested that understanding the importance of spatial variability in aerodynamic roughness length across a debris-covered glacier surface needs to be investigated through surface energy balance modelling (Rounce et al., 2015; Miles et al., 2017) and boundary layer wind profiles (e.g. Quincey et al., 2017). From time spent in the field it is apparent that a single aerodynamic roughness length value cannot represent the highly heterogeneous nature of a debris-covered glacier surface (Figures 5.2 and Figure 8.3), as has been assumed in previous research (e.g. Reid et al., 2012; Fyffe et al., 2014). However, research into accurately quantifying aerodynamic roughness length effectively is in its infancy (Rounce et al., 2015; Smith et al., 2016; Miles et al., 2017; Quincey et al., 2017), greatly aided by the use of Structure-from-Motion technology. The main difficultly in determining aerodynamic roughness length effectively is its scale dependence (Brock et al., 2006; Rees and Arnold, 2006; Miles et al., 2017). The surface roughness map presented here for Khumbu Glacier does not address the issue of scale for the aerodynamic roughness lengths calculated, but does provide an insight into the high level of spatial variability in surface roughness that exists across a debris-covered glacier such as Khumbu Glacier.

The extensive spatial variability in surface roughness observed on Khumbu Glacier may not occur on debris-covered glaciers where debris grains may not be as variable in size and lithology, or for debris layers of lesser thickness such as those present on the majority of debris-covered glaciers outside of the Himalaya-Karakoram (e.g Mihalcea et al., 2008b). The variability in debris grain size across a glacier will be dependent on the distance travelled by debris in the glacier system, and the extent to which sediment has been reworked and redistributed by additional glacial processes, such as hydrological networks (Sharp, 1949; Boulton, 1978; Irvine-Fynn et al., 2011). Such redistribution and reworking may also cause different debris lithologies to mix more thoroughly and form a less spatially heterogonous debris surface. Different debris lithologies will also weather at different rates, due to the hardness of minerals within them, which would affect grain size of supraglacial debris. Thinner debris layers would also exhibit smaller grain sizes, which may result in a lower surface roughness of the debris layer, as well as influencing debris layer porosity, and consequently moisture content and debris albedo. These considerations need further investigation, through comparative studies of debris-covered glaciers in which spatiotemporal variability of debris properties is investigated for a range of glaciers with differing supraglacial debris lithologies, and a range of grain sizes and debris layer thicknesses. Controls on the range of aerodynamic roughness lengths between glaciers could then be determined.

Inclusion of spatially variable albedo and aerodynamic roughness length independently varied mass balance estimates by –48% and +4%, respectively, when compared to a spatially constant debris layer. Whilst the difference in ablation due to spatially variable albedo was substantial (48%), spatially variable aerodynamic roughness length caused minimal variation in total specific mass balance values (4%). However, even a difference of 4% would produce a noteworthy difference in glacier annual mass, and without incorporating variability in such properties we will never gain a comprehensive understanding of how an extensive supraglacial debris layer affects ablation across an entire glacier surface.

The next stage in refinement of surface energy balance and heat transfer modelling for debris-covered glaciers is to ascertain the extent to which additional variables not

investigated in this thesis affect estimations of ablation. Whilst moisture content was included in the modelling undertaken in Chapter 8, and varied over the monsoon season with varying precipitation and air temperature, no consideration was given to spatiotemporal variability in porosity, and therefore moisture content, of the debris layer. These variables, although recognised to be important for surface energy balance and heat transfer of a supraglacial debris layer (Mattson, 2000; Collier et al., 2014; Evatt et al., 2015), were not investigated in Chapter 5's field data collection due to the complexity in measuring them precisely, and an inability to monitor the changes in these variables through time remotely. Future studies should therefore focus on quantifying spatially variable moisture content in supraglacial debris layers, and ways in which such variability can be simulated in numerical models. Variability in the timing of increasing near-surface debris temperature between sites, following the major snowfall event that occurred over the study period (Figure 5.3a,b), and the identified dependence of spatial variability is near-surface debris temperature on slope and aspect (Chapter 5), indicates that evaporation rate varies between sites, and so moisture content would also be expected to vary across a debris-covered glacier surface. Variation in porosity also needs to be investigated further, as the porosity of a debris layer affects the amount of convection between debris grains, and therefore the energy exchange that occurs with a debris layer (Brock et al., 2010; Evatt et al., 2015).

Q2: *Over what timescale does a supraglacial debris layer evolve?*

It is widely accepted that there is high spatial variability in thickness of supraglacial debris across a glacier surface, particularly for glaciers in the Himalaya-Karakoram (e.g. Mihalcea et al., 2006; 2008; Zhang et al., 2011; Foster et al., 2012; Rounce and McKinney, 2014; Minora et al., 2015; Soncini et al., 2016). However, little consideration has previously been given to temporal variation in debris distribution. The variability in debris distribution identified in Chapter 7 not only confirms temporal variability in distribution of supraglacial debris on Baltoro Glacier, but also that this variability can occur on sub-decadal timescales. Important variations in debris thickness were identified between 2001 and 2012 on Baltoro Glacier, which may have caused some areas of the supraglacial debris layer to increase in thickness over an critical thickness threshold of

around 0.05, or over a thickness of around 1 m, above which ablation is 90% less than debris free conditions (Reznichenko et al., 2010).

Sub-decadal variability in debris distribution on Baltoro Glacier has been attributed to short term variability in the amount of debris entering a glacier system and the surface velocity at which this debris load is transported. Baltoro Glacier, at around 62 km long, is a relatively large debris-covered glacier with a high surface velocity, and would therefore be considered to have a large supraglacial sediment load. It may be that for smaller debris-covered glaciers debris input to the glacier system would not be sufficient to cause notable variation in supraglacial debris layer thickness over sub-decadal timescales. Similarly, on low velocity glaciers, of which many debris-covered glaciers are (e.g. Khumbu, Ngozumpa or Imja Glacier (Quincey et al., 2009a)), debris transport would be slower, which would affect the rate of redistribution across a glacier surface. A low glacier surface velocity would also imply low englacial and subglacial ice velocity, which may cause the emergence of en- and sub-glacial debris to be slower.

The input and distribution of supraglacial debris in a glacier system is also controlled by the regional location of a glacier. The Himalaya-Karakoram has high rock uplift and subsequent erosion rates, and relatively high levels of precipitation, although frequency and magnitude of precipitation vary across the mountain range (Anders et al., 2006; Bookhagen and Burbank, 2010). Spatial variability in air temperature, and the range of air temperatures recorded, are also wide-ranging across the mountain range (Immerzeel et al., 2009). Both air temperature and precipitation will affect weathering and erosion rates of bedrock and consequently input of debris to glacier systems located in the region (Bishop et al., 2008). In mountainous regions where rock uplift rates are lower, or where precipitation and the range of air temperature experienced is less, erosion rates and therefore input of debris to glacier systems would be expected to be lower. Rates of erosion would also be affected by lithology of hillslopes surrounding glaciers (West et al, 2002). All of these controls on glacier systems differ between glaciers globally, and would result in differing rates of change in debris distribution through time.

Although the influence of glacier size, ice velocity and erosion rates on the rate of change in debris distribution can be discussed, minimal research has been undertaken that

allows comparison of these parameters and their influence on debris distribution. As the research presented in Chapter 7 includes, to the author's knowledge, the first glacier-wide sediment flux maps, and as this thesis is the first to consider the influence of spatiotemporal variability in supraglacial debris characteristics in detail, identifying a connection between regional and glacier characteristics and spatiotemporal variability in debris distribution is yet to be investigated. Previous work considering the evolution of debris distribution in a theoretical glacier system has simulated the processes by which debris is distributed (Rowan et al., 2015; Anderson and Anderson, 2016), rather than observed the rate at which such change in debris distribution occurs in a true glacier system, and have not compared different glacier systems with regards to the variation in the way in which debris is distributed. Using the work undertaken in Chapter 7 as a base, comparison studies of debris distribution, including the rates of change in debris input, transport and distribution, and the glacier characteristics that control differences in such distribution, should therefore be the focus of future research to understand the evolution of debris-covered glaciers in more detail.

***Q3**: How does incorporating spatially and temporally varying debris parameter values into numerical models affect estimates of glacier mass balance?*

The modelling results presented in Chapter 8 show distinct variability in specific mass balance estimates (b_w) over an ablation season when (a) each of the tested variables (debris layer thickness, albedo and aerodynamic roughness length) are included in the point model, and (b) when spatial variability in these three debris properties are incorporated into the distributed model. Each of the variables affected b_w when varied individually, and a hierarchy of variables was also present. Consequently, incorporating spatially variable debris properties into the surface energy balance and heat transfer model, CMB-DEB, does influence estimates of b_w derived from this model.

The most notable result was the difference in b_w between the distributed model runs that included a spatially constant and a spatially variable debris layer input, where the latter of these model runs produced a specific mass balance estimate 223% higher than the former. The large difference in these results highlights the importance of including debris layer thickness in numerical models for debris-covered glaciers, but does not confirm the accuracy of these two results compared to the true change in mass balance over an

ablation season, due to a lack of *in situ* data for comparison. However, these results do highlight the extent of variability in specific mass balance that may be occurring between models that do and do not incorporate spatially variable debris layer thickness. Incorporation of spatial variable albedo and aerodynamic roughness length in addition to debris thickness reduced b_w, suggesting that if only spatially variable debris thickness is incorporated into such a model estimates of mass balance may be overestimated. These results therefore suggest that the greater number of well-parameterised spatially variable debris properties that can be contained will enable less uncertainty in these model results, but should be confirmed with comparison to field data.

Although the results presented in Chapter 8 provide an interesting insight into how different spatially variable debris properties affect specifc mass balance at a debris-covered glacier surface, no consideration of temporally variability in these debris properties was considered in these model simulations. Incorporation of such temporal variability in debris properties was not included due to an absence of field and satellite data from which to derive such variability in debris properties, and the likelihood that over the studied period changes in spatiotemporal variation in debris properties would likely be over smaller distances than the resolution of the spatially variable debris inputs used in these simulations. However, the change in debris distribution observed on Baltoro Glacier confirms the need to consider spatiotemporal variation in debris distribution in numerical model simulations for medium- to long-term timescales.

To enable the incorporation of spatiotemporal variability in debris distribution, the next stage in numerical modelling of debris-covered glaciers systems should focus on bringing together the two methods by which debris-covered glaciers are modelled; glacier change and surface energy balance models. Debris-covered glaciers have been modelled with the aim of simulating debris transport through a glacier system (e.g. Konrad and Humphrey, 2000; Banerjee and Shankar, 2013; Rowan et al., 2015; Anderson and Anderson, 2016). These studies have been concerned with the evolution of supraglacial debris cover and, in particular, development of moraines through time. With the exception of iSOSIA used by Rowan et al. (2015) these numerical models are two-dimensional flow models and so only simulate the evolution of a debris layer along the longitudinal glacier surface. Whilst these model results provided a useful insight into the dynamics of debris-covered

glaciers, their lack of a third dimension meant spatial variability in debris distribution, as observed on Baltoro Glacier (Chapter 7) was not fully represented.

The second aspect of numerical modelling; the simulation of surface energy balance and heat transfer through a debris layer, as a similarly limited field of application, in most cases to point data over one ablation season (e.g. Lejeune et al., 2013; Collier et al., 2014; Evatt et al., 2015), with the except of Reid et al. (2012) and Fyffe et al. (2014). To enable spatiotemporal variability in debris properties to be incorporated into the modelling process these point models need to be developed to be fully functioning distributed models, with interaction between cells to enable turbulent fluxes to be influenced by surrounding topography, and optimization of the resolution of these distributed models to use the most accurate resolution for input data. Thus far, such a model has been limited by our understanding of the controls on turbulent fluxes, but recent work into aerodynamic roughness (Rounce et al., 2105; Miles et al., 2017; Quincey et al., 2017) has initiated filling this knowledge gap.

Following the development of such distributed models a two-fold modelling approach could be developed, where the debris layer evolved through time using a three-dimensional flow model, which provides the input debris layer for a surface energy balance and heat transfer model. With such an approach debris distribution could be spatially variable and incorporate the effects of debris content on glacier dynamics and glacier extent (as is the focus in Anderson and Anderson, 2016 and Rowan et al., 2015) with the effects of differing supraglacial debris distribution on surface ablation. Ultimately, to develop a comprehensive model of these debris-covered systems debris emergence would need to be incorporated into these models and the surface energy balance models for debris-covered ice used alongside surface energy balance models for ice cliffs and supraglacial ponds, such as those developed by Brun et al. (2016) and Miles et al. (2016) and similar to the modelling approach undertaken by Douglas et al. (2016). Additionally, more needs to be known about the amount of debris help englacially and the rate at which it emerges. Such a modelling approach would be computationally expensive, and would not be applicable for regional application. However, these modelling results could provide glacier-specific estimations of specific mass balance for some glaciers, to which regional modelling results could be compared.

Q4: *Could incorporation of spatiotemporal variability in supraglacial debris layers increase the accuracy of predictions for the response of Himalayan-Karakoram debris-covered glaciers to climate change?*

The focus on glaciers in the Himalaya-Karakoram stemmed from a need for a greater understanding of debris-covered glaciers, and their role in estimating glacier change in the region. As the proportion of debris-covered glacier area increases in the Himalaya-Karakoram, such as change is consequently likely to have an increasingly important role in the response of these glaciers to climate change (Scherler et al., 2011; Bolch et al., 2012). Therefore, gaining a comprehensive understanding of all the processes by which supraglacial debris affects glacier ablation is important to ascertain now, so predictions of future glacier change can incorporate accurate representations of these debris layers into models of these glacier system, and subsequently provide more accurate estimations of future glacier change.

A lack of a comprehensive modelling approach for debris-covered glaciers, thus far, stems from the complexity of debris-covered glacier systems. This complexity has led to previous research concerned with simulating debris-covered glaciers to focus on specific aspects of glacier dynamics (e.g. Anderson and Anderson, 2016). However, through focusing on specific glacier dynamics, finer details such as the spatial and temporal variability in debris properties have previously been overlooked. The identification of spatiotemporal variability in debris distribution, and the confirmation that incorporation of spatial variation in supraglacial debris distribution does affect glacier mass balance highlights the importance of considering such variability in mass balance estimations, and provides an important step in linking controls on ablation under a debris layer derived from field- and remotely sensed to simulating these debris-covered glacier systems with sufficient precision that they can provide useful and accurate estimations of the mass balance regimes of these glaciers through time, and in determining the response of these glaciers to climate change.

When considering the impact of simplifying estimates of glacier mass change, omission of precise glacier conditions will affect the extent to which estimations are trusted by the scientific community and general public. With up to a third of all glaciers in the Himalaya-Karakoram displaying supraglacial debris cover across a large proportion of their

ablation areas (Nuimura et al., 2012; Thakuri et al., 2014), omitting or simplifying the effects of a supraglacial debris layer in ablation will cause estimations of glacier change to be taken less seriously, due to the lack of a robust reconstruction of these glacier systems.

When considering climate change and its influence on debris-covered glacier mass balance, both air temperature and precipitation patterns in the Himalaya-Karakoram are predicted to change over the coming decades (IPCC, 2014). Research presented here highlights the importance of air temperature and the rate of air temperature change on temporal variability in near-surface debris temperature, and therefore energy flux into a debris layer. Albedo was also identified as an important driver of spatial variability in ablation across a glacier surface, which is influenced by moisture content in the debris, a factor controlled by the type, frequency and magnitude of precipitation. Understanding the role of these climate changes in glacier change is not only restricted to their direct influence on ablation, but also how they will affect energy transfer through supraglacial debris layers. Consequently, although spatiotemporal variability in supraglacial debris properties may be a minor aspect of estimating glacier ablation refinement of these estimations can only provide more accurate, and therefore more reliable predictions, of future changes in glacier mass.

Chapter 10: Conclusion

10. Conclusion

The research presented in this thesis ultimately confirms that a supraglacial debris layer is neither static in space or time, and that such variability affects energy flux at the debris surface and through the debris layer, and consequently the amount of ice mass loss that occurs beneath a debris-covered glacier surface. The advantages of utilising a range of techniques to understand glacier systems at a variety of scales are highlighted by the variety of methods undertaken in this thesis to achieve its aim, whilst the limitations of field-based studies and remotely sensed data are also highlighted. The model results presented here also suggest that omitting, or partially omitting, consideration of spatiotemporal variability in supraglacial debris properties may affect predictions of mass balance for debris-covered glaciers considerably.

Much of the research presented in this thesis is specific to the glaciers in the Himalaya-Karakoram, due to the dynamics of these glaciers, the sediment flux into the glacier system due to high erosion rates, elevation and monsoonal weather system that affects Khumbu Glacier, and the vast size of Baltoro Glacier, in particular, in comparison to other debris-covered glaciers around the world. The research presented here was undertaken on glaciers in the Himalaya-Karakoram because the region contains a large proportion of debris-covered glaciers that vary in size, location and have differing supraglacial debris layers with regards to layer thickness, lithology and other debris properties. Debris-covered glaciers in the region therefore provide an extensive dataset on which to undertake research. These glaciers continue to be challenging to research; they are remote, difficult to access and monitor due to their elevation, and lack a developed infrastructure surrounding them. Additionally, these glaciers are controlled by the monsoonal climate and so exhibit a different ablation regime to the majority of other glaciers globally. As a result, research undertaken on glaciers in other regions of the world cannot be assumed to apply directly to glaciers in the region, and vice versa.

This thesis has highlighted the suite of methods that are available to provide information on glacier systems at a variety of different scales. It is with such a combination of methods that a comprehensive analysis of glacier systems can be achieved; field data alone provide detailed data sets, but can only give a limited insight into debris-covered glacier systems as a whole. Conversely, satellite data provide glacier-wide information,

but the resolution of much of the data available is not at a scale similar to that of spatial variability in supraglacial debris properties observed across a debris-covered glacier surface. A balance needs to be met between the level of detail needed to represent a supraglacial debris cover effectively with including too much information, which is beyond what is needed to understand these glacier systems comprehensively. To enable the effective use of remotely sensed data an optimal scale at which data should be collected to represent a debris-covered glacier effectively needs to be identified. A similar scale needs to be identified for numerical models of these glacial environments, to enable models to provide useful estimations of ablation that have a suitable computational efficiency.

The work presented in this thesis has highlighted a number of areas in which further research is needed. Simulations of turbulent fluxes, based on aerodynamic roughness length, still need development, particularly with regard to the scale dependence and representing spatial variability in aerodynamic roughness length in distributed surface energy balance models accurately. Following these developments, a two-fold modelling approach should be developed, in which the evolution of a debris load within a glacier system would be modelled alongside glacier surface energy balance, to determine the surface ablation variation that occurs with an evolving debris layer. This modelling procedure should be undertaken alongside further primary data collection in which controls on evolution of a supraglacial debris layer are the focus. Specific questions with regards to the evolution of debris-covered glaciers still exist, such as to whether a threshold at which the area of debris cover becomes influential to glacier mass balance exists, and whether all valley glaciers in mountainous regions have the potential to become debris-covered, especially with changes in erosion and weathering rates due to climate change. Such questions should be the focus of future research for such changing glacial environments as the Himalaya-Karakoram.

References

Abrams, M., Hook, S., Ramachandran, B. 2002. ASTER User Handbook [v.2]. Jet propulsion laboratory, Californian Institute of Technology. Accessed online at: http://glcf.umd.edu/library/guide/aster_user_guide_v2.pdf.

Ageta, Y, Higuchi, K. 1984. Estimation of Mass Balance Components of a Summer-Accumulation Type Glacier in the Nepal Himalaya. *Geografiska Annaler: Series A, Physical Geography* **66**, 249–255. DOI: 10.2307/520698

Ageta, Y. 1976. Characteristics of Precipitation during Monsoon Season in Khumbu Himal. *Journal of the Japanese Society of Snow and* Ice **38**, 84–88. DOI: 10.5331/seppyo.38.Special_84

Ageta, Y., Higuchi, K.: Estimation of Mass Balance Components of a Summer-Accumulation Type Glacier in the Nepal Himalaya, *Geografiska Annaler: Series A, Physical Geography*, **66**(3), 249–255, DOI: 10.2307/520698, 1984.

Akhtar, M., Ahmad, N., Booij, M.J. 2008. The impact of climate change on the water resources of Hindukush–Karakorum–Himalaya region under different glacier coverage scenarios. *Journal of Hydrology*, **355**(1-4), 148-163.

Akhtar, M., Ahmad, N., Booij, M.J. 2009. Use of regional climate model simulations as input for hydrological models for the Hindukush-Karakorum-Himalaya region. *Hydrology and Earth System Sciences*, **13**(7), 1075-1089.

Alexander, D. J., Davies, T. R., Shulmeister, J. 2011. A stead-state mas-balance model for the Franz Josef Glacier, New Zealand: testing and application. *Geografiska Annaler: Series A, Physical Geography*, **93**(1), 41-54.

Allen, M.R., Barros, V.R., Broome, J., Cramer, W., Christ, R., Church, J.A., Clarke, L., Dahe, Q., Dasgupta, P., Dubash, N.K., Edenhofer, O., Elgizouli, I., Field, C.B., Forster, P., Friedlingstein, P., Fuglestvedt, J., Gomez-Echeverri, L., Hallegatte, S., Hegerl, G., Howden, M., Jiang, K., Cisneros, B.J., Kattsov, V., Lee, H., Mach, K.J., Marotzke, J., Mastrandrea, M.D., Meyer, L., Minx, J., Mulugetta, Y., 'Brien, K.O., Oppenheimer, M., Pachauri, R.K., Pereira, J.J., Pichs-Madruga, R., Plattner, G.-K., Pörtner, H.-O., Power, S.B., Preston, B., Ravindranath, N.H., Reisinger, A., Riahi, K., Rusticucci, M., Scholes, R., Seyboth, K., Sokona, Y., Stavins, R., Stocker, T.F., Tschakert, P., van Vuuren, D., van Ypersele, J.-P., Blanco, G., Eby, M., Edmonds, J., Fleurbaey, M., Gerlagh, R., Kartha, S., Kunreuther, H., Rogelj, J., Schaeffer, M., Sedláček, J., Sims, R., Ürge-Vorsatz, D., Victor, D., Yohe, G., 2014. IPCC Fifth Assessment Synthesis Report - Climate Change 2014 Synthesis Report. *116*.

Alley, R. B., Cuffey, K. M., Evenson, E. B., Strasser, J. C., Lawson, D. E., Larson, G. J. 1997. How glaciers entrain and transport basal sediment: physical constraints. *Quaternary Science Reviews*, **16**(9), 1017-1038.

Anders, A.M., Roe, G.H., Hallet, B., Montgomery, D.R., Finnegan, N.J., Putkonen, J. 2006. Spatial patterns of precipitation and topography in the Himalaya. *Geological Society of America Special Papers*, **398**, 39-53.

Anderson, L.S., Anderson, R.S., 2016. Modeling debris-covered glaciers: response to steady debris deposition. *The Cryosphere,* **10**, 1105–1124.

Anderson, R.S., 2000. A model of ablation-dominated medial moraines and the generation of debris-mantled glacier snouts. *Journal of Glaciology,* **46**, 459–469. doi:10.3189/172756500781833025.

Andreas, E. L. 2002. Parameterizing scalar transfer over snow and ice: a review. *Journal of Hydrometeorology*, **3**(4), 417-432.

Apaloo, J, Brenning, A, Bodin X. 2012. Interactions between Seasonal Snow Cover, Ground Surface Temperature and Topography (Andes of Santiago, Chile, 33.5°S). *Permafrost and Periglacial Processes,* **23**: 277–291. DOI: 10.1002/ppp.1753.

Archer, D. R., Fowler, H. J. 2004. Spatial and temporal variations in precipitation in the Upper Indus Basin, global teleconnections and hydrological implications. *Hydrology and Earth System Sciences* Discussions, **8**(1), 47-61.

Arendt, A., Bolch, T., Cogley, J. G., Gardner, A. and Hagen, J. O. 2012. Randolph glacier inventory [v 3.2]: A dataset of global glacier outlines. global land ice measurements from space, Boulder Colorado, USA, Digital Media, DOI:10.1029/2012JF002523/full.

Arnold, N.S., Rees, W.G. 2003. Self-similarity in glacier surface characteristics. *Journal of Glaciology*, **49**(167), 547-554.

Arnold, N. S., Rees, W. G., Hodson, A. J., Kohler, J. 2006. Topographic controls on the surface energy balance of a high Arctic valley glacier. *Journal of Geophysical Research: Earth Surface*, **111**(F2).

Arsenault, A. M., Meigs, A. J. 2005. Contribution of deep-seated bedrock landslides to erosion of a glaciated basin in southern Alaska. *Earth Surface Processes and Landforms*, **30**(9), 1111-1125.

Bajraharya, S. Shrestha, F. 2011. The Status of Glaciers in the Hindu Kush-Himalaya Region. Kathmandu: ICIMOD.

Bajracharya, S. (submitter), Shrestha, F., Bajracharya, S., Maharjan, S. B., Guo, W. (analysts). 2014. GLIMS Glacier database. Boulder, CO: National Snow and Ice Data Center. DOI:10.7265/N5V98602.

Ballantyne, C. K., Harris, C. 1994. The Periglaciation of Great Britain. Cambridge University Press, Cambridge, UK.

Banerjee, A., Shankar, R. 2014. Estimating the avalanche contribution to the mass balance of debris covered glaciers. *The Cryosphere Discussions*, **8**(1), 641-657.

Banwell, A. F., Arnold, N. S., Willis, I. C., Tedesco, M., Ahlstrøm, A. P. 2012. Modeling supraglacial water routing and lake filling on the Greenland Ice Sheet. *Journal of Geophysical Research: Earth Surface*, **117**(F4). DOI:10.1029/2012JF002393

Barnard, P. L., Owen, L. A., Sharma, M. C., Finkel, R. C. 2001. Natural and human-induced landsliding in the Garhwal Himalaya of northern India. *Geomorphology*, **40**(1–2), 21–35. DOI:10.1016/S0169-555X(01)00035-6.

Bayr, K. J., Hall, D. K., Kovalick, W. M. 1994. Observations on glaciers in the eastern Austrian Alps using satellite data. *International Journal of Remote Sensing*, **15**(9), 1733-1742.

Beavers, G. S., Joseph, D. D. 1967. Boundary conditions at a naturally permeable wall. *Journal of fluid mechanics*, **30**(1), 197-207.

Belò, M., Mayer, C., Smiraglia, C., Tamburini, A. 2008. The recent evolution of Liligo Glacier, Karakoram, Pakistan, and its present quiescent phase. *Annals of Glaciology*, **48**(1), 171–176. DOI:10.3189/172756408784700662

Benn, D.I., Bolch, T., Hands, K., Gulley, J., Luckman, A., Nicholson, L.I., Quincey, D., Thompson, S., Toumi, R., Wiseman, S. 2012. Response of debris-covered glaciers in the Mount Everest region to recent warming, and implications for outburst flood hazards. *Earth Science Reviews*, **114**, 156–174. DOI: 10.1016/j.earscirev.2012.03.008

Benn, D.I., Evans, D. J. A. 2010. *Glaciers and Glaciation.* 2nd edition. Hodder Education, London.

Benn, D.I., Lehmkuhl, F. 2000. Mass balance and equilibrium-line altitudes of glaciers in high-mountain environments. *Quaternary International,* **65-66**, 15–29. DOI: 10.1016/S1040-6182(99)00034-8

Benn, D.I., Owen, L.A. 1998. The role of the Indian summer monsoon and the mid-latitude westerlies in Himalayan glaciation: review and speculative discussion. *Journal of the Geological Society*, **155**(2), 353-363.

Benn, D.I., Owen, L.A. 2002. Himalayan glacial sedimentary environments: a framework for reconstructing and dating the former extent of glaciers in high mountains. *Quaternary International,* **97**, 3-25.

Beniston, M. 2003. Climatic change in mountain regions: a review of possible impacts. *Climatic change*, **59**(1), 5-31.

Berthier, E., Arnaud, Y., Kumar, R., Ahmad, S., Wagnon, P., Chevallier, P. 2007. Remote sensing estimates of glacier mass balances in the Himachal Pradesh (Western Himalaya, India). *Remote Sensing of Environment*, **108**(3), 327-338.

Bhambri, R., Bolch, T., Chaujar, R. K. 2011. Mapping of debris-covered glaciers in the Garhwal Himalayas using ASTER DEMs and thermal data. *International Journal of Remote Sensing*, **32**(23), 8095-8119.

Bishop, M. P., Kargel, J. S., Kieffer, H. H., MacKinnon, D. J., Raup, B. H., Shroder, J. F. 2000. Remote-sensing science and technology for studying glacier processes in high Asia. *Annals of Glaciology*, **31**(1), 164-170.

Bohner, J. 2006. General climatic controls and topoclimatic variations in Central and High Asia. *Boreas*, **35**(2), 279-295.

Bolch, T., 2007. Climate change and glacier retreat in northern Tien Shan (Kazakhstan/Kyrgyzstan) using remote sensing data. *Global and Planetary Change*, **56**(1), 1-12.

Bolch, T., Buchroithner, M., Pieczonka, T., Kunert, A. 2008. Planimetric and volumetric glacier changes in the Khumbu Himal, Nepal, since 1962 using Corona, Landsat TM and ASTER data, *Journal of Glaciology*, **54**(187), 592–600, DOI:10.3189/002214308786570782, 2008.

Bolch, T., Kamp, U. 2006. Glacier mapping in high mountains using DEMs, Landsat and ASTER data. *Grazer Schriften der Geographie und Raumforschung*, **41**, 37-48.

Bolch, T., Kulkarni, A., Kääb, A., Huggel, C., Paul, F., Cogley, J. G., Stoffel, M. 2012. The state and fate of Himalayan Glaciers. *Science*, **336**(6079), 310–314. DOI:10. 1126/science.1215828.

Bolch, T., Menounos, B., Wheate, R. 2010. Landsat based inventory of glaciers in western Canada, 1985–2005. *Remote Sensing of Environment*, **114**(1), 127–137. DOI: 10.1016/j.rse.2009.08.015.

Bolch, T., Pieczonka, T. Benn, D. I. 2011. Multi-decadal mass loss of glaciers in the Everest area (Nepal Himalaya) derived from stereo imagery. *The Cryosphere*, **5**(2), 349-358.

Bollasina, M., Bertolani, L., Tartari, G. 2002. Meteorological observations at high altitude in the Khumbu Valley, Nepal Himalayas, 1994-1999. *Bulletin of Glaciological Research***, 19**, 1–11.

Bookhagen, B., Burbank, D.W. 2006. Topography, relief, and TRMM-derived rainfall variations along the Himalaya. *Geophysical Research Letters*, **33**(8).

Bookhagen, B., Burbank, D.W. 2010. Toward a complete Himalayan hydrological budget: Spatiotemporal distribution of snowmelt and rainfall and their impact on river discharge. *Journal of Geophysical Research* **115**, F03019–25. DOI: 10.1029/2009JF001426

Bookhagen, B., Thiede, R. C., Strecker, M. R. 2005. Late quaternary intensified monsoon phases control landscape evolution in the Northwest Himalaya. *Geology*, **33**(2), 149–152. DOI: 10.1130/G20982.1

Borradaile, G.J. 2013. *Statistics of Earth Science data: their distribution in time, space and orientiation.* Springer Science and Business Media. London.

Boos, W.R., Kuang, Z. 2010. Dominant control of the South Asian monsoon by orographic insulation versus plateau heating. *Nature*, **463**(7278), 218.

Boulton, G. S. 1971. Till genesis and fabric in Svalbard, Spitsbergen. In *Till: a symposium*. Columbus, Ohio: Ohio State University Press, **41**, 72.

Boulton, G.S., 1978. Boulder shapes and grain-size distributions of debris as indicators of transport paths through a glacier and till genesis. *Sedimentology*, **25**(6), 773-799.

Boulton, G.S., Eyles, N. 1979. Sedimentation by valley glaciers: a model and genetic classification. *Moraines and varves*, **33**, 11-23.

Braithwaite, R. J. 1995. Aerodynamic stability and turbulent sensible-heat flux over a melting ice surface, the Greenland ice sheet*, Journal of Glaciology*, **41**(139), 562–571.

Brazel, A. J., Chambers, F. B., Kalkstein, L.S. 1992. Summer energy balance on West Gulkana Glacier, Alaska, and linkages to a temporal synoptic index. *Zeitschrift fur Geomorphologie* **86**: 15–34.

Bretar, F., Arab-Sedze, M., Champion, J., Pierrot-Deseilligny, M., Heggy, E., Jacquemoud, S. 2013. An advanced photogrammetric method to measure surface roughness: Application to volcanic terrains in the Piton de la Fournaise, Reunion Island. *Remote Sensing of Environment*, **135**, 1-11.

Brock, B. W., Mihalcea, C., Kirkbride, M.P., Diolaiuti, G., Cutler, M. E., Smiraglia, C. 2010. Meteorology and surface energy fluxes in the 2005–2007 ablation seasons at the Miage debris-covered glacier, Mont Blanc Massif, Italian Alps. *Journal of Geophysical Research: Atmospheres,* **115**, 112. DOI: 10.1029/2009JD013224

Brock, B. W., Willis, I.C., Sharp, M.J., Arnold, N. S. 2000. Modelling seasonal and spatial variations in the surface energy balance of Haut Glacier d'Arolla, Switzerland. *Annals of Glaciology* **31,** 53–62. DOI: 10.3189/172756400781820183

Brock, B., Willis, I. C. and Sharp, M. J. 2006. Measurement and parameterization of aerodynamic roughness length variations at Haut Glacier d'Arolla, Switzerland, *Journal of Glaciology*, **52**(177), 281–297, DOI:10.3189/172756506781828746.

Brock, B., Rivera, A., Casassa, G., Bown, F., Acuñn, C. 2007. The surface energy balance of an active ice-covered volcano: Villarrica Volcano, southern Chile. *Annals of Glaciology*, **45**(1), 104-114.

Brookfield, M.E. 1998. The evolution of the great river systems of southern Asia during the Cenozoic India-Asia collision: rivers draining southwards. *Geomorphology*, **22**(3), 285-312.

Brown, M. E., Racoviteanu, A. E., Tarboton, D. G., Gupta, A. S., Nigro, J., Policelli, F., Habib, S., Tokay, M., Shrestha, M. S., Bajracharya, S., Hummel, P. 2014. An integrated modeling system for estimating glacier and snow melt driven streamflow from remote sensing and earth system data products in the Himalayas. *Journal of Hydrology*, **519**, 1859-1869.

Brun, F., Buri, P., Miles, E. S., Wagnon, P., Steiner, J., Berthier, E., Ragettli, S., Kraaijenbrink, P., Immerzeel, W. W., Pellicciotti, F. 2016. Quantifying volume loss from ice cliffs on debris-covered glaciers using high-resolution terrestrial and aerial photogrammetry. *Journal of Glaciology,* **62**(234), 684-695.

Brun, F., Berthier, E., Wagnon, P., Kääb, A., Treichler, D. 2017. A spatially resolved estimate of High Mountain Asia glacier mass balances from 2000 to 2016. *Nature Geoscience*, **10**, 668– 673.

Burbank, D. W., Leland, J., Fielding, E., Anderson, R. S. 1996. Bedrock incision, rock uplift and threshold hillslopes in the northwestern Himalayas. *Nature*, **379**(6565), 505.

Carenzo, M., Pellicciotti, F., Mabillard, J., Reid, T., Brock, B. W. 2016. An enhanced temperature index model for debris-covered glaciers accounting for thickness effect. *Advances in Water Resources*, **94**, 457-469.

Casey, K.A., Kääb, A., Benn, D.I. 2012. Geochemical characterization of supraglacial debris via in situ and optical remote sensing methods: a case study in Khumbu Himalaya, Nepal. *The Cryosphere*, **6**(1), 85-100.

Chevallier, P., Arnaud, Y., Ahmad, B. 2011. Snow cover dynamics and hydrological regime of the Hunza River basin, Karakoram Range, Northern Pakistan. *Hydrology and Earth System Sciences*, **15**(7), 2259-2274.

Cierniewski, J., Verbrugghe, M. 1997. Influence of soil surface roughness on soil bidirectional reflectance, *International Journal of Remote Sensing*, **18**(6), 1277–1288, DOI: 10.1080/014311697218412, 1997.

Clark, D. H., Clark, M. M., Gillespie, A. R. 1994. Debris-Covered Glaciers in the Sierra Nevada, California, and Their Implications for Snowline Reconstructions. *Quaternary Research,* **41**, 139–153. DOI: 10.1006/qres.1994.1016

Cogley, J. G. 2016. Glacier shrinkage across High Mountain Asia. *Annals of Glaciology*, **57**(71), 41-49.

Collier, E., Nicholson, L. I., Brock, B. W., Maussion, F., Essery, R., Bush, A. 2014. Representing moisture fluxes and phase changes in glacier debris cover using a reservoir approach. *The Cryosphere* **8**: 1429–1444. DOI: 10.5194/tc-8-1429-2014

Collier, E., Mölg, T., Maussion, F., Scherer, D., Mayer, C., Bush, A. B. G. 2013. High-resolution interactive modelling of the Mountain Glacier–atmosphere interface: An application over the Karakoram. *The Cryosphere*, **7**(3), 779–795. DOI:10.5194/tc-7-779-201.

Collins, D. N. 1998. Suspended sediment flux in meltwaters draining from Batura glacier as an indicator of the rate of glacial erosion in the Karakoram mountains. Journal of Quaternary *Science*, **13**(6), 1-10.

Conway, W. M. 1894. *Climbing and exploration in the Himalayas*. Fischer Unwin, London.

Conway, H., Rasmussen, L. A. 2000. Summer temperature profiles within supraglacial debris on Khumbu Galcier, Nepal. In *Debris-covered Glaciers: Proceedings of an international workshop held at the University of Washington*. Seattle, Washington, USA **264**: 89–97.

Copland, L., Pope, S., Bishop, M. P., Shroder, J. F., Clendon, P., Bush, A., Kamp, U., Seong, Y. B., Owen, L. A. 2009. Glacier velocities across the central Karakoram. *Annals of Glaciology* **50**, 41–49. DOI:10.3189/172756409789624229.

Cruz, R. V., Harasawa, H., Lal, M., Wu, S., Anokhin, Y., Punsalmaa, B., Honda, Y., Jafari, M., Li, C., Huu Ninh, N. 2007. Climate Change 2007: Impacts, Adaptation and Vulnerability. Contribution of Working Group II to the Fourth Assessment Report of the Intergovernmental Panel on Climate Change. Cambridge University Press. Cambridge, UK. 469–506.

Cuffey, K. M., Paterson, W. S. 2010. *The Physics of Glaciers*. Elsevier. London, UK.

Cutler, P.M., Munro, D.S. 1996. Visible and near-infrared reflectivity during the ablation period on Peyto Glacier, Alberta, Canada. *Journal of Glaciology*, **42**(141), 333-340.

Davis, R. E., Kalkstein, L. S. 1990. Development of an automated spatial synoptic climatological classification. *International Journal of Climatology,* **10**: 769–794.

Decheng, M. 1978. *The map of snow mountains in China, K2 (Mount Quogori).* Lanzhou Institute of Glaciology and Geocryology, Lanzhou, China.

Deline, P. 2005. Change in surface debris cover on Mont Blanc massif glaciers after the "Little Ice Age" termination. *Holocene*, **15**, 302–309. DOI:10.1191/0959683605hl809rr.

Deline, P., Broccolato, M., Noetzli, J., Ravanel, L., Tamburini, A. 2013. The December 2008 Crammont rock avalanche, Mont Blanc massif area, Italy. *In Landslide Science and Practice*, Springer, Berlin Heidelberg, 403-408.

Desio, A. 1930. Geological work of the Italian expedition to the Karakoram. *The Geographical Journal*, **75**(5), 402-411.

Desio, A. 1954. An exceptional advance in the Karakoram-Ladakh region. *Journal of Glaciology* **2**, 383–385.

Desio, A. and Longinelli, A., 1961. The age of the Baltoro Granite (Karakoram–Himalaya). *Atti. accad. nazl. Lincei. Rend., Classe sci. fis., mat. e nat.,* **30**.

Diolaiuti, G., Pecci, M., Smiraglia, C. 2003. Liligo Glacier, Karakoram, Pakistan: a reconstruction of the recent history of a surge-type glacier. *Annals of Glaciology,* **36**, 168–172. DOI:10.3189/172756403781816103

Dortch, J. M., Dietsch, C., Owen, L. A., Caffee, M. W., Ruppert, K. 2011. Episodic fluvial incision of rivers and rock uplift in the Himalaya and Trans-Himalaya. *Journal of the Geological Society*, **168**(3), 783-804.

Douglas, J.S., Huss, M., Swift, D.A., Jones, J.M., Salerno, F. 2016. Incorporating Distributed Debris Thickness in a Glacio-Hydrological Model: Khumbu Himalaya, Nepal. *The Cryosphere Discussion, in review.*

Douville, H., Royer, J. F., Polcher, J., Cox, P., Gedney, N. 2000. Impact of CO^2 doubling on the Asian summer monsoon. *Journal of the Meteorological Society of Japan*, **78**(4), 421-439.

Driscoll, F. G. 1980. Formation of the neoglacial surge moraines of the Klutlan Glacier, Yukon Territory, Canada. *Quaternary Research*, **14**(1), 19-30.

Dunning, S. A., Rosser, N. J., McColl, S. T., Reznichenko, N. V. 2015. Rapid sequestration of rock avalanche deposits within glaciers. *Nature communications,* **6**, 7964.

Dyurgerov, M. B., Meier, M. F. 2005. *Glaciers and the changing Earth system: a 2004 snapshot*. Institute of Arctic and Alpine Research, University of Colorado, Boulder.

Evans, D. J. A., Rea, B. R. 1999. Geomorphology and sedimentology of surging glaciers: A land-systems approach. *Annals of Glaciology*, **28**(1), 75–82. doi:10.3189/172756499781821823

Evatt, G. W., Abrahams, D., Heil, M., Mayer, C., Kingslake, J., Mitchell, S. L., Clark, C. D. 2015. Glacial melt under a porous debris layer. *Journal of Glaciology*, **61**(229), 825–836. DOI:10.3189/2015JoG14J235.

Evatt, G., Mayer, C., Abrahams, I.D., Nicholson, L., Mallinson, A., Heil, M. 2016. The life cycle of Ice Sails. *EGU General Assembly Conference Abstract*, *18*, 6955).

Fassnacht, S. R., Williams, M. W., Corrao, M. V. 2009. Changes in the surface roughness of snow from millimetre to metre scales*. Ecological Complexity*, **6**(3), 221-229.

Finkel, R. C., Owen, L. A., Barnard, P. L., Caffee, M. W. 2003. Beryllium-10 dating of Mount Everest moraines indicates a strong monsoon influence and glacial synchroneity throughout the Himalaya. *Geology*, **31**(6), 561-564.

Førland, E. J., Allerup, P., Dahlström, B., Elomaa, E., Jónsson, T., Madsen, H., Perälä, J., Rissanen, P., Vedin, H., Vejen, F. 1996. Manual for operational correction of Nordic precipitation data, *DNMI report*, **24**, 96.

Fort, M. 2000. Glaciers and mass wasting processes: their influence on the shaping of the Kali Gandaki valley (higher Himalaya of Nepal). *Quaternary International*, **65**, 101-119.

Foster, L. A., Brock, B.W., Cutler, M. E. J., Diotri, F. 2012. A physically based method for estimating supraglacial debris thickness from thermal band remote-sensing data. *Journal of Glaciology*, **58**, 677–691. DOI: 10.3189/2012JoG11J194

Frey, H., Machguth, H., Huss, M., Huggel, C., Bairacharaya, S., Bolch, T., Kulkarni, A, LInsbauer, A., Salzmann, N., Stoffel, M. 2014. Estimating the volume of glaciers in the Himalayan–Karakoram region using different methods. *The Cryosphere*, **8**(6), –2333.

Fuchs, M., Owen, L. A. 2008. Luminescence dating of glacial and associated sediments: review, recommendations and future directions. *Boreas*, **37**(4), 636-659.

Fujii, Y., Higuchi, K. 1977. Statistical analyses of the forms of the glaciers in the Khumbu Himal. *Journal of the Japanese Society of Snow and Ice*, **39**, 7-14.

Fujita, K., Suzuki, R., Nuimura, T., Sakai, A. 2008. Performance of ASTER and SRTM DEMs, and their potential for assessing glacial lakes in the Lunana region, Bhutan Himalaya. *Journal of Glaciology*, **54**(185), 220-228.

Fujita, K., Nuimura, T. 2011. Spatially heterogeneous wastage of Himalayan glaciers. *Proceedings of the National Academy of Sciences*, **108**(34), 14011-14014.

Fushimi, H. 1977. Structural studies of glaciers in the Khumbu region. *Journal of the Japanese Society of Snow and Ice*, **39**, 30-39.

Fushimi, H., Yoshida, M., Watanabe, O., Upadhyay, B. P. 1980. Distributions and Grain Sizes of Supraglacial Debris in the Khumbu Glacier, Khumbu Region, East Nepal. *Journal of the Japanese Society of Snow and Ice*, **41**, 18–25. DOI: 10.5331/seppyo.41.Special_18

Fyffe, C. L., Reid, T. D., Brock, B. W., Kirkbride, M. P., Diolaiuti, G., Smiraglia, C., Diotri, F. 2014. A distributed energy-balance melt model of an alpine debris-covered glacier. *Journal of Glaciology,* **60**(221), 587–602, DOI: 10.3189/2014JoG13J148, 2014.

Fyffe, C. L. 2012. *The hydrology of debris-covered glaciers*, Doctoral Dissertation, University of Dundee.

Gabbi, J., Carenzo, M., Pellicciotti, F., Bauder, A., Funk, M. 2014. A comparison of empirical and physically based glacier surface melt models for long-term simulations of glacier response. *Journal of Glaciology*, **60**(224), 1140-1154.

Gades, A., Conway, H., Nereson, N., Naito, N., Kadota, T. 2000. Radio echo-sounding through supraglacial debris on Lirung and Khumbu Glaciers, Nepal Himalayas. in *Debris-covered Glaciers: Proceedings of an international workshop held at the University of Washington.* Seattle, Washington, USA, **264**, 13-24.

Galewsky, J. 2009. Orographic precipitation isotopic ratios in stratified atmospheric flows: Implications for paleoelevation studies. *Geology*, **37**(9), 791-794.

Gantayat, P., Kulkarni, A.V., Srinivasan, J. 2014. Estimation of ice thickness using surface velocities and slope: case study at Gangotri Glacier, India. *Journal of Glaciology*, **60**(220), 277-282.

Gao, H., Ding, Y., Zhao, Q., Hrachowitz, M., Savenije, H. H. G. 2017. The importance of aspect for modelling the hydrological response in a glacier catchment in Central Asia. *Hydrological Processes*, 31(16), 2842–2859. DOI: 10.1002/hyp.11224.

Gao, B. C. 1996. NDWI – A normalized difference water index for remote sensing of vegetation liquid water from space. *Remote Sensing of Environment*, **58**, 257–266. doi:10.1016/S0034-4257(96)00067-3.

Gardelle, J., Berthier, E., Arnaud, Y. 2012. Slight mass gain of Karakoram glaciers in the early twenty-first century. *Nature Geoscience*, **5**, 322–325. DOI:10.1038/ngeo1450.

Gergan, J.T., Dobhal, D.P. and Kaushik, R., 1999. Ground penetrating radar ice thickness measurements of Dokriani bamak (glacier), Garhwal Himalaya. Current Science, pp.169-173.

Gardelle, J., Berthier, E., Arnaud, Y., Kääb, A. 2013. Region-wide glacier mass balances over the Pamir-Karakoram-Himalaya during 1999-2011. *The Cryosphere*, **7**(6), 1885-1886.

Gibson, M. J., Glasser, N. F., Quincey, D. J., Rowan, A. V., Irvine-Fynn, T. D. I. 2016 Changes in glacier surface cover on Baltoro Glacier, Karakoram, north Pakistan, 2001–2012, *Journal of Maps*, **13**(2), 100–108.

Gibson, M. J., Irvine-Fynn, T. D. I., Wagnon, P., Rowan, A. V., Quincey, D. J., Homer, R., Glasser, N. F. 2017a. Variations in near-surface debris temperature through the summer monsoon on khumbu Glacier, Nepal Himalaya. *Earth Surface Processes and Landforms*, in review.

Gibson M. J., Glasser, N. F., Quincey, D. J., Mayer, C., Rowan, A. V., Irvine-Fynn, T.D.I. 2017. Temporal variations of supraglacial debris distribution on Baltoro Glacier, Karakoram, between 2001 and 2012. *Geomorphology*, **295**, 572–585.

Gisnås, K., Westermann, S., Schuler, T. V., Litherland, T., Isaksen K, Boike J, Etzelmüller B. 2014. A statistical approach to represent small-scale variability of permafrost temperatures due to snow cover. *The Cryosphere*, **8**, 2063–2074. DOI: 10.5194/tc-8-2063-2014

Glasser, N. F., Holt, T. O., Evans, Z. D., Davies, B. J., Pelto, M., Harrison, S. 2016. Recent spatial and temporal variations in debris cover on Patagonian glaciers. *Geomorphology*, **273**, 202–216. DOI: 10.1016/j.geomorph.2016.07.036

Google Earth [v. 7.1.5.1557]. Baltoro Glacier, northern Pakistan. 35°44' 53.97' N, 76°18' 33.66''E, Eye altitude 10.09 km. DigitalGlobe 2016. Retrieved April 30, 2016, from http://earth.google.com

Gubler, S., Fiddes, J., Keller, M., Gruber, S. 2011. Scale-dependent measurement and analysis of ground surface temperature variability in alpine terrain. *The Cryosphere,* **5**, 431–443. DOI: 10.5194/tc-431-2011

Guglielmin, M., Worland, M. R., Cannone, N. 2012. Spatial and temporal variability of ground surface temperature and active layer thickness at the margin of maritime Antarctica, Signy Island. Geomorphology, **155-156**, 20–33.

Guglielmin, M. 2006. Ground surface temperature (GST), active layer and permafrost monitoring in continental Antarctica. *Permafrost and Periglacial Processes*, **17**, 133–143. DOI: 10.1002/ppp.553.

Gulley, J., Benn, D.I. 2007. Structural control of englacial drainage systems in Himalayan debris-covered glaciers. *Journal of Glaciology*, **53**(182), 399-412.

Haeberli, W., Beniston, M. 1998. Climate change and its impacts on glaciers and permafrost in the Alps. *Ambio*, **27**(4), 258-265.

Hales, T.C., Roering, J.J. 2005. Climate-controlled variations in scree production, Southern Alps, New Zealand. *Geology*, **33**(9), 701-704.

Hales, T.C., Roering, J.J. 2009. A frost "buzzsaw" mechanism for erosion of the eastern Southern Alps, New Zealand. *Geomorphology*, **107**(3), 241-253.

Hallet, B., Molnar, P. 2001. Distorted drainage basins as markers of crustal strain east of the Himalaya. *Journal of Geophysical Research: Solid Earth*, **106**(B7), 13697-13709.

Hambrey, M. J., Quincey, D. J., Glasser, N. F., Reynolds, J. M., Richardson, S. J., Clemmens, S. 2008. Sedimentological, geomorphological and dynamic context of debris-mantled glaciers, Mount Everest (Sagarmatha) region, Nepal. *Quaternary Science Reviews,* **27**, 2361–2389. DOI: 10.1016/j.quascirev.2008.08.010

Hambrey, M. J., Glasser, N. F. 2003. The role of folding and foliation development in the genesis of medial moraines: Examples from Svalbard Glaciers. *The Journal of Geology*, **111**(4), 471–485. doi:10.1086/375281

Hambrey, M. J., Bennett, M. R., Dowdeswell, J. A., Glasser, N. F., Huddart, D. 1999. Debris entrainment and transfer in polythermal valley glaciers. *Journal of Glaciology*, **45**, 69–86. DOI: 10.3198/1999JoG45-149-69-86.

Hannah, D. M., Smith, B. P., Gurnell, A. M., McGregor, G. R. 2000. An approach to hydrograph classification. *Hydrological processes*, **14**, 317-338.

Harris, S. A., Pedersen, D. E. 1998. Thermal regimes beneath coarse blocky materials. *Permafrost and Periglacial Processes*, **9**(2), 107-120.

Heimsath, A. M., McGlynn, R. 2008. Quantifying periglacial erosion in the Nepal high Himalaya. *Geomorphology*, **97**, 5–23.

Hewitt, K. 2005. The Karakoram anomaly? Glacier expansion and the 'elevation effect,'Karakoram Himalaya. *Mountain Research and Development*, **25**(4), 332-340.

Hewitt, K. 2009. Rock avalanches that travel onto glaciers and related developments, Karakoram Himalaya, Inner Asia. *Geomorphology*, **103**(1), 66-79.

Higuchi, K., Ageta, Y., Yasunari, T. 1982. Characteristics of precipitation during the monsoon season in high-mountain areas of the Nepal Himalaya. *Hydrological Aspects of Alpine and High-Mountain Areas,* **138**, 21–30.

Hochstein, M. P., Claridge, D., Henrys, S. A., Pyne, A., Nobes, D. C. and Leary, S. F. 1995. Downwasting of the Tasman Glacier, South Island, New Zealand: changes in the terminus region between 1971 and 1993. *New Zealand Journal of Geology and Geophysics*, **38**(1), 1-16.

Hock, R., Holmgren, B. 1996. Some Aspects of Energy Balance and Ablation of Storglaciaren, Northern Sweden. *Geografiska Annaler: Series A, Physical Geography* **78**: 121.

Hock, R. 2003. Temperature index melt modelling in mountain areas. *Journal of Hydrology*, **282**, 104–115.

Hock, R. 2005. Glacier melt: a review of processes and their modelling. *Progress in Physical Geography,* **29**(3), 362-391.

Hock, R., Noetzli, C. 1997. Areal melt and discharge modelling of Storglaciaren, Sweden. *Annals of Glaciology,* **24**, 211–216.

Horvatic, D., Stanley, H. E., Podobnik, B. 2011. Detrended cross-correlation analysis for non-stationary timeseries with periodic trends. *Europhysics Letters*, 94, 18007.

Hubbart, J., Link, T., Campbell, C., Cobos, D. 2005. Evaluation of a low-cost temperature measurement system for environmental applications. *Hydrological Processes*, **19**(7), 1517-1523.

Humlum, O. 1997. Active layer thermal regime at three rock glaciers in Greenland. *Permafrost and Periglacial Processes,* **8**(4), 383-408.

Huss, M., Farinotti, D. 2012. Distributed ice thickness and volume of all glaciers around the globe. *Journal of Geophysical Research: Earth Surface*, **117**(F4).

Ichiyanagi, K., Yamanaka, M. D., Muraji, Y., Vaidya, B. K. 2007. Precipitation in Nepal between 1987 and 1996. *International Journal of Climatology*, **27**(13), 1753-1762.

ICIMOD. 2016. *Hindu Kush Himalaya Region*. Accessed on 31st July 2017 at: http://www.icimod.org/?q=1137

Igathinathane, C., Pordesimo, L. O., Columbus, E. P., Batchelor, W. D., Sokhansanj, S. 2009. Sieveless particle size distribution analysis of particulate materials through computer vision. *Computers and Electronics in Agriculture*, **66**, 147–158.

Immerzeel, W. W., Droogers, P., De Jong, S. M., Bierkens, M. F. P. 2009. Large-scale monitoring of snow cover and runoff simulation in Himalayan river basins using remote sensing. Remote sensing of Environment, 113(1), pp.40-49.

Immerzeel, W. W., Pellicciotti, F., Bierkens, M. F. P. 2013. Rising river flows throughout the twenty-first century in two Himalayan glacierized watersheds. *Nature Geoscience*, **6**(9), 742.

Immerzeel, W. W., Petersen, L., Ragettli, S., Pellicciotti, F. 2014. The importance of observed gradients of air temperature and precipitation for modeling runoff from a glacierized watershed in the Nepalese Himalayas. *Water Resources Research*, **50**(3), 2212-2226, 2014.

Immerzeel, W., van Beek, L., Bierkens, M. 2010. Climate Change Will Affect the Asian Water Towers. *Science*, **328**(5984), 1382–1385, DOI: 10.1126/science.1183188, 2010.

Immerzeel, W. W., van Beek, L., Konz, M., Shrestha, A., Bierkens, M. F. 2011. Hydrological response to climate change in a glacierized catchment in the Himalayas. *Climatic Change*, **110**(3-4), 721–736, DOI: 10.1007/s10584-011-0143-4, 2011.

Immerzeel, W. W., van Beek, L. P. H., Konz, M., Shrestha, A. B., Bierkens, M. F. P. 2012. Hydrological response to climate change in a glacierized catchment in the Himalayas. *Climatic change*, **110**(3-4), 721-736.

Inoue J. 1977. Mass Budget of Khumbu Glacier. *Journal of the Japanese Society of Snow and Ice,* **39**, 15–19. DOI: 10.5331/seppyo.39.Special_15

Inoue, J., Yoshida, M. 1980. Ablation and Heat Exchange over the Khumbu Glacier. *Journal of the Japanese Society of Snow and Ice*, **41**, 26–33, DOI: 10.5331/seppyo.41.

IPCC. 2014. Summary for Policymakers. In Edenhofer, O., R. Pichs-Madruga, Y. Sokona, E. Farahani, S. Kadner, K. Seyboth, A. Adler, I. Baum, S. Brunner, P. Eickemeier, B. Kriemann, J. Savolainen, S. Schlömer, C. von Stechow, T. Zwickel and J.C. Minx (eds.). *Climate Change 2014: Mitigation of Climate Change Contribution of Working Group III to the Fifth Assessment Report of the Intergovernmental Panel on Climate Change*. Cambridge University Press, Cambridge, United Kingdom and New York, NY, USA.

Irvine-Fynn, T. D. L., Moorman, B. J., Willis, I. C., Sjogren, D. B., Hodson, A. J., Mumford, P. N., Walter, F. S. A., Williams, J. L. M. 2005. Geocryological processes linked to High Arctic proglacial stream suspended sediment dynamics: examples from Bylot Island, Nunavut, and Spitsbergen, Svalbard. *Hydrological Processes,* **19**, 115–135. DOI: 10.1002/hyp.5759.

Irvine-Fynn, T.D.L., Barrand, N.E., Porter, P.R., Hodson, A.J., Murray, T. 2011. Recent High-Arctic glacial sediment redistribution: A process perspective using airborne lidar. *Geomorphology*, **125**(1), 27-39.

Irvine-Fynn, T., Sanz-Ablanedo, E., Rutter, N., Smith, M., Chandler, J. 2014. Measuring glacier surface roughness using plot-scale, close-range digital photogrammetry. *Journal of Glaciology*, **60**(223), 957–969, DOI: 10.3189/2014JoG14J032.

Iverson, N. R., Cohen, D., Hooyer, T. S., Fischer, U. H., Jackson, M., Moore, P. L., Lappegard, G., Kohler, J. 2003. Effects of basal debris on glacier flow. *Science*, **301**(5629), 81-84.

Ives, J.D., Shrestha, R.B., Mool, P.K. 2010. *Formation of glacial lakes in the Hindu Kush-Himalayas and GLOF risk assessment.* ICIMOD, Kathmandu.

Iwata, S., Watanabe, O., Fushimi, H. 1980. Surface Morphology in the Ablation Area of the Khumbu Glacier. *Journal of the Japanese Society of Snow and Ice*, **41**, 9–17. DOI: 10.5331/seppyo.41.special_9

Iwata, S., Aoki, T., Kadota, T., Seko, K., Yamaguchi, S. 2000. Morphological evolution of the debris cover on Khumbu Glacier, Nepal, between 1978 and 1995. In *Debris-covered Glaciers, Proceedings of an international workshop held at the University of Washington*. Seattle, Washington, USA **264**, 3–11.

James, M. R., Robson, S. 2014. Mitigating systematic error in topographic models derived from UAV and ground-based image networks. *Earth Surface Processes and Landforms*, **39**(10), 1413-1420.

Jamieson, S. S. R., Sinclair, H. D., Kirstein, L. A., Purves, R. S. 2004. Tectonic forcing of longitudinal valleys in the Himalaya: morphological analysis of the Ladakh Batholith, North India. *Geomorphology*, **58**(1), 49-65.

Jansson, P., Fredin, O. 2002. Ice sheet growth under dirty conditions: implications of debris cover for early glaciation advances. *Quaternary International*, **95-96**, 35–42. DOI: 10.1016/S1040-6182(02)00025-3

Juen, M., Mayer, C., Lambrecht, A., Wirbel, A., Kueppers, U. 2013. Thermal properties of supraglacial debris with respect to lithology and grain size. *Geografiska Annaler: Physical Geography,* **95**, 197–209. DOI: 10.1111/geoa.12011

Juen, M., Mayer, C., Lambrecht, A., Han, H., Liu, S. 2014. Impact of varying debris cover thickness on ablation: A case study for Koxkar Glacier in the Tien Shan. *The Cryosphere*, **8**(2), 377–386.

Jouvet, G., Huss, M., Funk, M., Blatter, H. 2011. Modelling the retreat of Grosser Aletschgletscher, Switzerland, in a changing climate. *Journal of Glaciology*, **57**(206), 1033-1045.

Kääb, A. 2005. Combination of SRTM3 and repeat ASTER data for deriving alpine glacier flow velocities in the Bhutan Himalaya. *Remote Sensing of Environment*, **94**(4), 463-474.

Kääb, A., Berthier, E., Nuth, C., Gardelle, J., Arnaud, Y. 2012. Contrasting patterns of early twenty-first-century glacier mass change in the Himalayas. *Nature*, **488**(7412), 495–498, doi:10.1038/nature11324.

Kadota, T., Seko, K, Aoki, T., Iwata, S., Yamaguchi, S. 2000. Shrinkage of the Khumbu Glacier, east Nepal from 1978 to 1995. In *Debris-covered Glaciers: Proceedings of an*

International workshop held at the University of Washington, Seattle, IAHS publication, Washington, **264**, 235–243.

Kayastha, R. B., Ohata, T., Ageta, Y. 1999. Application of a mass-balance model to a Himalayan glacier. *Journal of Glaciology*, **45**(151), 559-567.

Kayastha, R. B., Takeuchi, Y., Nakawo, M. and Ageta, Y. 2000. Practical prediction of ice melting beneath various thickness of debris cover on Khumbu Glacier, Nepal, using a positive degree-day factor, in *Debris-covered Glaciers: Proceedings of an International workshop held at the University of Washington, Seattle*, IAHS publication, Washington, **264**, 71–81.

King, O., Quincey, D. J., Carrivick, J. L., Rowan, A. V. 2017. Spatial variability in mass loss of glaciers in the Everest region, central Himalayas, between 2000 and 2015. *The Cryosphere*, **11**, 407–426.

Kirkbride M. P. 2000. Ice-marginal geomorphology and Holocene expansion of debris-covered Tasman Glacier, New Zealand. In *Debris-covered Glaciers: Proceedings of an international workshop held at the University of Washington*. Seattle, Washington, USA, **264**, 211–218.

Kirkbride, M. P., 2011. Debris-covered glaciers. In *Encyclopedia of snow, ice and glaciers*. Springer, New York. 180–182.

Kirkbride, M. P., Deline, P., 2013. The formation of supraglacial debris covers by primary dispersal from transverse englacial debris bands. *Earth Surface Processes and Landforms*, **38**, 1779–1792. DOI: 10.1002/esp.3416

Kirkbride, M. P., Warren, C. R., 1999. Tasman Glacier, New Zealand: 20th-century thinning and predicted calving retreat. *Global and Planetary Change*, **22**, 11–28.

Klok, E.J., Oerlemans, J. 2002. Model study of the spatial distribution of the energy and mass balance of Morteratschgletscher, Switzerland. *Journal of Glaciology*, **48**(163), 505-518.

Kodama, H., Mae, S. 1976. The flow of glaciers in the Khumbu region. *Journal of the Japanese Society of Snow and Ice*, **38**, 31-36.

Konrad, S. K., Humphrey, N. F. 2000. Steady-state flow model of debris-covered glaciers (rock glaciers). In *Debris-covered Glaciers: Proceedings of an international workshop held at the University of Washington*. Seattle, Washington, USA, **264**, 255-266.

Kraaijenbrink, P.D.A., Bierkens, M.F.P., Lutz, A.F., Immerzeel, W.W. 2017. Impact of a global temperature rise of 1.5 degrees Celcius on Asia's glaciers. *Nature*, **549**, 257–260.

Krause, P., Boyle, D. P., Bäse, F. 2005. Comparison of different efficiency criteria for hydrological model assessment. *Advances in Geosciences*, **5**, 89–97.

Kristoufek, L. 2014. Detrending moving-average cross-correlation coefficient: Measuring cross-correlations between non-stationary series. *Physical A: Statistical Mechanics and its Applications,* **406**, 169-175.

Kuhle, M. 1993. A short report of the Tibet excursion 14-A, Part of the XIII INQUA Congress 1991 in Beijing. *GeoJournal*, **29**(4), pp.426-427.

Kuhle, M. 1995. Glacial isostatic uplift of Tibet as a consequence of a former ice sheet. *GeoJournal*, **37**(4), 431-449.

Lang, T. J., Barros, A. P. 2004. Winter storms in the central Himalayas. *Journal of the Meteorological Society of Japan*. **82**(3), 829-844.

Leech, M. L., Klemperer, S. L., Mooney, W. D. 2010. *Proceedings of the 25th Himalaya-Karakoram-Tibet Workshop.* U.S. Geological Survey Open-File Report 2010.

Legates, D. R., McCabe, G. J. 1999. Evaluating the use of "goodness-of-fit" Measures in hydrologic and hydroclimatic model validation. *Water Resources Research,* **35**, 233–241. DOI: 10.1029/1998WR900018.

Lejeune, Y., Bertrand, J. M., Wagnon, P., Morin, S. 2013. A physically based model of the year-round surface energy and mass balance of debris-covered glaciers. *Journal of Glaciology*, **59**(214), 327–344, DOI: 10.3189/2013JoG12J149.

Leprince, S., Ayoub, F., Klingert, Y., Avouac, J. P., 2007. Co-registration of Optically Sensed Images and Correlation (COSI-Corr): an operational methodology for ground deformation measurements. *IGARSS*, 1943–1946. DOI: 10.1109/IGARSS.2007.4423207

Lettau, H. 1969. Note on Aerodynamic Roughness-Parameter Estimation on the Basis of Roughness-Element Description. *Journal of Applied Meteorology*, **8**(5), 828–832. DOI: 10.1175/1520-0450(1969)008<0828:NOARPE>2.0.CO;2.

Li, C., Yanai, M. 1996. The onset and interannual variability of the Asian summer monsoon in relation to land–sea thermal contrast. *Journal of Climate*, **9**(2), 358-375.

Lillesand, T., Keifer, R., Chipman, J. 2014. *Remote sensing and image interpretation*. John Wiley and Sons, Chichester.

Luckman, A., Quincey, D., Bevan, S. 2007. The potential of satellite radar interferometry and feature tracking for monitoring flow rates of Himalayan glaciers. *Remote sensing of* Environment, **111**(2), 172-181.

Lundquist, J. D., Cayan, D. R. 2007. Surface temperature patterns in complex terrain: Daily variations and long-term change in the central Sierra Nevada, California. *Journal of Geophysical Research: Atmospheres*, **112**(D11): 124. DOI: 10.1029/2006JD007561

Lutz, A. F., Immerzeel, W. W., Shrestha, A.B., Bierkens, M. F. P. 2014. Consistent increase in High Asia's runoff due to increasing glacier melt and precipitation. *Nature Climate Change*, **4**(7), 587.

MacDonell, S., Kinnard, C., Mölg, T., Nicholson, L. 2013. Meteorological drivers of ablation processes on a cold glacier in the semi-arid Andes of Chile. *The Cryosphere*. **7**(5), 1513.

Maisch, M., Haeberli, W., Hoelzle, M., Wenzel, J. 1999. Occurrence of rocky and sedimentary glacier beds in the Swiss Alps as estimated from glacier-inventory data. *Annals of Glaciology*, **28**(1), 231-235.

Marzeion, B., Jarosch, A. H., Hofer, M. 2012. Past and future sea-level change from the surface mass balance of glaciers. *The Cryosphere*, **6**(6), 1295.

Matson, L. E., Gardner, J. S., Young, G. J. 1993. Ablation on debris covered glaciers: an example from the Rakhoit Glacier, Punjab, Himalaya. In *Snow and Glacier Hydrology*, IAHS Publication, **218**, 289–296.

Mattauer, M. 1986. Intracontinental subduction, crust-mantle décollement and crustal-stacking wedge in *The Himalayas and other collision belts*. Geological Society, London, Special Publications, **19**(1), 37-50.

Matthias, A., Fimbres, A., Sano, E., Post, D., Accioly, L., Batchily, A., Ferreira, L. G. 2000. Surface Roughness Effects on Soil Albedo. *Soil Science Society of America Journal*, **64**(3), 1035, DOI: 10.2136/sssaj2000.6431035x, 2000.

Mattson L. E. 2000. The influence of a debris cover on the mid-summer discharge of Dome Glacier, Canadian Rocky Mountains. in *Debris-covered Glaciers: Proceedings of an international workshop held at the University of Washington*. Seattle, Washington, USA, **264**, 25–34.

Maussion, F., Scherer, D., Mölg, T., Collier, E., Curio, J., Finkelnburg, R. 2014. Precipitation seasonality and variability over the Tibetan Plateau as resolved by the High Asia Reanalysis. *Journal of Climate*, **27**(5), 1910-1927.

Mayer, C., Lambrecht, A., Belò, M., Smiraglia, C., Diolaiuti, G. 2006. Glaciological characteristics of the ablation zone of Baltoro Glacier, Karakoram, Pakistan. *Annals of Glaciology*, **43**(1), 123–131. DOI: 10.3189/172756406781812087

McCarthy, M., Pritchard, H., Willis, I., King, G. 2017. Ground-penetrating radar measurements of debris thickness on Lirung Glacier, Nepal. *Journal of Glaciology*, **63**, 543–555.

McFeeters, S. 1996. The use of the Normalized Difference Water Index (NDWI) in the delineation of open water features. *International Journal of Remote Sensing*, **17**(7), 1425–1432, DOI: 10.1080/01431169608948714.

Meier, M. F., Post, A. 1969. What are glacier surges? *Canadian Journal of Earth Sciences*, **6**, 807-817.

Meehl, G. A., Covey, C., Taylor, K. E., Delworth, T., Stouffer, R. J., Latif, M., McAvaney, B., Mitchell, J.F. 2007. The WCRP CMIP3 multimodel dataset: A new era in climate change research. *Bulletin of the American Meteorological Society*, **88**(9), 1383-1394.

Mihalcea, C., Mayer, C., Diolaiuti, G., Lambrecht, A., Smiraglia, C., Tartari, G. 2006. Ice ablation and meteorological conditions on the debris-covered area of Baltoro glacier, Karakoram, Pakistan. *Annals of Glaciology*, **43**, 292–300. DOI: 10.3189/172756406781812104.

Mihalcea, C., Brock, B. W., Diolaiuti, G., D'Agata, C., Citterio, M., Kirkbride, M. P., Cutler, M. E. J., Smiraglia, C. 2008a. Using ASTER satellite and ground-based surface temperature measurements to derive supraglacial debris cover and thickness patterns on Miage Glacier (Mont Blanc Massif, Italy). *Cold Regions Science and Technology*, **52**, 341-354.

Mihalcea C, Mayer C, Diolaiuti G, D'Agata C, Smiraglia C, Lambrecht A, Vuillermoz E, Tartari G. 2008b. Spatial distribution of debris thickness and melting from remote-sensing and meteorological data, at debris-covered Baltoro glacier, Karakoram, Pakistan. *Annals of Glaciology*, **48**, 49–57. DOI: 10.3189/172756408784700680

Miles, E. S., Pellicciotti, F., Willis, I. C., Steiner, J. F., Buri, P., Arnold, N. S. 2016. Refined energy-balance modelling of a supraglacial pond, Langtang Khola, Nepal. *Annals of Glaciology*, **57**(71), 29–40.

Miles, E. S., Steiner, J. F., Brun, F. 2017. Highly variable aerodynamic roughness length (z_0) for a hummocky debris-covered glacier. *Journal of Geophysical Research: Atmospheres*, in press.

Miller, J. D., Immerzeel, W. W., Rees, G. 2012. Climate Change Impacts on Glacier Hydrology and River Discharge in the Hindu Kush–Himalayas: A Synthesis of the Scientific Basis. *Mountain Research and Development*, **32**(4), 461-467.

Minder, J. R., Mote, P. W., Lundquist, J. D. 2010. Surface temperature lapse rates over complex terrain: Lessons from the Cascade Mountains. *Journal of Geophysical Research: Atmosphere*, **115**, 1–13.

Minora, U., Bocchiola, D., D'Agata, C., Maragno, D., Mayer, C., Lambrecht, A., Mosconi, B., Vuillermoz, E., Senese, A., Compostella, C. and Smiraglia, C. 2013. 2001–2010 glacier changes in the Central Karakoram National Park: a contribution to evaluate the magnitude and rate of the" Karakoram anomaly". *The Cryosphere Discussions*, **7**(3), 2891-2941.

Minora, U., Senese, A., Bocchiola, D., Soncini, A., D'agata, C., Ambrosini, R., Mayer, C., Lambrecht, A., Vuillermoz, E., Smiraglia, C., Diolaiuti, G. 2015. A simple model to evaluate ice melt over the ablation area of glaciers in the Central Karakoram National Park, Pakistan. *Annals of Glaciology*, **56**, 202-216. DOI: 10.3189/2015AoG70A206

Mölg T, Cullen NJ, Kaser G. 2009. Solar radiation, cloudiness and longwave radiation over low-latitude glaciers: implications for mass-balance modelling. *Journal of Glaciology*, **55**, 292–302. DOI: 10.3189/002214309788608822.

Mölg, T., Cullen, N. J., Kaser, G. 2009. Solar radiation, cloudiness and longwave radiation over low-latitude glaciers: implications for mass-balance modelling. *Journal of Glaciology*, **55**(190), 292-302.

Mölg, T., Hardy, D. R. 2004. Ablation and associated energy balance of a horizontal glacier surface on Kilimanjaro. *Journal of Geophysical Research: Atmospheres*, **109**, 159. DOI: 10.1029/2003JD004338.

Mölg, T., Cullen, N. J., Hardy, D. R., Kaser, G., Klok, L. 2008. Mass balance of a slope glacier on Kilimanjaro and its sensitivity to climate. *International Journal of Climatology*, **28**(7), 881–892, DOI: 10.1002/joc.1589, 2008.

Mölg, T., Kaser, G. 2011. A new approach to resolving climate-cryosphere relations: Downscaling climate dynamics to glacier-scale mass and energy balance without statistical scale linking. *Journal of Geophysical Research: Atmospheres*, **116**(D16).
Mölg, T., Maussion, F., Yang, W., Scherer, D. 2012. The footprint of Asian monsoon dynamics in the mass and energy balance of a Tibetan glacier. *The Cryosphere*, **6**(6), 1445–1461, DOI: 10.5194/tc-6-1445-2012, 2012.

Mölg, T., Maussion, F., Scherer, D. 2014. Mid-latitude westerlies as a driver of glacier variability in monsoonal High Asia. *Nature Climate Change*, **4**(1), 68.

Molnar, P., Anderson, R.S., Anderson, S.P. 2007. Tectonics, fracturing of rock, and erosion. *Journal of Geophysical Research: Atmosphere*, **112**, F03014. DOI:10.1029/2005JF000433.

Müller, H. 1985. On the radiation budget in the Alps. *International Journal of Climatology*, **5**(4), 445-462.

Muller, F. 1968. Mitterlfristige Schwankungen der Oberflachen-geschwindigkeit des Khumbu Gletscher am Mt. Everest. *Schweizerische Bauzeitung*, **86**, 2.

Munro, D.S. 1989. Surface roughness and bulk heat transfer on a glacier: comparison with eddy correlation. *Journal of Glaciology*, **35**(121), 343-348.

Munro, D. S. 1990. Comparison of melt energy computations and ablatometer measurements on melting ice and snow. *Arctic and Alpine Research*, **22**, 153-162.

Nagai, H., Fujita, K., Nuimura, T. and Sakai, A. 2013. Southwest-facing slopes control the formation of debris-covered glaciers in the Bhutan Himalaya. *The Cryosphere*, **7**(4), 1303-1314.

Naito, N., Nakawo, M., Kadota, T., Raymond, C. F. 2000, September. Numerical simulation of recent shrinkage of Khuinbu Glacier, Nepal Himalayas. In *Debris-covered Glaciers: Proceedings of an International Workshop Held at the University of Washington in Seattle*. IAHS, Washington, USA, **264**, 245–254.

Nakawo, M., Iwata, S., Watanabe, O., Yoshida, M. 1986. Processes which distribute supraglacial debris on the Khumbu Glacier, Nepal Himalaya. *Annals of Glaciology*, **8**(1), 129-131.
Nakawo, M., Rana, B. 1999. Estimate of Ablation Rate of Glacier Ice under a Supraglacial Debris Layer. *Geografiska Annaler: Series A, Physical Geography,* **81**, 695–701. DOI: 10.1111/1468-0459.00097.

Nakawo, M., Young, G. J. 1981. Field Experiments to Determine the Effect of A Debris Layer on Ablation of Glacier Ice. *Annals of Glaciology*, **2**, 85–91. DOI: 10.3189/172756481794352432

Nakawo, M., Young, G. J. 1982. Estimate of glacier ablation under a debris layer from surface temperature and meteorological variables. *Journal of Glaciology*, **28**, 29–34.

Nayava, J. L. 1974. Heavy monsoon rainfall in Nepal. *Weather*, **29**, 443–450. DOI: 10.1002/j.1477-8696.1974.tb03299.x.

Nicholson, L., Benn, D. I. 2006. Calculating ice melt beneath a debris layer using meteorological data. *Journal of Glaciology*, **52**, 463–470. DOI: 10.3189/172756506781828584.

Nicholson, L., Benn, D. I. 2012. Properties of natural supraglacial debris in relation to modelling sub-debris ice ablation. *Earth Surface Processes and Landforms,* **28**, 490–501.

Nicholson, L. I., Prinz, R., Mölg, T., Kaser, G. 2013. Micrometeorological conditions and surface mass and energy fluxes on Lewis Glacier, Mt Kenya, in relation to other tropical glaciers. *The Cryosphere,* **7**(4), 1205–1225. DOI: 10.5194/tc-7-1205-2013.

Nicholson, L., Benn, D. I. 2006. Calculating ice melt beneath a debris layer using meteorological data. *Journal of Glaciology*, **52**(178), 463–470. DOI: 10.3189/172756506781828584.

Niemelä, S., Räisänen, P., Savijärvi, H. 2001. Comparison of surface radiative flux parameterizations: Part I: Longwave radiation. *Atmospheric Research*, **58**(1), 1-18.

Nobes, D. C., Leary, S. F., Hochstein, M. P., Henry, S. A. 1994. Ground-penetrating radar profiles of rubble-covered temperate glaciers: Results from the Tasman and Mueller glaciers of the Southern Alps of New Zealand. In *SEG Technical Program Expanded Abstracts 1994*, Society of Exploration Geophysicists, 826-829.

Noh, M. J., Howat, I. M. 2015. Automated stereo-photogrammetric DEM generation at high latitudes: Surface Extraction with TIN-based Search-space Minimization (SETSM) validation and demonstration over glaciated regions. *GIScience & Remote Sensing*, **52**, 198–217. DOI: 10.1080/15481603.2015.1008621.

Nolin, A. W., Fetterer, F. M., Scambos, T. A. 2002. Surface roughness characterizations of sea ice and ice sheets: Case studies with MISR data. *IEEE transactions on Geoscience and Remote Sensing*, **40**(7), 1605-1615.

Nuimura, T., Fujita, K., Fukui, K., Asahi, K., Aryal, R., Ageta, Y. 2011. Temporal Changes in Elevation of the Debris-Covered Ablation Area of Khumbu Glacier in the Nepal Himalaya since 1978. *Arctic, Antarctic and Alpine Research*, **43**, 246–255. DOI: 10.1657/1938-4246-43.2.246

Nuimura, T., Fujita, K., Yamaguchi, S., Sharma, R. R. 2012. Elevation changes of glaciers revealed by multitemporal digital elevation models calibrated by GPS survey in the Khumbu region, Nepal Himalaya, 1992–2008. *Journal of Glaciology,* **58**(210), 648–656, DOI: 10.3189/2012JoG11J061.

Oerlemans, J. 2001. *Glaciers and climate change.* CRC Press, USA.

Oh, Y. 2004. Quantitative retrieval of soil moisture content and surface roughness from multipolarized radar observations of bare soil surfaces. *IEEE Transactions on Geoscience and Remote Sensing*, **42**(3), 596-601.

Ohmura, A. 2001. Physical basis for the temperature-based melt-index method. *Journal of applied meteorology*, **40**(4), 753-761.

Østrem G. 1959. Ice melting under a thin layer of moraine, and the existence of ice cores in moraine ridges. *Geografiska Annaler*, **41**, 228–230. DOI: 10.2307/4626805.

Owen, L. A., Finkel, R. C., Caffee, M. W. 2002. A note on the extent of glaciation throughout the Himalaya during the global Last Glacial Maximum. *Quaternary Science Reviews*, **21**(1), 147-157.

Owen, L. A., Benn, D.I., 2005. Equilibrium-line altitudes of the Last Glacial Maximum for the Himalaya and Tibet: an assessment and evaluation of results. *Quaternary International*, **138**, 55-78.

Owen, L.A., Thackray, G., Yi, C., 2009. Mountain glaciation and landscape evolution. *Geomorphology*, **103**(2), 155-157.

Owen, L. A. 2009. Latest Pleistocene and Holocene glacier fluctuations in the Himalaya and Tibet. *Quaternary Science Reviews*, **28**(21), 2150-2164.

Owen, L. A., Dortch, J. M., 2014. Nature and timing of Quaternary glaciation in the Himalayan–Tibetan orogen. *Quaternary Science Reviews*, **88**, 14-54.

Pachauri, R. K., Allen, M. R., Barros, V. R., Broome, J., Cramer, W., Christ, R., Church, J. A., Clarke, L., Dahe, Q., Dasgupta, P., Dubash, N. K. 2014. *Climate change 2014: synthesis report. Contribution of Working Groups I, II and III to the fifth assessment report of the Intergovernmental Panel on Climate Change.* Cambridge University Press, Cambridge, UK.

Pan, B. T., Geng, H. P., Hu, X. F., Sun, R. H., Wang, C. 2010. The topographic controls on the decadal-scale erosion rates in Qilian Shan Mountains, NW China. *Earth and Planetary Science Letters*, **292**(1), 148-157.

Parry, M. L., Canziani, O., Palutikof, J., van der Linde, P., Hanson, C. 2007. *Climate change 2007-impacts, adaptation and vulnerability: Working group II contribution to the fourth assessment report of the IPCC (4).* Cambridge University Press, Cambridge, UK.

Paterson, W. 1994. *The Physics of Glaciers.* Butterworth-Heinemann, Oxford.

Paul, F., Huggel, C., Kääb, A. 2004. Combining satellite multispectral image data and a digital elevation model for mapping debris-covered glaciers. *Remote sensing of Environment*, **89**(4), 510-518.

Paul, F., Frey, H., Le Bris, R. 2011. A new glacier inventory for the European Alps from Landsat TM scenes of 2003: Challenges and results. *Annals of Glaciology*, **52**(59), 144–152. DOI: 10.3189/172756411799096295.

Pecci, M., Smiraglia, C. 2000. Advance and retreat phases of the Karakorum glaciers during the 20th century: case studies in Braldo Valley (Pakistan). *Geogr. Fıs. Din. Quat*, **23**(1), 73-85.

Peizhen, Z., Molnar, P., Downs, W. R., 2001. Increased sedimentation rates and grain sizes 24 Myr ago due to the influence of climate change on erosion rates. *Nature*, **410**, 891–897. DOI: 10.1038/35073504.

Pellicciotti, F., Brock, B., Strasser, U., Burlando, P., Funk, M., Corripio, J. 2005. An enhanced temperature-index glacier melt model including the shortwave radiation balance: development and testing for Haut Glacier d'Arolla, Switzerland. *Journal of Glaciology*, **51**(175), 573-587.

Pellicciotti, F., Carenzo, M., Helbing, J., Rimkus, S., Burlando, P. 2009. On the role of subsurface heat conduction in glacier energy-balance modelling. *Annals of Glaciology*, **50**(50), 16-24.

Pellicciotti, F., Buergi, C., Immerzeel, W. W., Konz, M., Shrestha, A. B. 2012. Challenges and uncertainties in hydrological modeling of remote Hindu Kush–Karakoram–Himalayan (HKH) basins: suggestions for calibration strategies. *Mountain Research and Development*, **32**(1), 39-50.

Petersen, L., Pellicciotti, F., Juszak, I., Carenzo, M., Brock, B. 2013. Suitability of a constant air temperature lapse rate over an Alpine glacier: testing the Greuell and Böhm model as an alternative. *Annals of Glaciology*, **54**, 120–130. DOI: 10.3189/2013AoG63A477,

Powell, C. M., Conaghan, P. J. 1973. Plate tectonics and the Himalayas. *Earth and Planetary Science Letters*, **20**(1), 1-12.

Pritchard, H.D. 2017. Asia's glaciers are a regionally important buffer against drought. *Nature*, **545**(7653), 169-174.

Prive, N. C., Plumb, R. A. 2007. Monsoon dynamics with interactive forcing. Part I: Axisymmetric studies. *Journal of Atmospheric Science*, **64**, 1417–1430.

Quincey, D. J., Lucas, R. M., Richardson, S. D., Glasser, N. F., Hambrey, M. J., Reynolds, J. M. 2005. Optical remote sensing techniques in high-mountain environments: application to glacial hazards. *Progress in Physical Geography*, **29**(4), 475-505.
Quincey, D. J., Luckman, A., Benn, D. I. 2009a. Quantification of Everest region glacier velocities between 1992 and 2002, using satellite radar interferometry and feature tracking. *Journal of Glaciology*, **55**, 596–605.

Quincey, D. J., Copland, L., Mayer, C., Bishop, M., Luckman, A., Belò, M. 2009b. Ice velocity and climate variations for Baltoro Glacier, Pakistan. *Journal of Glaciology*, **55**(194), 1061–1071. DOI: 10.3189/002214309790794913

Quincey, D. J., Smith, M., Rounce, D., Ross, A., King, O., Watson, C. 2017. Evaluating morphological estimates of the aerodynamic roughness of debris covered glacier ice. *Earth Surface Processes and Landforms*, in press.

Racoviteanu, A. E., Williams, M. W., Barry, R. G. 2008. Optical remote sensing of glacier characteristics: a review with focus on the Himalaya. *Sensors*, **8**(5), 3355-3383.

Radic, V., Hock, R. 2011. Regionally differentiated contribution of mountain glaciers and ice caps to future sea-level rise. *Nature Geoscience*, **4**(2), 91.

Ragettli, S., Pellicciotti, F. 2012. Calibration of a physically based, spatially distributed hydrological model in a glacierized basin: On the use of knowledge from glaciometeorological processes to constrain model parameters. *Water Resources Research*, **48**(3).

Ragettli, S., Pellicciotti, F., Immerzeel, W. W., Miles, E. S., Petersen, L., Heynen, M., Shea, J. M., Stumm, D., Joshi, S., Shrestha, A. 2015. Unravelling the hydrology of a Himalayan catchment through integration of high resolution in situ data and remote sensing with an advanced simulation model. *Advances in Water Resources*, **78**, 94–111. DOI: 10.1016/j.advwatres.2015.01.013, 2015.

Rahman, M. M., Moran, M. S., Thoma, D. P., Bryant, R., Collins, C. H., Jackson, T., Orr, B. J., Tischler, M. 2008. Mapping surface roughness and soil moisture using multi-angle radar imagery without ancillary data. *Remote Sensing of Environment*, **112**(2), 391-402.

Rajagopalan, B., Molnar, P. 2013. Signatures of Tibetan Plateau heating on Indian summer monsoon rainfall variability. *Journal of Geophysical Research: Atmospheres*, **118**(3), 1170-1178.

Ranzi, R., Grossi, G., Iacovelli, L., Taschner, S. 2004. Use of multispectral ASTER images for mapping debris-covered glaciers within the GLIMS project. *IEEE*, **2**, 1144–1147.

Rasband, W. S. 2008. ImageJ [online] Available from: http://rsbweb. nih. gov/ij/.

Rees, H. G., Collins, D. N. 2006. Regional differences in response of flow in glacier-fed Himalayan rivers to climatic warming. *Hydrological processes*, **20**(10), 2157-2169.

Regmi, D., Watanabe, T., 2009. Rockfall activity in the Kangchenjunga area, Nepal Himalaya. *Permafrost and Periglacial Processes*, **20**(4), 390-398.

Reid, T. D., Brock, B. W. 2010. An energy-balance model for debris-covered glaciers including heat conduction through the debris layer. *Journal of Glaciology*, **56**(199), 903–916. DOI: 10.3189/002214310794457218, 2010.

Reid, T. D., Carenzo, M., Pellicciotti, F., Brock, B. W. 2012. Including debris cover effects in a distributed model of glacier ablation. *Journal of Geophysical Research: Atmospheres*, **117**. DOI: 10.1029/2012JD017795

Reid, T. D., Brock, B. W. 2014. Assessing ice-cliff backwasting and its contribution to total ablation of debris-covered Miage glacier, Mont Blanc massif, Italy. *Journal of Glaciology*, **60**(219), 3–13. DOI: 10.3189/2014JoG13J045

Reijmer, C. H., Hock, R. 2008. Internal accumulation on Storglaciären, Sweden, in a multi-layer snow model coupled to a distributed energy- and mass-balance model. *Journal of Glaciology*, **54**(184), 61–72. DOI: 10.3189/002214308784409161, 2008.

Reynolds, J. M. 2000. On the formation of supraglacial lakes on debris-covered glaciers. In *Debris-covered Glaciers: Proceedings of an international workshop held at the University of Washington*. Seattle, Washington, USA, **264**, 153–161.

Reznichenko, N., Davies, T., Shulmeister, J., McSaveney, M. 2010. Effects of debris on ice-surface melting rates: an experimental study. *Journal of Glaciology*, **56**, 384–394. DOI: 10.3189/002214310792447725

RGI Consortium. 2017. *Randolph Glacier Inventory – A Dataset of Global Glacier Outlines*. Version 6.0. Global Land Ice Measurements from Space, Colorado, USA. Digital Media. DOI: https://doi.org/10.7265/N5-RGI-60

Richards, B. W. 2000. Luminescence dating of Quaternary sediments in the Himalaya and High Asia: a practical guide to its use and limitations for constraining the timing of glaciation. *Quaternary International*, **65**, 49-61.

Richardson, S. D., Reynolds, J. M. 2000. An overview of glacial hazards in the Himalayas. *Quaternary International*, **65**, 31-47.

Ridley, J., Wiltshire, A., Mathison, C. 2013. More frequent occurrence of westerly disturbances in Karakoram up to 2100. *Science of The Total Environment*, **468**, 31-35.

Rignot, E. 1996. Tidal motion, ice velocity and melt rate of Petermann Gletscher, Greenland, measured from radar interferometry. *Journal of Glaciology*, **42**(142), 476-485.

Romanovsky, V. E., Osterkamp, T. E. 2000. Effects of unfrozen water on heat and mass transport processes in the active layer and permafrost. *Permafrost and Periglacial Processes,* **11**, 219–239. DOI: 10.1002/1099-1530(200007/09)11:3<219::AID-PPP352>3.0.CO;2-7,

Rounce, D. R., McKinney, D. C. 2014. Debris thickness of glaciers in the Everest area (Nepal Himalaya) derived from satellite imagery using a nonlinear energy balance model. *The Cryosphere*, **8**, 1317–1329. DOI: 10.5194/tc-8-1317-2014.

Rounce D. R., Quincey, D. J., McKinney, D. C. 2015. Debris-covered glacier energy balance model for Imja-Lhotse Shar Glacier in the Everest Region of Nepal. *The Cryosphere*, **9**, 2295–2310. DOI: 10.5194/tc-9-2295-2015.

Rounce, D.R., Watson, C.S., McKinney, D.C. 2017. Identification of hazard and risk for glacial lakes in the Nepal Himalaya using satellite imagery from 2000–2015. *Remote Sensing*, **9**(7), 654.

Rowan, A. V., Egholm, D. L., Quincey, D. J., Glasser, N. F. 2015. Modelling the feedbacks between mass balance, ice flow and debris transport to predict the response to climate change of debris-covered glaciers in the Himalaya. *Earth and Planetary Science Letters,* **430**, 427–438. DOI: 10.1016/j.epsl.2015.09.004.

Rowan, A.V. 2017. The 'Little Ice Age' in the Himalaya: A review of glacier advance driven by Northern Hemisphere temperature change. *The Holocene*, **27**(2), 292-308.

Sakai, A., Nakawo, M., Fujita, K. 1998. Melt rate of ice cliffs on the Lirung Glacier, Nepal Himalayas, 1996. *Bull Glacier Research*, **16**, 57–66.

Sakai, A., Takeuchi, N., Fujita, K., Nakawo, M. 2000. Role of supraglacial ponds in the ablation process of a debris-covered glacier in the Nepal Himalayas. In *Debris-covered Glaciers: Proceedings of an international workshop held at the University of Washington*. Seattle, Washington, USA, **264**, 119-132.

Sakai, A., Nakawo, M., Fujita, K. 2002. Distribution characteristics and energy balance of ice cliffs on debris-covered glaciers, Nepal Himalaya. *Arctic, Antarctic, and Alpine Research*, **34**(1), 12–19. DOI: 10.2307/1552503.

Sakai, A., Fujita, K., Kubota, J. 2004. Evaporation and percolation effect on melting at debris-covered Lirung Glacier, Nepal Himalayas, 1996. *Bulletin of Glaciological Research*, **21**, 9-16.

Salerno, F., Guyennon, N., Thakuri, S., Viviano, G., Romano, E., Vuillermoz, E., Cristofanelli, P., Stocchi, P., Agrillo, G., Ma, Y., Tartari, G. 2015. Weak precipitation, warm winters and springs impact glaciers of south slopes of Mt. Everest (central Himalaya) in the last 2 decades (1994–2013). *The Cryosphere*, **9**, 1229–1247. DOI: 10.5194/tc-9-1229-201

Sappington, J., Longshore, K., Thompson, D. 2007. Quantifying landscape ruggedness for animal habitat analysis: a case study using bighorn sheep in the Mojave Desert. *Journal of Wildlife Management*, **71**, 1419-1426.

Schauwecker, S., Rohrer, M., Huggel, C., Kulkarni, A., Ramanathan, A. L., Salzmann, N., Stoffel, M. and Brock, B. 2015. Remotely sensed debris thickness mapping of Bara Shigri glacier, Indian Himalaya. *Journal of Glaciology*, **61**(228), 675-688.

Scherler, D., Bookhagen, B., Strecker, M. R. 2011. Spatially variable response of Himalayan glaciers to climate change affected by debris cover. *Nature Geoscience*, **4**, 156–159. DOI: 10.1038/ngeo1068.

Scherler, D. 2014. Climatic limits to headwall retreat in the Khumbu Himalaya, eastern Nepal. *Geology,* **42**, 1019–1022.

Searle, M. P. 1991. Geology and tectonics of the Karakoram Mountains. John Wiley & Sons, New Jersey, USA.

Searle, M. P., Parrish, R. R., Thow, A. V., Noble, S. R., Phillips, R. J., Waters, D. J. 2010. Anatomy, age and evolution of a collisional mountain belt: The Baltoro granite batholith and Karakoram Metamorphic Complex, Pakistani Karakoram. *Journal of the Geological Society*, **167**(1), 183–202. DOI: 10.1144/0016-76492009-043

Searle, M. P., Simpson, R. L., Law, R. D., Parrish, R. R., Waters, D. J. 2003. The structural geometry, metamorphic and magmatic evolution of the Everest massif, High Himalaya of Nepal–South Tibet. *Journal of the Geological Society*, **160**(3), 345-366.

Searle, M. P., Windley, B. F., Coward, M. P., Cooper, D. J. W., Rex, A. J., Rex, D., Tingdong, L., Xuchang, X., Jan, M. Q., Thakur, V. C., Kumar, S. 1987. The closing of Tethys and the tectonics of the Himalaya. *Geological Society of America Bulletin*, **98**(6), 678-701.

Seong, Y. B., Owen, L. A., Bishop, M. P., Bush, A., Clendon, P., Copland, L., Shroder, J. F. 2007. Quaternary glacial history of the Central Karakoram. *Quaternary Science Reviews*, **26**(25–28), 3384–3405. DOI: 10.1016/j.quascirev.2007.09.015

Seong, Y. B., Owen, L. A., Caffee, M. W., Kamp, U., Bishop, M. P., Bush, A., Copland, L., Shroder, J. F. 2009. Rates of basin-wide rockwall retreat in the K2 region of the Central Karakoram defined by terrestrial cosmogenic nuclide 10 Be. *Geomorphology*, **107**, 254-262.

Sharma P., Pratap T. 1994. Population, Poverty, and Development issues in the Hindu Kush Himalayas in *Development of Poor Mountain Areas*, Proceedings of an international forum, ICIMOD, Beijing.

Shaw, T. E., Brock, B. W., Fyffe, C. L., Pellicciotti, F., Rutter, N., Diotri, F. 2016. Air temperature distribution and energy-balance modelling of a debris-covered glacier. *Journal of Glaciology,* **62**, 185–198. DOI: 10.1017/jog.2016.31

Shea, J. M., Immerzeel, W. W., Wagnon, P., Vincent, C., Bajracharya, S. 2015. Modelling glacier change in the Everest region, Nepal Himalaya. *The Cryosphere,* **9**, 1105–1128. DOI: 10.5194/tc-9-1105-2015.

Shekhar, M. S., Chand, H., Kumar, S. 2010. Climate-change studies in the western Himalaya. *Annals of Glaciology*, **51**, 105–112. DOI: 10.3189/172756410791386508.

Sherpa, S. F., Wagnon, P., Brun, F., Berthier, E., Vincent, C., Lejeune, Y., Arnaud, Y., Kayastha, R. B., Sinisalo, A. 2017. Contrasted surface mass balance of debris-free glaciers

observed between the southern and inner parts of the Everest region (2007–2015). *Journal of Glaciology*, in press.

Shi, Y. 2002. Characteristics of late Quaternary monsoonal glaciation on the Tibetan Plateau and in East Asia. *Quaternary International*, **97**, 79-91.

Shrestha, A. B., Wake, C. P., Dibb, J. E., Mayewski, P. A. 2000. Precipitation fluctuations in the Nepal Himalaya and its vicinity and relationship with some large scale climatological parameters. *International Journal of Climatology*, **20**(3), 317-327.

Shrestha, A. B., Aryal, R. 2011. Climate change in Nepal and its impact on Himalayan glaciers. *Regional Environmental Change*, **11**(1), 65-77.

Shroder, J. F., Bishop, M. P., Copland, L., Sloan, V. F. 2000. Debris-covered Glaciers and Rock Glaciers in the Nanga Parbat Himalaya, Pakistan. *Geografiska Annaler: Series A, Physical Geography,* **82**, 17–31. DOI: 10.1111/j.0435-3676.2000.00108.x.

Shroder Jr, J.F., Scheppy, R.A., Bishop, M.P. 1999. Denudation of small alpine basins, Nanga Parbat Himalaya, Pakistan. Arctic, *Antarctic, and Alpine Research*, **31**, 121-127.

Shugar, D. H., Rabus, B. T., Clague, J. J., Capps, D. M. 2012. The response of Black Rapids Glacier, Alaska, to the Denali earthquake rock avalanches. *Journal of Geophysical Research: Earth Surface*, **117**(F1).

Shukla, A., Gupta, R. P., Arora, M. K. 2010. Delineation of debris-covered glacier boundaries using optical and thermal remote sensing data. *Remote Sensing Letters*, **1**(1), 11-17.

Sicart, J. E., Pomeroy, J. W., Essery, R. L. H., Bewley, D. 2006. Incoming longwave radiation to melting snow: observations, sensitivity and estimation in Northern environments. *Hydrological Processes*, **20**, 3697–3708. DOI: 10.1002/hyp.6383.

Sirocko, F., Sarnthein, M., Lange, H., Erlenkeuser, H. 1991. Atmospheric summer circulation and coastal upwelling in the Arabian Sea during the Holocene and the last glaciation. *Quaternary Research*, **36**(1), 72-93.

Smiraglia, C., Mayer, C., Mihalcea, C., Diolaiuti, G., Belò, M., Vassena, G. 2007. 26 Ongoing variations of Himalayan and Karakoram glaciers as witnesses of global changes: recent studies on selected glaciers. *Developments in Earth Surface Processes*, **10**, 235-247.

Smith, G. D. 1985. *Numerical solution of partial differential equations: finite difference methods.* Oxford University Press, Oxford.

Smith, M. W., Quincey, D. J., Dixon, T., Bingham, R. G., Carrivick, J. L., Irvine-Fynn, T. D. L., Rippin, D. M. 2016. Aerodynamic roughness of glacial ice surfaces derived from high-resolution topographic data. *Journal of Geophysical Research: Earth Surface*, **121**(4), 748–766, DOI: 10.1002/2015JF003759, 2016.

Smithson, P. A. 2002. Climate change 2001: the scientific basis. Contribution of Working Group 1 to the Third Assessment Report of the Intergovernmental Panel on Climate Change. *International Journal of Climatology*, **22**(9), 1144-1144.

Solano, N. A., Clarkson, C. R., Krause, F. F. 2016. Characterization of fine-scale rock structure and differences in mechanical properties in tight oil reservoirs: An evaluation at the scale of elementary lithological components combining photographic and X-ray computed tomographic imaging, profile-permeability and microhardness testing. *Journal of Unconventional Oil and Gas Resources*, **15**, 22-42.

Soncini, A., Bocchiola, D., Confortola, G., Minora, U., Vuillermoz, E., Salerno, F., Viviano, G., Shrestha, D., Senese, A., Smiraglia, C., Diolaiuti, G. 2016. Future hydrological regimes and glacier cover in the Everest region: The case study of the upper Dudh Koshi basin. *Science of The Total Environment*, **565**, 1084–1101. DOI: 10.1016/j.scitotenv.2016.05.138

Steiner, J. F., Pellicciotti, F. 2015. Variability of air temperature over a debris-covered glacier in the Nepalese Himalaya. *Annals of Glaciology*, **57**, 295–307. DOI: 10.3189/2016AoG71A066.

Stern, N. H. 2007. *The economics of climate change*. Cambridge University Press, Cambridge, UK.

Strasser, U., Corripio, J., Pellicciotti, F., Burlando, P., Brock, B., Funk, M. 2004. Spatial and temporal variability of meteorological variables at Haut Glacier d'Arolla (Switzerland) during the ablation season 2001: Measurements and simulations. *Journal of Geophysical Research: Atmospheres*, **109**. DOI: 10.1029/2003JD003973

Sutton, R. T., Dong, B., Gregory, J. M. 2007. Land/sea warming ratio in response to climate change: IPCC AR4 model results and comparison with observations. *Geophysical Research Letters*, **34**(2).

Suzuki, R., Fujita, K., Ageta, Y. 2007. Spatial distribution of thermal properties on debris-covered glaciers in the Himalayas derived from ASTER data. *Bulletin of Glaciological Research*, **24**, 13.

Swift, D. A., Nienow, P. W., Hoey, T. B., Mair, D. W. 2005. Seasonal evolution of runoff from Haut Glacier d'Arolla, Switzerland and implications for glacial geomorphic processes. *Journal of Hydrology*, **309**(1), 133-148. DOI: 10.1016/j.jhydrol.2004.11.016.

Tahir, A. A., Chevallier, P., Arnaud, Y., Neppel, L., Ahmad, B. 2011. Modeling snowmelt-runoff under climate scenarios in the Hunza River basin, Karakoram Range, Northern Pakistan. *Journal of Hydrology*, **409**(1), 104-117.

Takeuchi, Y., Kayastha, R. B., Nakawo, M. 2000. Characteristics of ablation and heat balance in debris-free and debris-covered areas on Khumbu Glacier, Nepal Himalayas, in the pre-monsoon season. In *Debris-covered Glaciers: Proceedings of an international workshop held at the University of Washington*. Seattle, Washington, USA, **264**, 53–62.

Thakuri, S., Salerno, F., Smiraglia, C., Bolch, T., D'Agata, C., Viviano, G., Tartari, G. 2014. Tracing glacier changes since the 1960s on the south slope of Mt. Everest (central Southern Himalaya) using optical satellite imagery. *The Cryosphere,* **8**(4), 1297–1315. DOI: 10.5194/tc-8-1297-2014.

Thayyen, R. J., Gergan, J. T. 2010. Role of glaciers in watershed hydrology: a preliminary study of a" Himalayan catchment". *The Cryosphere*, **4**(1), 115.

Tovar, D. S., Shulmeister, J., Davies, T. R., 2008. Evidence for a landslide origin of New Zealand's Waiho Loop moraine. *Nature Geoscience*, **1**, 524–526. DOI: 10.1038/ngeo249

Turner, A. G., Annamalai, H. 2012. Climate change and the South Asian summer monsoon, *Nature Climate change*, **2**(8), 587–595. DOI: 10.1038/nclimate1495, 2012.

Van Den Broeke, M., Reijmer, C., Van As, D., Boot, W. 2006. Daily cycle of the surface energy balance in Antarctica and the influence of clouds. *International Journal of Climatology*, **26**, 1587–1605. DOI: 10.1002/joc.1323.

Ueda, H., Iwai, A., Kuwako, K., Hori, M. E. 2006. Impact of anthropogenic forcing on the Asian summer monsoon as simulated by eight GCMs. *Geophysical Research Letters*, **33**(6).

Verbunt, M., Gurtz, J., Jasper, K., Lang, H., Warmerdam, P., Zappa, M. 2003. The hydrological role of snow and glaciers in alpine river basins and their distributed modeling. *Journal of Hydrology*, **282**, 36–55.

Vincent, C., Wagnon, P,, Shea, J., Immerzeel, W., Kraaijenbrink, P., Shrestha, D., Sorunco, A., Arnaud, Y., Brun, F., Berthier, E., Sherpa, S. 2016. Reduced melt on debris-covered glaciers: investigations from Changri Nup Glacier, Nepal. *The Cryosphere*, **10**, 1845–1858.

Wake, C. P. 1989. Glaciochemical investigations as a tool for determining the spatial and seasonal variation of snow accumulation in the central Karakoram, northern Pakistan. *Annals of Glaciology*, **13**, 279-284.

Wagnon, P., Ribstein, P., Francou, B., Pouyaud, B. 1999. Annual cycle of energy balance of Zongo Glacier, Cordillera Real, Bolivia. *Journal of Geophysical Research: Atmospheres*, **104**, 3907–3923. DOI: 10.1029/1998JD200011.

Wagnon, P., Lafaysse, M., Lejeune, Y., Maisincho, L., Rojas, M., Chazarin, J. P. 2009. Understanding and modeling the physical processes that govern the melting of snow cover in a tropical mountain environment in Ecuador. *Journal of Geophysical Research: Atmospheres*, **114**(D19). DOI: 10.1029/2009JD012292, 2009.

Warren, S. G. 2017. Impurities in Snow: Effects on Albedo and Snowmelt (Review). *Annals of Glaciology,* **5**, 177–179. DOI: 10.1017/S0260305500003700.

Watanabe, O., Iwata, S., Fushimi, H. 1986. Topographic characteristics in the ablation area of the Khumbu Glacier, Nepal Himalaya. *Annals of Glaciology*, **8**(1), 177-180.

Watson, C. S., Quincey, D. J., Carrivick, J. L., Smith, M. W. 2016. The dynamics of supraglacial ponds in the Everest region, central Himalaya. *Global and Planetary Change*, **142**, 14–27. DOI: 10.1016/j.gloplacha.2016.04.008.

Wentworth, C. K. 1914. A scale of grade and class terms for grainic sediments, *The Journal of Geology,* **30**(5), 377–392.
Wessels, R. L., Kargel, J. S., Kieffer, H. H. 2002. ASTER measurement of supraglacial lakes in the Mount Everest region of the Himalaya. *Annals of Glaciology*, **34**(1), 399–408. DOI: 10.3189/172756402781817545.

Westoby, M. J., Brasington, J., Glasser, N. F., Hambrey, M. J., Reynolds, J. M. 2012. "Structure-from-Motion" photogrammetry: A low-cost, effective tool for geoscience applications. *Geomorphology*, **179**, 300–314. DOI: 10.1016/j.geomorph.2012.08.021.

Westoby, M.J., Brasington, J., Glasser, N.F., Hambrey, M.J., Reynolds, J.M., Hassan, M.A.A.M., Lowe, A. 2015. Numerical modelling of glacial lake outburst floods using physically based dam-breach models. *Earth Surface Dynamics*, **3**(1), 171.

Willis, I., Arnold, N., Brock, B. 2002. Effect of snowpack removal on energy balance, melt and runoff in a small supraglacial catchment. *Hydrological processes*, **16**, 2721–2749.

Winkler, S., Matthews, J. A. 2010. Observations on terminal moraine-ridge formation during recent advances of southern Norwegian glaciers. *Geomorphology*, **116**, 87–106.

Wissman, H.V. 1959. The Present Day Glacier Cover and Snowline in High Asia. *Akad. D wis. Und d Litt*, **14**, .1101-1436.

Wu, C., Wu, J., Luo, Y., Zhang, L., DeGloria, S. D. 2009. Spatial Prediction of Soil Organic Matter Content Using Cokriging with Remotely Sensed Data. *Soil Science Society of America Journal*, **73**(4), 1202–1208. DOI: 10.2136/sssaj2008.0045.

Xu, J., Ma, Y. 2009. Response of the hydrological regime of the Yellow River to the changing monsoon intensity and human activity. *Hydrological Sciences Journal*, **54**(1), 90-100.

Yanai, M., Wu, G. X. 2006. Effects of the Tibetan Plateau. In *The Asian Monsoon*. Springer Science and Business Media, Berlin, Germany. 513-549.

Yasunari T. 1976. Seasonal Weather Variations in Khumbu Himal. *Journal of the Japanese Society of Snow and Ice*, **38**, 74–83. DOI: 10.5331/seppyo.38.Special_74.

Yasunari T. 1979. Cloudiness fluctuations associated with the Northern Hemisphere summer monsoon. *Journal of the Meteorological Society of Japan*, **57**, 227–242.

Yihui, D., Chan, J. C. 2005. The East Asian summer monsoon: an overview. *Meteorology and Atmospheric Physics*, **89**(1), 117-142.

Young, G. J., Hewitt, K. 1990. Glaciohydrological features of the Karakoram Himalaya: Measurement possibilities and constraints. In *Hydrology of mountainous areas*. IAHS Publication, Wallingford. 273–284.

Zhang, Y., Fujita, K., Liu, S., Liu, Q., Nuimura, T. 2011. Distribution of debris thickness and its effect on ice melt at Hailuogou glacier, southeastern Tibetan Plateau, using in situ surveys and ASTER imagery. *Journal of Glaciology*, **57**, 1147–1157. DOI: 10.3189/002214311798843331.

Zhisheng, A., Kutzbach, J. E., Prell, W. L., Porter, S. C. 2001. Evolution of Asian monsoons and phased uplift of the Himalaya-Tibetan plateau since Late Miocene times. *Nature*, **411**(6833), 62.

Zhong, D., Ding, L. 1996. Rising process of the Qinghai-Xizang (Tibet) Plateau and its mechanism. *Science in China Series D: Earth Sciences*, **39**(4), 369-379.

Appendices

i. Temperature sensor assessment

Previous studies have established that iButton sensors are not waterproof (Lewkowicz, 2008) and so mitigated against device failure by sealing the sensors in laminate pouches (e.g. Gubler et al., 2011). However, these studies either overlooked the potential effect of waterproof casing on temperature measurements, or did not test the sensors in such waterproof casing in extreme environments (e.g. Roznik et al., 2012; Minder et al, 2010). We therefore tested the effects of a waterproof casing on measurement accuracy and precision under extreme conditions prior to sensor deployment in the field. The iButton sensors were tested in controlled environments alongside TinyTag sensors (Plus 2 TGP-4520) to determine the accuracy of the iButton sensors with and without a waterproof casing, following a similar procedure to Minder et al. (2010). Three pairs of iButton sensors were placed in polycarbonate plastic containers (0.2 × 0.2 × 0.1 m in size) of free-flowing air, water and water ice for 62 days (340 hrs), along with TinyTag sensors placed in the same air and water containers for comparison. A Tinytag sensor was not placed in water due to a restriction on equipment available, and so preference was given to the two environments the iButtons were most likely to experience during a monsoon season on the debris-covered surface of Khumbu Glacier. In each case, one iButton was encased in a polyethylene bag and one was not. The containers of air and water were placed outside in indirect solar radiation, while the container of ice was stored in a laboratory freezer at -26°C, to replicate the potential range of conditions which may occur on a mountain glacier. All sensors recorded ambient temperatures at hourly intervals (Figure A1).

The TinyTag sensors measured temperature to a greater accuracy than the iButton sensors (a resolution of ±0.4 °C rather than ±1.0 °C), resulting in smaller variations in temperature measured by these sensors. A consistent offset in measured temperature was observed between the iButtons encased in a waterproof bag and those that were not. The encased iButtons recorded temperatures commonly around 0.5 °C lower than those in free-flowing air, and recorded temperatures typically around 0.5 °C higher in the water and ice experiments (Figure A1). The mean difference in temperature series between iButtons were 0.23 ± 0.11 °C, -0.33 ± 0.23 °C, in air and water respectively; the mean contrast between unenclosed iButtons and the TinyTag data was -0.12 ± 0.22 °C and 0.14

± 0.22 °C for air and water respectively. Although temperatures measured between free iButtons, encased iButtons and Tinytag temperature sensors varied, all variations were less than 1°C; this uncertainty is below the manufacturers' stated accuracy for iButton sensors. The higher deviations for the iButtons in ice suggested that there was the potential for elevated uncertainties of ~1°C if sensors were in direct contact with ice. Nonetheless, the use of a combination of iButton and Tinytag temperature sensors, and of polyethylene bags as waterproof casing for the iButtons (as Tinytag sensors have a waterproof design) was deemed appropriate for field measurements. The continued function of iButtons not encased and placed in water or ice also suggested the iButtons exceeded the water resistance stated by the manufacturer.

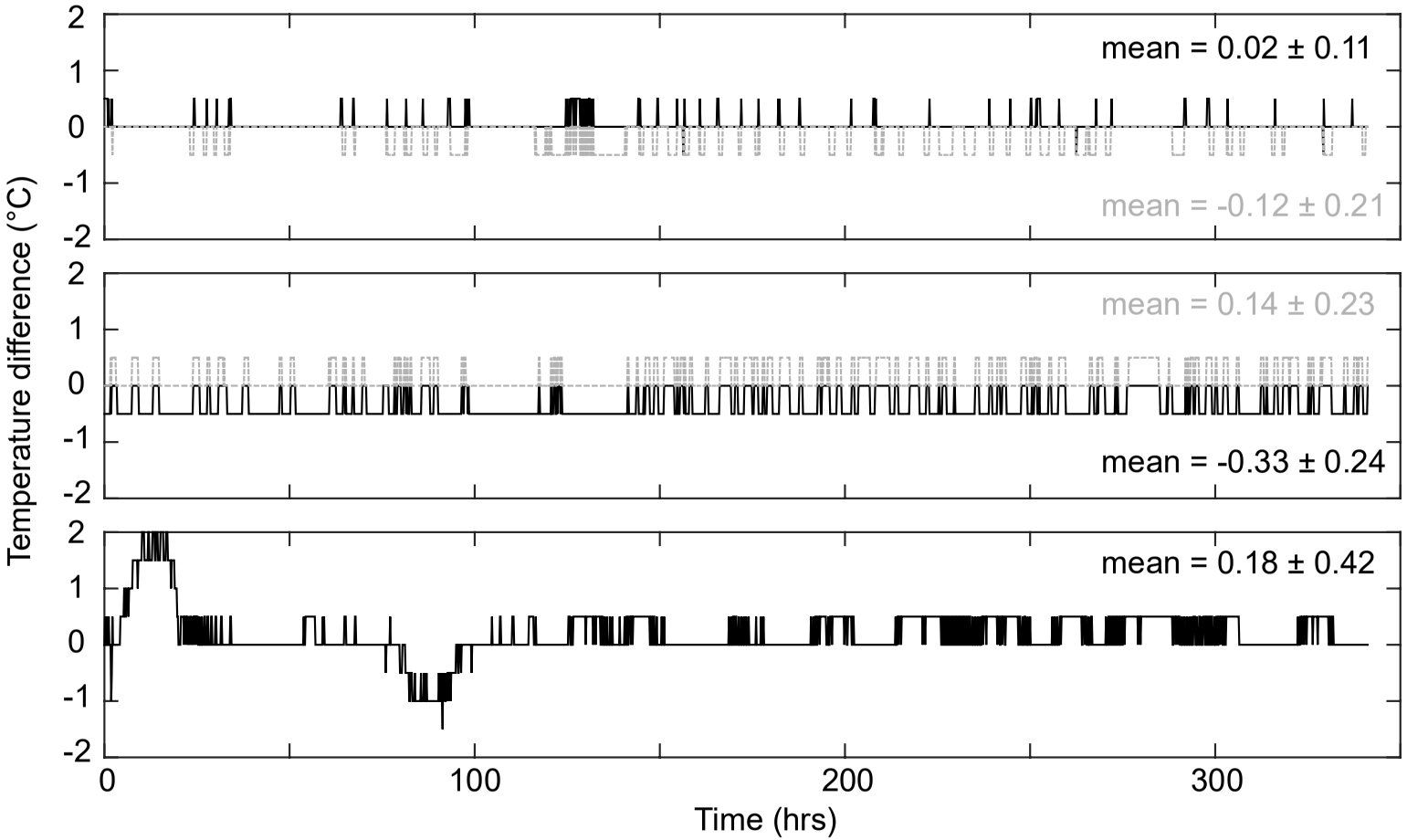

Figure A1: Temperature differences recorded by free and contained iButton sensors (black), and Tinytag sensors (grey), for (a) air, (b) water and (c) ice in laboratory conditions.

ii. Supplementary material 2

Table A2: Rules used to classify surface reflectance and surface roughness using Pleiades data in RSGISLib, and the hierarchal rules assigned to each class to create the inputs maps for the distributed model simulations.

Surface cover type	Classification rules		Values assigned
Surface reflectance			
Granite debris cover	Mean Blue	>1550	0.61
	Mean Red	>1700	
	Mean Green	>1500	
	Normalised difference vegetation index	>–0.05	
	Near infrared standard deviation	<180	
Ice	Mean Near infrared	> 1870	0.34
	Near infrared standard deviation	>180	
Water	Normalised difference water index	>0.03	No data
Soil	Normalised difference vegetation index	>0.03	0.27
Schist debris cover	Normalised difference vegetation index	<0.03	0.43
Surface roughness	Near infrared standard deviation		
Boulders:			0.01473
Granite		≥120	
Schist		≥160	
Soil		≥95	
Gravel to cobbles:			0.00878
Granite		<120	
Schist		<160	
Soil		<95	
Sand			0.00218
Granite		<105	
Schist		<130	
Soil		<60	0.00136
Ice		N/A	0.001
Water		N/A	No data

iii. Supplementary material 3

Table A3: Error matrix for surface reflectance classification, calculated through comparison of *in situ* data and classification of the cell in which point data were located.

Reference data

Classification data		Granite	Schist	Soil	Row total	User's accuracy
	Granite	34	3	3	*40*	85 %
	Schist	2	16	2	*20*	80 %
	Soil	25	2	58	*85*	68 %
	Column total	*61*	*21*	*63*	*145*	
	Producer's accuracy:	56 %	76 %	92 %		**Overall accuracy: 74 %**

iv. Supplementary material 4

Table A4: Error matrix for surface roughness classification, calculated through comparison of *in situ* data and classification of the cell in which point data were located.

Reference data

Classification data		Boulders	Gravel	Sand	Soil	Row total	User's accuracy
	Boulders	66	17	7	0	*90*	73 %
	Gravel	8	36	0	0	*44*	82 %
	Sand	0	3	6	0	*9*	67 %
	Soil	0	0	0	2	*2*	100 %
	Column total	*74*	*56*	*13*	*2*	*145*	
	Producer's accuracy:	89 %	64 %	46 %	100 %		**Overall accuracy: 76 %**